

Carlos Eduardo Leme Nóbrega
Nisio Carvalho Lobo Brum
Editors

Desiccant-Assisted Cooling

Fundamentals and Applications

 Springer

Desiccant-Assisted Cooling

Carlos Eduardo Leme Nóbrega
Nisio Carvalho Lobo Brum
Editors

Desiccant-Assisted Cooling

Fundamentals and Applications

 Springer

Editors

Carlos Eduardo Leme Nóbrega
Centro Federal de Educação Tecnológica
Celso Suckow da Fonseca
Rio de Janeiro
Brazil

Nisio Carvalho Lobo Brum
Universidade Federal do Rio de Janeiro
Rio de Janeiro
Brazil

ISBN 978-1-4471-5564-5 ISBN 978-1-4471-5565-2 (eBook)
DOI 10.1007/978-1-4471-5565-2
Springer London Heidelberg New York Dordrecht

Library of Congress Control Number: 2013949252

© Springer-Verlag London 2014

This work is subject to copyright. All rights are reserved by the Publisher, whether the whole or part of the material is concerned, specifically the rights of translation, reprinting, reuse of illustrations, recitation, broadcasting, reproduction on microfilms or in any other physical way, and transmission or information storage and retrieval, electronic adaptation, computer software, or by similar or dissimilar methodology now known or hereafter developed. Exempted from this legal reservation are brief excerpts in connection with reviews or scholarly analysis or material supplied specifically for the purpose of being entered and executed on a computer system, for exclusive use by the purchaser of the work. Duplication of this publication or parts thereof is permitted only under the provisions of the Copyright Law of the Publisher's location, in its current version, and permission for use must always be obtained from Springer. Permissions for use may be obtained through RightsLink at the Copyright Clearance Center. Violations are liable to prosecution under the respective Copyright Law. The use of general descriptive names, registered names, trademarks, service marks, etc. in this publication does not imply, even in the absence of a specific statement, that such names are exempt from the relevant protective laws and regulations and therefore free for general use.

While the advice and information in this book are believed to be true and accurate at the date of publication, neither the authors nor the editors nor the publisher can accept any legal responsibility for any errors or omissions that may be made. The publisher makes no warranty, express or implied, with respect to the material contained herein.

Printed on acid-free paper

Springer is part of Springer Science+Business Media (www.springer.com)

Preface

The air-conditioning industry is facing important environmental and regulatory challenges, such as the phase-out of CFC refrigerants, the requirement of higher ventilation rates, and improved air quality by new design standards. There is a close relation among ventilation rates, air quality, and capital and operating costs. This pictures a favorable scenario for the development of technology to supplement or even replace traditional vapor-compression cycles. Evaporative cooling systems are environmentally friendly, but are usually restrained to climates with low average levels of relative humidity. However, the development of both liquid and solid desiccant systems has significantly widened the range of application of such cycles. In addition, the use of desiccants in HVAC systems allows for independent temperature and humidity control in innovative designs, such as hybrid desiccant/vapor-compression systems, or radiant cooling panels. Desiccants also play an important role in energy recovery in air-conditioning facilities, allowing for the chilling units to be unburdened to extra sensible and latent loads associated with ventilation air.

Accordingly, this book addresses fundamental aspects of desiccant systems and recent developments associated with this technology. “[An Introduction to Solid Desiccant Cooling Technology](#)” and “[Status of Liquid Desiccant Technologies and System](#)” are, respectively, devoted to fundamentals of solid and liquid desiccant systems, whereas the mathematical modeling and formulation of desiccant wheels are presented in “[Mathematical Modeling of Heat and Mass Transfer in Regenerators with Desiccant Materials](#)”. “[Influence of Altitude on the Behaviour of Solid Desiccant Dehumidification System](#)” discusses the influence of atmospheric pressure over desiccant wheels, while “[The Performance of Desiccant Wheels for Desiccant Air-Conditioning](#)” analyzes design aspects. “[Separate Sensible and Latent Cooling](#)” presents a hybrid desiccant/vapor-compression system with separate sensible latent load handling. “[Adsorption/Desorption Characteristics of Solid Particles in Desiccant Bed for Different Design Configurations](#)” discusses design aspects of column-based systems, whereas “[Desiccant Dehumidification Integrated with Hydronic Radiant Cooling](#)” addresses the matching of a desiccant system with a radiant cooling panel.

While we are glad to acknowledge the invaluable and cordial assistance of renowned experts who contributed to each chapter, we believe that many

outstanding research efforts, due to different reasons, could not be contemplated in the present edition, for which we express our sincere apologies. Nevertheless, we firmly believe that this book will represent a valuable contribution to the dissemination of desiccant technology. We express our gratitude for the invitation from Mr. Anthony Doyle from Springer, as well as to Ms. Christine Velarde, for the kind and professional assistance throughout the publishing process.

C. E. L. Nóbrega
N. C. L. Brum

Contents

An Introduction to Solid Desiccant Cooling Technology	1
Carlos Eduardo Leme Nóbrega and Nísio Carvalho Lobo Brum	
Status of Liquid-Desiccant Technologies and Systems	25
W. M. Worek and A. Lowenstein	
Mathematical Modeling of Heat and Mass Transfer in Regenerators with Desiccant Materials	47
L. A. Sphaier	
Influence of Altitude on the Behavior of Solid Desiccant Dehumidification System	85
C. R. Ruivo, J. J. Costa and A. R. Figueiredo	
The Performance of Desiccant Wheels for Desiccant Air-Conditioning	109
Mark Goldsworthy and Stephen White	
Separate Sensible and Latent Cooling	143
Jiazhen Ling, Yunho Hwang and Reinhard Radermacher	
Adsorption/Desorption Characteristics of Solid Particles in Desiccant Bed for Different Design Configurations	189
Ahmed M. Hamed	
Desiccant Dehumidification Integrated with Hydronic Radiant Cooling System	217
A. Z. Zainal and A. S. Binghooth	
Application of Liquid Desiccant System	249
Xiaohua Liu and Yi Jiang	

An Introduction to Solid Desiccant Cooling Technology

Carlos Eduardo Leme Nóbrega and Nísio Carvalho Lobo Brum

1 Introduction

Although a thermal comfort zone has been defined by standards in a psychrometric chart, the actual sensation of thermal comfort is an individual response, which requires input from physical, physiological, and even psychological nature [47]. Among other factors, skin evaporation has a major impact over the skin temperature. It has been estimated that evaporation accounts for as much as 20 % of the energy balance in a human body [7]. Moreover, it is well known that allergic and respiratory diseases are closely related to inadequate humidity levels. The most common air-conditioning system, the vapor compression system, operates running air through a cooling coil which operates below air dew point temperature, thereby promoting air cooling and dehumidification in a single process. In a later section, it will be shown that this technique might result in an ineffective and costly humidity control method.

In addition, the increasing concern with environmental impacts and indoor air quality over the last three decades has challenged HVAC designers to develop new technologies to assist or even replace the conventionally used vapor compression systems. Although the Montreal Protocol has recommended some traditionally employed refrigerants to be phased out, potential replacement substances still feature issues related to leak detection, flammability and global warming potential (GWP) [53]. In face of the economic, regulatory, and environmental challenges that have been imposed to the air-conditioning industry, evaporative cooling systems represent a promising solution regarding the ozone layer depletion and the

C. E. L. Nóbrega (✉)

Centro Federal de Educação Tecnológica, Celso Suckow da Fonseca,
CEFET-RJ, Rio de Janeiro, Brazil
e-mail: cadoo1967@gmail.com

N. C. L. Brum

Universidade Federal do Rio de Janeiro, COPPE, Rio de Janeiro, Brazil

indoor air quality standards. It is estimated that there are 30 million of evaporative coolers currently working around the world [10].

Evaporative coolers rely on the water evaporation into an air stream to lower the air temperature. The sensible cooling corresponds to the water enthalpy difference in the vapor and liquid states. Although it offers an alternative from the economical and environmental viewpoints, the use of evaporative coolers is, however, limited to places with low local average humidity levels. Since the temperature drop of the airstream is usually low, evaporative systems typically have to handle high airflow rates, so as to meet a given thermal load. Accordingly, the air movement in the conditioned space is often higher than if vapor compression system is used. This usually results in an increased convective coefficient, improving the thermal comfort sensation.

In any case, the lower the absolute humidity of the airstream, the higher will the cooling capacity evaporative unit. If the air stream can be artificially dried before it is admitted to the evaporative unit, the application of evaporative coolers can be extended to locations with higher average levels of moisture. One way of accomplishing very low levels of humidity is by forcing the airstream through a dehumidifying unit such as a desiccant wheel, which consist of a porous disk strongly impregnated with a hygroscopic material, such as silica gel or molecular sieves. Accordingly, the present chapter describes how desiccant wheels widen the range of applicability of evaporative coolers, in a number of alternative arrangements.

In addition to improving the performance of evaporative systems, it will be shown that solid desiccants can provide a more effective and economical way of air dehumidification, when compared with the conventional mechanical compression systems, which promotes the air cooling and dehumidification in a single process. Accordingly, desiccants allow for the decoupling of the thermal load in latent and sensible components, providing accurate humidity control, and unburdening the evaporator capacity. Moreover, the condenser heat rejection can be used to regeneration air preheat, resulting in rational design energywise, often referred to as hybrid cycle, which are latter described in greater detail.

2 Evaporative Cooling

Figure 1 shows a schematic diagram of an evaporative cooler, which is essentially a device which uses directly recirculated water from a sump. The water is lifted to a distribution system and runs down through a packing media, evaporating into the air as it flows through the wetted surfaces. The non-evaporated liquid is collected by the sump to get recirculated. The use of a packing media, usually made of glass fiber or impregnated cellulose, aims at increasing the surface area per unit volume, usually offering $300 \text{ m}^2/\text{m}^3$ without a considerable pressure loss. Alternatively, an equivalent effect may be obtained by using a bank of spray nozzles [32]. Eliminator plates are usually placed at the air outlet so as to avoid water droplets to be carried out into the air stream.

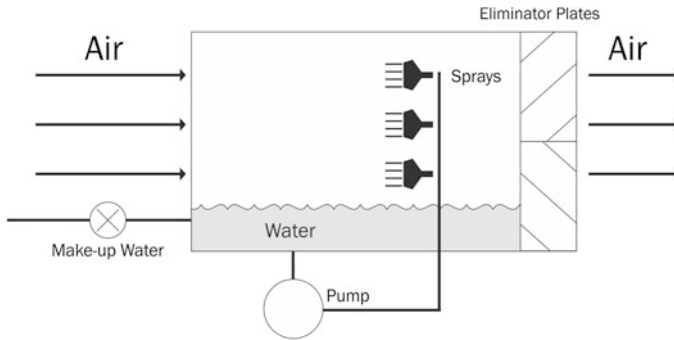
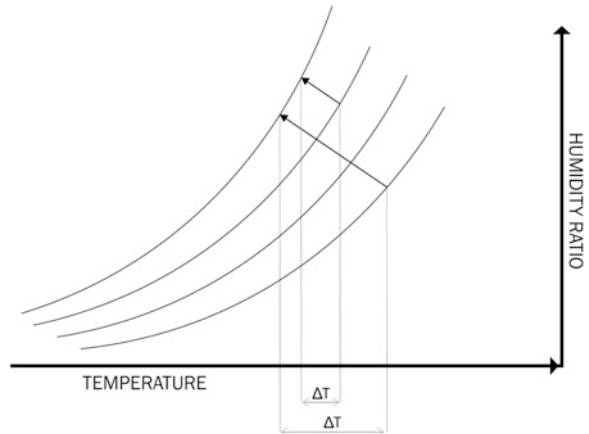


Fig. 1 Schematic of an evaporative cooler

A fundamental characteristic of evaporative coolers is the complete air renovation (100 % of outside air), which requires all the insufflated air to be eventually exhausted. This contrasts to conventional vapor compression systems, which typically recirculate the greater part of the air volume, allowing for air renovation rates as low as 20 %. However, low indoor air quality has been of increasing concern by health authorities, since there is a well-established relation between air pollutant concentrations and respiratory diseases. Indoor environments are often contaminated by toxic substances, in addition to pollutants of biological origin, such as CO, bacteria, and fungus. The outbreak of *Legionella* in the mid-1980s, as well as the SARS, concurred to foster the concern with air quality. The term sick building syndrome has been coined to address such environments [22]. Additional advantages of evaporative coolers include:

- **Increased Particles Removal:** Both the size and amount of particles removed from the air are greater than conventional filters and are comparable to HEPA filters. A 90 % efficiency for 10 micron particles is a typical figure [10]. Accordingly, costs associated with conventional filters are also downsized.
- **Increased Liability:** This is a direct consequence of the simplified maintenance requirements, since the recirculating water pump and the air fan are the only moving parts. Accordingly, replacement parts are commercially available and do not require highly skilled maintenance staff.
- **Reduced Operating Costs:** The electric power required by the pump and the fan is typically much less than a refrigerant compressor. Moreover, improved design allows for reduced water use and a greater useful life. The life of the equipment can be maintained by keeping an algae control, periodical cleaning of the packing and reservoir
- **Reduced Environmental Impacts:** The environmental concern has brought refrigerants to be classified by their GWP and ozone depletion potential (ODP). Traditionally used refrigerants which yield cycles with reasonable pressure ratios and good coefficient of performance (COP) have been ruled out by exhibiting high GWP and ODP indexes. Potential replacements often exhibit

Fig. 2 Psychrometric representation of the evaporative cooling process



issues related to leak detection, flammability, increased condensing pressures, and poor performance. Moreover, decreased heat of vaporization often implies in high refrigerant mass flow rates, implying in larger compressors and refrigerant inventory. Conversely, evaporative coolers use only water as refrigerant.

By observing Fig. 2, it can be concluded that the decrease in the air temperature is strongly dependent on its relative humidity. If the air relative humidity is high, it will not allow for a significant temperature drop before it reaches the saturation state. Even for favorably lower values of relative humidity, the air temperature drop across the evaporative cooler is not typically higher than 6 °C or less. Accordingly, the cooling capacity can be significantly boosted by drying the air before it is admitted to the evaporative cooler. The combination of solid desiccants and evaporative coolers in a single cooling system is usually referred to as desiccant cooling system, which are later described in greater detail. An indirect evaporative cooler offers an alternative of taking advantage of the evaporative cooling effect without increasing the absolute humidity of the process air stream. In this configuration, the water is sprayed over an auxiliary air stream, which is kept apart from the process air stream by a heat exchanger surface. Accordingly, the cooling effect is communicated to the process air stream without contaminating it with moisture. Naturally, indirect evaporative coolers always exhibit a lower effectiveness than direct evaporative systems, since the heat exchanger surface adds to the thermal resistance between the evaporative water droplets and the air stream.

3 Humidity Control in Conventional Systems

Figure 3 shows a schematic of a conventional vapor compression air-conditioning system. Return air from the conditioned room is mixed with outside fresh air in a prescribed proportion which allows for the required indoor air quality. The mixture

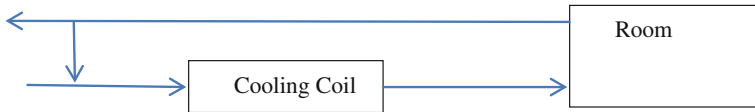


Fig. 3 Schematic representation of single-zone air-conditioning system

is then forced through the cooling coil, where it is simultaneously cooled and dehumidified. Figure 4 shows that the cooling coil line eventually intersects the line which characterizes the room thermal load, known as room sensible heat factor, RSHF. This intersection determines the air state at the room supply condition (SA). The room exhaust air is assumed to be at the thermal comfort condition.

It should be noted that the air at the supply condition is usually located in the immediate vicinity of the saturation curve, and its precise location is dependent on a cooling coil design parameter, known as the bypass factor, (BF). Since the cooling coil operates below the air dew point, the air stream fraction which is in close contact with the coil is at the saturated state, whereas a small fraction of the air stream exits the cooling coil unaffected, at the same state as the inlet. Accordingly, the cooling coil outlet state can be regarded as a mixture of the inlet and the saturation state, typically closer to the later. It should also be noted that the cooling coil inlet state also determines the cooling coil line inclination, the higher the outside air proportion (i.e., the greater the air renovation), the steepest will be the cooling coil line. This eventually will make it difficult, or even impossible, to intersect the RSHF. This also could happen if the RSHF is high, that is, if the room thermal load has a significant latent component. This can be either a characteristic of the original thermal load or the result of a part load condition, in which the sensible contribution is diminished in comparison with the latent. Should that be the case, Fig. 5 shows that an acceptable supply air condition can only be reached with the incorporation of a reheat coil to the system. Accordingly, the air is cooled below the adequate supply air temperature, until a satisfactory humidity level has

Fig. 4 Schematic representation of vapor compression air-conditioning system

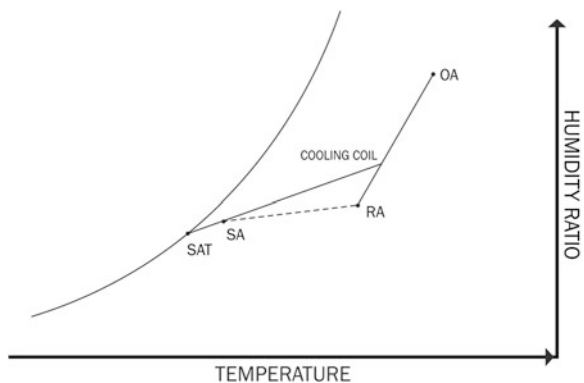
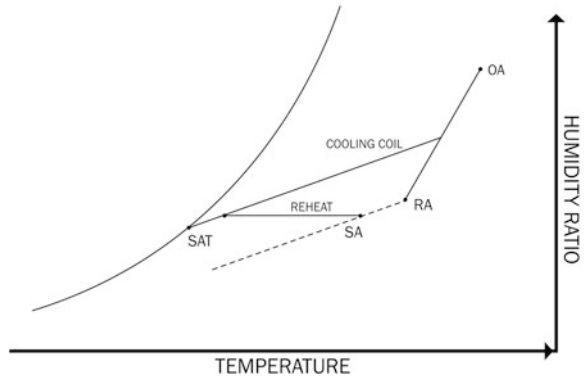


Fig. 5 Schematic representation of vapor compression (reheat) air-conditioning system



been reached. Then, it is admitted to a reheat coil (usually electrically powered) to have its temperature raised back to the adequate supply level, resulting in an energy intensive process. The origin of the problem is the cooling coil inability of simultaneously handling both load components. It is also important to acknowledge that the sensible load has been mitigated over the last four decades, due to improved building envelope design and more efficient lighting, which tends to impose a disproportional dehumidification load on the cooling coil [9].

An additional challenge to vapor compression system arises when the part load performance of the system is analyzed. Chillers are designed to meet the peak of the thermal load and are estimated to run on part load conditions about 90 % of the time. When controlled by a thermostat, the compressor is shut down and the dehumidifying capacity is reduced to zero. Accordingly, all the ventilation fresh air will be admitted to the room without being dehumidified, which will likely result in an excessively humid ambient. It has been suggested that unless the compressor running time exceeds 40 min of each hour, the dehumidifying capacity can be taken as negligible [23]. Surprisingly, a common design malpractice consists of adding capacity to the system, which actually makes the problem more critical. A better solution consists of slightly under dimensioning the system, thereby increasing the number of operating minutes each hour.

In addition to the energy consumption, design aspects of the mechanical dehumidification system can contribute to an unhealthy indoor environment, such as the growth of fungus and microbial organisms in the condensate drainage pans, which can be easily introduced in the supply air ducts, resulting in the increase in allergic reactions and respiratory illness. Moreover, when the adequate supply air temperature is reached, the compressor shuts off, and the water which has not been drained re-evaporates and is carried out into the ambient, resulting in a discomfort condition [29]. As shown in a later section, solid desiccants can assist the vapor compression system by capturing and dumping the excessive moisture contained in the fresh air stream, before it hits the cooling coil. This can be accomplishing by placing an enthalpy recovery wheel swinging between the fresh and exhaust air streams, preventing the excessive humidity to reach the cooling coil. Alternatively,

an active desiccant wheel can be combined with a vapor compression system to form a hybrid cycle, in which the sensible cooling is provided by the later, while the dehumidification is carried out by the former.

4 Desiccant Wheels

Figure 6 shows a schematic diagram of an active desiccant wheel. It consists of a rotating drum fitted with a honeycomb packing. The structure material is coated with a desiccant material, with a resulting desiccant density of $80\text{--}320\text{ kg/m}^3$. The air is force through the microchannels, which are usually have a sinusoidal cross section, with a hydraulic diameter ranging from 0.25 to 1.0 mm and a length ranging from 10 to 20 cm. The desiccant coated walls capture the humidity from the airstream as it flows between each microchannel inlet and outlet. The desiccant material continues the moisture uptake until half or three-quarters of the period of revolution, when the microchannel reaches the regeneration sector. The objective is to purge out the humidity from the desiccant, so as to make it available for the following adsorptive period, ensuring the cyclic operation. The regeneration is achieved by using hot air, which can be obtained from a variety of sources, such as solar energy [18], natural gas [6], internal combustion engine waste heat [2], and geothermal [11]. A combination of thermal and microwave energies to regenerate the wheel has showed promising results [31].

Figure 7 shows the schematic of a passive desiccant wheel, which is often referred to as enthalpy wheel. In enthalpy recovery applications, the regeneration is carried out by the exhaust air from the conditioned space, which still is in the comfort condition (cold and dry), but has to be exhausted for the sake of the indoor air quality. The fresh air stream is, conversely, at the outside air condition (hot and humid), and represents an extra burden for the cooling system. Accordingly, the enthalpy recovery wheel is placed between the fresh and exhaust streams, allowing the later to precool and dry the former. It typically rotates much faster (10–20 rpm) than a desiccant wheel (0.15–0.20 rpm). An important difference is that the

Fig. 6 Schematic representation of an active desiccant wheel

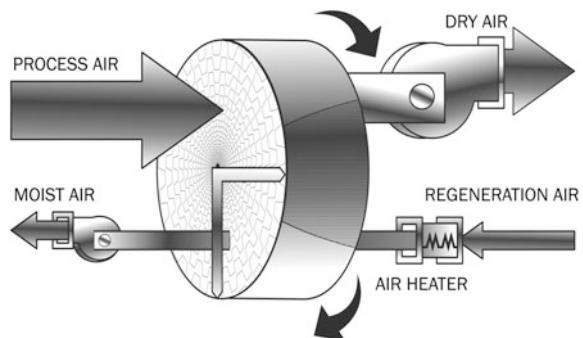
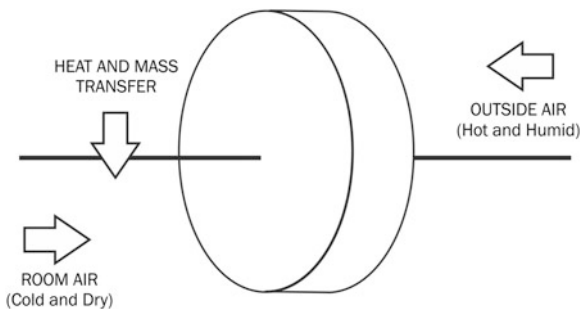


Fig. 7 Schematic representation of a passive desiccant wheel



regeneration is carried out by cold air, allowing for a reduced dehumidifying capacity when compared to an active desiccant wheel. A comparative study revealed that the enthalpy recovery in passive desiccant wheels is as much as twice as in heat wheels [42]. It also has been shown that passive desiccant wheels exhibit a fairly constant effectiveness over varying environmental conditions [44].

Solid desiccant materials offer a high capacity of air dehumidification, a mass transfer process driven by a difference on the vapor pressure in the air stream and the adsorbed layer. Physical adsorption occurs at all solid–fluid interfaces, but is negligible unless the solid has certain characteristics of high affinity to the fluid. Since adsorption is a surface phenomenon, a high level of porosity is a desirable property for a good adsorbent. For instance, 0.03 m^3 of regular density silica gel has an approximate surface area of $8,000 \text{ m}^2$. In addition to the total area, a good adsorbent must exhibit a strong attraction to the fluid to be adsorbed. To better understand this phenomenon, it is useful to compare the state of a solid substance molecule near the surface with the state of a molecule in the interior of the body. In the interior of the body, a particle is uniformly surrounded by similar particle in all directions, being in a state of neutral equilibrium and local minimum potential energy. In contrast, a particle over the body surface is under an unbalanced van der Waals force field and has a greater potential energy. Fluid molecules in the immediate surface neighborhood will be attracted so as to restore the balance in the bonding forces, in a spontaneous process.

Since adsorption is a surface phenomenon, a water molecule has three degrees of movement in the vapor phase, being restricted to two degrees once it is captured by the surface. Accordingly, the loss of a degree of freedom corresponds to a decrease in the disorder of the system, which is represented by a decrease in the system entropy. Even for a reversible process, this can only be accomplished by a heat transfer from the system to its surroundings, which is usually referred to as heat of adsorption.

Polarization, dipole, and quadrupole electrostatic interactions also play an important role in the case of ionic structured adsorbents. Indeed, the adsorption of dipolar H_2O molecules in zeolites may exhibit a large contribution from electrostatic forces, resulting in increased values for the heat released as a consequence of adsorption process. The heat of adsorption provides an accurate estimate of the strength of the bonding between the sorbate and the sorbent [51].

There are several commercially available desiccants. The most commonly applied in desiccant wheels are silica gel and lithium chlorides. Activated carbon, activated alumina, molecular sieves, activated clay and calcium chlorides are also used. Silica gel is a form of silicon dioxide derived from sodium silicate and sulfuric acid, although it is non-toxic and non-corrosive. Regular density (RD) silica gel has a porous size of 2 nm, with a pore volume of 0.3–0.4 cm³/g. It shows a significant pore area per unit volume and is theoretically able to hold up to 40 % of its weight in water vapor, although 0.15 g of adsorbate per gram of dry adsorbent is a more realistic figure in practice. It has been widely used in desiccant wheels, due to its favorable adsorption isotherm over a wide range of relative humidity levels. It is also not resistant to heat and can rapidly deteriorate. Lithium chloride is not a solid desiccant per se, but can be impregnated in solid porous matrices. It offers a higher dehumidification capacity when compared to silica gel, but is subjected to the formation of a crystalline hydrate, which is detrimental to its adsorptive capacity. Moreover, it is corrosive when it reaches saturation. Nevertheless, the combination of silica gel and haloids results in a composite material with increased dehumidification capacity with inhibited crystallization and corrosion effects [33].

Zeolites are synthetic desiccants derived from sodium or calcium crystalline aluminosilicates and can be manufactured with specific pore sizes so as to allow for the adsorption of a particular molecule characteristic. For instance, decreasing the Si/Al ratio in aluminosilicate zeolites results in a structure with increased hydrophilic characteristics [5]. They have a good adsorption capacity over low levels of air relative humidity. When compared to silica gel, it exhibits half of average capacity per unit weight, although it also exhibits an adsorption capacity less sensible to increased temperatures. It is an efficient desiccant, allowing for the humidity to be lowered beyond detectable levels. Moreover, it can be shaped to 3 Å, providing a selective sorption of 2.8 Å water molecules, mitigating indirect contamination [24].

Activated clay is a natural occurring substance, widely used as a consequence of its low cost. It exhibits a similar performance of silica gel in the 25–30 % range of relative humidity.

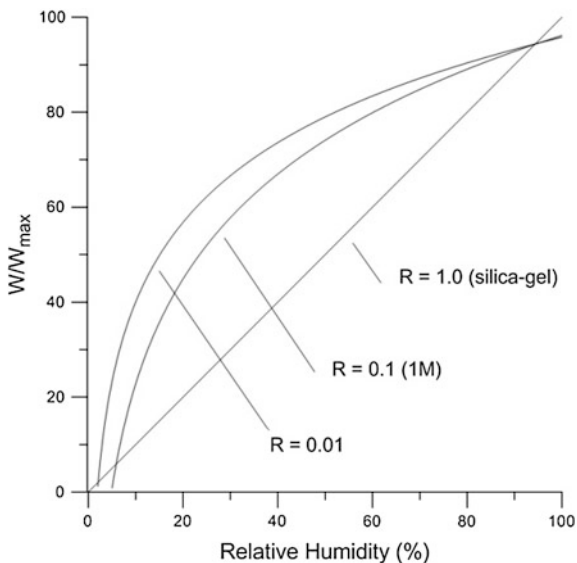
Figure 8 shows the form of different materials isotherms [14], which can be represented by a general formula given by

$$\frac{W}{W_{\max}} = \frac{1}{1 - R + \left(\frac{R}{RH}\right)} \quad (1)$$

In which W is the humidity content of the desiccant, RH is the relative humidity of the air layer in contact with the desiccant, and R is the separation factor, which defines the isotherm shape.

At a first glance, it seems that a strong adsorbent is always desirable, due to the high capacity of moisture detainment. However, a strong adsorbent will naturally also offer a strong resistance to moisture purging, which is detrimental to the cyclic operation and overall dehumidification capacity. Accordingly, an isotherm

Fig. 8 Different types of isotherms



compatible with 1 M is likely to yield better dehumidification effectiveness [13, 43]. An experimental research identified that a composite of salt and a host adsorbent yield an isotherm behavior similar to 1 M [46]. In fact, there is a great amount of research dedicated to the development of new solid desiccant materials. It has been shown that when silica gel is doped with boron and subjected to neutron irradiation, it can have its adsorptive capacity increased by as much as 23 %, as a result of the increased micropore zones [12]. It has been also shown that the contamination with silica gel can improve the adsorptive capacity of activated carbon by as much as 40 % [55].

Hydrophilic polymers have long been used in water purification processes and can have tailor made isotherm shapes which allows for selective adsorption of a given gas mixture component. Also, polymeric structures can be designed to provide high diffusivities of water vapor [15]. It has been proposed the use of a hydrophilic channeling agent blended with a hydrophobic polymer, producing hydrophilic interconnecting microchannel within the polymeric structure. A desiccant material is then applied as a coat to the hydrophilic channels [39]. The channeling structure allows for increased mass transport throughout the composite medium. A new polymeric material, obtained by ion modification of polyacrylic acid sodium salt, has showed to have as much as twice the adsorptive of silica gel, with negligible deliquescence over 40,000 sorption/desorption cycles [36].

Similarly, salt in a porous matrix (SPM) adsorbents have been proposed, in which mesopore adsorbent such as silica gel is contaminated with an inorganic salt second adsorbent component, creating an active composite [3]. The concept is to use the porous matrix not only as an adsorbent but as a dispersion medium as well. A combination of silica gel and lithium chloride has been reported to have an

adsorptive capacity as much as three times that of pure silica gel [4]. It has been tested on a desiccant wheel, exhibiting higher dehumidification effectiveness than silica gel and a lower optimum regeneration temperature [25]. The better capacity is credited to the additional adsorptive mechanisms, such as liquid absorption and chemisorption as a consequence of crystalline salt hydrates formation. The impregnation of a mesopore host matrix with CaCl_2 has been reported to result in an adsorptive capacity of 0.75 g of H_2O per gram of dry adsorbent [57].

In addition to the synthetic substances, several natural substances such as coconut coir have desiccant properties. It has been shown that the heat of adsorption associated with the coconut coir is less intense, when compared to silica gel, which is a desirable feature for air-conditioning applications [30]. Corn grits are rich in starch, which has an adsorptive capacity of 196 mg of water per gram, at 25 °C and 300 kPa, and is a suitable option to synthetic zeolites and alumina in pressure swing adsorption reactors, although the drying performance was shown to be poorer than that of zeolites [35]. As a biodegradable substance, it offers a natural advantage over synthetic substance, as they have no disposal restrictions. A calcium chloride/bentonite desiccant has been proposed for grain drying and humidity control in grain storage, allowing for a reduction in crop loss due to mycotoxin infestation [56].

4.1 Desiccant Cooling Cycles

If a thorough dehumidification of the fresh air stream is to be attained, then the regeneration stream must be thermally activated. This promotes an intensive dry out of the desiccant material, allowing for a greater moisture uptake during the adsorptive period. It should be noted that in this case, the fresh air is heated during the drying process and often results in an inadequate temperature for thermal comfort purposes. Accordingly, (active) desiccant wheels are often used in conjunction with rotary regenerators (heat wheels) which allow for the fresh air stream to be cooled after the drying process. Moreover, the air dehumidification is often significant enough to allow for an evaporative cooler to provide a cooling effect similarly significant, even for locations with high average humidity levels. The first desiccant cooling cycle was proposed in the mid-1950s [48] and is represented in Fig. 9. In this configuration, the fresh air and the exhaust streams interact through the heat and the desiccant wheels. The fresh air is dried and heated as it passes through the desiccant wheel. The temperature is then lowered as the air passes through the heat wheel and further lowered as it passes through the supply evaporative cooler (EC1). The air is then supplied to the room at the EC1 outlet condition, following the characteristic line of the thermal load associated with the conditioned room (RSHF), line 4–5 in Fig. 10. The air is then exhausted at state (5), which is taken as the thermal comfort position, and it is admitted to a second evaporative cooler (EC2) so as to boost the supply air precooling, which is promoted by the heat wheel. Conversely, the supply air preheats the exhaust air before

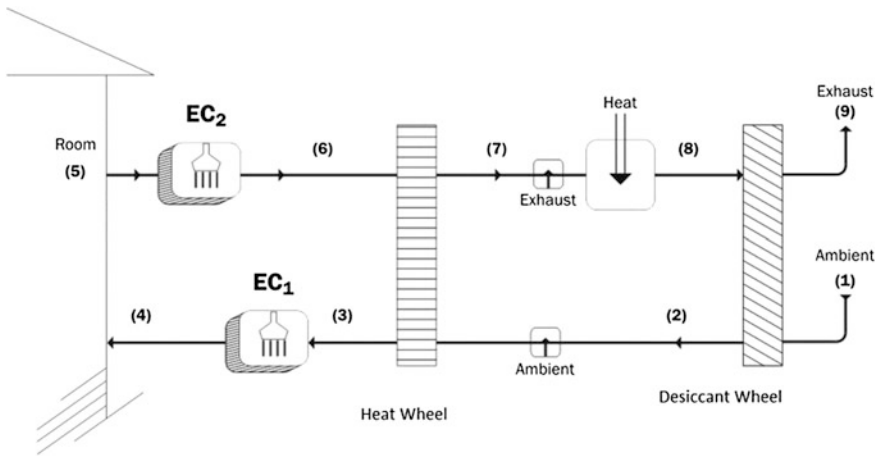
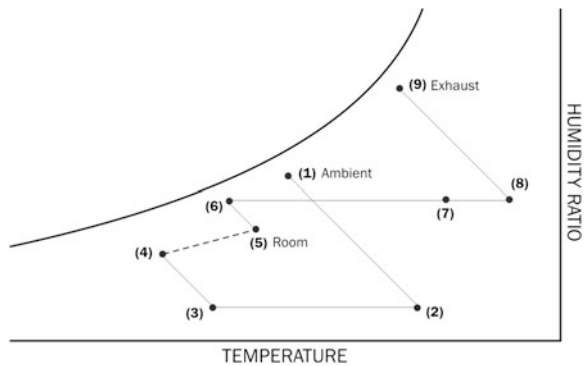


Fig. 9 Schematic of desiccant cooling cycle (ventilation)

Fig. 10 Psychrometric diagram of desiccant cooling cycle (ventilation)



it is admitted to the heat source, where its temperature is raised to the level required by the desiccant wheel regeneration. The exhaust air is finally dumped to the atmosphere at state (9). This configuration has been extensively analyzed numerically and experimentally. An experimental setup with a lithium chloride desiccant wheel operating on ARI conditions (outside air, 36 °C, 45 % RH, room air, 26 °C, 55 %) had a reported COP of 0.78, with a regeneration temperature of 72.3 °C [37]. It was measured a COP of 0.345 using a low-performance natural zeolite desiccant wheel [28]. A COP of 0.28–0.59 was measured for various values of ambient conditions, using a silica gel desiccant wheel and an aluminum heat wheel with 0.7 effectiveness [8]. A numerical simulation of the ventilation and recirculation cycles based on the effectiveness figures of individual components was performed, for room conditions of 25 °C and 50 % RH, with a COP of 0.8 or less obtained in all calculations [54]. It was also found that, for a given value of the COP, the required evaporative coolers effectiveness (supply air and exhaust) are

complementary, that is the higher ϵ_{EC1} , the lesser ϵ_{EC2} . It was also observed that the heat wheel effectiveness ϵ_{hw} has a major influence over the cycle COP.

The recirculation arrangement of a desiccant cooling cycle is shown in Figs. 11 and 12. In opposition to the ventilation mode, the air is constantly reconditioned in a closed loop, whereas the regeneration is provided by outside air. From the point of view of thermodynamics, the continuous reprocessing of cold air is an advantage, but in the recirculation mode, the heat wheel operates with outside air and thus at a higher temperature than in the ventilation mode. Accordingly, one effect offsets the other and recirculating the air might be disadvantageous, for instance if the regeneration temperature required by the solid desiccant is high. Since the cooling air is fully recirculated, the fresh air to the room would have to be supplied by window and door infiltration, which would limit its application to very low capacity cooling systems or conditioned warehouses. The value of the COP has been reported to be of the same magnitude as the ventilation cycle.

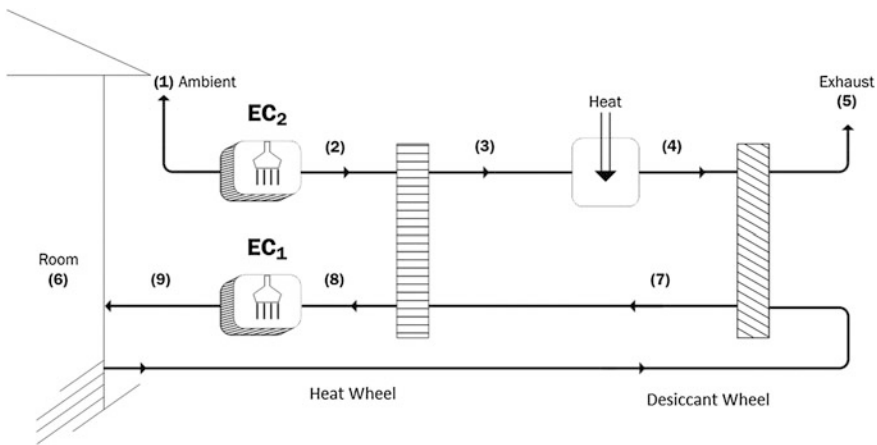
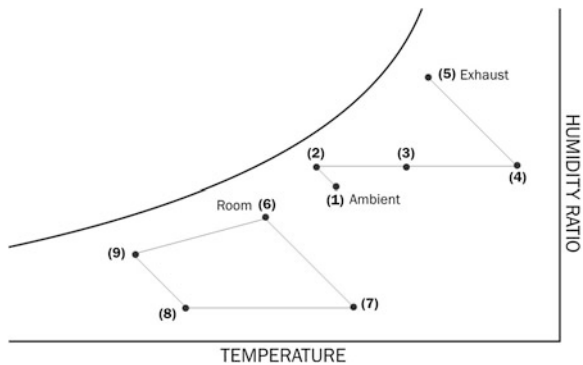


Fig. 11 Schematic of desiccant cooling cycle (recirculation)

Fig. 12 Psychrometric diagram of desiccant cooling cycle (recirculation)



The cycle illustrated at Figs. 13 and 14 combines the two principles in a single cycle. For a partial opening of valves (A), (B), (C), and (D), it is possible to partially discard the return air, mixing the remaining flow rate to the fresh air stream. Accordingly, the air will be supplied to the desiccant wheel at state (2). By mass conservation, the mix of outside air with the room exhaust air occurs in an inverse proportion and results in state (7). By observing Figs. 13 and 14, one concludes that as valves (A) and (C) are continuously closed, state (2) moves

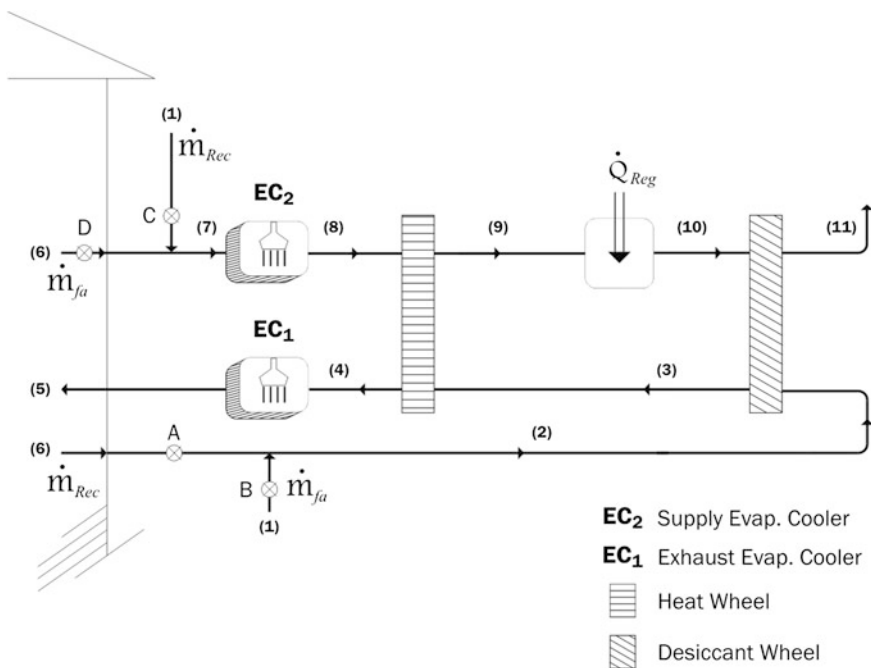
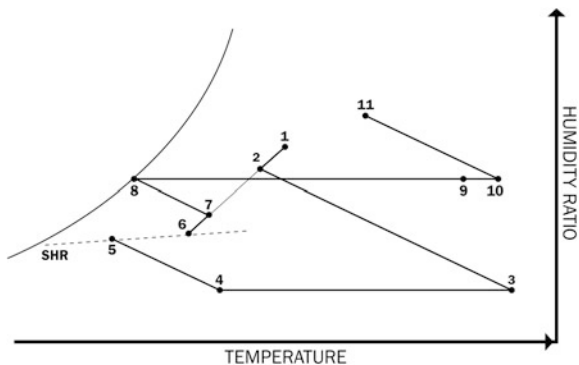


Fig. 13 Schematic of desiccant cooling cycle (general cycle)

Fig. 14 Psychrometric diagram of desiccant cooling cycle (general cycle)



toward state (1), whereas state (7) moves toward state (6). Finally, the cycle turns into the ventilation mode, and Fig. 14 will be identical to Fig. 10. Conversely, if valves (B) and (D) are closed and valves (A) and (C) are progressively opened, the movement of states (2) and (7) are reversed. Now, state (7) will move toward state (1), as state (2) will move toward state (6). When state (2) reaches state (6), the line joining states (6) and (1) is disrupted, and the cycle then executes a closed loop, reproducing the recirculation mode as shown in Fig. 12.

Many possible arrangements with desiccant wheels, heat wheels and evaporative coolers have been proposed, simulated, and tested. Figure 15 shows the schematic diagram of the SENS cycle [38]. As illustrated, the outside air is forced through a desiccant wheel and subsequently regenerated by two heat wheels in sequence. The air is then cooled at an air/water heat exchanger, where it is cooled due to the evaporative cooling effect which takes place in the cooling tower, which uses dry air bled from the process stream. The simulation of this cycle with ideal components at ARI condition resulted in a COP of 2.58 [27], compared to a COP of 1.04 for the ventilation cycle at the same conditions. It was also suggested [27] that removing one heat wheel would not significantly affect the performance of the SENS cycle. Accordingly, the SENC cycle is represented in Fig. 16. It has been analyzed in an experimental work [40], with a reported COP ranging from 0.61 to 1.97 at regeneration temperatures spanning from 54.1 to 90.4 °C. Another configuration, known as the REVERS cycle, is illustrated in Fig. 17. When compared to the SENS cycle, it can be seen that the REVERS cycle has a lesser cooling effect, since the air at state (4) would be at a higher temperature in REVERS cycle. However, the later takes advantage on harvesting the preheated air at state (7) to regenerate the desiccant wheel, in contrast to the former, which collects the

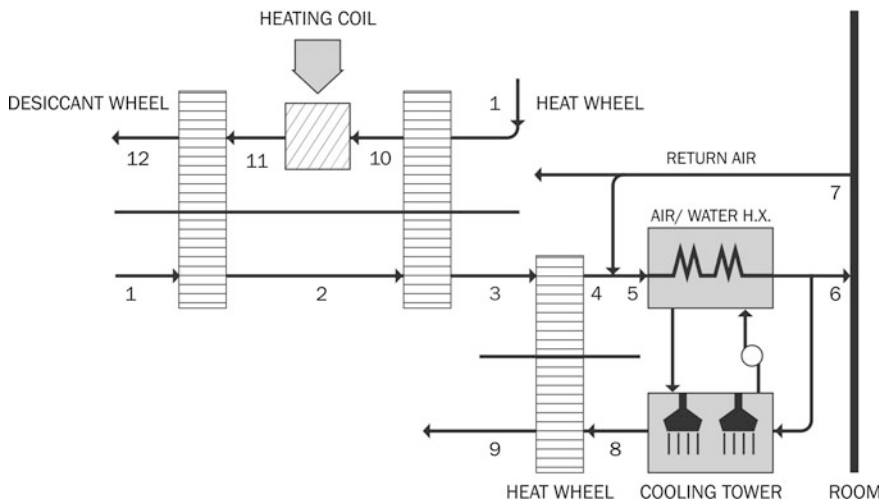


Fig. 15 Schematic of SENS cycle

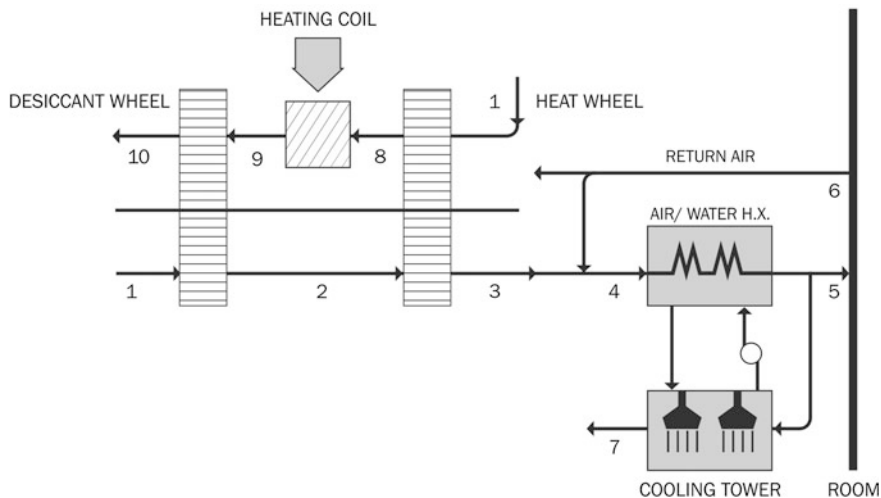


Fig. 16 Schematic of SENC cycle

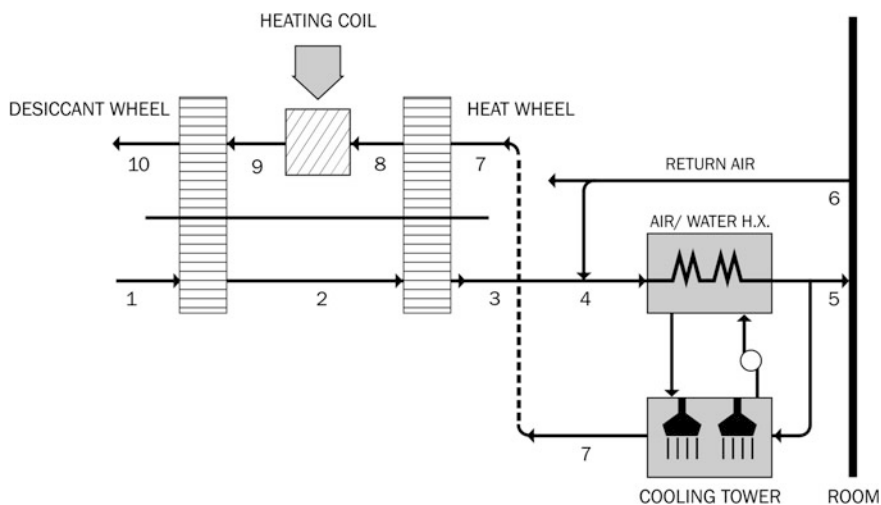


Fig. 17 Schematic of REVERS cycle

regeneration air at ambient temperature. Accordingly, the REVERS cycle requires less regeneration heat and produces a lesser cooling effect than the SENS cycle.

In addition to the described CFC-free cooling systems, desiccant wheels are also suitable for working in conjunction with vapor compression systems. Figure 18 shows a schematic diagram of a hybrid cooling [16]. Outside air is forced through a desiccant wheel, where it is dried and heated. The temperature is restored to the ambient level at an indirect evaporative cooler (IEC), before it is

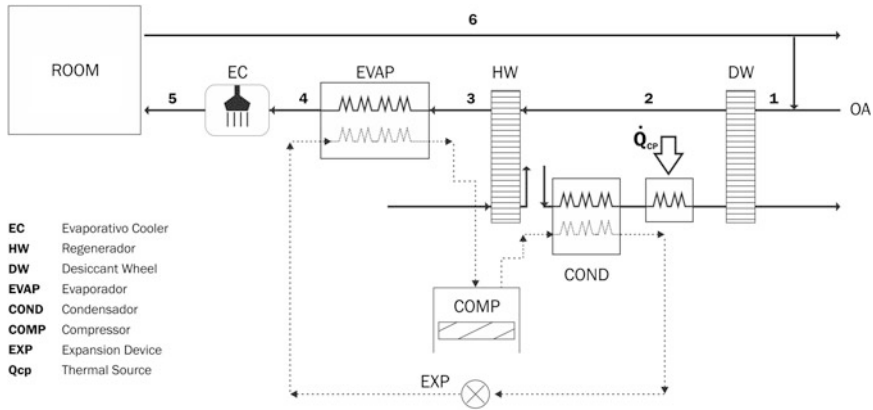


Fig. 18 The hybrid desiccant/vapor compression cycle

admitted to an evaporator where it undergoes a sensible cooling process. Accordingly, the latent load is handled by the desiccant wheel, whereas the sensible load is handled by an evaporator of a vapor compression system. Since the evaporator is to accomplish only sensible cooling, it has a diminished capacity than if it had to handle to full thermal load. A case study revealed a reduction of 35 % in the evaporator cooling capacity [21]. Experimental monitoring of rooftop units equipped with desiccant wheels revealed a downsize of as much as 50 % in the required evaporator capacity [52]. Moreover, since the cooling coil works at above the air dew point, it mitigates the compressor work demanded by the cycle. It has been estimated the compressor work of a hybrid cycle is 50–70 % less than that of a conventional cycle [16]. Experimental results showed a COP increase of 41 % in comparison with a standard vapor compression cycle [25], which is consistent with a 35 % COP increase verified by a numerical simulation [58].

Another advantage is the harvesting of the condenser heat rejection to preheat the desiccant wheel regeneration air. Hybrid desiccants are particular suitable for supermarket conditioning systems, since the maintenance of humidity at lower levels minimizes the frost formation in shelves, preserving the integrality and visibility of exposed good, as well as in less and faster defrost cycles executed by each refrigerated display cabinet, which are known to be energy intensive processes.

5 Emerging Concepts

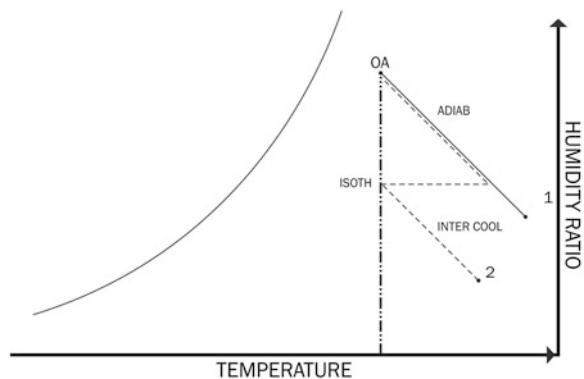
5.1 Isothermal Dehumidification

As previously described, adsorption is a spontaneous process, during which a quantity called heat of adsorption is released. This concurs to increase the internal energy of the air and the desiccant material. The increase in the air temperature is

unwelcome to a cooling technique and is usually mitigated by regenerating the process air after it exits the desiccant wheel. The increase in the desiccant material temperature is also unwanted, since it is detrimental to the adsorptive capacity. Accordingly, it has been suggested that an isothermal adsorptive process would be more effective than the adiabatic adsorptive process. Theoretically, that could be accomplished by using an infinite number of desiccant stages intercalated with infinite intercoolers. An experimental investigation of a two-stage intercooled process, using two desiccant rotors in tandem, showed that a given value of absolute humidity can be reached with lower temperatures than a single-stage process would require [20]. A one-rotor dual-process desiccant system has been proposed [19]. In this arrangement, the wheel is divided into quadrants, intercalating adsorptive and desorption processes. The process air is driven through the first stage of dehumidification and is cooled back to ambient temperature before it is admitted to the second dehumidification stage. Figure 19 shows that the intercooled two-stage process allows for a more intensive dehumidification than if it has been carried out in a single stage. An experimental investigation determined that the COP of a cycle driven by a two-stage desiccant rotor is 16 % higher than that of a one-stage rotor cycle [20]. A desiccant cycle with two desiccant wheels separated by an intercooler has been analyzed and showed to have exergetic efficiency three times higher than that of the ventilation cycle [34].

The combination of desiccants with phase-change materials in a porous bed has been proposed as an alternative way for achieving isothermal adsorption [49, 50]. The adsorption heat is partially consumed by the phase-change process, allowing for the adsorption to occur with a lesser temperature variation. Accordingly, the outlet air temperature during adsorption is lower for the composite bed, when compared to a pure desiccant bed. The phase-change material showed to substantially increase the dehumidifying capacity; however, there is an upper level for the phase-change material fraction, since it implies in a lesser fraction of desiccant materials per unit bed volume, which is detrimental for the overall dehumidifying capacity.

Fig. 19 Isothermal, intercooled, and adiabatic adsorption



5.2 Desiccants and the Brayton Refrigeration Cycle

Humidity infiltration is a major concern in the operation of cold storage warehouses. In addition to frost formation, which is detrimental to the cooling system performance and to the quality of stored goods, icing in loading docks is responsible for a significant number of work accidents every year. Loading areas are usually kept at low temperatures so as to minimize the infiltration of hot air in the cold rooms. Accordingly, it was proposed that a cold storage warehouse would operate with an air refrigeration cycle, which supplies the cold air, while the cold room air is recirculated through a desiccant wheel to keep the moisture level to a minimum [17]. The desiccant wheel is regenerated by harvesting the waste heat from the air cycle. It was shown that the desiccant can lower the absolute humidity to 4 g/kg of air, at which point the dew point is of $-25\text{ }^\circ\text{C}$. Figure 20 shows a desiccant-Brayton cascade cycle [45]. The desiccant cycle harvests the waste heat from the Brayton cycle to precool the air before it enters the expander. It was shown that the cascade cycle COP can be as much as 30 % higher than the COP of a standard Brayton cycle.

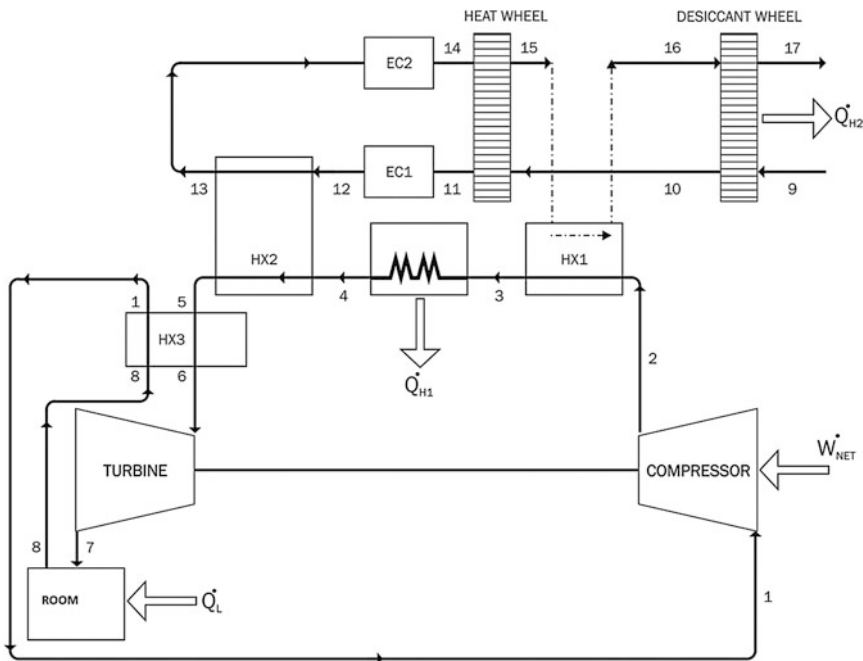


Fig. 20 The desiccant-Brayton cascade cycle

5.3 Desiccant-Assisted Radiant Cooling Systems

The use of ceiling radiant panels to provide sensible cooling have been long investigated as an alternative to conventional systems, which provide the chilling effect by insufflating cold air at the conditioned room. This technology features some advantages when compared to conventional systems, such as a reduction in the energy consumption required to provide the cooling effect. Radiant panels require cold water pumping through the inner tubes of the panel, which is usually less than the power required by the fans in an air-based system. Moreover, the radiant energy transport improves the thermal comfort, allowing for the cooling effect to be distributed more evenly and more silently, since there are no moving parts located inside the room. In addition, for multi-zone system, the zone control is greatly simplified. On the negative side, the use of radiant cooling panels requires an independent air ventilation system to be set. Moreover, if the local ambient air condition is rich in moisture, some condensation is expected to occur on the chilling panel's surface. Accordingly, the moisture content of the ventilation air has to be carefully controlled, aiming at the thermal comfort of the occupants as well as zero condensation on the panels. This constitutes a favorable scenario for the application of desiccant wheels. It has been shown that the desiccant-assisted radiant-assisted cooling system saves up to 44 % of the energy consumed in the conventional all air cooling system [41].

6 Conclusion

The last decades has brought a social consciousness about the impact of human activities over the environment. In particular, air-conditioning systems are known to be energy intensive systems, which can represent over 40 % over the total power demand on an office building [1]. Moreover, refrigeration systems feature design aspects which directly impact the global warming, greenhouse effects, ozone layer depletion, and summer peaking electrical energy demands. As a result, HVAC industry has been continuously challenged in face of changing regulation of refrigerant substances, efficiency standards and indoor air quality. These factors have triggered a market demand for economical and environment-friendly technologies. HVAC designers have been increasingly challenged to seek a balance between air quality and comfort with systems capital and operating costs, which often shows to be fragile. Among all emerging air-conditioning technologies, solid desiccant cooling seems to play the most versatile role, given its application on CFC-free evaporative systems and also on currently used vapor compression systems, unburdening the cooling coil from the latent component of the thermal load while allowing for a more rational and efficient humidity control. Problems associated with poor performance and corrosion have been overcome by the development of a new generation of adsorptive materials. The variety of adsorptive

materials, ranging from natural substances to composite synthetic desiccants, is an important factor in the dissemination of the technology. Moreover, the consumption of low-grade thermal energy allows for the use of alternative energy sources, such as solar energy or waste heat from an engine, which makes it appealing from the economical perspective. In addition, the application of solid desiccants provides a good solution for some issues of vapor compression systems, mainly related with energy consumption and adequate humidity control. The increasing ventilation rates prescribed in air quality standards are also more efficiently handled with enthalpy recovery wheels, which remove some of the extra thermal load associated with the outside air condition. Accordingly, the market for desiccant system evolved from special applications (pharmaceutical and optical industry, ammunition storage) to more common applications, such as supermarket and office building air-conditioning systems. The use of building energy simulation programs to compare alternative systems plays an important role in the decision-making process. Accordingly, the market acceptance of desiccant systems relies on a collective effort of researchers, HVAC engineers, market developers and regulators, in a continuous move toward environment-friendly technologies.

References

1. Aneel (2002) Atlas Nacional de Energia Elétrica do Brasil. Agência Nacional de Energia Elétrica, Brasília
2. Angrisani G, Capozzoli A, Minichiello F, Roselli C, Sasso M (2011) Desiccant wheel regenerated by thermal energy from a microgenerator: experimental assessment of the performances. *Appl Energ* 88:1354–1365
3. Aristov YI, Gordeeva LG (2009) “Salt in a porous matrix” adsorbents: design of the phase composition and sorption properties. *Kinet Catal* 50(1) 65–72
4. Aristov YI, Tokarev MM, Restuccia G, Cacciola G (1996) Selective water sorbents for multiple applications, CaCl₂ confined in micropores of silica-gel: sorption properties. *React Kinet Catal Lett* 59(2):335–342
5. Aristov YI (2013) Challenging Offers of Material Science for Adsorption Heat Transformation: A Review, *Appl Therm Eng* 50(2):1610–1618
6. Bellia L, Mazzei P, Minichiello F, Palma D (2000) Air conditioning systems with desiccant wheel for Italian climates. *Int J Arch Sci* 1(4):193–213
7. Berglund LG (1988) Thermal comfort: a review of recent research, In: Mejavik IB, Banister EW, Morrison JB (ed) *Environmental ergonomics*. Taylor & Francis, London
8. Boudoukan P, Wurtz E, Joubert P (2010) Comparison between the conventional and recirculation modes in desiccant cooling cycles and deriving critical efficiencies of components. *Energy* 35(2):1057–1067
9. Brandemuehl MJ, Katejanekarn T (2004) Dehumidification characteristics of commercial building applications. *ASHRAE Trans* 110(2) 65–76
10. Camargo JR (2009) *Resfriamento Evaporativo* (ed) Ciência Moderna, Rio de Janeiro
11. Casas W, Schmitz G (2005) Experiences with a gas driven, desiccant assisted air conditioning system with geothermal energy for an office building. *Energ Build* 37:493–501
12. Chung TW, Chung CC (1998) Increase in the amount of adsorption on modified silica-gel by using neutron flux irradiation. *Chem Eng Sci* 53(16):2967–2972

13. Chung JD, Lee DY (2009) Effect of Desiccant Isotherm on the Performance of a Desiccant Wheel. *Int J Refrig* 32:720–726
14. Czachorsy W, Wurm J (1996) Evaluation of desiccant and heat exchange matrices, gas research institute, Report GRI-97/0148. Des Plaines, Illinois
15. Czanderna AW(1992) *Polymers as Advanced Materials for Desiccant Applications, 1: Commerically Available Polymers, Desiccant Cooling and Dehumidification*, ASHRAR, Atlanta, GA, USA, 88–97
16. Dhar PL, Singh SK (2001) Studies on solid desiccant based hybrid air-conditioning systems. *Appl Therm Eng* 21:119–134
17. Elsayed SS, Hamamoto Y, Prasad Akisawa A (2008). Analysis of an air cycle refrigerator driving air conditioning system integrated desiccant system. *Int J Refrig* (31) 189–196
18. Finocchiaro P, Becalli M, Nocke B (2012) Advanced solar assisted desiccant and evaporative cooling system equipped with wet heat exchangers. *Sol Energy* 86:608–618
19. Ge TS, Dai YJ, Wang RZ, Li Y (2008) Experimental investigation on a one-rotor two-stage rotary desiccant cooling system. *Energy* 33:1807–1815
20. Ge TS, Li Y, Wang RZ, Dai YJ (2009) Experimental study on a two-stage rotary desiccant cooling system. *Int J Refrig* 32:498–508
21. Ghali K (2008) Energy savings potential of a hybrid desiccant dehumidification air conditioning system in Beirut. *Energy Convers Manage* 49:3387–3390
22. Goodish T (2001) *Indoor environmental quality*. Lewis Publishers, Boca Raton
23. Harriman LGIII (2002) Dehumidification equipment advances. *ASHRAE J Aug* 22–29
24. Jeong JW, Mumma SA (2005) Practical thermal performance correlations for molecular sieve and silica-gel loaded enthalpy wheels. *Appl Therm Eng* 25:719–740
25. Jia CX, Dai YJ, Wu YJ, Wang RZ (2006) Analysis of a hybrid desiccant air-conditioning system. *Appl Therm Eng* 26:2393–2400
26. Jia CX, Dai YJ, Wu YJ, Wang RZ (2006) Experimental comparison of two honeycombed desiccant wheels fabricated with silica-gel and composite desiccant material. *Energy Convers Manage* 47:2523–2534
27. Kang TS (1985) *Adiabatic desiccant open cooling cycles*. M.S. Thesis, University of New South Wales
28. Kanoglu M, Bolatturk A, Aluntop N (2007) Effect of ambient conditions on the first and second law performance of an open desiccant cooling process. *Renew Energy* 32:931–946
29. Khattar M, Ramanan M, Swami M (1985) Fan cycling effects on air condition moisture removal performance in warm, humid climates. In: *Proceedings of the international symposium on moisture and humidity*, Washington D.C
30. Khedari J, Rawangkul R, Chimchavee W, Hirunlab J, Watanasungsuit A (2003) Feasibility study of using agriculture waste as desiccant for air conditioning system. *Renew Energy* (28) 1617–1628
31. Kubota M, Hanada T, Yabe S, Kuchar D, Matsuda M (2011) Water Desorption Behavior of desiccant rotor under microwave irradiation, *Appl Therm Eng* 31:1482–1486
32. Kuehn TH, Ramsey JW, Threlkeld JL (1998) *Thermal environmental engineering*, 3rd edn. Prentice-Hall, New-Jersey
33. La D, Dai YJ, Li Y, Wang RZ, Ge TS (2010) Technical development of rotary desiccant dehumidification and air conditioning: a review. *Renew Sustain Energy Rev* 14:130–147
34. La D, Li Y, Dai YJ, Ge TS, Wang RZ (2012) Development of a novel rotary desiccant cooling cycle with isothermal dehumidification and regenerative evaporative cooling using thermodynamic analysis method. *Energy* 44:778–791
35. Ladisch MR (1997) Biobased adsorbents for drying of gases. *Enzyme Microb Technol* 20(3):162–164
36. Lee J, Lee DY (2012) Sorption characteristics of a novel polymeric desiccant. *Int J Refrig* 35:1940–1949
37. Lof GOG, Cler G, Brisbane T (1988) Performance of a Solar Desiccant System. *J Sol Energy Eng* 110:165–171

38. Maclaine-Cross IL (1985) High-performance adiabatic desiccant open-cooling cycles. *J Sol Energ Eng* 107:102–104
39. Mathiowitz E, Jacob E, Jong YS, Hekal TM, Spano W, Guemonprez E (2001) Novel desiccants based on designed polymeric blends. *J Appl Polym Sci* 80(3):317–327
40. McLay B. (1989) Analysis and simulation of an advanced open-cycle solid desiccant cooling system. M.S. Thesis, Colorado State University
41. Niu JL, Zhang LZ, Zuo HG (2002) Energy savings potential of chilled ceiling combined with desiccant cooling in hot and humid climates. *Energy and Buildings* 34:487–495
42. Nóbrega CE, Brum NCL (2009) Modeling and simulation of heat and enthalpy recovery wheels. *Energy* 34:2063–2068
43. Nóbrega CEL, Brum NCL, (2009b) Influence of isotherm shape over desiccant cooling cycle performance. *Heat Trans Eng* 30(4) 322–328
44. Nóbrega CE, Brum NCL (2012) An analysis of the heat and mass transfer roles in air dehumidification by solid desiccants. *Energ Build* 50:251–258
45. Nóbrega CE, Sphaier LA (2012) Modeling and simulation of a desiccant-Brayton cascade refrigeration cycle. *Energ Build* 55:575–584
46. Ostrovskii NM, Chumakova NA, Bukhavtsova NM, Vernikovskaya NV, Arsitov YI (2007) *Theor Found Chem Eng* 41(1):83–90
47. Parsons Ken (2003) *Human thermal Environments*. Taylor & Francis, London
48. Pennington NA (1955) Humidity changer for air conditioning. USA patent No 2(700):537
49. Rady MA (2009) Heat and mass transfer in a composite bed or silica-gel and macro encapsulated PCM for performance of dehumidification of desiccant beds composed of silica-gel and thermal energy storage particles. *Heat Mass Transf* 45(5):545–561
50. Rady M, Huzayyin AS, Arquís E, Monneyron P, Lebot C, Palomo E (2009) Study of heat and mass transfer in dehumidifying desiccant bed with macro-encapsulated phase change materials. *Renew Energ* 34:718–726
51. Rutheven D (1984) *Principles of adsorption and adsorption processes*. Wiley, New York
52. Sand JR, Fischer JC (2005) Active desiccant integration with packaged rooftop HVAC equipment. *Appl Therm Eng* 25:3138–3148
53. Spatz M, Yana Motta S, Achaicha N (2011) Low global warming potential refrigerants for stationary air conditioning applications. In: *Proceedings of the 23rd international congress of refrigeration and air-conditioning*, Prague, Czech Republic, paper 919
54. Sphaier LA, Nóbrega CE (2012) Parametric analysis of components effectiveness on desiccant cooling systems performance. *Energy* 38:157–166
55. Tashiro Y, Kubo M, Katsumi Y, Meguro Y, Komeya K (2004) Assessment of adsorption-desorption characteristics of adsorbents for adsorptive desiccant cooling systems. *J Mater Sci* 39(9):1315–1319
56. Thoruwa TFN, Johnstone CM, Grant AD, Smith JE (2000) Feasibility study of using agriculture waste as desiccant for air conditioning system. *Renew Energ* 19:513–520
57. Tokarev M, Gordeeva L, Romannikov V, Glaznev I, Aristov Y (2002) New composite sorbent CaCl₂ in mesopores for sorption cooling/heating. *Int J Therm Sci* 4:470–474
58. Worek WM, Moon CJ (1988) Desiccant integrated hybrid vapour compression cooling performance sensitivity to outdoor conditions. *Heat Recovery Syst CHP* 8(6):489–501

Status of Liquid-Desiccant Technologies and Systems

W. M. Worek and A. Lowenstein

1 Introduction

Liquid desiccants have been successfully used to produce dry air for a surprisingly long time. Dr. Francis Russell Bichowsky, working for the Frigidaire Division of General Motors, first used solutions of lithium chloride to dry air in the 1930s. Frigidaire sold the technology to Surface Combustion Corporation (SCC) in the mid-1930s. A residential liquid-desiccant dehumidifier was field-tested by SCC shortly after they acquired the technology, but no product was introduced into the market. Although there have been several changes in name and ownership, Kathabar Dehumidification Systems, Inc., which manufactures and sells liquid-desiccant systems based on lithium chloride, is a direct descendent of the SCC from the 1930s.

Both the energy crisis of the 1970s and the gas bubble of the 1980s spurred interest in liquid desiccants for commercial and residential HVAC. Although most of this interest was limited to R&D activities, at least one company, the Albers Corporation (Tempe, AZ), showed a liquid desiccant product targeted at HVAC applications at an ARI Exposition in the 1990s. A second company, Tecogen, Inc (Waltham, MA), field-tested two residential liquid-desiccant air conditioners in the late 1980s, but no commercial product was introduced. In 1997, an Israeli company, Drykor, was started that would eventually sell several thousand liquid-desiccant air conditioners before it ceased operating in about 2004.

Interest in liquid-desiccant systems applied to HVAC is once again increasing. Much of this interest follows from two characteristics of liquid-desiccant air conditioners (LDAC):

W. M. Worek
Michigan Technologic University, Houghton, MI, USA

A. Lowenstein (✉)
A.I.L. Research, Inc, Princeton, NJ, USA
e-mail: ail@ailr.com

- LDACs run mostly on heat; their electric demand is typically one-fourth that of a vapor-compression air conditioner.
- LDACs are exceptionally good at dehumidifying air; almost all of the cooling they provide can be latent cooling.

As discussed elsewhere in this volume, these advantages allow LDACs (as well as solid-desiccant systems) to overcome problems now facing compressor-based air conditioners.

2 The Basics of Liquid-Desiccant Air Conditioners

A desiccant is a material that has a strong affinity for water. It is common to classify desiccants as either solid or liquid depending on their normal physical state (although a material such as lithium chloride can be both, absorbing water vapor both as a solid, hydrated salt or as an aqueous solution). Both solid and liquid desiccants are commonly used in industrial applications where low dewpoint air is needed. Solid desiccants are also increasingly being used in HVAC systems to either increase an air conditioner's latent cooling or exchange enthalpy between the exhaust and make-up air streams in a building (i.e., total energy recovery).

The strength of a desiccant can be measured by its equilibrium vapor pressure, i.e., pressure of water vapor that is in equilibrium with the desiccant. This equilibrium vapor pressure increases roughly exponentially with the temperature of the desiccant/water system. It also increases as the desiccant absorbs water, i.e., a dilute liquid desiccant will have a higher equilibrium vapor pressure than a concentrated liquid desiccant.

When the humidity ratio of air that has come into equilibrium with a liquid desiccant of fixed concentration is plotted on a psychrometric chart, the equilibrium line closely follows a line of constant relative humidity. Figure 1 illustrates this behavior for solutions of lithium chloride. A liquid desiccant that is alternately exposed to two environments that are at different relative humidities will move moisture from high to low relative humidity.

Fig. 1 Equilibrium relative humidity for lithium chloride

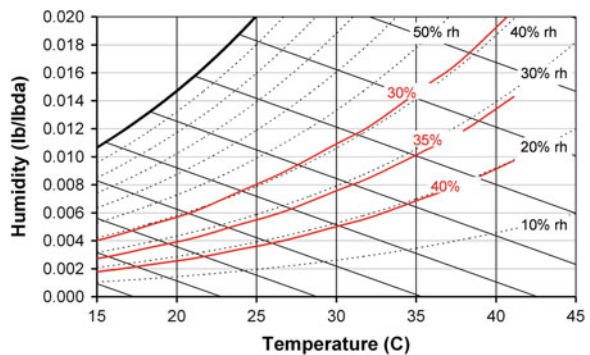
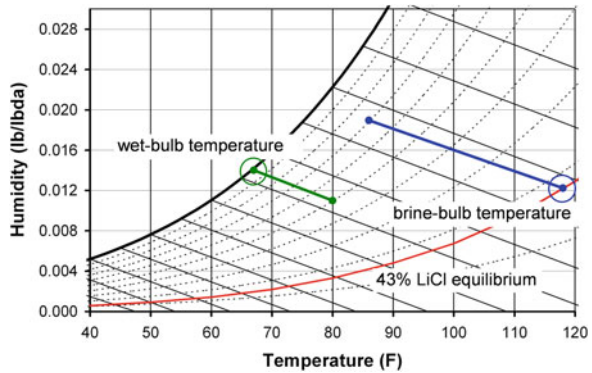


Fig. 2 Psychrometric description of the brine-bulb temperature for lithium chloride



A liquid desiccant can enhance heat transfer by a mechanism that is the inverse of evaporative cooling. When air flows over a surface wetted with water, evaporation from the film of water will lower the temperature of the water–air interface toward the wet-bulb temperature of the air. This wet-bulb temperature is a function of the air’s initial temperature and humidity ratio. A line of constant enthalpy that passes through the air’s state point intersects the saturation line on a psychrometric chart at approximately the wet-bulb temperature. As shown in Fig. 2, the wet-bulb temperature for air at 80 °F (26.7 °C) and 50 % rh is 66.7 °F (19.3 °C).

When air flows over a surface that is wetted with a liquid desiccant, the desiccant can either absorb or desorb water depending on whether the desiccant’s “equilibrium” relative humidity is above or below the air’s relative humidity. If the desiccant absorbs water from the air, heat will be released and the desiccant’s temperature will increase. This heating is the inverse of evaporative cooling. By analogy to evaporative cooling, one can define a brine-bulb temperature as the temperature that the desiccant–air interface approaches.

The brine-bulb temperature is a function of a liquid desiccant’s concentration and the air’s temperature and humidity. As shown in Fig. 2, the brine-bulb temperature will always be slightly higher than the temperature at which a line of constant enthalpy from the air state point intersects the equilibrium relative humidity curve for the desiccant. This is because the heat that is released as the desiccant absorbs the water vapor includes the chemical heat of mixing between the desiccant and water in addition to the vapor–liquid latent heat for the water vapor.

As shown in Fig. 2, the brine-bulb temperature for a 43 % solution of lithium chloride and air at 86/78 °F (30.0/25.6 °C) dry-bulb/wet-bulb will be 118 °F (47.8 °C). With an ambient wet-bulb temperature of 78 °F (25.6 °C), a typical cooling tower might supply water at 85 °F (29.4 °C). While it would be impractical to cool the ambient air using this cooling water in a conventional heat exchanger (i.e., the cooling water is only one degree below the air temperature), a strong cooling effect could be achieved by wetting the surfaces of the heat exchanger with the 43 % lithium chloride.

Of course, one does not get this enhanced cooling for free. After the desiccant has absorbed water, energy must be expended to regenerate it back to its original concentration if the cooling process is to be continuous.

If ambient air from the preceding example is brought into equilibrium with 43 % lithium chloride at 85 °F (29.4 °C), the air will have a dewpoint of 33.5 °F (0.8 °C), a wet-bulb of 57.8 °F (14.3 °C), and its enthalpy will be reduced from 41.5 Btu/lb (96.3 kJ/kg) to 24.9 Btu/lb (57.8 kJ/kg). This large cooling effect, both in terms of latent cooling and total cooling, and low dewpoint—both of which are achieved without a compressor—demonstrate the potential of liquid desiccants to become an important part of HVAC systems.

A typical industrial application of a liquid-desiccant system is shown in Fig. 3. The conditioner (also commonly called an absorber) is the component that cools and dries the process air. As shown in this figure, the conditioner is a bed of structured contact media, similar to the corrugated fill that might be used in a cooling tower. Liquid desiccant is first cooled in a heat exchanger and then sprayed onto the contact media. The desiccant flow rate must be sufficiently high to insure complete wetting of the media (i.e., about 5 gpm per square foot of face area [3.4 l/s-m²]). The process air is cooled and dried as it comes in contact with the desiccant-wetted surfaces of the contact media. Heat is released as the desiccant absorbs water from the air, but the high flow rate of desiccant limits its temperature rise to a few degrees.

The regenerator removes the water that the desiccant has absorbed in the conditioner. The desiccant is regenerated by first heating it to raise its equilibrium

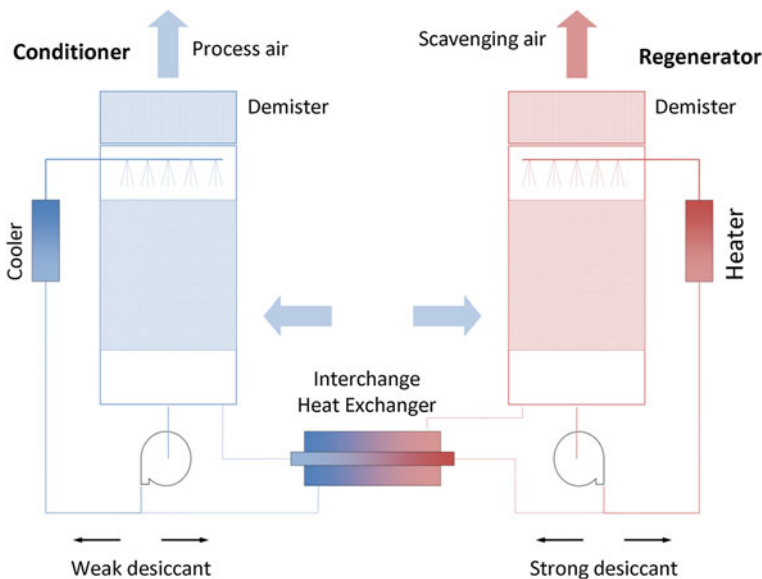


Fig. 3 Conceptual layout of industrial liquid-desiccant system

vapor pressure. The hot desiccant, typically between 160 °F (71.1 °C) and 200 °F (93.3 °C), is sprayed over a bed of random fill (e.g., Raschig rings). Flooding rates are again sufficiently high to insure complete wetting of the media. The hot desiccant desorbs water to the air that flows through the bed. This moisture-laden air is typically exhausted to ambient.

Both the regenerator and conditioner require droplet filters (also referred to as mist eliminators) to ensure that desiccant is not entrained in either the supply air to the building or the exhaust from the regenerator. Droplet formation is fundamental to both the spray distributor and the highly flooded beds of contact media used in industrial equipment. Droplet filters can suppress desiccant carryover to parts per billion of air flow, but these filters do increase air-side pressure drops and require maintenance.

An interchange heat exchanger (IHX) can be used to preheat the weak desiccant that flows to the regenerator using the hot, concentrated desiccant that leaves the regenerator. This IHX reduces both the thermal energy use of the regenerator and the cooling requirements of the conditioner.

3 Alternatives for Liquid Desiccants

The choice of desiccant will have a profound effect on the design of the liquid-desiccant air conditioner. Both glycols and solutions of halide salts are routinely used in industrial equipment, each having important advantages and disadvantages. Halide salts such as lithium chloride and lithium bromide are very strong desiccants: a saturated solution of lithium bromide can dry air to 6 % relative humidity and lithium chloride to 11 %. Although lithium bromide has the potential to dry air more deeply, the bromide ion is more easily oxidized than the chloride ion (a standard oxidation potential of -1.07 V for the bromide ion versus -1.36 V for the chloride ion). Because of this difference, lithium chloride is more commonly used in open systems such as LDACs that directly contact the solution with air, while lithium bromide is more commonly used in closed systems (i.e., absorption chillers).

Unfortunately, halide salts are corrosive to most ferrous and non-ferrous metals. LDACs that use halide salts are commonly designed to minimize the exposed area of metal to the desiccant. Shell, sumps, piping, and beds of contact media are typically made of plastic, fiberglass, or other non-metallic materials. Where metal must be used, as may be the case for heat exchangers, titanium is commonly specified.

Glycols are the second class of liquid desiccants now used in industrial equipment. Both triethylene and propylene glycol have low toxicity and are compatible with most metals. However, all glycols have one undesirable characteristic in HVAC applications: they are volatile. A mixture of 96 % triethylene glycol (TEG) and 4 % water will dry air to the same dewpoint as a 42 % lithium chloride solution. However, at equilibrium, the molar concentration of the glycol

in air will be in the order of 1 % that of the water vapor. In an HVAC application where a 6,000-cfm (10,200 m³/h) LDAC operates for 2,000 h per year, the annual loss of TEG in the conditioner would be more than 10,000 lbs (4,500 kg). Both the economic penalty and the environmental impact of this loss would be unacceptable in an HVAC system (although glycol systems are successfully used in low-temperature refrigeration systems where the intrinsic vapor pressure of the glycol is very low).

The cost of lithium-based desiccants can be an obstacle to their use in applications where the storage of concentrated desiccant is important, e.g., a solar cooling system that must provide cooling during hours when solar insolation is low or zero. Based on quotes for delivery in January 2012, the price for industrial-grade anhydrous lithium chloride in large volumes was about \$2.80 per pound (\$6.15 per kilogram). At this price and a concentration swing from 43 % to 39 %, the desiccant can store latent cooling about \$135 per ton-hour. (The concentrated desiccant can be stored in an uninsulated, plastic tank, which might increase the storage cost to \$165 per ton-hour.)

Ertas et al. [1] studied mixtures of lithium chloride and calcium chloride as a lower-cost alternative to lithium chloride. The cost for calcium chloride is less than one-tenth that of the lithium salt. By itself, calcium chloride is a moderately strong desiccant: A solution saturated at 77 °F (25 °C) would be in equilibrium with air at 29 % relative humidity. Ertas, et al. [1] examined a solution in which the combined salt content was 20 % by weight at 80 °F (26.7 °C). For solutions in which the fraction of calcium chloride was less than half, the equilibrium vapor pressure for the mixture was more heavily weighted toward the value for pure lithium chloride, e.g., the equilibrium vapor pressure for the 50/50 mixture is a 71/29 weighted average of the values for solutions of pure lithium chloride and pure calcium chloride. If this weighted average holds at higher solution concentrations, then 43 % solutions of calcium chloride, lithium chloride, and a 50/50 mixture at 85 °F (29.4 °C) would have equilibrium dewpoints of 52.1 °F (11.2 °C), 33.5 °F (0.8 °C), and 40.2 °F (4.6 °C), respectively. The 43 % solution of the 50/50 mixture would behave in the LDAC the same as a 40 % solution of pure lithium chloride (whereas a 43 % calcium chloride solution behaves like a 34 % lithium chloride solution). A complete design study of the LDAC and its performance would be needed to decide whether the LDAC operating with the 50/50 mixture is an attractive alternative.

3.1 Thermophysical Properties of Calcium Chloride and Lithium Chloride

The design of liquid-desiccant systems requires knowledge of the desiccant's thermophysical properties. Engineering has prepared a manual on property data for both lithium chloride and calcium chloride that summarizes the work of numerous

researchers [2]. The complete manual is available from several Web-based sources (<http://www.mrceng.com/Downloads/Aqueous%20LiCl&CaCl2%20Solution%20Props.pdf>). With the permission of the manual’s author, several useful analytical expressions for the properties of the two salt solutions are reproduced here.

3.1.1 Solubility

The solubility in water of both lithium chloride and calcium chloride is a function of temperature. The temperature-concentration boundaries that identify a saturated solution for these two salts are shown in Figs. 4 and 5. On these boundaries, a saturated liquid phase can exist in equilibrium with a solid phase. Depending on the concentration of the saturated liquid phase, the solid phase will be either ice or a hydrated crystal of the salt. For both lithium chloride and calcium chloride, several salt hydrates exist. Typically, the liquid/solid boundaries will have discontinuities in their slopes at the transition points where the solid phase in equilibrium with the liquid phase changes. These transition points are included in Figs. 4 and 5.

Fig. 4 Phase diagram for lithium chloride

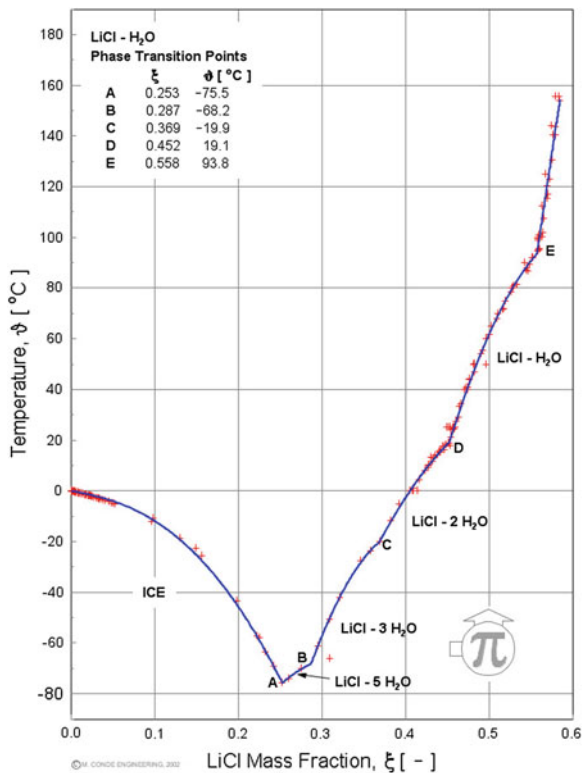
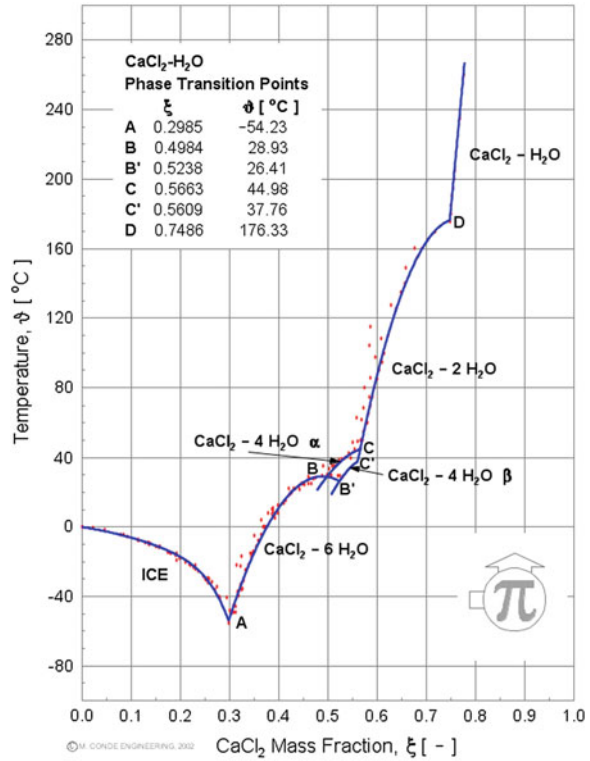


Fig. 5 Phase diagram for calcium chloride



Each segment of the solubility boundary between the liquid phase and a lithium chloride hydrate can be analytically described by an equation in the form:

$$\theta = \sum_{i=0}^2 A_i \zeta^i; \quad \theta \equiv \frac{T}{T_{c,*H_2O}} \tag{1}$$

where ζ is the mass fraction of the salt in the solution, T is the temperature in degrees Kelvin, and T_{c,H_2O} is the critical point of water (i.e., 647.1 K). A slightly different analytical expression describes the liquid–ice boundary:

$$\theta = A_o + A_1 \zeta + A_2 \zeta^{2.5} \tag{2}$$

Table 1 lists the A-coefficients for the preceding two equations for lithium chloride.

As shown in Fig. 5, the solubility boundary for calcium chloride has a multi-valued region where the solid salt can exist as different tetrahydrates. Only the solubility boundaries for the α and β tetrahydrates are shown in Fig. 5.

The analytical expression of the boundary between the liquid and the salt hydrate again takes the form of Eq. 1. For the liquid/ice boundary, the form of the analytical expression is:

Table 1 A-coefficients for the preceding two equations for lithium chloride

Boundary	A_0	A_1	A_2
Ice line	0.422088	-0.090410	-2.936350
LiCl-5H ₂ O	-0.005340	2.015890	-3.114590
LiCl-3H ₂ O	-0.560360	4.723080	-5.811050
LiCl-2H ₂ O	-0.315220	2.882480	-2.624330
LiCl-H ₂ O	-1.312310	6.177670	-5.034790
LiCl	-1.356800	3.448540	0.0

$$\theta = \sum_{i=0}^2 A_i \zeta^i + A_3 \zeta^{7.5} \tag{3}$$

Table 2 lists the A-coefficients for the calcium chloride solubility expressions.

3.1.2 Equilibrium Vapor Pressure

The critical property of a liquid desiccant is its ability to reduce the vapor pressure of water in an air/water-vapor mixture to a value that is significantly below the saturation pressure of water at the same temperature. This property is commonly represented as the desiccant’s equilibrium vapor pressure. Conde [2] presents analytical expressions for the equilibrium vapor pressure of both lithium chloride and calcium chloride solutions.

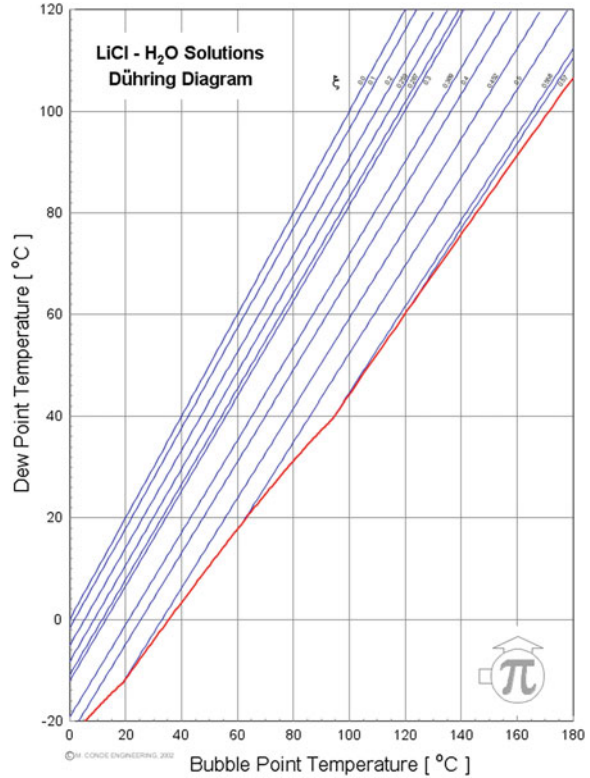
A useful alternative to equilibrium vapor pressure for a liquid desiccant is its equilibrium dewpoint temperature, which is defined as the dewpoint of an air/water-vapor mixture that is in equilibrium with the liquid desiccant. As shown in Figs. 6 and 7, plots of the equilibrium dewpoint temperature versus the solution’s temperature (labeled “Bubble Point Temperature” on the *x*-axis of the figures) have the simplifying characteristic that they are straight lines for a constant value of concentration.

A plot of a liquid desiccant’s equilibrium dewpoint with concentration and temperature as independent parameters is referred to as a Dühring chart. The lines in the Dühring chart for both lithium chloride and calcium chloride can be derived from the following analytical expression:

Table 2 A-coefficients for the calcium chloride solubility expressions

Boundary	A_0	A_1	A_2	A_3
Ice line	0.422038	-0.066933	-0.282395	-355.514247
CaCl ₂ -6H ₂ O	-0.378950	3.456900	-3.531310	0.0
CaCl ₂ -4H ₂ O α	-0.519970	3.400970	-2.851290	0.0
CaCl ₂ -4H ₂ O β	-1.149044	5.509111	-4.642544	0.0
CaCl ₂ -2H ₂ O	-2.335836	8.084829	-5.303476	0.0
CaCl ₂ -H ₂ O	-2.807560	4.673250	0.0	0.0

Fig. 6 Dühring chart for lithium chloride



$$T_{\text{dp}} = \sum_{i=0}^3 B_i \xi^i + (B_4 + B_5 \xi) * T' \quad (4)$$

where once again ξ is the mass fraction of the salt in the solution, but the temperatures T_{dp} and T' are now in degrees Celsius. Table 3 has the B -coefficients for both lithium chloride and calcium chloride (For $0.15 \leq \xi \leq 0.45$ and $-10 \leq T_{\text{dp}} \leq 100^\circ\text{C}$, Eq. 4 yields dewpoint temperatures that are consistent to within 0.5°C with dewpoints that are calculated from the equilibrium vapor pressure analysis in Conde [2]).

3.1.3 Density

As shown in Figs. 8 and 9, the density for both lithium chloride and calcium chloride normalized on the density of water at the same temperature is a function of the mass fraction ratio of solute to solvent, $\xi/(1 - \xi)$. The functional form for the curves in the preceding two figures is:

Fig. 7 Dühring chart for calcium chloride

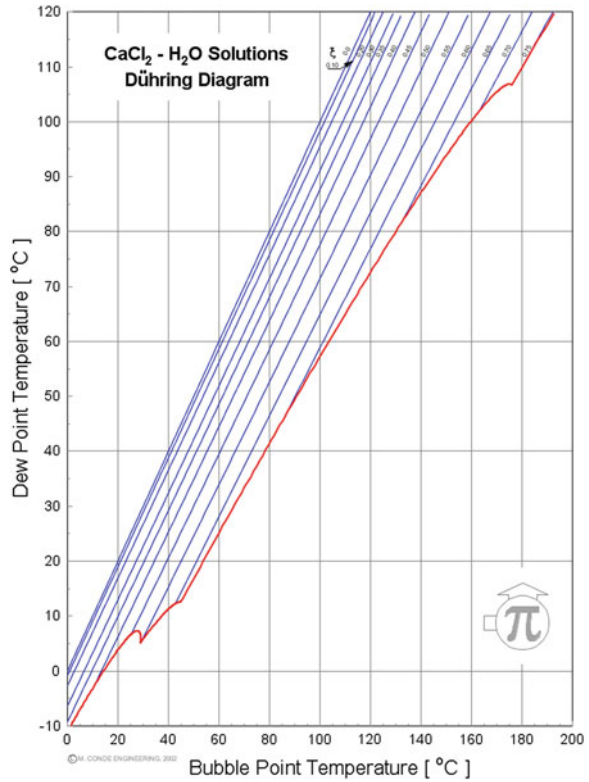


Table 3 B-coefficients for both lithium chloride and calcium chloride

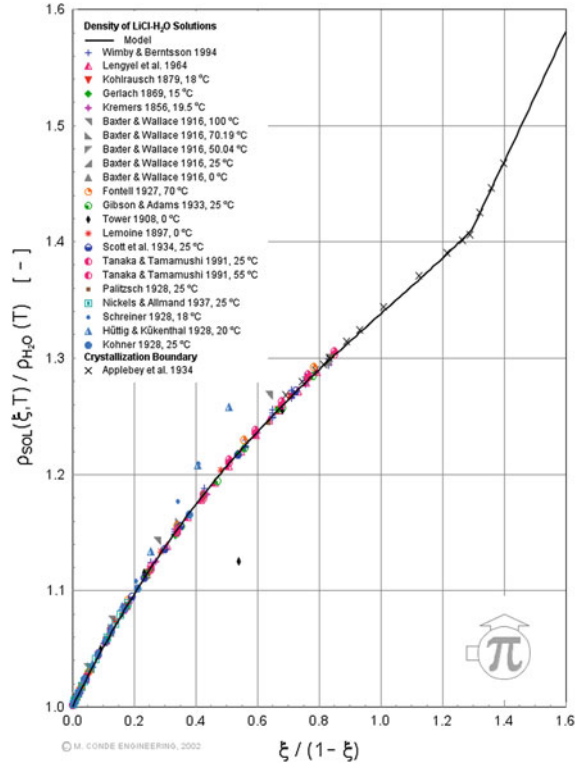
	B ₀	B ₁	B ₂	B ₃	B ₄	B ₅
LiCl	-10.8073	112.529	-483.193	320.350	1.02366	-0.311181
CaCl ₂	0.5731	-19.831	63.045	-251.967	1.00196	-0.086577

$$\rho_{sol}(\xi, T) = \rho_{water}(T) \sum_{i=0}^3 \rho_i \left(\frac{\xi}{(1 - \xi)} \right)^i \tag{5}$$

where ρ_{sol} and ρ_{water} are the mass density of the liquid desiccant and water in common dimensional units. The coefficients ρ_i in the preceding equation appear in Table 4.

As shown in Fig. 8, the normalized curve for the density of lithium chloride has a transition point at approximately $\xi/(1 - \xi)$ equal to 1.3. The concentration of the solution at this point is close to 56 %, which is well above a practical operating concentration for a liquid-desiccant air conditioner.

Fig. 8 Relative density of lithium chloride solutions



3.1.4 Dynamic Viscosity

The dynamic viscosity for solutions of lithium chloride and calcium chloride is most conveniently expressed relative to the dynamic viscosity of water. Dynamic viscosity of the liquid desiccant, η_{sol} , can be expressed as

$$\eta_{sol}(\zeta, \theta) = \eta_{water}(\theta) e^{\eta_1 \zeta^{3.6} + \eta_2 \zeta + \eta_3 \frac{\zeta}{\theta} + \eta_4 \zeta^2} \quad (6)$$

where ζ equals $\xi / (1 - \xi)^{1.667}$ and θ is the temperature of the solution normalized on the critical temperature of water (both expressed as absolute temperatures). Table 5 lists the η -coefficients for Eq. 6.

3.1.5 Thermal Conductivity

As reported by Conde [2], “the thermal conductivity of aqueous solutions of lithium and calcium chloride are, perhaps, their less well known property”. Recognizing the considerable scatter between the measured thermal conductivity reported by different researchers, Conde [2] focuses on the data reported by

Fig. 9 Relative density of calcium chloride solutions

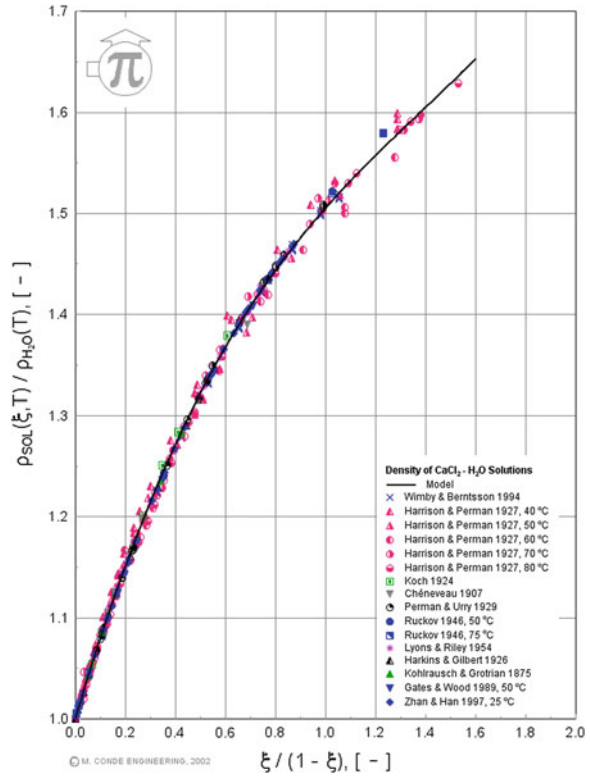


Table 4 The coefficients ρ_i in the preceding equation

	LiCl-H ₂ O	CaCl ₂ -H ₂ O
ρ_0	1.0	1.0
ρ_1	0.540966	0.836014
ρ_2	-0.303792	-0.436300
ρ_3	0.100791	0.105642

Table 5 The η -coefficients for Eq. (6)

	LiCl-H ₂ O	CaCl ₂ -H ₂ O
η_1	0.090481	-0.169310
η_2	1.390262	0.817350
η_3	0.675875	0.574230
η_4	-0.583517	0.398750

Uemura [3] for lithium chloride and Riedel [4, 5]. These two sets of experimental data are well correlated at 20 °C by the following analytical representation suggested by Riedel [4, 5]:

$$\alpha_R = \alpha_0 + \alpha_1 \zeta \quad (7)$$

where α_R is the equivalent thermal conductivity depression defined by:

$$\alpha_R = \frac{k_{\text{water}}(T) - k_{\text{sol}}(T, \zeta)}{\gamma_{\text{eq}}} \quad \text{and} \quad \gamma_{\text{eq}} = \frac{\zeta * \rho_{\text{sol}}(T, \zeta) * I_s}{M}$$

In the preceding equations, k_{water} and k_{sol} are the thermal conductivity of water and the liquid desiccant in dimensional units of W/m-C, the density of the desiccant is expressed in kg/m³, γ_{eq} is the equivalent ionic concentration (as named by Riedel [4, 5]), I_s is the ionic strength of the species in solution (1 for LiCl and 2 for CaCl₂), M is the molar mass of the salt (42.39 for LiCl and 110.98 for CaCl₂, and the coefficients α_0 and α_1 are shown in Table 6. For lithium chloride, Eq. 7 agrees well with the experimental data of Uemura [3] at a temperature between 10 and 100 °C. For calcium chloride, the agreement between Eq. 7 and experimental data is not as good over the same temperature range. (The interested reader is referred to Conde [2] for a more detailed comparison between Eq. 7 and experimentally measured values of thermal conductivity.)

3.1.6 Specific Thermal Capacity

Conde [2] proposes the following analytical expression for specific thermal capacity of the two salt solutions:

$$C_{p_{\text{sol}}}(T, \zeta) = C_{p_{\text{water}}}(T) * (1 - f_1(\zeta) * f_2(T)) \quad (8)$$

The function $f_1(\zeta)$ can be expressed as

$$f_1(\zeta) = A * \zeta + B * \zeta^2 + C * \zeta^3 \quad (9)$$

for calcium chloride and lithium chloride at concentrations below 0.31. At higher concentrations for lithium chloride, $f_1(\zeta)$ is a linear function of concentration:

$$f_1(\zeta) = D + E * \zeta \quad (10)$$

For both salts, the function $f_2(\zeta)$ takes the form:

$$f_2(\zeta) = F * \vartheta^{0.02} + G * \vartheta^{0.04} + H * \vartheta^{0.06} \quad (11)$$

Table 6 The coefficients α_0 and α_1

	LiCl	CaCl ₂
α_0	10.8958×10^{-3}	5.9473×10^{-3}
α_1	-11.7832×10^{-3}	-1.3988×10^{-3}

Table 7 The values for the constants that appear in Eqs. (9–11)

	A	B	C	D	E	F	G	H
LiCl–H ₂ O	1.43980	–1.24317	–0.12070	0.12825	0.62934	58.5225	–105.6343	47.7948
CaCl ₂ –H ₂ O	1.63799	–1.69002	1.05124	0.0	0.0	58.5225	–105.6343	47.7948

where $\vartheta = T/228 - 1$ and the units for T are degrees Kelvin. Table 7 has the values for the constants that appear in Eqs. (9–11).

3.1.7 Heat of Dilution and Enthalpy

An energy analysis of a liquid-desiccant system requires that the enthalpy of the desiccant to be known over the temperatures and concentrations that occur throughout the system. Although it is possible to calculate the enthalpy of the liquid desiccant using experimentally measured values of its heat of dilution,¹ a more consistent approach applies the Clausius–Clayperon equation to calculate a heat of dilution that is consistent with the desiccant’s equilibrium vapor pressure.

The Clausius–Clayperon equation for a liquid desiccant in equilibrium with a vapor phase is

$$\frac{dP}{dT} = \frac{h'_{fg}}{T * V'_{fg}} \quad (12)$$

where T and P are the temperature and pressure of the system, and h'_{fg} and V'_{fg} are the enthalpy and volume differences between the vapor and liquid phases, respectively. To a very close approximation, V'_{fg} equals the volume of the vapor phase, V' , and the preceding equation can be simplified as,

$$\frac{dP}{dT} = \frac{h'_{fg}}{T * V'} \quad (13)$$

Since ionic salts such as lithium chloride and calcium chloride do not have an intrinsic vapor pressure, h'_{fg} is the difference between the enthalpy of water vapor and the partial enthalpy of water in the desiccant,

$$h'_{fg} = h_{\text{vapor}} - h_{\text{water}}^* \quad (14)$$

where h_{water}^* is the partial enthalpy of water in the desiccant. The heat of dilution, h_{dil} , is the difference in enthalpy of pure water and the partial enthalpy of water in the desiccant

$$h_{\text{dil}} = h_{\text{water}}^* - h_{\text{water}} \quad (15)$$

¹ The heat of dilution is the heat that evolves when an increment of water is added to the liquid desiccant at a fixed temperature and pressure.

Eliminating h_{water}^* from Eqs. 14 and 15 yields

$$h'_{\text{fg}} = h_{\text{fg}} - h_{\text{dil}} \quad (16)$$

where h_{fg} is the phase-change enthalpy for pure water (i.e., $h_{\text{vapor}} - h_{\text{water}}$).

Since the vapor that is in equilibrium with either lithium chloride or calcium chloride will be pure water, the dewpoint temperature of water, T_{dp} , can replace the water vapor pressure in Eq. 13,

$$\frac{dP}{dT} = \frac{dP}{dT_{\text{dp}}} * \frac{dT_{\text{dp}}}{dT} \quad (17)$$

Equations 13, 16, and 17 can be combined and solved for the heat of dilution

$$h_{\text{dil}} = h_{\text{fg}} - T * V' * \frac{dP}{dT_{\text{dp}}} * \frac{dT_{\text{dp}}}{dT} \quad (18)$$

The temperature derivative of the dewpoint temperature in the preceding equation is the slope of a constant-concentration line on the Dühring chart. This slope can be calculated from Eq. 4. Since all other terms on the right side of Eq. 18 are derived from the properties of pure water, the information in the Dühring chart allows the heat of dilution to be calculated for the desiccant.

The heat of dilution applies to an isothermal and isobaric process in which the concentration of the desiccant changes. If the enthalpy of the desiccant is known at one concentration, ξ_o , and a reference pressure, P_o , it can be calculated at other concentrations using the heat of dilution in the following integration:

$$h(T, P_o, \xi) = \left(\frac{\xi}{\xi_o} \right) * \left\{ h(T, P_o, \xi_o) + \int_{\xi_o}^{\xi} (h_{\text{dil}} + h_{\text{water}}) * d \left(\frac{\xi_o}{\eta} \right) \right\} \quad (19)$$

where η is the integration variable. The quantity $h(T, P_o, \xi_o)$ in the preceding representation can be calculated from Eq. 8 for the specific thermal capacity $C_{p_{\text{sol}}}(T, \xi)$ in the following integration:

$$h(T, P_o, \xi_o) = h(T_o, P_o, \xi_o) + \int_{T_o}^T C_{p_{\text{sol}}}(\eta, \xi_o) d\eta \quad (20)$$

The interested reader is referred to Conde [2] for analytical expressions for surface tension, enthalpy of dilution, and diffusion coefficient of water into the salt solutions.

3.2 Contactors with External or Internal Heat Exchange

It is useful to differentiate between liquid-desiccant systems in which the desiccant is either heated or cooled before it is supplied to the contactor with those in which heat exchange can occur within the contactor. For the first type, the contactor is

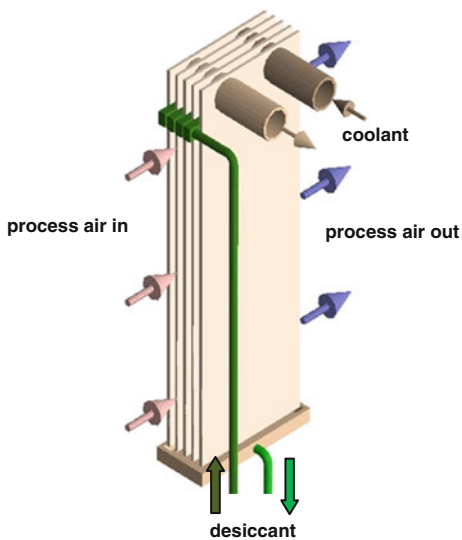
composed of a packed bed of structured media (similar to the fill in a cooling tower) or random packing (similar to the Raschig rings that might be used in a distillation column). Depending on whether the contactor is a conditioner or a regenerator, the liquid desiccant is cooled or heated before it is sprayed or dripped onto the packed bed, and air is drawn through the packing. The industrial system shown in Fig. 3 uses this type of contactor with external heat exchange for both the conditioner and regenerator.

As shown in Fig. 10, the alternative to a contactor with external heat exchange is the one in which the contactor is a heat exchanger. For this contactor with internal heat exchange, a heat transfer fluid flows within the plates of the heat exchanger, desiccant flows on the outer surface of the plates, and air flows between the plates. If the contactor is a conditioner, the heat transfer fluid is typically water from a cooling tower or chiller, and air is dried and cooled as it flows between the plates coming in direct contact with the liquid desiccant. If the contactor is a regenerator, the heat transfer fluid typically is hot water or a hot water/glycol mixture, and the air carries away the water released by the heated desiccant.

Systems that use contactors with heat exchangers external to the packed bed must operate at high desiccant-flooding rates to insure that the desiccant’s temperature does not change as water is either absorbed by the desiccant, which is an exothermic process, in the conditioner or released by the desiccant, which is an endothermic process, in the regenerator. Systems with heat exchange within the contactor do not rely on the thermal mass of the desiccant flow to control its temperature, and so they can operate at lower flooding rates.

The difference in flooding rates can be illustrated by comparing the performance of the two types of conditioners that process the same air stream. For this comparison, air at 86 °F (30 °C) and 0.0192 lb/lb (19.2 g/kg-dry-air) is processed

Fig. 10 Internally cooled contactor



by the conditioner. Cooling water is available at 65 °F (18.3 °C). For the externally cooled conditioner, this cooling water cools desiccant to 70 °F (21.1 °C) in a separate heat exchanger before the desiccant is supplied to the conditioner (as is shown in Fig. 3). For the internally cooled conditioner, which in this example is implemented as the plate-type heat exchanger shown in Fig. 10, the cooling water flows within the plates, desiccant flows on the outer surface of the plates, and the process air flows between the plates. The desiccant supplied to both conditioners is 38 % lithium chloride by mass.

With a desiccant-to-air mass flow ratio (L/G) of 2.22, the externally cooled contactor, under typical operating conditions, supplies air at 77.5 °F (25.3 °C) and 0.0072 lb/lb (7.20 g/kg). The desiccant leaves the conditioner at 37.8 % and 81.0 °F (27.2 °C). The latent effectiveness for this dehumidification process is 0.77 (where a latent effectiveness of 1.0 is defined by a process that supplied air in equilibrium with the cool, strong desiccant that is supplied to the conditioner).

In this example, the humidity ratio for air in equilibrium with the entering and leaving desiccant increases from 0.00359 lb/lb (3.59 g/kg) to 0.00543 lb/lb (5.43 g/kg). This increase of 0.00184 lb/lb (1.84 g/kg) is due mostly to the increase in the desiccant's temperature: 0.00175 lb/lb (1.75 g/kg) is due to the change in temperature and only 0.00009 lb/lb (0.009 g/kg), to the change in concentration.

The conditioner with the internally cooled contactor will supply air at the same humidity ratio (7.20 g/kg) when operating with a desiccant flooding rate that is 1/20th of that used with the externally cooled contactor: L/G equals 0.10 for the internally cooled contactor. Also, with the cooling water flowing within the contactor, air is supplied at a slightly lower temperature: 75.4 °F (24.1 °C) versus 77.5 °F (25.3 °C).

Heat exchange within the contactor will also improve the performance of a regenerator. In the most common configuration for a liquid desiccant regenerator, which includes the one shown in Fig. 10, the desiccant is heated to raise its equilibrium vapor pressure. A stream of scavenging air with significantly lower water vapor pressure flows through a bed of contact media that is flooded with the hot desiccant. The difference in vapor pressures moves water from the desiccant to the scavenging air stream.

In a scavenging-air regenerator that operates with unheated ambient air, the three parameters that typically have the strongest influence on its thermal efficiency are (1) the heat of dilution for the desiccant, (2) the ratio of sensible and latent heat exchange between the desiccant and the air, and (3) the amount of heat that can be exchanged between the hot, strong desiccant exiting the regenerator and the cool, weak desiccant entering the regenerator. The concentration of the desiccant supplied to the regenerator affects all three parameters, with the first and second parameters degrading the regenerator's thermal efficiency at higher concentrations, and the third, improving it.

In the preceding comparison of an externally cooled conditioner and internally cooled conditioner, the inlet-to-outlet change in desiccant concentration for the externally cooled conditioner was 0.2 points (e.g., 38.0–37.8 %) and for the internally cooled conditioner, 4.0 points. A similar difference in the concentration change

will also occur between the two types of regenerators. Thus, a lithium–chloride LDAC with an internally cooled conditioner and an internally heated regenerator could operate in a “once through” mode in which 38 % solution is supplied to the conditioner from the regenerator and 34 % solution is supplied to the regenerator from the conditioner. By comparison, an LDAC with contactors that use external heat exchange operates in a high recirculation mode in which approximately 38 % solution is recirculated over the conditioner, but 42 % solution is recirculated over the regenerator. The difference in the concentration of the weak and strong desiccant exchanged between the regenerator and the conditioner is 4 points in both cases, so the exchange flow rate of desiccant is almost the same (assuming that the water absorption rate in the condition is equal for the two systems).

In this example, the average desiccant concentration is 36 % in the internally heated regenerator and 42 % in the externally heated regenerator. The heats of dilution for lithium chloride at 80 °C for these two concentrations are 75.7 Btu/lb (175.7 kJ/kg) at 36 % and 108.2 Btu/lb (251.1 kJ/kg) at 42 %. The thermal efficiency for regeneration expressed as a coefficient of performance (COP) is the ratio of the thermal energy required to remove a unit of water from the desiccant divided by the liquid–vapor phase change energy for a unit of pure water (i.e., h_{fg} equal to 1059 Btu/lb [2,458 kJ/kg]). Since the heat of dilution equals the additional energy required to evaporate water from the desiccant (compared to h_{fg}), the preceding heats of dilution will then limit the regeneration COP to 0.928 for the 36 % solution and 0.898 for the 42 % solution.

A second effect that further limits the regenerator’s COP is the change in the fraction of heat transfer between the desiccant and the scavenging air that is latent. For scavenging air regenerators that directly heat the desiccant (as opposed to those that might work with hot air), most of the thermal energy supplied to the desiccant leaves the regenerator as either an increase in the sensible energy or latent energy of the exhaust air. Only the increase in the air’s latent energy is useful, the air’s increase in sensible energy being a parasitic loss for the regeneration process.

The driving potential for sensible energy exchange between the desiccant and the air is the temperature difference between the two flows, and the driving potential for latent energy exchange is the difference in the water vapor pressure. Since a desiccant’s equilibrium water vapor pressure decreases as its concentration increases, a scavenging-air regenerator that operates with a higher desiccant concentration will have a lower latent energy exchange than one that operates with a lower desiccant concentration (where this conclusion assumes both regenerators operate at the same desiccant temperature and desiccant/air boundary layer characteristics). Since latent energy exchange is equivalent to water removed from the desiccant, the higher desiccant concentration degrades the regenerator’s COP.

For the 6-point difference in regeneration concentration between LDACs with external and internal heat exchange and both regenerators operating with source hot water at 185 °F (85 °C), the latent fraction for heat exchange between the desiccant and the scavenging air might typically decrease from 0.762 to 0.663 as

the desiccant concentration increases. Combining the limit on COP imposed by the heat of dilution with the parasitic loss associated with the sensible heating of the scavenging air produces an overall limit on the COP of 0.71 for the internally heated regenerator and 0.60 for the externally heated regenerator.

The third of the three parameters that will have a strong influence on the regenerator's COP is the amount of preheating required to bring the weak desiccant up to the operating temperature of the regenerator. Since the specific heat of the desiccant will typically decrease with increasing concentration, the regeneration penalty imposed by preheating is smaller at higher concentrations.

Assuming that the weak desiccant flowing from the conditioner to the regenerator must be preheated from 95 °F (35 °C) to 167 °F (75 °C), the preheating requirements for 38 % and 34 % lithium chloride are 45.7 Btu/lb (106.1 kJ/kg) and 47.5 Btu/lb (110.3 kJ/kg), respectively. With the strong desiccant that returns to the conditioner having a concentration that is four points higher than the weak supply to the regenerator, the mass flow of desiccant to the regenerator will be ten times greater than the regenerator's water removal rate. Multiplying the preceding preheating requirements by ten (since ten units of desiccant are exchanged per unit of water removed in the regenerator) produces values that when normalized on h_{fg} are 0.43 and 0.45. The complements of these normalized values, 0.57 and 0.55, are a measure of the thermal energy supplied to the regenerator that would be available for evaporating water from the desiccant. Adding in the degrading effects of heat of dilution and the parasitic sensible heat transfer to the scavenging air leads to limits on the COP of 0.34 for the externally heated regenerator and 0.39 for the internally heated regenerator.

The thermal requirement for preheating the weak desiccant supplied to the regenerator can be greatly reduced by recovering thermal energy from the hot, strong desiccant that leaves the regenerator (a function that is performed by the IHX shown in Fig. 3). The heat available when 42 % lithium chloride is cooled from 167 °F (75 °C) to 95 °F (35 °C) is 43.8 Btu/lb (101.7 kJ/kg). Thus, in the ideal limit where 100 % of this thermal energy is transferred to the weak desiccant flowing to the regenerator, the preheating requirements again expressed as a fraction of h_{fg} would be reduced to 0.018 for the externally heated regenerator and 0.035 for the internally heated regenerator. Under this ideal condition of a 100 % effective heat exchanger transferring thermal energy between the desiccant flows into and out of the regenerator and adding in the degrading effects of heat of dilution and sensible heat exchange to the scavenging air, the upper bound on COP would be 0.685 for the internally heated regenerator and 0.589 for the externally heated regenerator.

The preceding example is intended to illustrate the effects that limit a regenerator's COP. It is not intended to be a prediction of the performance of a particular regenerator. In addition to showing the modest gain in thermal COP for the LDAC that has contactors with internal heat exchange, the example does show

the importance of recovering heat from the hot, concentrated desiccant that leaves the regenerator regardless of the type of contactor. Although the 100 % effective heat exchanger that was used to determine the upper limit for the regenerator's COP is clearly impractical, most of the performance benefit could be captured by a high-effectiveness heat exchanger.

The lower desiccant flow in an LDAC with internally heated and cooled contactors leads to other efficiency improvements, mostly for lower pump and fan powers. As previously noted, the desiccant-to-air mass flow ratio (L/G) for externally cooled and internally cooled conditioners are in the order of 2.2 and 0.1, respectively. For an LDAC that processes 6,000 cfm (10,200 m³/h) of air, the desiccant flows to the conditioner would be 49.4 gpm (187 l/min) and 2.25 gpm (8.5 l/min) for the externally cooled and internally cooled units, respectively. The pump power for the higher flow would be in the order of 2.5–3.5 kW, while for the lower flow, it would be between 150 and 250 W. A similar difference in powers would apply to the pumps that supply desiccant to the regenerators.

The highly flooded, externally cooled contactor will also have higher air-side pressure drops than its internally cooled counterpart. With a face velocity of 394 fpm (2 m/s), representative pressure drops across the externally cooled and internally cooled contactors would be 1.2" w.c. (300 Pa) and 0.6" w.c. (150 Pa), respectively, and fan power for moving air across the conditioners would be 1,500 and 750 W.

3.3 Commercially Available Liquid-Desiccant Systems

At the beginning of 2012, two companies had been actively manufacturing and selling liquid-desiccant air conditioners and dehumidifiers for more than two years: Kathabar Dehumidification Systems, Inc, based in Somerset, NJ, US, and Advantix Systems based in Sunrise, FL, US, (in cooperation with DuCool). The LDACs of these companies use contactors with external heat exchange. Based on the information available on the Internet, two other companies began selling LDACs in 2012: Dyna-Air, based in Japan, and the Nanjing Hanwei Nanleng Refrigeration Group, based in Nanjing, China. Several other companies were either selling LDACs in limited numbers, demonstrating precommercial LDACs or developing LDAC products with support from either private investors or government grants. These precommercial activities include work at the following companies: (1) M. Conde Engineering, (2) Menerga Apparatebau, GmbH, (3) 7 AC Technologies, (4) L-DCS, and (5) AIL Research, Inc. With the exception of Menerga, these companies are all developing LDACs that use internally cooled contactors.

References

1. Ertas A, Anderson EE, Kiris I (1992) Properties of a new liquid desiccant solution—lithium chloride and calcium chloride mixtures. *Sol Energy* 49(2):205
2. Conde M (2004) Properties of aqueous solutions of lithium and calcium chlorides: formulations for use in air conditioning equipment design. *Int J Therm Sci* 43:367–382
3. Uemura T (1967) Studies on the lithium chloride water absorption refrigerating machine, vol 9. Technology Reports for the Kansai University, pp 71–88
4. Riedel L (1950) Wärmeleitfähigkeitsmessungen an kältetechnisch wichtigen Salzlösungen. *Kältetechnik* 2:99–109
5. Riedel L (1948) Wärmeleitfähigkeitsmessungen an Flüssigkeiten, Habilitationsschrift, Technische Hochschule Karlsruhe

Mathematical Modeling of Heat and Mass Transfer in Regenerators with Desiccant Materials

L. A. Sphaier

List of Symbols

\mathcal{A}_p	Flow area
\mathcal{A}_s	Surface area
\mathcal{A}_w	Wall area (perpendicular to flow direction)
c, c_p	Specific heats
\mathcal{D}	Mass-diffusivity
\mathcal{D}_g^T	Soret or thermal-diffusion coefficient
e_{sor}	Fraction by which sorption heat exceeds vaporization heat
f_s	Mass fraction of adsorbent material in felt
h	Convective heat transfer coefficient between felt and process stream
h_m	Convective mass transfer coefficient between felt and process stream
h_w	Heat transfer coefficient between felt and wall
h_π	Mass transfer coefficient between pores and vapor in equilibrium with desiccant
i	Specific enthalpy
\tilde{i}	Specific enthalpy on dry basis
i_{vap}	Latent heat of vaporization
i_{wet}	Differential heat of wetting
Δi_w	Integral heat of wetting
i_{sor}	Heat of sorption
\mathbf{j}''	Mass flux vector
j''	Mass flux component
k	Thermal conductivity
K	Number of sections in regenerator
L	Regenerator length
p	Pressure
\mathcal{P}_s	Wetted perimeter

L. A. Sphaier

Department of Mechanical Engineering, Universidade Federal Fluminense, Rua Passo da Pátria 156, Niterói, RJ, Brazil

e-mail: lasphaier@id.uff.br

\mathcal{P}_w	Contact perimeter at felt-wall interface
$\dot{\mathbf{q}}''$	Mass flux vector
\dot{q}'	Heat flux component
\dot{q}_i''	Heat flux at felt-stream interface
\dot{q}_w''	Heat flux at felt-wall interface
\mathcal{S}	Surface or interface
\mathcal{S}_p	Felt-stream interface
\mathcal{S}_w	Felt-wall interface
\dot{s}_{sor}'''	Volumetric rate of sorption heating
T	Temperature
t	Time
t_f	Total cycle time
W	Concentration in adsorbed phase
Y	Concentration in gas phases

Greek Symbols

ε	Porosity
ϕ	Relative humidity
λ_m	Dufour diffusion coefficient
ρ	Density or specific mass
τ_{dw}	Dwell time
τ_G, τ_S	Tortuosities
ω	Wheel rotation speed
ϕ	Relative humidity

Subscripts

a	Dry air
f	Porous sorbent medium
g	Gas phase of porous medium
i	At or related to the felt-stream interface
k	In a given regenerator section k
l	Adsorbed phase
ls	Saturated liquid
s	Solid phase of porous medium
v	Water vapor

Superscripts

*	Dimensionless quantity
+	Modified quantity

1 Introduction

The phenomenon of Physical Adsorption has been known for over two centuries and extensively studied over the past couple of decades. The fact that porous solids could reversibly take up large volumes of vapor was identified in the late eighteenth century, by the studies of Scheele and Fontana, and the term adsorption appears to have been introduced by Kayser, as mentioned by Gregg and Sing [21]. Nevertheless, it was only several decades later that adsorption technologies gained widespread application to large-scale industrial processes. Among these major applications, regenerative heat and mass exchangers that employ sorbent materials have become an attractive option in a variety of industrial processes.

In HVAC applications, two classes of heat and mass regenerators with sorbent materials are frequently employed: *total heat regenerators*¹ and *regenerative dehumidifiers*. In order to achieve a large surface area in a compact structure, the regenerators are composed of mini-channels, whose walls are partly composed of an adsorbent, which exchanges heat and moisture with the process fluid stream. During operation, two process streams are alternately fed to the channels, resulting in two distinct operating periods, which form a complete cycle. The regenerator channels are arranged in a matrix, which is either of *fixed-bed* (or stationary) type, or *rotary* type. Although both designs can perform equivalently, the fixed-bed type requires two matrices for continuous operation, since each matrix needs to be switched between the two process streams at the beginning of every period. As an alternative, in rotary regenerators, a single rotating matrix allows uninterrupted operation by being continuously cycled between the two process streams.

According to the given application, rotary regenerative exchangers are respectively termed *enthalpy wheels*—used for energy recovery—and *desiccant wheels*—employed in dehumidification. Although this has been the traditional terminology adopted in the literature, an alternative terminology in classifying rotary heat and mass regenerators has been recently proposed [49]. This terminology involves using the term *desiccant wheel* for both types of exchangers; however, enthalpy exchangers are termed *passive desiccant wheels*, since they require no activation energy for regeneration, while dehumidifiers (traditionally referred to as desiccant wheels) are actually termed *active desiccant wheels*, since these, in fact, require an activation energy for regeneration. In this text, the terminology *active desiccant wheel* will be employed for referring to dehumidifiers, whereas *passive desiccant wheel* or simply *enthalpy wheel* will be adopted to denote energy exchangers.

The main difference between an enthalpy wheel and an active desiccant wheel is that the former possesses a low matrix sorbate-capacity, whereas the latter has a high matrix sorbate-capacity. In other words, active desiccant wheels, employ a greater amount of hygroscopic material in their matrix while compared to enthalpy wheels, such that they can uptake a much larger amount of water than enthalpy

¹ Also known as energy or enthalpy exchangers.

exchangers. In regard to operation, dehumidifiers operate at relative low rotation rates, for maximizing the drying potential, while enthalpy exchangers operate at higher rotational speeds, for maximizing heat and mass transfer between the matrix and process streams. In the HVAC industry, a common application of active desiccant wheels is in the so-called *desiccant cooling systems* [22, 33, 48, 50, 71], which rely on water evaporation to meet the required cooling loads. These systems have been gaining popularity over the last decades due to their environmental friendliness, due to the facts that they require no specialized refrigeration fluid and that they can be powered by low-grade energy sources. Also amongst HVAC applications, enthalpy wheels are commonly employed for reducing air-conditioning costs in ventilated buildings by recovering energy from the exhaust air to the supply air [81].

While compared to regenerative sensible heat exchangers [35, 64], or periodic sensible heat exchangers, heat and mass transfer regenerators exhibit similar characteristics. The main difference, is the additional transport phenomena due to the presence of mass transfer, which is highly coupled with heat transfer and conventionally results from normal condensation/evaporation or sorption/desorption. Clearly, the former requires that an adsorbent medium be present. In most formulations of enthalpy wheels and active desiccant wheels, however, the normal condensation and evaporation is not taken into account; nevertheless, this type of phase change is usually unwanted in these devices. Due to the inherent complexity of the phenomena involved in heat and mass regenerators with sorbent materials, a thorough understanding of the transport mechanisms is crucial for obtaining an accurate mathematical formulation; as a consequence, numerous mathematical models for these types of regenerators have been proposed throughout the last decades.

While the mathematical modeling and analysis of sensible heat regenerators can be dated to studies published almost a century ago, such as the works of Hausen [23, 24], models for describing the operation of heat and mass transfer regenerators were only available a few decades later. In addition, the first studies that evaluated the operation of these exchangers were overly simplified. Before periodic solutions were available, the performance of regenerative exchangers with sorbent materials was predicted by models in which the mass transfer breakthrough curves were analyzed. These early models addressed the problem of isothermal mass transfer in fluid flow through an adsorbent porous media. In addition, the transfer rates between the adsorbed phase and the fluid stream were evaluated by considering gas-side resistances, using convective (or film-controlled) transport coefficients. Some formulations also allowed for solid-side resistances, by means of overall (often termed *pseudo*) transfer coefficients. Examples of these models are the studies by Hougen and Marshall [28], and the Schumann-Anzelius solutions, tabulated in [37]. Rosen [52] proposed a model that was probably the first to treat the solid-side transport as an actual diffusional process. He considered a porous medium consisting of spherical particles and applied a linear equilibrium relation. The non-isothermal case of flow through a sorbent porous medium was later considered in the studies by Bullock and Threlkeld [5], and Chi and Wasan [9], in

which the coupled heat and mass transport rates were evaluated using overall transfer coefficients. Meyer and Weber [43] proposed a general treatment for the problem of coupled heat and mass transfer in flow through an adsorbing medium, considering diffusion in spherical particles and using a nonlinear equilibrium relation.

Apparently, until 1970, no provisions had been made to account for flow at the boundaries of the region in which the diffusional transport occurs, as it actually happens in the channeled matrix of a regenerator. The earliest formulation encountered in literature to consider this case was that of Chase et al. [8], who proposed a simple adiabatic two-dimensional linear model with constant coefficients, including the diffusional effects through the thickness of the sorbent medium.

In the 1970s and 1980s, various investigations related to the mathematical modeling of the transport phenomena in periodically operated exchangers were conducted [2, 3, 7, 27, 30–32, 39, 41, 42, 53, 78, 79]. These studies employed one-dimensional formulations in which overall transfer coefficients were used to predict the transfer rates between the two phases, but with the bulk fluid stream flowing through channels rather than the porous media itself. The studies of Close, Banks and Maclaine-Cross [1, 12, 39], presented an approach in which the governing partial differential equations with temperature and humidity ratio as the dependent variables are written in terms of characteristic potentials. This approach leads to a non-linear analogy methodology for predicting the operation of heat and mass transfer regenerators [2, 3]. In addition to these one-dimensional formulation studies, models that accounted for the diffusional processes within the porous material as local phenomena were developed. Ghezelayagh and Gidaspow [18] presented a formulation for the isothermal case considering both micro-pore and macro-pore diffusion mechanisms. Pesaran and Mills [51] proposed a model that allowed for the diffusional process within isothermal spherical particles in fluid flow through an adiabatic sorbent bed, and Charoensupaya and Worek [6] considered the diffusional phenomena within the thickness of the porous sorbent matrix instead of particles and presented periodic solutions for a hypothetical linear equilibrium relationship. Later, Majumdar and Worek [40] proposed a formulation in which the diffusional effects were included in particles and through the sorbent thickness, providing single-blow solutions for nonlinear equilibrium relations curve-fitted from experimental data.

During the 1990s, mathematical formulations were developed for adsorption-based regenerative exchangers, with emphasis on enthalpy wheels. Klein et al. [36] presented one of the first studies dedicated to enthalpy exchangers, and employed the non-linear analogy method presented in [2, 3]. Stiesch et al. [77] analyzed the performance of enthalpy exchangers by a simple approach using curve fitted data from the numerical solution of heat and mass transport equations. Simonson and Besant [67–70] employed a one-dimensional model that includes axial heat diffusion in the matrix, and used the data to develop correlations for predicting the performance of enthalpy exchangers in terms of dimensionless groups; an interesting point observed in these works is that the heating due to adsorption is divided

between the process stream and channel wall. Besides studies focused on enthalpy wheels, new investigations dedicated to modeling and assessing the performance of active desiccant wheels also continued to be developed. Zheng et al. [83–85] employed a simple one-dimensional model without local diffusion transport terms.

Since the turn of the millennium, a number of studies focused on the mathematical modeling and simulation of active desiccant and enthalpy wheels have appeared in the literature. Particularly interesting is the work of Ge et al. [16], who present a review of mathematical models used in different investigations. Dai et al. [14] utilized a two-dimensional model that included diffusion of heat and moisture within the rotary matrix in both axial and angular directions. Niu and Zhang [45], Zhang and Niu [82] adopted a two-dimensional model for the transport phenomena in the sorbent material for analyzing both active and passive desiccant wheels. The model utilized by Gao et al. [15] also included transport terms in the angular direction; however, local diffusion terms were only included in the axial direction within the rotary matrix. Golubovic and Worek [20] considered a simple one-dimensional model, similar to the one employed in [83–85]; however, a modification was included to account for condensation within channels which are prone to occur at higher operating pressures. Later on, Golubovic et al. [19] employed this simple one-dimensional model to predict the performance of rotary regenerators with and without heated purge. Jeong and Mumma [29] utilized a model similar to the one adopted in [67–70] for determining correlations for estimating the performance of enthalpy exchangers. In 2004, Sphaier and Worek proposed a unified formulation that contemplates both enthalpy exchangers and active desiccant wheels. This general formulation considered multi-dimensional heat and mass diffusion within the adsorbent layer. Later on Sphaier and Worek [72], the same authors compared a two-dimensional version of this formulation with a simple one-dimensional counterpart (similar to the one used in most one-dimensional models), and the presented results suggested that one-dimensional models are better suited for active desiccant wheels rather than for enthalpy wheels. The importance of including axial diffusion effects in active desiccant wheels and enthalpy exchangers was analyzed in a separate study Sphaier and Worek [73]. In following studies, the same authors presented a numerical scheme for solving the employed model [74], and presented a generalized effectiveness-NTU approach [75], extending the classical methodology for sensible heat regenerators proposed by Coppage and London [13], to heat and mass transfer regenerators with local diffusion in the rotary matrix.

Over the last half decade, different investigations related to modeling and simulation of heat and mass transfer regenerators have been published. Ruivo et al. [55–61] presented a series of studies regarding to the mathematical modeling simulation of heat and mass exchangers. A one dimensional model was employed in [56] for evaluating the impact of different simplifications mostly related to the diffusion effects in the adsorbent material. A comparison between one- and two-dimensional models, assuming parallel plates channels, was carried out in [57] and the results indicated that a one-dimensional model for the flow in channels (bulk-flow formulation) could be used with small error for channels lengths smaller than

100 mm. A one-dimensional model with axial diffusion in the matrix was also used in [55, 59, 60], and a two-dimensional model for the desiccant matrix, assuming parallel plates-channels, and considering a one-dimensional bulk-flow model for the airstream, was employed in [61]. Chung and Lee [10], Chung et al. [11], and Stabat and Marchio [76] considered a simple one-dimensional model for the airstream and matrix, but included no effects of axial diffusion, and Shang and Besant [65, 66] employed a totally-lumped model. Nóbrega and Brum [46, 47, 49] also employed simple one-dimensional models with no local diffusion phenomena, and considered further simplifications such as negligible heat and mass storage in the airstream. Ge et al. [17] and Heidarinejad and Pasharshahi [25, 26] utilized a one-dimensional model with axial diffusion effects in the matrix. Narayanan et al. [44] also utilized one-dimensional models, but presented a comparison between models with and without axial diffusion effects. Ruan et al. [54] also used a one-dimensional model with axial diffusion effects to analyze an enthalpy wheel with purge air.

As seen from the presented literature review, different mathematical models have been used over the last couple of decades for simulating the operation of heat and mass transfer regenerators. When looking into the differences between these models, one can notice that the main distinctions occur in the heat and mass transport equations for the sorbent material. In this context, the purpose of this chapter is to present different types of mathematical models for heat and mass transfer regenerators, with emphasis on the transport processes within the porous sorbent material. The derivation of these formulations will be discussed, and models with different levels of details in the spatial description of the temperature and humidity concentration in the sorbent material will be presented, from complex multidimensional forms to simple one-dimensional ones.

2 Problem Description and Common Assumptions

The general problem considered in this study is that of a rotary exchanger, which periodically alternates between different process streams, as shown in Fig. 1. The rotary matrix is composed of numerous mini-channels through which the streams flow, transferring mass and energy to the channels' walls, which are composed of porous sorbent materials. The overall process is adiabatic such that during an entire cycle the net energy (as well as mass) transfer rate to the matrix is zero; this means that, if two process streams are employed, for an entire cycle the energy (and mass) removed from one stream is entirely delivered to the other one, and vice versa.

The rotary matrix can be subdivided in K sections, delimited by angles, as shown in Fig. 1. Naturally the sum of all angles add up to 2π :

$$\sum_{k=1}^K \theta_k = 2\pi. \quad (1)$$

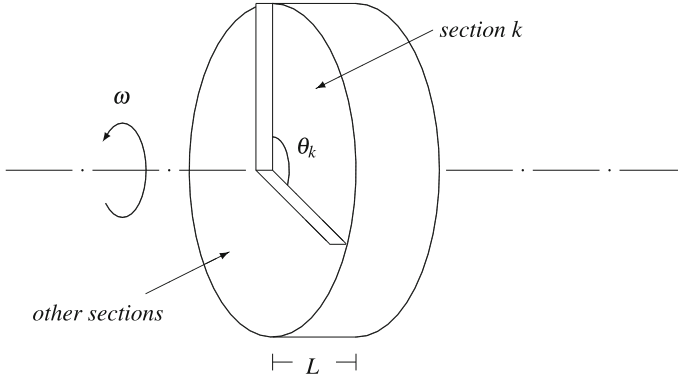


Fig. 1 Rotary exchanger

The wheel operates at a constant angular speed ω , such that if a fixed point is followed as it rotates, each section gives rise to a different operating periods. The duration of these K periods are easily calculated as:

$$\delta t_k = \frac{\theta_k}{\omega}, \quad (2)$$

and the summation of all these periods yield the total cycle time, t_f :

$$\sum_{k=1}^K \delta t_k = t_f. \quad (3)$$

The summation of the δ_k up to a given number of sections smaller than the total sections yield @@@@a partial cycle time:

$$\sum_{p=1}^k \delta t_p = t_k, \quad (4)$$

such that t_K corresponds to the total cycle time t_f .

Despite the rotation, the channels are analyzed as stationary, by choosing a proper reference coordinate system, fixed to a representative channel. The walls of each channel are composed of a porous *sorbent felt*, which may be laid upon an impermeable supporting wall, as displayed in Fig. 2. As shown in this figure, surface \mathcal{S}_p represents the interface between the process stream and the porous sorbent, which is called the *felt-stream interface*. Moreover, surface \mathcal{S}_w represents the interface between the porous sorbent felt and the impermeable structure, termed the *felt-wall interface*. The channels are assumed independent of each other such that the surfaces between adjacent channel-structures are considered adiabatic and impermeable. Due to the actual geometry of these channels, an exact, three-dimensional, representation of the system could be too complex, requiring a prohibitive computational effort for obtaining excessively detailed information.

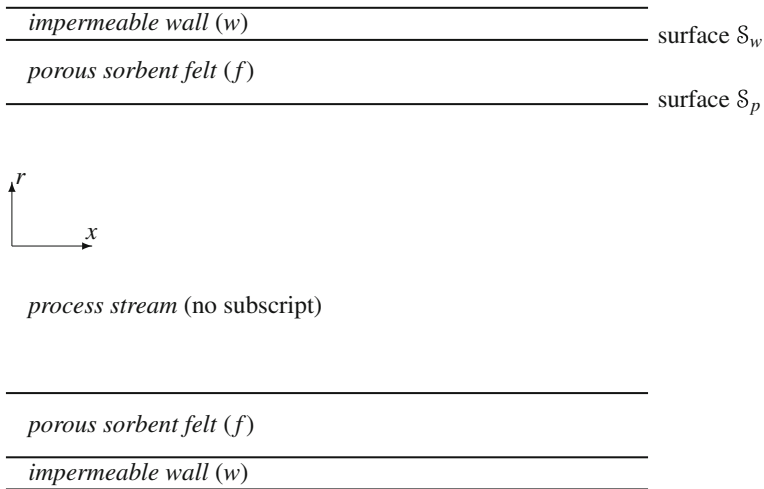


Fig. 2 Single channel-structure

Then again, a one-dimensional description may be overly simplified, and a balance between these two could be required. Different levels of formulations will be presented in this chapter, and the simplifications involved in each case will be discussed, allowing a proper formulation to be chosen according to the considered type of problem.

The porous adsorbent material is modeled as a homogeneous medium composed of a solid portion and pores, in which both gas and adsorbed phases coexist. In order to facilitate the analysis, a subscripting scheme indicating the considered phase is employed. Starting with the solid portion of the material, the subscript *s* refers to quantities in this solid phase. Conversely, within pores, *g* is employed for the gaseous phase. The subscript *l* is employed for the adsorbed phase; nevertheless, since the adsorption occurs on the surface of the solid phase, the subscript *s* is also employed to describe quantities related to the adsorbed phase, e.g. surface diffusion of the adsorbate. For quantities within the bulk porous material with no required phase distinction, a simple *f* subscript is used. In the process stream, a single-phase is present, and for the sake of simplicity, no subscript is employed for this phase.

2.1 Common Assumptions

Some common assumptions employed for modeling heat and mass transfer in rotary regenerators can be summarized as:

1. Radiation effects are neglected, as a result of relatively small temperatures.

2. No chemical reaction takes place, nor are there any energy sources within the system.
3. The effects of field forces, such as gravity, on the fluid mixture are negligible.
4. The channel flow is incompressible and viscous dissipation is negligible.
5. The channels are equal and uniformly distributed throughout the wheel.
6. The state properties of each inlet-stream are radially uniform at the inlet face of the wheel; also, the mass flow rate of dry air is constant at each inlet face.
7. Heat and mass transfer between adjacent flow-channels is negligible; heat and mass transfer from the exchanger to the surroundings (besides the channel inflow and outflow) are also negligible.
8. The pressure drop along the axial flow length due to skin friction is small compared to the total pressure, such that thermodynamic properties are unaffected.
9. All sorption phenomena are thermodynamically reversible.
10. Axial diffusion in the process stream is small compared to convective transfer, and is neglected.
11. The channel flow is laminar and fully developed; the convective heat and mass transfer between channels and the felt surface can be evaluated by employing bulk properties and film coefficients.²
12. The gaseous components of the fluid mixture are treated as ideal gases with constant thermo-physical properties.
13. The concentration of fluid other than sorbate in the mixture is assumed constant.
14. The specific heats and thermal conductivities of dry sorbent and adsorbate are assumed constant.
15. The gas mixtures are dilute solutions.
16. The porous felt is assumed to be homogeneous and isotropic, and the concentration of material other than adsorbate is unaffected by sorption.
17. The mass diffusion rate in micro-pores is rapid compared to that of the macro-pores.
18. Thermodynamic equilibrium exists at every point between the sorbate in the gas-phase and on the solid surface (adsorbed phase).
19. No phase change, other than that related to the sorption process, occurs in the exchanger.
20. There is no explicit transfer coupling through *Soret* or *Dufour* effects.

The majority of studies that present mathematical formulations for simulating the operation of active and passive desiccant wheels are based on a list of similar assumptions. Naturally, there are some variations in assumptions that consequently lead to different formulations. The formulations presented in this text are mainly based on the aforementioned assumptions; however, the implications of relaxing some of these assumptions, or even considering additional simplifications, will be

² Convective heat and mass transfer coefficients.

discussed and the modifications in formulations resulting from these considerations will be presented.

3 Concentrations, Enthalpies and Heat of Sorption

Before going into the details of the heat and mass transfer balances that lead to the mathematical model equations, some fundamental quantities are introduced, such as the concentration variables, enthalpies and quantities related to the sorption phenomenon.

3.1 Concentrations

Since it is common practice in enthalpy and active desiccant wheels to assume an invariable density of dry air, it becomes useful to employ dry-basis concentrations. This section introduces the concentration variables used to describe the water concentration in gaseous and adsorbed phases, in both volumetric basis (kg/m^3) and dry basis ($\text{kg water}/\text{kg dry air}$).

The water vapor concentrations in the gas phase, denoted ρ_v (in process stream) and $\rho_{v,f}$ (in void spaces within the sorbent material), are related to the dry-basis concentrations Y and Y_f as:

$$\rho_v = \rho_a Y, \quad \rho_{v,f} = \rho_a Y_f, \quad (5)$$

where ρ_a is the dry air density, which is assumed constant. In this form, the dry basis vapor concentration is equivalent to the traditional *humidity ratio* or *absolute humidity* used in psychrometrics.

In addition, the adsorbed phase concentration, denoted ρ_l is related to its dry-basis counterpart, W , as:

$$\rho_l = \rho_s f_s W, \quad (6)$$

where f_s is the *mass fraction of adsorbent material in the felt*.

While the water vapor concentration $\rho_{v,f}$ is defined per unit volume of pores (excluding dead pores), the adsorbed water concentration ρ_l is given in terms of the actual structural volume of the solid sorbent (including dead pores). As a result, the total mass of water contained in the adsorbent material can be calculated by

$$\int_{\mathcal{V}_f} \varepsilon \rho_{v,f} + (1 - \varepsilon) \rho_l d\mathcal{V}, \quad (7)$$

where \mathcal{V}_f corresponds to the volume of the porous felt and ε to its porosity.

For problems involving active and passive desiccant wheels, the adsorbed phase concentration is generally assumed to be in local equilibrium with the gas phase in the pore space adjacent to it. As a result W is expressed as a function of the temperature and gas-phase concentration of the pore space:

$$\Phi(W, Y_f, T_f) = 0, \quad (8)$$

where Φ is a general function. Many times this relation can be written in an simpler explicit form:

$$W = \Phi(Y_f, T_f). \quad (9)$$

The specific function relation for W is a constitutive equation called an *equilibrium relation* or an *adsorption isotherm*.

3.2 Enthalpies and Heat of Sorption

Since ideal gases are considered, the enthalpies of the gaseous phases depend only on temperature. The dry air and vapor enthalpies are written as:

$$i_a = i_a(T), \quad i_{a,f} = i_{a,f}(T_f), \quad i_v = i_v(T), \quad i_{v,f} = i_{v,f}(T_f), \quad (10)$$

where the subscripts have been included to distinguish between the air and vapor in the felt from those quantities in the process streams (where no subscript is used). The enthalpy of saturated liquid and the solid matrix also depend on temperature only, and are given by:

$$i_{ls} = i_{ls}(T_f), \quad i_s = i_s(T_f), \quad (11)$$

in which no special phase subscript is needed since these only occur within the porous felt. The enthalpy associated with the adsorbed phase is somewhat similar to that of a liquid phase; however, the additional surface attraction associated with the physical adsorption phenomenon imply in enthalpy values that are generally smaller than that of saturated liquid at the same temperature. This enthalpy is defined as:

$$i_l = i_l(T_f, W) = i_{ls}(T_f) + i_{\text{wet}}(T_f, W), \quad (12)$$

where i_{wet} is the *differential heat of wetting*, which is generally a negative value as normally $i_l \leq i_{ls}$. The relations above also reflect the fact that i_{wet} , and consequently i_l , depend on the adsorbed content. The heat of wetting will generally have a larger magnitude for smaller values of W , due to the stronger adsorption forces associated with the first layers of adsorbate on the adsorbent surface.

The heat of wetting also occurs in an integral form, called the *integral heat of wetting* and defined as:

$$\Delta i_{\text{wet}} = \Delta i_{\text{wet}}(T_f, W) = \int_0^W i_{\text{wet}}(T_f, W') dW', \quad (13)$$

where the parenthesis denote the dependence of i_{wet} on the adsorbed content.³ Since the quantity i_{wet} decreases with increasing W , using constant i_{wet} values could lead to overestimated values of Δi_{wet} . Based on the definition of Δi_{wet} , an averaged differential heat of wetting is also defined:

$$\bar{i}_{\text{wet}}(T_f, W) = \frac{\Delta i_{\text{wet}}(T_f, W)}{W} = \frac{1}{W} \int_0^W i_{\text{wet}}(T_f, W') dW', \quad (14)$$

such that the integral heat of wetting for a given adsorbed content W can be simply obtained by multiplying this quantity by \bar{i}_{wet} .

The *heat of vaporization* is defined as the difference between the saturated vapor and saturated liquid enthalpies:

$$i_{\text{vap}} = i_{\text{vap}}(T_f) = i_{v,f}(T_f) - i_{ls}(T_f), \quad (15)$$

in which $i_{v,f}$ equals the saturated vapor enthalpy due to the ideal gas assumption. Similar to the definition of the heat of vaporization, the *differential heat of sorption*⁴ is defined as the difference between the enthalpy of saturated vapor and that of the adsorbed phase:

$$i_{\text{sor}} = i_{\text{sor}}(T_f, W) = i_{v,f}(T_f) - i_l(T_f, W), \quad (16)$$

emphasizing the dependence of i_{sor} on the adsorbed content W . It is useful to know that the difference between the heat of sorption and heat of vaporization leads to the heat of wetting:

$$i_{\text{wet}} = i_{\text{vap}} - i_{\text{sor}}, \quad (17)$$

which implies that i_{sor} is larger than i_{vap} as $i_{\text{wet}} < 0$.

As similarly done for the heat of wetting, an averaged specific enthalpy of the adsorbed phase is also defined:

$$\bar{i}_l = i_{ls} + \bar{i}_{\text{wet}}, \quad (18)$$

such that the enthalpy per mass of dry sorbent of adsorbed water can be simply written as $W\bar{i}_l$.

³ However, the heat of wetting may also depend on temperature.

⁴ For simplicity, the differential heat of sorption is commonly referred to as just *heat of sorption*.

4 Conservation Balances

This section presents heat and mass conservation balances for the process stream and the sorbent material. Although a simple bulk-flow model is presented for the process stream, as employed by the majority of previous investigators, different type of balances will be presented for the transport processes in the sorbent material.

4.1 Conservation Balances for Process Stream

Although a few works may employ more complex formulations for describing the heat and mass transfer within the process streams, most studies employ simple bulk transport equations for describing the heat and mass transfer in the flow. Since the purpose of this text is to present different formulations for the transport within the adsorbent material, simple one-dimensional convection equations, as found in a number of active and passive desiccant wheels studies, are used. Nevertheless, a few nuances that are seen in different literature studies will be commented.

The convective mass transfer in the process stream is described by the mean stream concentration ρ_v , which is obtained from a simple mass balance:

$$\mathcal{A}_p \left(\frac{\partial \rho_v}{\partial t} + u \frac{\partial \rho_v}{\partial x} \right) = \mathcal{P}_s j_i'' , \quad (19)$$

in which \mathcal{P}_s is the wetted perimeter (i.e. based on the heat and mass transfer area at the felt-stream interface), \mathcal{A}_p is the flow area and j_i'' is the mass transfer flux at this interface. Naturally, the adopted convention is that j_i'' be positive when water is transferred from the sorbent felt to the process stream. Using the dry-basis concentration the previous equation may be simplified to:

$$\rho_a \left(\frac{\partial Y}{\partial t} + u \frac{\partial Y}{\partial x} \right) = \frac{\mathcal{P}_s}{\mathcal{A}_p} j_i'' . \quad (20)$$

The convective heat transport equation is also given in terms of a mean stream energy balance:

$$\mathcal{A}_p \frac{\partial}{\partial t} (\rho_a i_a + \rho_v i_v) = - \frac{\partial}{\partial x} (\mathcal{A}_p u (\rho_a i_a + \rho_v i_v)) + \mathcal{P}_s \dot{q}_i'' + \mathcal{P}_s j_i'' i_{v,i} , \quad (21)$$

where i_a and i_v are the mean stream enthalpies of dry air and water vapor, u is the bulk velocity of the flow, and \dot{q}_i'' is the heat flux from the sorbent felt to the process stream. Rearranging Eq. (21) and simplifying yields:

$$\rho c_p \left(\frac{\partial T}{\partial t} + u \frac{\partial T}{\partial x} \right) = \frac{\mathcal{P}_s}{\mathcal{A}_p} \dot{q}_i'' + \frac{\mathcal{P}_s}{\mathcal{A}_p} j_i'' (i_{v,i} - i_v), \quad (22)$$

in which ρc_p is the volumetric heat capacity of moist air, given by:

$$\rho c_p = \rho_a c_{p,a} + \rho_v c_{p,v} = \rho_a (c_{p,a} + c_{p,v} Y). \quad (23)$$

The vapor enthalpy $i_{v,i}$ represents the specific enthalpy associated with the mass transfer from the sorbent felt. Many studies omit the term involving the enthalpy difference ($i_{v,i} - i_v$) in their formulations, which corresponds to assuming either that $i_{v,i} \approx i_v$ or that the total contribution of the entire energy transfer term due to mass transfer from the felt is negligible.

Despite the fact that the process stream balances are written in terms of bulk, or mean stream properties, and the average velocity u is constant, it can assume different values for each stream. As a matter of fact, for counterflow arrangements the velocities will have different signs. In order to work with positive velocity values, the flow transport equations are written as:

$$\rho_a \left(\frac{\partial Y}{\partial t} + (-1)^\gamma u \frac{\partial Y}{\partial x} \right) = \frac{\mathcal{P}_s}{\mathcal{A}_p} j_i'', \quad (24)$$

$$\rho c_p \left(\frac{\partial T}{\partial t} + (-1)^\gamma u \frac{\partial T}{\partial x} \right) = \frac{\mathcal{P}_s}{\mathcal{A}_p} \dot{q}_i'' + \frac{\mathcal{P}_s}{\mathcal{A}_p} j_i'' (i_{v,i} - i_v), \quad (25)$$

where $\gamma = 0$ for parallel flow arrangements and $\gamma = 1$ for counterflow arrangements during reversed flow periods.

Another common simplification among formulations for heat and mass transfer in both active and passive desiccant wheels involves assuming that the energy and water vapor storage terms in the fluid flow is negligible compared to the advective term, which leads to the following simplified forms:

$$(-1)^\gamma \rho_a u \frac{\partial Y}{\partial x} = \frac{\mathcal{P}_s}{\mathcal{A}_p} j_i'', \quad (26)$$

$$(-1)^\gamma \rho c_p u \frac{\partial T}{\partial x} = \frac{\mathcal{P}_s}{\mathcal{A}_p} \dot{q}_i'' + \frac{\mathcal{P}_s}{\mathcal{A}_p} j_i'' (i_{v,i} - i_v), \quad (27)$$

4.2 Balance for Impermeable Supporting Structure

As already mentioned, in many cases, the sorbent felt is laid upon an impermeable supporting structure, which will consequently have an influence on the heat and mass transfer in the sorbent material. The impermeability condition only requires that an energy balance be used. This balance can be written in simple one-dimensional form:

$$\mathcal{A}_w \rho_w c_w \frac{\partial T_w}{\partial t} = -\mathcal{A}_w \frac{\partial \dot{q}''_{w,x}}{\partial x} - \mathcal{P}_w \dot{q}''_w, \quad (28)$$

where \mathcal{A}_w is the conduction heat transfer area of the wall (perpendicular to the flow direction), \mathcal{P}_w is the contact perimeter at the felt-wall interface, \dot{q}''_w is the heat flux from the wall to the sorbent material, $\dot{q}''_{w,x}$ is the conduction heat flux in the wall, and $\rho_w c_w$ is the wall thermal capacity. The heat fluxes $\dot{q}''_{w,x}$ and \dot{q}''_w will be introduced in a latter section.

4.3 One-Dimensional Conservation Balances for Sorbent

The simplest formulation for describing active desiccant and enthalpy wheels is a one-dimensional one, which takes into account variations in the flow direction only. These one-dimensional balances are herein presented, and variations between formulations will be discussed according to the application of different simplifying assumptions.

4.3.1 Mass Transport

The mass transport equation is given by the following mass balance for water in the felt:

$$\mathcal{A}_f \left(\varepsilon \frac{\partial \rho_{v,f}}{\partial t} + (1 - \varepsilon) \frac{\partial \rho_l}{\partial t} \right) = -\mathcal{P}_s j''_i - \mathcal{A}_f \frac{\partial j''_{g,x}}{\partial x} - \mathcal{A}_f \frac{\partial j''_{s,x}}{\partial x}, \quad (29)$$

in which \mathcal{A}_f is the frontal area (area perpendicular to the flow direction) of the adsorbent material. The fluxes $j''_{g,x}$ and $j''_{s,x}$ are due to axial mass diffusion in the sorbent material, in the gas-phase (vapor) and adsorbed phase (on the pore surface), respectively. Using the dry-basis concentrations, Eq. (29) can be rewritten as:

$$\varepsilon \rho_a \frac{\partial Y_f}{\partial t} + (1 - \varepsilon) \rho_s f_s \frac{\partial W}{\partial t} = -\frac{\mathcal{P}_s}{\mathcal{A}_f} j''_i - \frac{\partial j''_{g,x}}{\partial x} - \frac{\partial j''_{s,x}}{\partial x}. \quad (30)$$

Based on the previous equations, the *volumetric rate of sorption*, for the one-dimensional balance, is defined as:

$$\dot{g}'''_{\text{sor}} = (1 - \varepsilon) \frac{\partial \rho_l}{\partial t} + \frac{\partial j''_{s,x}}{\partial x} = (1 - \varepsilon) \rho_s f_s \frac{\partial W}{\partial t} + \frac{\partial j''_{s,x}}{\partial x}, \quad (31)$$

representing the actual rate of water adsorption, which comprises for the rate of increase in adsorbed water and less the rate of inflow of adsorbed water through diffusion.

While some investigations consider the axial mass diffusion through the sorbent layer, a common simplification among a number of studies is that the mass diffusion in the axial direction is small compared to the mass transfer in the airstream, such that Eq. (30) could be simply written as:

$$\varepsilon \rho_a \frac{\partial Y_f}{\partial t} + (1 - \varepsilon) \rho_s f_s \frac{\partial W}{\partial t} = - \frac{\mathcal{P}_s}{\mathcal{A}_f} j_i'' \quad (32)$$

and the rate of sorption is simplified to:

$$\dot{g}_{\text{sor}}''' = (1 - \varepsilon) \rho_s f_s \frac{\partial W}{\partial t} \quad (33)$$

More insight on the rate of sorption can be obtained if the mass conservation Eq. (30) is employed to rewrite the rate of sorption as:

$$\dot{g}_{\text{sor}}''' = - \frac{\mathcal{P}_s}{\mathcal{A}_f} j_i'' - \frac{\partial j_{g,x}''}{\partial x} - \varepsilon \rho_a \frac{\partial Y_f}{\partial t} \quad (34)$$

In this form, if one considers that the convective mass transfer to the process stream is much larger in magnitude than the storage in gas-phase and the gas-phase diffusion transfer, the rate of sorption could be alternatively simplified to:

$$\dot{g}_{\text{sor}}''' = - \frac{\mathcal{P}_s}{\mathcal{A}_f} j_i'' \quad (35)$$

This simplification is considered by different investigators and generally also implies that vapor storage effect in the gas-phase is small compared to that of the adsorbed phase. For these cases, one could simplify Eq. (32) to:

$$(1 - \varepsilon) \rho_s f_s \frac{\partial W}{\partial t} = - \frac{\mathcal{P}_s}{\mathcal{A}_f} j_i'' \quad (36)$$

Nevertheless, while this could be a good approximation for some active desiccant wheels, when enthalpy wheels are considered, the fraction of adsorbent material in the felt (f_s) may assume small values, and this approximation could lead to incorrect results.

4.3.2 Energy Transport

With the assumptions of small pressure variation, the energy transport equation can be obtained from an enthalpy balance within the sorbent felt:

$$\begin{aligned}
& \mathcal{A}_f \frac{\partial}{\partial t} \left(\varepsilon (\rho_a i_a + \rho_{v,f} i_{v,f}) + (1 - \varepsilon) \left(\rho_s i_s + \int_0^{\rho_l} i_l d\rho_l \right) \right) \\
&= -\mathcal{A}_f \frac{\partial \dot{q}_{f,x}''}{\partial x} - \mathcal{P}_s \dot{q}_i'' - \mathcal{P}_s j_i'' i_{v,i} + \mathcal{P}_w \dot{q}_w'' - \mathcal{A}_f \frac{\partial (i_{v,f} j_{g,x}'')}{\partial x} - \mathcal{A}_f \frac{\partial (\bar{i}_l j_{s,x}'')}{\partial x},
\end{aligned} \tag{37}$$

which can also be written in terms of the dry-basis concentrations:

$$\begin{aligned}
& \mathcal{A}_f \frac{\partial}{\partial t} \left(\varepsilon \rho_a (i_a + Y_f i_{v,f}) + (1 - \varepsilon) \rho_s \left(i_s + \int_0^w i_l dW' \right) \right) \\
&= -\mathcal{A}_f \frac{\partial \dot{q}_{f,x}''}{\partial x} - \mathcal{P}_s \dot{q}_i'' - \mathcal{P}_s j_i'' i_{v,i} + \mathcal{P}_w \dot{q}_w'' - \mathcal{A}_f \frac{\partial (i_{v,f} j_{g,x}'')}{\partial x} - \mathcal{A}_f \frac{\partial (\bar{i}_l j_{s,x}'')}{\partial x},
\end{aligned} \tag{38}$$

where $\dot{q}_{f,x}''$ is the conduction heat flux in the sorbent material. The integrated enthalpy of adsorbed water needs to be used due to the dependence of the enthalpy of the adsorbed phase (i_l) on the adsorbed concentration, which occurs due to the nature of the heat of wetting.

Another point worth noting is that the energy transfer associated with the diffusion in the adsorbed phase is written in terms of the averaged enthalpy \bar{i}_l . Hence, the enthalpy of the diffused amount is the averaged value of all adsorbed layers, which implies an assumption that the diffusion is equally distributed among different adsorbed layers. Indeed, the ‘‘exact’’ value of the specific enthalpy of the diffused adsorbed water would involve an integral over the different diffusion rates associated with different adsorbed layers. On the other hand, using i_l instead of \bar{i}_l involves an assumption that the amount of diffused water, regardless of its quantity, will have an enthalpy value of the last adsorbed layer. Although \bar{i}_l is herein adopted as the enthalpy of the diffused layer, one could easily modify the formulation if a better approximation or the actual enthalpy of the diffused adsorbed water is available.

The rearrangement of Eq. (38) leads, after simplification, to:

$$\begin{aligned}
\rho_f c_f \frac{\partial T_f}{\partial t} + j_{g,x}'' \frac{\partial i_{v,f}}{\partial x} + j_{s,x}'' \frac{\partial \bar{i}_l}{\partial x} &= -\frac{\partial \dot{q}_{f,x}''}{\partial x} - \frac{\mathcal{P}_s}{\mathcal{A}_f} \dot{q}_i'' \\
&\quad - \frac{\mathcal{P}_s}{\mathcal{A}_f} j_i'' (i_{v,i} - i_{v,f}) + \dot{s}_{\text{sor}}''' + \frac{\mathcal{P}_w}{\mathcal{A}_f} \dot{q}_w'',
\end{aligned} \tag{39}$$

where \dot{s}_{sor}''' is the *volumetric rate of sorption heating*, which, for the one-dimensional balance, is defined as:

$$\dot{s}_{\text{sor}}''' = (1 - \varepsilon) \rho_s f_s \frac{\partial W}{\partial t} (i_{v,f} - i_l) + \frac{\partial j_{s,x}''}{\partial x} (i_{v,f} - \bar{i}_l), \tag{40}$$

and the *volumetric thermal capacity of the felt* includes contributions from the moist air in pores, the solid adsorbent and the adsorbed water:

$$\rho_f c_f = \varepsilon \rho_a (c_{p,a} + c_{p,v} Y_f) + (1 - \varepsilon) \rho_s (c_s + f_s W c_l), \quad (41)$$

in which the specific heat of the adsorbed phase is defined by

$$W c_l = \frac{\partial}{\partial T_f} \left(\int_0^W i_l dW \right)_W \quad \text{or} \quad c_l = \left(\frac{\partial \bar{i}_l}{\partial T_f} \right)_W, \quad (42)$$

where the subscript W indicates differentiation holding W constant. Equation (41) shows that the energy storage term in Eq. (39) represents the combined energy storage in all three phases present at a point in the sorbent material.

Observing the left-hand-side of Eq. (39), one notices that besides the energy storage term, there are two advective energy transport terms due to the water motion in gas and adsorbed phases. Since these mass transfer rates are due to diffusion, these terms are assumed negligible and removed from the transport equation. Finally, with the introduction of the heat of sorption from Eq. (16), one obtains:

$$\rho_f c_f \frac{\partial T_f}{\partial t} = - \frac{\partial \dot{q}_{f,x}''}{\partial x} - \frac{\mathcal{P}_s}{\mathcal{A}_f} \dot{q}_i'' - \frac{\mathcal{P}_s}{\mathcal{A}_f} J_i'' (i_{v,i} - i_{v,f}) + \dot{s}_{\text{sor}}''' + \frac{\mathcal{P}_w}{\mathcal{A}_f} \dot{q}_w'', \quad (43)$$

Introducing the definition of the heat of sorption (16) in Eq. (40) leads to:

$$\dot{s}_{\text{sor}}''' = (1 - \varepsilon) \rho_s f_s \frac{\partial W}{\partial t} i_{\text{sor}} + \frac{\partial J_{s,x}''}{\partial x} (i_{v,f} - \bar{i}_l). \quad (44)$$

The sorption heating can be also written in terms of the rate of sorption:

$$\dot{s}_{\text{sor}}''' = \dot{g}_{\text{sor}}''' i_{\text{sor}} + \frac{\partial J_{s,x}''}{\partial x} (i_l - \bar{i}_l), \quad (45)$$

in which the last term represents an additional contribution due to diffusion in the adsorbed layers. An example of the manifestation of this term is a situation in which no adsorption occurs, but due to a difference in surface concentration, there is movement in the adsorbed phase, thereby resulting in a redistribution of adsorbate within different adsorbed layers. The enthalpy difference associated with different layers will produce a heating or cooling effect, which is represented by the last term in equation. Naturally, if there is no surface diffusion, \dot{s}_{sor}''' is simply given by:

$$\dot{s}_{\text{sor}}''' = \dot{g}_{\text{sor}}''' i_{\text{sor}} = (1 - \varepsilon) \rho_s f_s \frac{\partial W}{\partial t} i_{\text{sor}}. \quad (46)$$

Finally, since three dependent variables appear in the heat and mass balance, an extra equation is needed. This equation is the sorption isotherm, or equilibrium relation, as generally defined by Eq. (8) or (9), such that W is calculated directly

from the properties (T_f and Y_f) of the gas-phase in the void spaces of the sorbent felt.

4.4 Multidimensional Conservation Balances for Sorbent

The derivation of the mass and energy transport equations for a multidimensional formulation in the sorbent can also be easily obtained, as demonstrated in this section. As presented for the one-dimensional formulation, variation in equations arising from different simplifications are also discussed. A specific modification that will be shown is due to the inclusion of additional transport rates due to Soret and Dufor effects. This modification was not included in the one-dimensional sorbent equations to avoid repetition. Nevertheless, one can easily modify the one-dimensional transport equation for the sorbent material as similarly shown for the multi-dimensional formulation to include these effects.

4.4.1 Mass Transport

Considering a control volume \mathcal{V} with a bounding surface \mathcal{S} , within the sorbent material, an integral mass balance yields:

$$\frac{d}{dt} \int_{\mathcal{V}} (\varepsilon \rho_{v,f} + (1 - \varepsilon) \rho_l) d\mathcal{V} = - \int_{\mathcal{S}} (\mathbf{j}_g'' + \mathbf{j}_s'') \cdot \mathbf{n} d\mathcal{S}, \quad (47)$$

where \mathbf{j}_g'' and \mathbf{j}_s'' represent the mass flux vectors corresponding to diffusion of vapor in the gas-phase and adsorbed water on the surface of the pores, respectively. Then, applying Gauss' Divergence Theorem finally leads to:

$$\varepsilon \frac{\partial \rho_{v,f}}{\partial t} + (1 - \varepsilon) \frac{\partial \rho_l}{\partial t} = -\nabla \cdot \mathbf{j}_g'' - \nabla \cdot \mathbf{j}_s'', \quad (48)$$

which correspond to a statement that the water storage in gaseous and adsorbed form result from the net mass inflow due to gas-phase and surface diffusion, which are assumed to occur in parallel. Using the dry-basis concentration variables, Eq. (48) can be simplified to:

$$\varepsilon \rho_a \frac{\partial Y_f}{\partial t} + (1 - \varepsilon) \rho_s f_s \frac{\partial W}{\partial t} = -\nabla \cdot \mathbf{j}_g'' - \nabla \cdot \mathbf{j}_s''. \quad (49)$$

This is probably the most common form of the mass conservation equation used in multidimensional formulations for solid sorbents in active and passive desiccant wheels.

The equation can naturally be modified if some effects are considered unimportant. A common modification seen among literature studies involves assuming

that the adsorbed phase storage is much higher than that of the gas-phase storage, such that Eq. (49) is modified to the following form:

$$(1 - \varepsilon) \rho_s f_s \frac{\partial W}{\partial t} = -\nabla \cdot \mathbf{j}_g'' - \nabla \cdot \mathbf{j}_s''. \quad (50)$$

While the last modification simplifies Eq. (49), additional modifications can be made to include other phenomena. For instance, if the hypothesis of no *thermo-diffusion* is relaxed, this equation should be modified to include an additional transport term:

$$\varepsilon \rho_a \frac{\partial Y_f}{\partial t} + (1 - \varepsilon) \rho_s f_s \frac{\partial W}{\partial t} = -\nabla \cdot \mathbf{j}_g'' - \nabla \cdot \mathbf{j}_s'' - \nabla \cdot \mathbf{j}_T'', \quad (51)$$

where \mathbf{j}_T'' represents the mass flux vector due to thermo-diffusion, also known as *thermophoresis* or simply as Soret effect.

4.4.2 Energy Transport

As similarly carried out for the mass balance, an integral energy balance with a control volume \mathcal{V} yields:

$$\begin{aligned} \frac{d}{dt} \int_{\mathcal{V}} \left(\varepsilon (\rho_a i_a + \rho_{v,f} i_{v,f}) + (1 - \varepsilon) \left(\rho_s i_s + \int_0^{\rho_l} i_l d\rho_l \right) \right) d\mathcal{V} \\ = - \int_{\mathcal{S}} \dot{\mathbf{q}}_f'' \cdot \mathbf{n} d\mathcal{S} - \int_{\mathcal{S}} \left(i_{v,f} \mathbf{j}_g'' + \bar{i}_l \mathbf{j}_s'' \right) \cdot \mathbf{n} d\mathcal{S}, \end{aligned} \quad (52)$$

where $\dot{\mathbf{q}}_f''$ is the effective heat flux vector in the porous felt. Then, employing Gauss' Divergence Theorem and using the mass conservation Eq. (48) leads, after simplification, to:

$$\rho_f c_f \frac{\partial T_f}{\partial t} + \mathbf{j}_g'' \cdot \nabla i_{v,f} + \mathbf{j}_s'' \cdot \nabla \bar{i}_l = -\nabla \cdot \dot{\mathbf{q}}_f'' + \dot{s}_{\text{sor}}''', \quad (53)$$

where the last term on the right hand side of Eq. (53) represents the heating effects associated with the sorption phenomenon. The volumetric rate of sorption for the multidimensional formulation is given by:

$$\dot{s}_{\text{sor}}''' = (1 - \varepsilon) \frac{\partial \rho_l}{\partial t} + \nabla \cdot \mathbf{j}_s'', \quad (54)$$

and the rate of heating due to sorption is given by:

$$\dot{s}_{\text{sor}}''' = (1 - \varepsilon) \frac{\partial \rho_l}{\partial t} i_{\text{sor}} + (\nabla \cdot \mathbf{j}_s'') (i_{v,f} - \bar{i}_l) = \dot{g}_{\text{sor}}''' i_{\text{sor}} + (\nabla \cdot \mathbf{j}_s'') (i_l - \bar{i}_l), \quad (55)$$

as analogously defined for the one-dimensional formulation by Eqs. (31) and (44), respectively. Naturally, if the contribution of surface diffusion is negligible to the sorption heating term, one arrives at:

$$\dot{s}'_{\text{sor}} = \dot{g}'_{\text{sor}} i_{\text{sor}}. \quad (56)$$

As previously discussed, as the advective heat transport terms due to the diffusion mass fluxes can generally be assumed negligible compared to the other energy transport terms, Eq. (53) is simplified to give:

$$\rho_f c_f \frac{\partial T_f}{\partial t} = -\nabla \cdot \dot{\mathbf{q}}'_f + \dot{s}'_{\text{sor}}, \quad (57)$$

which is also a traditional form found in the literature for multidimensional heat transfer in sorbents of active and passive desiccant wheels. As done for the mass transport equation, modifications to Eq. (57) may be easily accomplished. If an additional heat transfer rate due to Dufour effects are considered, an additional transport term is incorporated:

$$\rho_f c_f \frac{\partial T_f}{\partial t} = -\nabla \cdot \dot{\mathbf{q}}'_f - \nabla \cdot \dot{\mathbf{q}}'_f + \dot{s}'_{\text{sor}}, \quad (58)$$

where $\dot{\mathbf{q}}'_f$ represents the heat flux due to the diffusion thermo-effect, or simply to the Dufour effect. Although boundary conditions are required for solving the presented heat and mass balance equations, an extra relation is needed due to the presence of three unknown dependent variables. As mentioned in the one-dimensional formulation, an equilibrium isotherm, such as Eqs. (8) and (9), is required for relating W with Y_f and T_f .

Equations (48) through (50) assume no mass transfer resistance between the water vapor in pores and the gaseous phase that is in equilibrium with the adsorbed phase, such that these two quantities are the same. Under some circumstances, however, it could be important to consider such resistances. One example would be in a desiccant material having larger and smaller pores. In this type of situation the vapor in the smaller pores (and near the surfaces of larger pores) could be in equilibrium with the the adsorbed phase, but the vapor in the larger pores would have a different concentration.

A relatively simple formulation for this case can be obtained if Eq. (49) is split into two parts:

$$\varepsilon \rho_a \frac{\partial Y_f}{\partial t} + \nabla \cdot \mathbf{j}''_g = j''_{\pi}, \quad (59)$$

$$(1 - \varepsilon) \rho_s f_s \frac{\partial W}{\partial t} + \nabla \cdot \mathbf{j}''_s = -j''_{\pi}. \quad (60)$$

Naturally, the addition of these two equations lead to Eq. (49). The mass flux j''_{π} will depend on the concentration at the pore Y_f , and another concentration Y_{π} , representing the vapor state that is in equilibrium with the adsorbed state:

$$j''_{\pi} = j''_{\pi}(Y_f, Y_{\pi}). \quad (61)$$

The other modification is that W be related to the temperatures and concentration in a different way:

$$W = W(T_f, Y_{\pi}), \quad (62)$$

so that W is in equilibrium with Y_{π} instead of Y_f . Note, however, that if $Y_{\pi} = Y_f$, the previous formulation is obtained. Finally, one must mention that this formulation still considers that there is thermal equilibrium between these two states, such that they possess the same temperature.

5 Constitutive Equations

5.1 Expressions for Heat and Mass Fluxes

The heat and mass diffusion fluxes within the sorbent felt, needed for the multi-dimensional formulation, are given in terms of Fourier's Law of heat conduction

$$\dot{\mathbf{q}}''_f = -k_{\text{eff}} \nabla T_f, \quad (63)$$

where, the heat diffusion in the solid desiccant also is given in terms of an apparent property: the effective thermal conductivity k_{eff} . However, different than the thermal capacity, there are a number of models available in the literature for expressing k_{eff} in terms of the different components found in the porous adsorbent material [38]. For the one-dimensional formulation, only the axial component of the flux is needed:

$$\dot{q}''_{f,x} = -k_{\text{eff}} \frac{f}{\partial x}. \quad (64)$$

Similar to the heat diffusion flux, the mass diffusion fluxes are given by Fick's Law expressions:

$$\mathbf{j}''_g = -\rho_a \mathcal{D}_{g,\text{eff}} \nabla Y_f, \quad (65)$$

$$\mathbf{j}''_s = -\rho_s f_s \mathcal{D}_{s,\text{eff}} \nabla W, \quad (66)$$

where the effective Fick diffusion coefficients account for tortuosities in the sorbent material, being given by:

$$\mathcal{D}_{g,\text{eff}} = \frac{\varepsilon \mathcal{D}_g}{\tau_G}, \quad \mathcal{D}_{s,\text{eff}} = \frac{(1 - \varepsilon) \mathcal{D}_s}{\tau_S}. \quad (67)$$

Many works model the gas-phase mass diffusion as a combination of molecular diffusion and Knudsen diffusion. These are assumed to be parallel processes [80],

such that the gas-phase diffusion coefficient is calculated from a combination of a molecular diffusion coefficient \mathcal{D}_M and a Knudsen diffusion coefficient \mathcal{D}_K :

$$\frac{1}{\mathcal{D}_g} = \frac{1}{\mathcal{D}_M} + \frac{1}{\mathcal{D}_K}. \quad (68)$$

The molecular diffusion coefficient can be obtained from expressions for binary air–water gas mixtures.

As analogously mentioned for the conduction flux, for the one-dimensional sorbent formulation only the axial components of the mass fluxes in the felt are needed. These are simply given by:

$$j_g'' = -\rho_a \mathcal{D}_{g,\text{eff}} \frac{\partial Y_f}{\partial x}, \quad (69)$$

$$j_s'' = -\rho_s f_s \mathcal{D}_{s,\text{eff}} \frac{\partial W}{\partial x}. \quad (70)$$

If Soret and Dufour effects are taken into account, additional expressions for these fluxes are needed. In a general way, the diffusion flux due to the Soret effect may be written as [4, 34]:

$$\mathbf{j}_T'' = -\mathcal{D}_{g,\text{eff}}^T \nabla(\log T) = \frac{\mathcal{D}_{g,\text{eff}}^T}{k_{\text{eff}} T} \dot{\mathbf{q}}_f'', \quad (71)$$

where \mathcal{D}_g^T is *thermal diffusion coefficient*. In a similar fashion, the heat flux due to a concentration difference, comprising the Dufour effect, may be expressed as [34]:

$$\dot{\mathbf{q}}_m'' = \lambda_m \mathbf{j}_g'', \quad (72)$$

in which λ_m is a coefficient that relates the heat flux due to concentration difference to the mass flux \mathbf{j}_g'' . Although Soret and Dufour effects were discussed and expressions for the associated heat and mass fluxes were presented, apparently no models found in the literature related to active and passive desiccant wheels include these effects. Since the inclusion of these terms involve simple modifications to the transport equations, and since no literature studies include these effects in simulations of heat and mass transfer regenerators, they will be assumed negligible from this point on for the sake of simplicity.

The convective heat flux from the sorbent felt to the process stream is given by Newton's Cooling Law:

$$\dot{q}_i'' = h (T_i - T), \quad (73)$$

where h is the convective heat transfer coefficient, and T_i is the temperature at the felt-stream interface. The value of T_i will depend on the type of formulation employed; for the one-dimensional sorbent formulation it is the actual sorbent temperature $T_s(x, t)$, whereas for the multidimensional sorbent model it is the sorbent temperature $T_s(\mathbf{x}, t)$ evaluated at the felt-stream interface.

Traditionally, the convective mass flux from the sorbent felt to the process stream is written in terms of a concentration difference, similarly to Newton’s Cooling Law:

$$j_i'' = h_m \rho_a (Y_i - Y), \tag{74}$$

where h_m is a convective mass transfer coefficient and Y_i is the vapor concentration in the felt, at the interface. As similar to T_i , this concentration can assume different values depending on the type of formulation employed for the adsorbent material; it will be simply given by $Y_i = Y_f(x, t)$ for the one-dimensional sorbent formulation and by $Y_i = Y_f(\mathbf{x}, t)$ with \mathbf{x} evaluated at the felt-stream interface for the multi-dimensional model.

The mass flux j_π'' used in the multidimensional formulation with an additional mass transfer resistance within the felt can also be written as a Newton’s Law-type expression:

$$j_\pi'' = h_\pi \rho_a (Y_\pi - Y_f), \tag{75}$$

where, h_π is the mass transfer coefficient across the additional resistance. Naturally, higher h_π values will lead to a lower mass transfer resistance, and in the limit with $h_\pi \rightarrow \infty$ this resistance becomes negligible.

The conduction heat flux in the supporting wall is simply given by Fourier’s Law:

$$\dot{q}_{w,x}'' = -k_w \frac{\partial T_w}{\partial x}. \tag{76}$$

Moreover, the heat flux from the impermeable wall to the sorbent felt (at the felt-wall interface), can be given in terms of a contact heat transfer coefficient:

$$\dot{q}_w'' = h_w (T_w - T_{fw}), \tag{77}$$

in which T_{fw} is the temperature of the sorbent material at the felt-wall interface. For the one-dimensional sorbent formulation T_{fw} is the actual temperature of the sorbent felt T_f ; however, for a multi-dimensional sorbent formulation T_{fw} is the temperature of the felt evaluated at this position.

5.2 Adsorption Isotherm and Heat of Sorption

A number of relations for expressing the equilibrium between water in adsorbed form and vapor in the air–water mixture in contact with it can be found in the literature. A commonly used simple isotherm is the explicit separation-factor based relation:

$$W = \frac{\phi_f W_{\max}}{r + (1 - r)\phi_f}, \quad (78)$$

where r is the separation factor and ϕ_f is the relative humidity of air in the pore space, i.e. $\phi_f = \phi_f(T_f, Y_f)$. As one can observe, this isotherm combines the temperature and absolute humidity dependence of W into a single parameter: the relative humidity. Equation (78) is further simplified if $r = 1$:

$$W = W_{\max} \phi_f, \quad (79)$$

which is known as the linear isotherm.

Equations (78) and (79) naturally apply to the case without the extra mass transfer resistance between the gas-phase and the layer in equilibrium with the adsorbed phase. For cases with the additional resistance, ϕ_f should be substituted by $\phi_\pi = \phi_\pi(T_f, \phi_\pi)$.

Another traditional isotherm relation is the Langmuir model:

$$W = W_{\max} \frac{bp_{v,f}}{1 + bp_{v,f}}, \quad (80)$$

where $p_{v,f}$ is the vapor partial pressure of the gas-phase in pores and b is a coefficient, which generally depends on temperature. The quantity W_{\max} represents the maximum water uptake by the desiccant, which can also depend on temperature.

The heat of sorption is commonly expressed in terms of the heat of vaporization:

$$i_{\text{sor}} = (1 + e_{\text{sor}})i_{\text{vap}}, \quad (81)$$

where e_{sor} is the fraction by which the heat of sorption exceeds the heat of vaporization. This implies that e_{sor} is related to the differential heat of wetting as:

$$e_{\text{sor}} = -\frac{i_{\text{wet}}}{i_{\text{vap}}}. \quad (82)$$

Jurinak and Mitchell [30] argument that a reasonable expression for water vapor being adsorbed on silica gel, based on the experimental data, is given by:

$$e_{\text{sor}} = \Delta e \frac{\exp(W^* \kappa) - \exp(\kappa)}{1 - \exp(\kappa)}, \quad (83)$$

in which $W^* = W/W_{\max}$. The parameters Δe and κ are constants, with $\kappa < 0$. It is interesting to note that, if $W = W_{\max}$, $e_{\text{sor}} = 0$ and the heat of sorption is reduced to the latent heat of vaporization. This reflects the fact that any change of phase (in the direction of moisture removal from the airstream) beyond this point can only occur by simple condensation. For illustration purposes, for a linear isotherm with $W_{\max} = 0.5$ kg water/kg sorbent, possible values for the constants are $\Delta e = 0.3$, $\kappa = 0.5$.

San and Hsiau [62, 63] also use a similar expression for silica-gel and water, in which e_{sor} is given by:

$$e_{\text{sor}} = 0.2843 \exp(-10.28W). \quad (84)$$

6 Equations in Terms of Temperature and Concentration

After the introduction of heat and mass fluxes, the transport equations arising from the presented conservation balances are written in terms of temperature and concentration.

6.1 Process Stream and Impermeable Wall

Starting with the process stream, the governing equations are given by:

$$\rho_a \left(\frac{\partial Y}{\partial t} + (-1)^\gamma u \frac{\partial Y}{\partial x} \right) = \frac{\mathcal{P}_s}{\mathcal{A}_p} h_m \rho_a (Y_i - Y), \quad (85)$$

$$\rho c_p \left(\frac{\partial T}{\partial t} + (-1)^\gamma u \frac{\partial T}{\partial x} \right) = \frac{\mathcal{P}_s}{\mathcal{A}_p} h (T_i - T) + \frac{\mathcal{P}_s}{\mathcal{A}_p} h_m \rho_a (Y_i - Y) (i_{v,i} - i_v). \quad (86)$$

By inspecting these equations, one notices that although T_i and Y_i are clearly defined, the value of $i_{v,i}$ is unclear. Physically, it must be within the values of the vapor enthalpy in the process stream i_v and the vapor enthalpy in the sorbent felt $i_{v,f}$. In order to facilitate matters, the parameter φ is introduced:

$$\varphi = \frac{i_{v,i} - i_v}{i_{v,f} - i_v}, \quad 1 - \varphi = \frac{i_{v,f} - i_{v,i}}{i_{v,f} - i_v}. \quad (87)$$

In addition, $i_{v,f} - i_v$ can be written in terms of a temperature difference:

$$i_{v,f} - i_v = c_{p,v} (T_i - T), \quad (88)$$

where T_i has been used for representing the temperature associated with the felt enthalpy because, $T_i = T_f$ for the one-dimensional sorbent balances and $T_i = T_f$ at the felt-stream interface for the multi-dimensional case. With Eq. (87) the energy Eq. (86) can be rewritten as:

$$\begin{aligned} \rho c_p \left(\frac{\partial T}{\partial t} + (-1)^\gamma u \frac{\partial T}{\partial x} \right) &= \frac{\mathcal{P}_s}{\mathcal{A}_p} h (T_i - T) \\ &+ \frac{\mathcal{P}_s}{\mathcal{A}_p} h_m \rho_a \varphi c_{p,v} (Y_i - Y) (T_i - T). \end{aligned} \quad (89)$$

The energy equation for the impermeable wall is given in terms of its temperature as:

$$\rho_w c_w \frac{\partial T_w}{\partial t} = k_w \frac{\partial^2 T_w}{\partial x^2} - \frac{\mathcal{P}_w}{\mathcal{A}_w} h_w (T_w - T_{fw}). \quad (90)$$

6.2 One-Dimensional Sorbent Equations

For the sorbent felt, if the one-dimensional balances are employed, one obtains the following equations:

$$\begin{aligned} \varepsilon \rho_a \frac{\partial Y_f}{\partial t} + (1 - \varepsilon) \rho_s f_s \frac{\partial W}{\partial t} = & -\frac{\mathcal{P}_s}{\mathcal{A}_f} h_m \rho_a (Y_f - Y) \\ & + \rho_a \frac{\partial}{\partial x} \left(\mathcal{D}_{g,\text{eff}} \frac{\partial Y_f}{\partial x} \right) + \rho_s f_s \frac{\partial}{\partial x} \left(\mathcal{D}_{s,\text{eff}} \frac{\partial W}{\partial x} \right), \end{aligned} \quad (91)$$

$$\begin{aligned} \rho_f c_f \frac{\partial T_f}{\partial t} = & k_{\text{eff}} \frac{\partial^2 T_f}{\partial x^2} - \frac{\mathcal{P}_s}{\mathcal{A}_f} h_m (T_f - T) \\ & + \frac{\mathcal{P}_s}{\mathcal{A}_f} h_m \rho_a (1 - \varphi) c_{p,v} (Y_f - Y) (T_f - T) + \dot{s}'_{\text{sor}} + \frac{\mathcal{P}_w}{\mathcal{A}_f} h_w (T_w - T_{fw}), \end{aligned} \quad (92)$$

where, naturally, if mass diffusion through the porous felt is negligible, Eq. (91) can be simplified to:

$$\varepsilon \rho_a \frac{\partial Y_f}{\partial t} + (1 - \varepsilon) \rho_s f_s \frac{\partial W}{\partial t} = -\frac{\mathcal{P}_s}{\mathcal{A}_f} h_m \rho_a (Y_f - Y). \quad (93)$$

It is interesting to note that, if rate of sorption term can be written in the form of Eq. (35), one arrives at:

$$\dot{s}'_{\text{sor}} = -\frac{\mathcal{P}_s}{\mathcal{A}_f} h_m \rho_a (Y_f - Y). \quad (94)$$

Then, if one further considers that the effects of surface diffusion are negligible to the sorption heating term, the energy equation can be written in the following form:

$$\rho_f c_f \frac{\partial T_f}{\partial t} = k_{\text{eff}} \frac{\partial^2 T_f}{\partial x^2} - \frac{\mathcal{P}_s}{\mathcal{A}_f} h_m (T_f - T) + \dot{s}'_{\text{sor}} i_{\text{sor}}^+ + \frac{\mathcal{P}_w}{\mathcal{A}_f} h_w (T_w - T_{fw}), \quad (95)$$

where i_{sor}^+ is a modified heat of sorption, defined as:

$$i_{\text{sor}}^+ = i_{\text{sor}} + (1 - \varphi) c_{p,v} (T_f - T), \quad (96)$$

which also involves a sensible heating portion.

It is also interesting to note that combining Eqs. (89), (90) and (92) leads to

$$\begin{aligned} \mathcal{A}_p \rho c_p \left(\frac{\partial T}{\partial t} + (-1)^\gamma u \frac{\partial T}{\partial x} \right) + \mathcal{A}_f \rho_f c_f \frac{\partial T_f}{\partial t} + \mathcal{A}_w \rho_w c_w \frac{\partial T_w}{\partial t} = \mathcal{A}_f k_{\text{eff}} \frac{\partial^2 T_f}{\partial x^2} \\ + \mathcal{A}_w k_w \frac{\partial^2 T_w}{\partial x^2} + \mathcal{P}_s h_m \rho_a c_{p,v} (Y_f - Y) (T_f - T) + \mathcal{A}_f \dot{s}'_{\text{sor}}, \end{aligned} \quad (97)$$

which actually represents the energy balance for the entire system, including the process stream, felt and supporting structure. From this equation, one notices that regardless of the value of φ , the complete system will have the same heating effect, which is represented in the last two terms of this equation. The last term represents the latent heating due to sorption, whereas the next-to-last term represents a sensible heating. Its interesting to note that depending on the signs of $T_f - T$ and $Y_f - Y$, the sensible heating term can assume positive or negative values, representing a heating or even a cooling effect. Finally, comparing Eqs. (89) and (92) it becomes clear that the φ parameter determines which medium is directly affected by the sensible heating term. If $\varphi = 1$ the sensible heating is entirely delivered to the process stream; on the other hand, if $\varphi = 0$ it is entirely delivered to the sorbent felt. Any other value will lead to a fraction of this effect being delivered to each of these media. A similar consideration is done in [67]; however, it is also considered that the latent fraction of the sorption heating effect can be delivered partly to the felt and partly to the process stream.

Equation (92) considers the effect of a thermal resistance between the impermeable structure and sorbent felt. This is actually a general case that can be used for other simple situations. For instance, if there is no impermeable wall, one can simply equal h_w to zero, removing the wall from the problem. On the other hand, if perfect contact is assumed between the wall and sorbent, h_w goes to infinity and the temperature difference $T_w - T_f$ goes to zero. As both the wall and felt are at the same temperature for this special case, Eqs. (90) and (92) can be combined into a single form:

$$\begin{aligned} \left(\rho_f c_f + \rho_w c_w \frac{\mathcal{A}_w}{\mathcal{A}_f} \right) \frac{\partial T_f}{\partial t} = \left(k_{\text{eff}} + k_w \frac{\mathcal{A}_w}{\mathcal{A}_f} \right) \frac{\partial^2 T_f}{\partial x^2} - \frac{\mathcal{P}_s}{\mathcal{A}_f} h_m (T_f - T) \\ + \frac{\mathcal{P}_s}{\mathcal{A}_f} h_m \rho_a (1 - \varphi) c_{p,v} (Y_f - Y) (T_f - T) + \dot{s}'_{\text{sor}}, \end{aligned} \quad (98)$$

which shows, for the perfect thermal contact, that the wall contributes to augmenting the thermal capacity and thermal conductivity of the felt.

6.3 Multi-Dimensional Sorbent Equations

Employing the more general model that includes an extra mass transfer resistance, the governing equations in terms of temperature and concentrations are given by:

$$\varepsilon \frac{\partial Y_f}{\partial t} - \nabla \cdot (\mathcal{D}_{g,\text{eff}} \nabla Y_f) = h_\pi (Y_\pi - Y_f), \quad (99)$$

$$(1 - \varepsilon) \rho_s f_s \frac{\partial W}{\partial t} - \rho_s f_s \nabla \cdot (\mathcal{D}_{s,\text{eff}} \nabla W) = -h_\pi \rho_a (Y_\pi - Y_f), \quad (100)$$

$$\rho_f c_f \frac{\partial T_f}{\partial t} = \nabla \cdot (k_{\text{eff}} \nabla T_f) + \dot{s}'_{\text{sor}}, \quad (101)$$

remembering that $W = W(T_f, Y_\pi)$. As previously mentioned, if $h_\pi \rightarrow \infty$, $Y_f = Y_\pi$, and Eqs. (99) and (100) can be combined into a single from:

$$\varepsilon \rho_a \frac{\partial Y_f}{\partial t} + (1 - \varepsilon) \rho_s f_s \frac{\partial W}{\partial t} = \rho_a \nabla \cdot (\mathcal{D}_{g,\text{eff}} \nabla Y_f) + \rho_s f_s \nabla \cdot (\mathcal{D}_{s,\text{eff}} \nabla W). \quad (102)$$

Regardless of the value of h_π , the heating rate due to sorption is given by:

$$\dot{s}'_{\text{sor}} = \rho_s f_s \left[\left((1 - \varepsilon) \frac{\partial W}{\partial t} - \nabla \cdot (\mathcal{D}_{s,\text{eff}} \nabla W) \right) i_{\text{sor}} - \nabla \cdot (\mathcal{D}_{s,\text{eff}} \nabla W) (i_t - \bar{i}_t) \right], \quad (103)$$

which for no surface diffusion is simply reduced to:

$$\dot{s}'_{\text{sor}} = \rho_s f_s (1 - \varepsilon) \frac{\partial W}{\partial t} i_{\text{sor}}. \quad (104)$$

7 Boundary and Periodicity Conditions

7.1 Process Stream and Impermeable Wall

The heat and mass convection equations for the process streams and the impermeable wall heat balance equation require boundary conditions in the axial direction only. For the supporting wall, convection heat transfer conditions can be written at $x = 0$ and $x = L$:

$$\dot{q}''_{w,x} = h_0 (T_0 - T_w), \quad \text{at } x = 0, \quad (105)$$

$$\dot{q}''_{w,x} = h_L (T_w - T_L), \quad \text{at } x = L, \quad (106)$$

where h_0 and h_L are convective heat transfer coefficients at the boundaries, and T_0 and T_L are the fluid temperatures at $x = 0$ and $x = L$, respectively. Nevertheless, it is generally considered that the heat transfer through these boundaries is insignificant compared to that exchanged with the sorbent felt, such that insulated conditions can be applied:

$$\dot{q}_{w,x}'' = 0, \text{ at } x = 0 \text{ and } x = L. \quad (107)$$

For the process stream, the presence of first order spatial derivatives only require a single boundary condition for each dependent variable. These are the inlet conditions of the different process streams:

$$T(\gamma_k L, t) = T_{in,k} \text{ and } Y(\gamma_k L, t) = Y_{in,k}, \text{ for } t_{k-1} \leq t < t_k, \quad (108)$$

for $k = 1, 2, \dots, K$, where $\gamma_k = 0$ for streams flowing in the positive x direction and, whereas $\gamma_k = 1$ for streams that flow in the opposite direction.

7.2 Sorbent Material

The remaining required boundary conditions involve the sorbent material. Since two types of balances were employed, different sets of boundary conditions will be used. At $x = 0$ and $x = L$, the boundary conditions will be the same for both one-dimensional and multi-dimensional balances. As similarly considered for the impermeable wall, the mass and energy transfers at the boundaries $x = 0$ and $x = L$ are negligible compared to the transfer rates to the process stream and wall, such that insulated and impermeable boundaries may be assumed. This leads to the following result

$$\dot{q}_{f,x}'' = 0, \text{ at } x = 0 \text{ and } x = L, \quad (109)$$

$$j_{g,x}'' = 0, \text{ at } x = 0 \text{ and } x = L, \quad (110)$$

$$j_{s,x}'' = 0, \text{ at } x = 0 \text{ and } x = L, \quad (111)$$

which can also be expressed in terms of temperature and gas-phase concentration:

$$\frac{\partial Y_f}{\partial x} = \frac{\partial T_f}{\partial x} = 0, \text{ at } x = 0 \text{ and } x = L. \quad (112)$$

For the one-dimensional sorbent balance, these are actually the only boundary conditions required. In fact, if axial diffusion through the supporting structure is assumed negligible, no boundary conditions are required at all.

For the multi-dimensional balances, additional conditions at the remaining interfaces are needed. At the felt-stream interface a mass balance yields the following boundary condition:

$$\left(\mathbf{j}_s'' + \mathbf{j}_g''\right) \cdot \mathbf{n} = j_i'' \text{ for } \mathbf{x} \in \mathcal{S}_p, \quad (113)$$

noting that in this case the interface concentration Y_i is given by the value of Y_f at the interface. Although thermodiffusion was not considered in this equation, one could easily modify it to include this effect. In a similar fashion, an energy balance can be written at the felt-stream interface:

$$\left(\bar{i}_l \mathbf{j}_s'' + i_{v,f} \mathbf{j}_g'' + \dot{\mathbf{q}}_f''\right) \cdot \mathbf{n} = \dot{q}_i'' + j_i'' i_{v,i} \text{ for } \mathbf{x} \in \mathcal{S}_p. \quad (114)$$

A simplified equation can be obtained if the mass balance at the interface is used, leading to:

$$\dot{\mathbf{q}}_f'' \cdot \mathbf{n} = \dot{q}_i'' + j_i'' (i_{v,i} - i_{v,f}) + (i_{v,f} - \bar{i}_l) \mathbf{j}_s'' \cdot \mathbf{n} \text{ for } \mathbf{x} \in \mathcal{S}_p, \quad (115)$$

where the last two terms on the right-hand-side are generally assumed negligible among most literature studies leading to

$$\dot{\mathbf{q}}_f'' \cdot \mathbf{n} = \dot{q}_i'' \text{ for } \mathbf{x} \in \mathcal{S}_p, \quad (116)$$

which implies that the heat conduction into the sorbent material is solely due to the sensible heat transfer from the process stream. As similarly mentioned for the interface mass balance, T_i [appearing in the definition of \dot{q}_i'' , Eq. (73)] is the value of T_f evaluated at this interface. In terms of concentration and temperature, the boundary conditions given by Eqs. (113) and (115) are written as:

$$-(\rho_a \mathcal{D}_{g,\text{eff}} \nabla Y_f + f_s \rho_s \mathcal{D}_{s,\text{eff}} \nabla W) \cdot \mathbf{n} = h_m \rho_a (Y_f - Y), \quad (117)$$

$$-k_{\text{eff}} \nabla T_f \cdot \mathbf{n} = h (T_f - T) +$$

$$+ h_m \rho_a (Y_f - Y) (i_{v,i} - i_{v,f}) - (i_{v,f} - i_l) \rho_s f_s \mathcal{D}_{s,\text{eff}} \nabla W \cdot \mathbf{n}, \quad (118)$$

At the felt-wall interface, the impermeability condition must hold:

$$\left(\mathbf{j}_s'' + \mathbf{j}_g''\right) \cdot \mathbf{n} = 0 \text{ for } \mathbf{x} \in \mathcal{S}_w. \quad (119)$$

In a similar fashion, an energy balance can be written at same interface:

$$\left(\bar{i}_l \mathbf{j}_s'' + i_{v,f} \mathbf{j}_g'' + \dot{\mathbf{q}}_f''\right) \cdot \mathbf{n} = -\dot{q}_w'' \text{ for } \mathbf{x} \in \mathcal{S}_w, \quad (120)$$

and this equation can be simplified by using the mass boundary condition (119):

$$\dot{\mathbf{q}}_f'' \cdot \mathbf{n} = -\dot{q}_w'' + (i_{v,f} - \bar{i}_l) \mathbf{j}_s'' \cdot \mathbf{n} \text{ for } \mathbf{x} \in \mathcal{S}_w. \quad (121)$$

Finally, in terms of concentration and temperatures, the boundary conditions given by Eqs. (119) and (121) are written as:

$$-(\rho_a \mathcal{D}_{g,\text{eff}} \nabla Y_f + f_s \rho_s \mathcal{D}_{s,\text{eff}} \nabla W) \cdot \mathbf{n} = 0, \quad (122)$$

$$-k_{\text{eff}} \nabla T_f \cdot \mathbf{n} = -h_w (T_w - T_f) - (i_{v,f} - \bar{i}_l) \rho_s f_s \mathcal{D}_{s,\text{eff}} \nabla W \cdot \mathbf{n}, \quad (123)$$

In the absence of a supporting structure, the surface \mathcal{S}_w is treated as impermeable and adiabatic. For these cases, it is easy to show that the boundary conditions at this interface are reduced to:

$$\nabla T_f \cdot \mathbf{n} = \nabla Y_f \cdot \mathbf{n} = 0 \quad \text{for } \mathbf{x} \in \mathcal{S}_w. \quad (124)$$

7.3 Periodicity Conditions

Although the regenerative exchanger problem associated with active and passive desiccant is transient, its solution is periodic, such that the following periodicity conditions must be satisfied:

$$T(x, t) = T(x, t + t_f), \quad (125)$$

$$Y(x, t) = Y(x, t + t_f), \quad (126)$$

$$T_f(\mathbf{x}, t) = T_f(\mathbf{x}, t + t_f), \quad (127)$$

$$Y_f(\mathbf{x}, t) = Y_f(\mathbf{x}, t + t_f), \quad (128)$$

$$T_w(x, t) = T_w(x, t + t_f), \quad (129)$$

remembering that t_f is the total operation period, as defined by Eq. (3). The position vector \mathbf{x} was used for the sorbent temperature and vapor concentration, since in the multi-dimensional formulation it can depend one more than one spatial variable.

8 Concluding Remarks

This chapter presented a detailed description of different mathematical models that can be applied for simulating the operation of both active and passive desiccant wheels. Following a trend seen in the vast majority of literature studies, the transport equations for the airstream were treated in a simple bulk-form, and most of the presented features were focused on the transport phenomena that occur within the porous desiccant material. The simplifying assumptions and required steps for obtaining the governing equations were properly discussed, and some of the resulting formulations are very similar to models available in the literature. In addition, suggestions for modifications in current literature models for this type of problem were also presented, as an attempt to motivate the development of new studies related to modeling and simulation of heat and mass transfer regenerators,

such as active and passive desiccant wheels. The presented set of equations are very general such that a variety of configurations can be simulated. As expected, due to the coupling and non-linearities involved, one should seek a numerical scheme for solving such equations. Nevertheless, such numerical schemes are readily available in the literature related to heat and mass transfer regenerators.

Acknowledgments The author would like to acknowledge the financial support provided by the Brazilian Government research funding agencies: CNPq (Federal Government) and FAPERJ (Rio de Janeiro State). The author would also like to express his gratitude for the Graduate students D. C. Moreira and D. J. M. N. Chalhub, and S. M. D. Santos, who assisted in proofreading the text.

References

1. Banks PJ (1972) Coupled equilibrium heat and single adsorbate transfer in fluid flow through a porous medium—I: characteristics potentials and specific capacity ratios. *Chem Eng Sci* 27:1143–1155
2. Banks PJ (1985) Prediction of heat and mass regenerator performance using nonlinear analogy method: Part I—Basis. *J Heat Transf (ASME)* 107:222–229
3. Banks PJ (1985) Prediction of heat and mass regenerator performance using nonlinear analogy method: Part II—Comparison of methods. *J Heat Transf (ASME)* 107:230–238
4. Bird RB, Stewart WE, Lightfoot EN (2002) *Transport phenomena*, 2nd edn. Wiley, New York
5. Bullock CE, Threlkeld JL (1966) Dehumidification of moist air by adiabatic adsorption. *ASHRAE Trans* 72:301–313
6. Charoensupaya D, Worek WM (1988) Effect of adsorbent heat and mass transfer resistances on performance of an open-cycle adiabatic desiccant cooling system. *Heat Recovery Syst CHP* 8(6):537–548
7. Charoensupaya D, Worek WM (1988) Parametric study of an open-cycle adiabatic, solid, desiccant cooling system. *Energy* 13(9):739–747
8. Chase CA Jr, Gidaspow D, Peck R (1970) Transient heat and mass transfer in an adiabatic regenerator—A Green's matrix representation. *Int J Heat Mass Transf* 13:817–833
9. Chi CW, Wasan DT (1970) Fixed bed adsorption drying. *AICHE J* 16(1):23–30
10. Chung JD, Lee DY (2009) Effect of desiccant isotherm on the performance of desiccant wheel. *Int J Refrig* 32(4):720–726
11. Chung JD, Lee DY, Yoon SM (2009) Optimization of desiccant wheel speed and area ratio of regeneration to dehumidification as a function of regeneration temperature. *Sol Energy* 83(5):625–635
12. Close DJ, Banks PJ (1972) Coupled equilibrium heat and single adsorbate transfer in fluid flow through a porous medium—II: predictions for a silica-gel-air-drier using characteristics charts. *Chem Eng Sci* 27:1157–1169
13. Coppage JE, London AL (1953) The periodic-flow regenerator—a summary of design theory. *Trans ASME* 75:779–787
14. Dai Y, Wang RZ, Zhang LZ (2001) Parameter analysis to improve rotary desiccant dehumidification using a mathematical model. *Int J Therm Sci* 40:400–408
15. Gao Z, Mei V, Tomlinson JJ (2005) Theoretical analysis of dehumidification process in a desiccant wheel. *Heat Mass Transf* 41(11):1033–1042
16. Ge T, Lia Y, Wang R, Dai Y (2008) A review of the mathematical models for predicting rotary desiccant wheel. *Renew Sustain Energy Rev* 12(6):1485–1528

17. Ge TS, Ziegler F, Wang RZ (2010) A mathematical model for predicting the performance of a compound desiccant wheel (a model of compound desiccant wheel). *Appl Therm Eng* 30(8–9):1005–1015
18. Ghezelayagh H, Gidaspow D (1982) Micro-macropore model for sorption of water on silica gel in a dehumidifier. *Chem Eng Sci* 37(8):1181–1197
19. Golubovic MN, Hettiarachchi HDM, Worek WM (2007) Evaluation of rotary dehumidifier performance with and without heated purge. *Int Commun Heat Mass Transfer* 34(7):785–795
20. Golubovic MN, Worek WM (2004) Influence of elevated pressure on sorption in desiccant wheels. *Numer Heat Transf Part A: applications* 45(9):869–886
21. Gregg SJ, Sing KSW (1982) Adsorption, surface area and porosity, 2nd edn. Academic, London
22. Gupta Y, Metchop L, Frantzis A, Phelan P (2008) Comparative analysis of thermally activated, environmentally friendly cooling systems. *Energy Convers Manage* 49(5):1091–1097
23. Hausen H (1929) Über die theorie des wärmeaustausches in regeneratoren. *ZAMM-Journal of Applied Mathematics and Mechanics/Zeitschrift für Angewandte Mathematik und Mechanik* 9(3):173–200
24. Hausen H (1930) Über den wärmeaustausch in regeneratoren. *Forsch Ingenieurwes* 1:250–256
25. Heidarinejad G, Pasharshahi H (2010) The effects of operational conditions of the desiccant wheel on the performance of desiccant cooling cycles. *Energy Build* 42(12):2416–2423
26. Heidarinejad G, Pasharshahi H (2011) Potential of a desiccant-evaporative cooling-system performance in a multi-climate country. *Int J Refrig* 34(5):1251–1261
27. Holmberg RB (1979) Combined heat and mass transfer in regenerators with hygroscopic materials. *J Heat Transf (ASME)* 101:205–210
28. Hougen OA, Marshall WR Jr (1947) Adsorption from a fluid stream flowing through a stationary granular bed. *Chem Eng Prog* 43(4):197–208
29. Jeong JW, Mumma SA (2005) Practical thermal performance correlations for molecular sieve and silica gel loaded enthalpy wheels. *Appl Therm Eng* 25(5–6):719–740
30. Jurinak JJ, Mitchell JW (1984) Effect of matrix properties on the performance of a counterflow rotary dehumidifier. *J Heat Transf (ASME)* 106:638–645
31. Jurinak JJ, Mitchell JW (1984) Recirculation of purged flow in an adiabatic counterflow rotary dehumidifier. *J Heat Transf (ASME)* 106:369
32. Jurinak JJ, Mitchell JW, Beckman WA (1984) Open-cycle desiccant air-conditioning as an alternative to vapor compression cooling in residential applications. *J Solar Energy Eng (ASME)* 106:252–260
33. Kanoğlu M, Bolattürk A, Altıntop N (2007) Effect of ambient conditions on the first and second law performance of an open desiccant cooling process. *Renew Energy* 32(6):931–946
34. Kays WM, Crawford ME, Weigand B (2004) Convective heat and mass transfer, 4th edn. McGraw-Hill, New York
35. Kays WM, London AL (1998) Compact heat exchangers, 3rd edn. Krieger Publishing Company, New York
36. Klein H, Klein SA, Mitchell JW (1990) Analysis of regenerative enthalpy exchangers. *Int J Heat Mass Transf* 33(4):735–744
37. Larsen FW (1967) Rapid calculation of temperature in a regenerative heat exchanger having arbitrary initial solid and entering fluid temperatures. *Int J Heat Mass Transf* 10:149–168
38. Luikov AV, Shashkov AG, Vasiliev LL, Fraiman YE (1968) Thermal conductivity of porous systems. *Int J Heat Mass Transf* 11:117–140
39. Maclaine-Cross IL, Banks PJ (1972) Coupled heat and mass transfer in regenerators—Predictions using an analogy with heat transfer. *Int J Heat Mass Transf* 15(6):1225–1242
40. Majumdar P, Worek WM (1989) Combined heat and mass transfer in a porous adsorbent. *Energy* 14(3):161–175

41. Mathiprakasam B, Lavan Z (1980) Performance predictions for adiabatic desiccant dehumidifiers using linear solutions. *J Solar Energy Eng (ASME)* 102:73–79
42. Mei VC, Lavan Z (1983) Performance of crossed-cooled desiccant dehumidifiers. *J Solar Energy Eng (ASME)* 105:300–304
43. Meyer OA, Weber TW (1967) Nonisothermal adsorption in fixed beds. *AIChE Journal* 13(3):457–465
44. Narayanan R, Saman WY, White SD, Goldsworthy M (2011) Comparative study of different desiccant wheel designs. *Appl Therm Eng* 31(10):1613–1620
45. Niu JL, Zhang LZ (2002) Effects of wall thickness on the heat and moisture transfers in desiccant wheels for air dehumidification and enthalpy recovery. *Int Commun Heat Mass Transfer* 29(2):255–268
46. Nóbrega CEL, Brum NCL (2009) Influence of isotherm shape over desiccant cooling cycle performance. *Heat Transfer Eng* 30(4):302–308
47. Nóbrega CEL, Brum NCL (2009) Modeling and simulation of heat and enthalpy recovery wheels. *Energy* 34(12):2063–2068
48. Nóbrega CEL, Brum NCL (2011) A graphical procedure for desiccant cooling cycle design. *Energy* 36(3):1564–1570
49. Nóbrega CEL, Brum NCL (2012) An analysis of the heat and mass transfer roles in air dehumidification by solid desiccants. *Energy Build* 50:251–258
50. Panaras G, Mathioulakis E, Belessiotis V (2011) Solid desiccant air-conditioning systems-design parameters. *Energy* 36(5):2399–2406
51. Pesaran AA, Mills AF (1987) Moisture transport in silica gel packed beds—I: theoretical study. *Int J Heat Mass Transf* 30(6):1037–1049
52. Rosen JB (1952) Kinetics of a fixed bed system for solid diffusion into spherical particles. *J Chem Phys* 20:387–394
53. Roy D, Gidaspow D (1974) Nonlinear coupled heat and mass exchange in a cross-flow regenerator. *Chem Eng Sci* 29:2101–2114
54. Ruan W, Qu M, Horton W (2012) Modeling analysis of an enthalpy recovery wheel with purge air. *Int J Heat Mass Transf* 55(17–18):4665–4672
55. Ruivo CR, Costa J, Figueiredo AR (2008) Numerical study of the cyclic behavior of a desiccant layer of a hygroscopic rotor. *Numer Heat Transf Part A: Appl* 53(10):1037–1053
56. Ruivo CR, Costa JJ, Figueiredo AR (2006) Analysis of simplifying assumptions for the numerical modeling of the heat and mass transfer in a porous desiccant medium. *Numer Heat Transf Part A: Appl* 49(9):851–872
57. Ruivo CR, Costa JJ, Figueiredo AR (2007) On the behaviour of hygroscopic wheels: Part I—Channel modelling. *Int J Heat Mass Transf* 50(23–24):4812–4822
58. Ruivo CR, Costa JJ, Figueiredo AR (2007) On the behaviour of hygroscopic wheels: Part II—Rotor performance. *Int J Heat Mass Transf* 50(23–24):4823–4832
59. Ruivo CR, Costa JJ, Figueiredo AR (2011) Influence of the atmospheric pressure on the mass transfer rate of desiccant wheels. *Int J Refrig* 34(3):707–718
60. Ruivo CR, Costa JJ, Figueiredo AR (2011) Numerical study of the influence of the atmospheric pressure on the heat and mass transfer rates of desiccant wheels. *Int J Heat Mass Transf* 54(7–8):1331–1339
61. Ruivo CR, Costa JJ, Figueiredo AR (2011) Parametric study of the cyclic behaviour of a hygroscopic matrix in a desiccant airflow system. *Heat Mass Transf* 47(9):1101–1112
62. San J (1993) Heat and mass transfer in a two-dimensional cross-flow regenerator with a solid conduction effect. *Int J Heat Mass Transf* 36(3):633–643
63. San JY, Hsiau SC (1993) Effect of axial solid heat conduction and mass diffusion in a rotary heat and mass regenerator. *Int J Heat Mass Transf* 36(8):2051–2059
64. Shah RK (1981) Thermal design theory for regenerators. In: Kakaç S, Bergles AE, Mayinger F (eds) *Heat exchangers: thermal-hydraulic fundamentals and design*. Hemisphere, New York, pp 721–763
65. Shang W, Besant R (2008) Theoretical and experimental methods for the sensible effectiveness of air-to-air energy recovery wheels. *HVAC&R Research* 14(3):373–396

66. Shang W, Besant R (2009) Effectiveness of desiccant coated regenerative wheels from transient response characteristics and flow channel properties part I: Development of effectiveness equations from transient response characteristics. *HVAC&R Research* 15(2):329–345
67. Simonson CJ, Besant RW (1997) Heat and moisture transfer in desiccant coated rotary energy exchangers: Part I. Numerical model. *HVAC&R Research* 3(4):325–350
68. Simonson CJ, Besant RW (1997) Heat and moisture transfer in desiccant coated rotary energy exchangers: Part II. Validation and sensitivity studies. *HVAC&R Research* 3(4):351–368
69. Simonson CJ, Besant RW (1999) Energy wheel effectiveness—part I: Development of dimensionless groups. *Int J Heat Mass Transf* 42:2161–2170
70. Simonson CJ, Besant RW (1999) Energy wheel effectiveness—part II: Correlations. *Int J Heat Mass Transf* 42:2171–2185
71. Sphaier LA, Nóbrega CEL (2012) Parametric analysis of components effectiveness on desiccant cooling system performance. *Energy* 38(1):157–166
72. Sphaier LA, Worek WM (2006) Comparisons between 2D and 1D formulations of heat and mass transfer in rotary regenerators. *Numer Heat Transf Part B: Fundamentals* 49(3):223–237
73. Sphaier LA, Worek WM (2006) The effect of axial diffusion in desiccant and enthalpy wheels. *Int J Heat Mass Transf* 49(7–8):1412–1419
74. Sphaier LA, Worek WM (2008) Numerical solution of periodic heat and mass transfer with adsorption in regenerators: Analysis and optimization. *Numer Heat Transf Part A: Appl* 53(11):1133–1155
75. Sphaier LA, Worek WM (2009) Parametric analysis of heat and mass transfer regenerators using a generalized effectiveness-NTU method. *Int J Heat Mass Transf* 52(9–10):2265–2272
76. Stabat P, Marchio D (2009) Heat and mass transfer modeling in rotary desiccant dehumidifiers. *Appl Energy* 86(5):762–771
77. Stiesch G, Klein SA, Mitchell JW (1995) Performance of rotary heat and mass exchangers. *HVAC&R Res* 1(4):308–323
78. Van den Bulck E, Mitchell JW, Klein SA (1985) Design theory for rotary heat and mass exchangers—I: Wave analysis of rotary heat and mass exchangers with infinite transfer coefficients. *Int J Heat Mass Transf* 28(8):1575–1586
79. Van den Bulck E, Mitchell JW, Klein SA (1985) Design theory for rotary heat and mass exchangers—II: Effectiveness-number-of-transfer-units method for rotary heat and mass exchangers. *Int J Heat Mass Transf* 28(8):1587–1595
80. Youngquist GR (1970) Diffusion and flow of gases in porous solids. *Ind Eng Chem* 62(8):52–63
81. Zhang LZ, Niu JL (2001) Energy requirements for conditioning fresh air and the long-term savings with a membrane-based energy recovery ventilator in hong kong. *Energy* 26(2):119–135
82. Zhang LZ, Niu JL (2002) Performance comparisons of desiccant of desiccant wheels for air dehumidification and enthalpy recovery. *Appl Therm Eng* 22(12):1347–1367
83. Zheng W, Worek WM (1993) Numerical simulation of combined heat and mass transfer processes in rotary dehumidifier. *Numer Heat Transf Part A: Appl* 23:211–232
84. Zheng W, Worek WM, Novosel D (1995) Effect of operating conditions on optimal performance of rotary dehumidifiers. *J Energy Res Technol (ASME)* 117:62–66
85. Zheng W, Worek WM, Novosel D (1995) Performance optimization of rotary dehumidifiers. *J Solar Energy Eng (ASME)* 117:40–44

Influence of Altitude on the Behavior of Solid Desiccant Dehumidification System

C. R. Ruivo, J. J. Costa and A. R. Figueiredo

List of Symbols

.	
a	Coefficient in Eq. (15)
A	Transfer area (m^2)
b	Exponent in Eq. (15)
c	Exponent in Eq. (15)
c_p	Specific heat ($\text{J kg}^{-1} \text{ }^\circ\text{C}^{-1}$)
c_{pf}^*	Specific heat of the moist air ($\text{J kg}^{-1} \text{ }^\circ\text{C}^{-1}$)
C	Heat capacity rate ($\text{J s}^{-1} \text{ }^\circ\text{C}^{-1}$)
CR	Ratio of heat capacity rates
d_h	Dydraulic diameter (m)
D_f	Diffusion coefficient of water vapor in the moist air ($\text{m}^2 \text{ s}^{-1}$)
F	Correction factor for the actual exchanger configuration
$F1, F2$	Combined potentials or characteristic potentials
h	Specific enthalpy of moist air (J kg^{-3})
h_h	Convective heat transfer coefficient ($\text{W m}^{-2} \text{ }^\circ\text{C}^{-1}$)
h_m	Convective mass transfer coefficient (m s^{-1})
H	Altitude (m)
j_h	Heat convective flux (W m^{-2})
j_m	Mass convective flux (W m^{-2})
\dot{J}_h	Heat transfer rate per unit of transfer area of a desiccant wheel (W m^{-2})
\dot{J}_m	Mass transfer rate per unit of transfer area of a desiccant wheel ($\text{kg s}^{-1} \text{ m}^{-2}$)

C. R. Ruivo (✉)

Instituto Superior de Engenharia, Universidade do Algarve, Campus da Penha,
8005-139 Faro, Portugal
e-mail: cruivo@ualg.pt

C. R. Ruivo · J. J. Costa · A. R. Figueiredo

ADAI-LAETA, Universidade de Coimbra, Rua Luís Reis Santos 3030-788 Coimbra,
Portugal

k	Correction factor for the effect of pressure decrease on the heat or mass transfer rates
Le	Lewis number
m	Mass (kg)
\dot{m}	Mass flow rate (kg s^{-1})
n_ϕ	Exponent in Eq. (18)
NTU	Number of transfer units
Nu	Nusselt number
P	Atmospheric pressure (Pa)
Pr	Prandtl number
P_v	Partial pressure of water vapor (Pa)
P_{vs}	Saturation pressure of water vapor (Pa)
\dot{Q}	Heat transfer rate (W)
R	Gas constant ($\text{J kg}^{-1} \text{ }^\circ\text{C}^{-1}$)
R	Thermal resistance ($^\circ\text{C W}^{-1}$)
Re	Reynolds number
Sh	Sherwood number
T	Temperature ($^\circ\text{C}$)
T_{sat}	Water saturation temperature ($^\circ\text{C}$)
U	Overall heat transfer coefficient ($\text{W m}^{-2} \text{ }^\circ\text{C}^{-1}$)
w_v	Water vapor content (kg kg^{-1})
v	Specific volume of moist air referred to the unity of dry air mass ($\text{m}^3 \text{ kg}^{-1}$)
v^*	Specific volume of the moist air ($\text{m}^3 \text{ kg}^{-1}$)
V	Volume (m^3)
\dot{V}	Volume flow rate ($\text{m}^3 \text{ s}^{-1}$)
X_ℓ	Adsorbed water content in the desiccant (kg kg^{-1})

Greek Symbols

ΔT_{lm}	Log mean temperature difference for a heat exchanger ($^\circ\text{C}$)
ε	Effectiveness
φ_v	Water vapor mass fraction
η_{F1}, η_{F2}	Effectiveness parameters based on variations in $F1$ and $F2$, respectively
η_ψ, η_h	Effectiveness parameters based on variations in ψ and h , respectively
λ	Thermal conductivity ($\text{W m}^{-1} \text{ }^\circ\text{C}^{-1}$)
ψ	Ratio of the partial vapor pressure to the saturation vapor pressure
ψ^*	Relative humidity
ρ	Density (kg m^{-3})
σ_w	Density ratio when T and w_v remain constant
σ_ψ	Density ratio when T and ψ remain constant

Subscripts

<i>a</i>	Air
cf	Counter-flow heat exchanger
coil	Heating coil
<i>f</i>	Airflow
in	Inlet
min	Minimum value
max	Maximum value
out	Outlet
ref	Reference condition at sea level
<i>s</i>	Surface
st	Standard air condition
<i>v</i>	Water vapor
<i>w</i>	Water
ϕ	Air (<i>a</i>) or water (<i>w</i>)

1 Introduction

Generally, published ratings of HVAC&R equipments are usually presented in manufacturer catalogs for standard air conditions. The adopted reference condition enables the comparison of the performance of equipments from different manufacturers, but a fundamental understanding about the effect of the atmospheric pressure on the performance of HVAC&R components is still important to avoid errors and troubleshoot problems when sizing equipment. It is very important to avoid equipment needlessly oversized, or worse, or undersized.

Open solid desiccant systems are a promising technology for air dehumidification and cooling applications. The performance of the individual components depends on altitude mainly through its influence on atmospheric pressure, affecting the density of the air and convective transfer coefficients between the airflows and the heat and/or mass exchangers. Although manufacturers present the specifications of the individual components in a technical catalog for standard conditions at sea level operation, the specifications can also be determined for a particular operation when selection software is available. Manufacturers of desiccant wheels have developed methods for restating performance, but some doubts still remain on the validation of such approaches, since most of the existing laboratories are not prepared to vary the ambient atmospheric pressure.

Detailed simulations of open solid desiccant systems can account for the effect of altitude through air properties. Many simulations of desiccant systems integrating a desiccant wheel have been conducted, using several methods and assuming different simplified treatments of the airflow and the porous channel wall domains of the desiccant matrix [1–11], but the majority considers sea level pressure.

The effect of altitude on the performance of the ventilation cycle desiccant cooling system was investigated by Pesaran and Heiden [1]. They investigated the behavior of the main components of the system for decreasing atmospheric pressure from 101,325 to 81,060 Pa. For either fixed-mass airflow rate or fixed-volume airflow rate operations, a decrease in the performance of the desiccant wheel and an increase in the coefficient of thermal performance were observed. The cooling capacity of the system presented a decrease of 14 % and an increase of 9 % when the system is operated with fixed-volume and fixed-mass airflow rates, respectively.

A numerical model accounting for the heat and mass transfer phenomena in the hygroscopic matrix was used by Ruivo et al. [12, 13] to derive correction factors for the mass and heat transfer rates in a desiccant wheel, when changing from sea level atmospheric pressure to locations with a pressure of 60,000 Pa. Both studies also concluded that those correction factors depend on the airflow rate/length ratio.

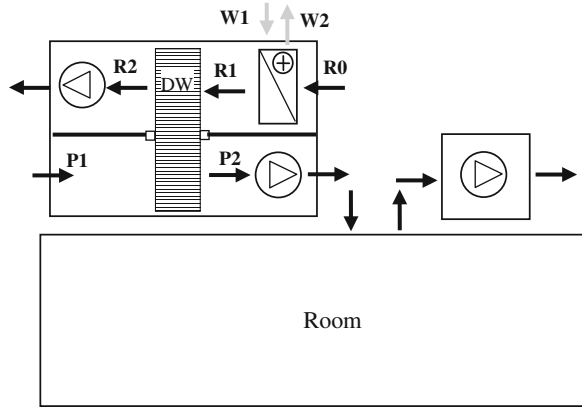
The present study is focussed on predicting the performance of a simple solid dehumidification system at different elevations by the analysis of the processes affected by altitude in each component, a subject with practical relevance as recognized by the ASHRAE Technical Committee TC 8.12 (call for proposals for the research project 1339-TRP, "Selection of Desiccant Equipment at Altitude," 2009).

The main components of the handling air unit investigated are the heating coil and the desiccant wheel. The heat required for the wheel regeneration is supplied by a hot water system (e.g., boiler, solar collector, or waste heat recovery systems). The analysis of this system is out of the scope of the present work. The heating coil performance is predicted by the ε -NTU method, using manufacturer data to evaluate the overall thermal resistance of the actual heat exchanger. The desiccant wheel performance is predicted by the detailed numerical model also used in previous works [12, 13]. The range of altitude considered in the study covers locations from sea level to locations with an atmospheric pressure of 60,000 Pa.

2 Problem Formulation

The open solid desiccant dehumidification system analyzed in the present work is depicted in Fig. 1, although other configurations exist, even with better performance. It is a single air-conditioned zone in which the air-handling unit (AHU) is composed by two fans, a desiccant wheel, and a heating coil. The required air filters are not represented. The supply air, usually called process air in desiccant systems, is fresh air as well as the regeneration air. Both airflow rates are assumed to be constant independently of the latent thermal load of the zone. The desiccant system is used to control the indoor air humidity. The sensible load is controlled by a parallel cooling system, not represented in Fig. 1. The exhaust air is removed from the room by an independent fan.

Fig. 1 Scheme of a simple air dehumidification system



According to the purposes of the present work, the system analysis requires a model that describes well the influence of the altitude on the behaviors of the heating coil and of the desiccant wheel. The influence of altitude on the fan performance can be assessed from the characteristic curves at standard air density, by applying the principles of dimensional analysis (fan laws). Two examples of cities with different elevations are Lisbon–Portugal (altitude 0 m) and La Paz–Bolivia (altitude 4,000 m).

2.1 Moist Air at Altitude

Moist air is a mixture of dry air and water vapor. When dealing with open solid desiccant systems, ideal gas behavior for the dry air and for the vapor can be assumed. The effect of altitude on the performance of the dehumidification system results from the variation in the air properties with atmospheric pressure.

The influence of the altitude H on the atmospheric pressure can be estimated by [14]:

$$P = P_{ref} (1.0 - 2.25577 \times 10^{-5} H)^{5.25588}, \tag{1}$$

where $P_{ref} = 101,325$ Pa is the atmospheric pressure at sea level, a value that applies to Lisbon. For La Paz, the atmospheric pressure is estimated to be 61,640 Pa. Besides this, the air properties are also affected by temperature and humidity. For the analysis of the AHU of Fig. 1, the variations observed in the weather conditions dictate the inlet conditions of both airflows. The air states in the different sections of the AHU are not equal due to the processes themselves, and they also vary due to the control strategy. When the AHU is operating with constant airflow rates, the regeneration air temperature will change significantly from peak-load to partial-load operations. The influence of changes on the air

states must be also considered on the correction of the air properties for sizing and simulation purposes.

The water vapor content or humidity ratio can be calculated through:

$$w_v = \frac{m_v}{m_a} = \frac{R_a}{R_v} \frac{P_v}{P - P_v} \quad (2)$$

where m_v and m_a are the masses of water vapor and of dry air and P_v is the partial pressure of water vapor in the moist air. The parameters R_a and R_v are the gas constant of air and water vapor, respectively ($R_a = 287 \text{ J Kg}^{-1} \text{ }^\circ\text{C}$, $R_v = 461.5 \text{ J Kg}^{-1} \text{ }^\circ\text{C}$).

The water vapor mass fraction is given by:

$$\varphi_v = \frac{m_v}{m_a + m_v} = \frac{w_v}{1 + w_v} \quad (3)$$

The relative humidity is defined by:

$$\psi^* = \left. \frac{P_v}{P_{vs}} \right|_{T,P} \quad (4)$$

the saturation pressure of water vapor P_{vs} being a function of temperature. According to this definition, the mathematical domain of temperature T ($^\circ\text{C}$) is $[-273.15, T_{\text{sat}}]$, where the water saturation temperature T_{sat} depends on the atmospheric pressure of the location. So, when dealing with desiccant dehumidification systems, it is important to mention that this concept of relative humidity must not be used when the air temperature is higher than the water saturation temperature for the given atmospheric pressure P . The following parameter must be used instead:

$$\psi = \left. \frac{P_v}{P_{vs}} \right|_T, \quad (5)$$

thus ensuring consistency of concepts. Moreover, when dealing with desiccants, the sorption isotherm must be written with ψ and not in terms of relative humidity ψ^* .

The specific volume of the moist air, $v^* = V/(m_v + m_a)$, can be estimated by:

$$v^* = \left[\frac{1}{T + 273.15} \left(\frac{P - P_v}{R_a} + \frac{P_v}{R_v} \right) \right]^{-1} \quad (6)$$

The specific volume of moist air referred to the unity of dry air mass ($v = V/m_a$) can be estimated by:

$$v = \left[\frac{P - P_v}{R_a(T + 273.15)} \right]^{-1} \quad (7)$$

The inverse of the specific volume, $\rho_a = 1/v$, is usually defined as dry air density that corresponds strictly to the concentration of dry air in the moist air. By convenience, it is normally used in psychrometric calculations and mass and

energy balances in HVAC&R systems on the basis of dry air mass flow rates, instead of using the inversed value of v^* .

A misleading concept is related to the airflow rate values used to characterize the behavior of HVAC&R equipments. Usually, the performance data of heating coils and of desiccant wheels are presented in the technical catalogs for volume airflow rates, $\dot{V}_{a,st}$, assuming a standard air density value $\rho_{a,st} = 1.2 \text{ kg m}^{-3}$.

The actual dry mass airflow rate is calculated by $\dot{m}_a = \rho_{a,st} \dot{V}_{a,st}$. The actual-volume airflow rates at the inlet and outlet of the device are calculated by $\dot{V}_{a,in} = \rho_{a,st} \dot{V}_{a,st} / \rho_{a,in}$ and $\dot{V}_{a,out} = \rho_{a,st} \dot{V}_{a,st} / \rho_{a,out}$, respectively. When an air state is characterized by P , T , and w_v , the dry air density can be estimated by:

$$\rho_a = \frac{P}{R_a(T + 273.15)} \left(1 - \frac{R_v w_v}{R_a + R_v w_v} \right) \quad (8)$$

If the particular state is defined by P , T , and ψ , the following relationship must be adopted:

$$\rho_a = \frac{P - \psi P_{vs}}{R_a(T + 273.15)}. \quad (9)$$

Both Eqs. (8) and (9) are derived from Eq. (7), the partial pressure of vapor P_v being obtained after Eqs. (2) and (5), respectively. The standard density $\rho_{a,st} = 1.2 \text{ kg m}^{-3}$ for fully dry air and for fully saturated air, at sea level, corresponds to states with the temperature of 21 and 15.8 °C, respectively. The ratio of the density at a certain altitude, ρ_a , to the density at sea level, $\rho_{a,ref}$, is an important parameter to characterize the dependence of the AHU equipment performance on the atmospheric pressure. When altitude changes, but T and ψ do not, the density ratio is given by:

$$\sigma_\psi = \frac{\rho_a}{\rho_{a,ref}} = \frac{P - \psi P_{vs}}{P_{ref} - \psi P_{vs}}. \quad (10)$$

If the values of T and w_v do not change, the density ratio is given by $\sigma_w = P/P_{ref}$, P_{ref} being the pressure at sea level. In the present application, system depicted in Fig. 1, and also in most of the HVAC&R applications, it can be considered that $\sigma_w \approx \sigma_\psi$ because the partial pressure of the water vapor ($P_v = \psi P_{vs}$) is much lower than the atmospheric values P_{ref} and P . So, it can be accepted that $\sigma_w \approx \sigma_\psi$.

The properties of dry air and of water vapor, such as dynamic viscosity, thermal conductivity, and specific heat, are assumed to be independent of the atmospheric pressure, as well as the Prandtl and Schmidt numbers. So, those properties of the moist air are also independent of the pressure for a given value of w_v . In fact, the water vapor content influences the air properties, but in most applications, such influence is negligible due to the low values of the water vapor mass fraction.

2.2 Heat and Mass Convective Phenomena at Altitude

The heat and mass convective fluxes between a surface and airflow can be expressed as follows:

$$j_h = h_h(T_s - T_f) \quad (11)$$

$$j_m = \rho_f h_m (\varphi_{v,s} - \varphi_{v,f}) \quad (12)$$

where T_s and T_f are the surface and air temperatures, respectively. The variables $\varphi_{v,s}$ and $\varphi_{v,f}$ represent the mass fractions of the water vapor at the surface and in the airflow, respectively. The air density used in Eq. (12) corresponds to $\rho_f = 1/v^*$.

When both surface and bulk air states are specified by the pairs (T_s, ψ_s) and (T_f, ψ_f) , an increase in pressure with altitude results for both mass fractions $\varphi_{v,s}$ and $\varphi_{v,f}$, which, however, do not vary if those air states are defined by T and w_v . For instance, in case of an air–water system similar to a swimming pool with controlled water temperature, as well as the air temperature and relative humidity, the decrease in pressure with altitude leads to an increase in the driving potential for mass transfer $(\varphi_{v,s} - \varphi_{v,f})$.

Regarding evaporative cooling, Pesaran and Heiden [1] and Qureshi and Zubair [15] describe that the process performance is improved at higher altitudes, which is related also to an increase in the driving potential for the mass transfer. In case of desiccant wheels, the analysis is more complex and could be made by detailed numerical modeling. According to the investigation by Ruivo et al. [12, 13], a reduction in the moisture removal capacity is observed for lower atmospheric pressures, fixed-mass airflow rates, and both inlet air states specified by T and w_v .

The convective heat and mass transfer coefficients are represented by h_h and h_m , respectively. They can be determined through Nusselt and Sherwood numbers:

$$\text{Nu} = \frac{h_h d_h}{\lambda_f} \quad (13)$$

$$\text{Sh} = \frac{h_m d_h}{D_f} \quad (14)$$

where d_h is a characteristic dimension that for an internal flow that usually assumes the meaning of the hydraulic diameter, λ_f is the moist air thermal conductivity and D_f is the diffusion coefficient of water vapor in the moist air.

For fully developed laminar flow, Nu and Sh are constants, and moreover, they are independent of pressure, an assumption taken into account in the simulations of desiccant wheels by Ruivo et al. [12, 13]. When modeling the behavior of a desiccant wheel, the convective coefficients in the adsorption and desorption processes are different, mainly due to the influence of temperature on the properties, such as the thermal conductivity, diffusion coefficients. Regarding the

influence of pressure, the coefficient h_m is affected but not the product $\rho_f h_m$ (mass transfer conductance), which is effectively used in the calculation of the convective mass flux [see Eq. (12)].

For internal turbulent flows, Nu can be estimated by a correlation in the form:

$$\text{Nu} = a \text{Re}^b \text{Pr}^c \quad (15)$$

where Re and Pr are the Reynolds and Prandtl numbers. Fixing the airflow velocity, Nu is affected by altitude as a result of the dependence of Re on the air density. A useful relation to determine Sherwood number is the Chilton–Colburn analogy:

$$\text{Sh} = \text{Nu} \text{Le}^{1/3} \quad (16)$$

the Lewis number being defined by

$$\text{Le} = \lambda_f / (\rho_f c_{pf}^* D_f) \quad (17)$$

The specific heat of the moist air is calculated by $c_{pf}^* = \varphi_v c_{pv} + (1 - \varphi_v) c_{pa}$, where c_{pv} and c_{pa} are the specific heat at constant pressure of the water vapor and of the dry air, respectively.

The well-known correlations for Nu are difficult to apply with accuracy in real cases due to (1) considerable uncertainties involved in the correlations, (2) lack of details about the geometry of the exchanger to select and apply an appropriate correlation, and (3) limited applicability of the correlations, in general developed for constant surface temperature or constant heat flux, and neglecting entrance effects. In spite of the practical limitations, the known correlations give important guidelines to develop simplified procedures instead of using CFD detailed and complex models.

In water–air heating coils, the heat transfer coefficient on the gas side is usually much lower than on the liquid side, and the thermal resistance of the solid wall is negligible. One of the methods to analyze the performance of heat exchangers is the ε -NTU method, based on effectiveness relations that have been developed for different types of heat exchangers and flow arrangements. Typically, actual heating coils are cross-flow heat exchangers of finned tube surfaces, with both fluids assumed unmixed. To assess the effect of altitude on the effectiveness, it is necessary to account for the variations in the gas-side convective heat coefficient with atmospheric pressure, by way of appropriate empirical correlations, and their influence on the NTU value. This approach was not considered by Pesaran and Heiden [1]; for system simulation, they assumed that the heating capacity is not affected by ambient pressure, which is strictly valid only for an electric heater, but not for a conventional water–air heat exchanger with unchanged inlet flow conditions.

The next section will address the analysis of the influence of atmospheric pressure on the thermal performance of a real heating coil, based on an approach that accounts for some manufacturer data.

2.3 Heating Coil at Altitude

The heating coil considered in the present work is a water–air heat exchanger type 3 to equip the KG Top 43 AHU of the manufacturer [16]. Like in most manufacturer catalogs, the values of the thermal resistance between hot and cold fluid are not indicated and likewise the geometric details of the device that are required to select and apply appropriate empirical correlations. To overcome this difficulty, the heating capacity table given by the manufacturer is used to derive specific correlations to estimate the gas-side and liquid-side thermal resistances, in the form of:

$$R_\phi = R_{\phi,\text{ref}} \left(\frac{\dot{m}_{\phi,\text{ref}}}{\dot{m}_\phi} \right)^{n_\phi}, \quad (18)$$

where the variables \dot{m}_ϕ represent the actual mass flow rate of the fluid ϕ ($\phi = w$: water; $\phi = a$: air). The thermal resistance $R_{\phi,\text{ref}}$ is associated with fluid ϕ at a very high airflow rate $\dot{m}_{\phi,\text{ref}}$ in the operating range of the published data in the manufacturer catalog. The actual mass flow rates relate to volume flow rates by $\dot{m}_\phi = \rho_\phi \dot{V}_\phi$. For the reference case, similar relationships apply $\dot{m}_{\phi,\text{ref}} = \rho_{\phi,\text{ref}} \dot{V}_{\phi,\text{ref}}$, $\dot{V}_{\phi,\text{ref}}$ being a standard value of the volume flow rate. Regarding the densities, the adopted values are $\rho_{w,\text{ref}} = \rho_{w,\text{st}} = 1,000 \text{ kg m}^{-3}$ and $\rho_{a,\text{ref}} = \rho_{a,\text{st}} = 1.2 \text{ kg m}^{-3}$. It should be noted that \dot{m}_a and $\dot{m}_{a,\text{ref}}$ represent dry air mass flow rates. The correlations given by Eq. (18) can be used after the determination of $R_{\phi,\text{ref}}$ and n_ϕ values. For that purpose, a simple approach is presented by combining theory and manufacturer data.

The overall thermal resistance of the heating coil relates with the overall heat transfer coefficient by $R = 1/(U \times A)$ and is estimated by $R = R_a + R_w$. It is assumed that the performance of the finned tube surface is included on the R value. This result enables the calculation of the number of transfer units by:

$$\text{NTU} = (R \times C_{\min})^{-1}, \quad (19)$$

without requiring the knowledge of the heat transfer areas on the gas and the liquid sides. The heat capacity rate of each fluid is defined by $C_\phi = \rho_\phi \dot{V}_\phi c_{p,\phi}$, where $c_{p,\phi}$ represents the specific heat at constant pressure. The minimum and maximum values of the heat capacity rates are used to define the capacity ratio $\text{CR} = C_{\min}/C_{\max}$.

The inlet and the outlet temperatures of the water flow are, respectively, $T_{w,\text{in}}$ (point W1 in Fig. 1) and $T_{w,\text{out}}$ (point W2) and correspondingly for the air flow: $T_{a,\text{in}}$ (point R0) and $T_{a,\text{out}}$ (point R1). The heat exchanger effectiveness is defined by:

$$\varepsilon = \frac{C_a(T_{a,\text{out}} - T_{a,\text{in}})}{C_{\min}(T_{w,\text{in}} - T_{a,\text{in}})}. \quad (20)$$

The effectiveness relation for cross-flow heat exchanger with both fluids unmixed, assuming a single pass of each flow [17], is:

$$\varepsilon = 1 - \exp\left(\frac{1}{CR} \text{NTU}^{0.22} (\exp(-CR \times \text{NTU}^{0.78}) - 1)\right). \quad (21)$$

The heating capacity of the heating coil can be estimated by one of the balance equations:

$$\dot{Q} = C_a(T_{a,\text{out}} - T_{a,\text{in}}) \quad (22.a)$$

$$\dot{Q} = C_w(T_{w,\text{in}} - T_{w,\text{out}}). \quad (22.b)$$

Alternatively, it can be predicted through the $\varepsilon - \text{NTU}$ method:

$$\dot{Q} = \varepsilon C_{\min}(T_{w,\text{in}} - T_{a,\text{in}}) \quad (23)$$

or by the log mean temperature difference (LMTD) method:

$$\dot{Q} = \frac{F}{R} \Delta T_{\text{lm,cf}} = \frac{F}{R} \frac{(T_{w,\text{in}} - T_{a,\text{out}}) - (T_{w,\text{out}} - T_{a,\text{in}})}{\ln\left(\frac{T_{w,\text{in}} - T_{a,\text{out}}}{T_{w,\text{out}} - T_{a,\text{in}}}\right)}. \quad (24)$$

where $\Delta T_{\text{lm,cf}}$ is the LMTD for a counter-flow heat exchanger and F is the correction factor for the actual exchanger configuration.

The parameters $R_{\phi,\text{ref}}$ and n_ϕ of Eq. (18) are estimated by a step by step procedure supported by the small set of operating conditions represented in Table 1, taken from the manufacturer catalog [16] for $T_{a,\text{in}} = 20^\circ\text{C}$ and sea level conditions. The cross-sectional area of the heating coil is estimated to be approximately 0.37 m^2 .

For each operating case listed in Table 1, $T_{c,\text{out}}$ and \dot{m}_h are calculated, in a first step, by the energy balance equations, Eqs. (22.a) and (22.b). The mass flow rate of dry air is calculated by $\dot{m}_a = \rho_{a,\text{st}} \dot{V}_{a,\text{st}}$. With the value of C_{\min} , the effectiveness is calculated by Eq. (20). Then, the number of transfer units NTU is iteratively calculated by using Eq. (21).

In a second step, $\Delta T_{\text{lm,cf}}$ is calculated for counter-flow exchanger, which is the reference configuration when using the LMDT method ($F = 1$). The overall thermal resistance of the counter-flow exchanger is calculated by $R_{\text{cf}} = \Delta T_{\text{lm,cf}} / \dot{Q}$ to predict the number of transfer units NTU_{cf} by using Eq. (19).

Finally, the overall thermal resistance of the actual cross-flow exchanger is calculated just by $R = R_{\text{cf}} \text{NTU}_{\text{cf}} / \text{NTU}$. This step procedure was applied to the 20 cases listed in Table 1. In each case, the overall thermal resistance R should be equal to $R^* = R_a + R_w$, with R_a and R_w estimated by Eq. (18). The assessment of the variables $R_{\phi,\text{ref}}$ and n_ϕ was performed by a trial-and-error procedure by testing different values of $R_{\phi,\text{ref}}$ and n_ϕ and checking the fitting between R and R^* . According to the data of the particular coil in Table 1, the chosen reference airflow rates were $\dot{m}_{a,\text{ref}} = 1.44 \text{ kg s}^{-1}$ and $\dot{m}_{w,\text{ref}} = 2.78 \text{ kg s}^{-1}$ ($\dot{V}_{a,\text{ref}} = 4,300 \text{ m}^3 \text{ h}^{-1}$

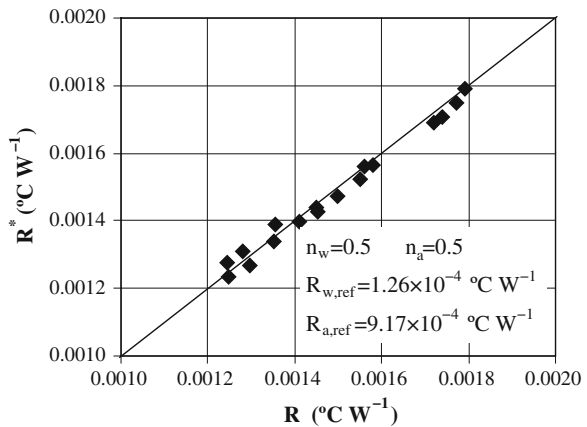
Table 1 Manufacturer data of the heating coil [16] ($\rho_{a,st} = 1.2 \text{ kg m}^{-3}$)

$T_{w,in} \text{ (}^\circ\text{C)}$	$T_{w,out} \text{ (}^\circ\text{C)}$	$\dot{V}_{a,st} \text{ (m}^3\text{h}^{-1}\text{)}$	$\dot{Q} \text{ (W)}$
80	50	2,000	15,200
		2,700	18,200
		3,300	20,800
		4,000	23,100
		4,300	24,000
80	60	2,000	18,500
		2,700	22,200
		3,300	25,600
		4,000	28,700
		4,300	29,800
90	70	2,000	22,600
		2,700	27,300
		3,300	31,500
		4,000	35,300
		4,300	36,800
110	90	2,000	30,600
		2,700	37,200
		3,300	43,100
		4,000	48,400
		4,300	50,500

and $\dot{V}_{w,ref} = 10 \text{ m}^3 \text{ h}^{-1}$). After a few tests, a good agreement was achieved as it is illustrated in Fig. 2 when using $R_{w,ref} = 1.26 \times 10^{-4}$, $R_{a,ref} = 9.17 \times 10^{-4} \text{ }^\circ\text{C W}^{-1}$, and $n_w = n_a = 0.5$. As expected, the thermal resistance on the air side is greater than that on the water side: For the set of cases considered in the analysis, the minimum, average, and maximum values of the ratio R_a/R are, respectively, 0.656, 0.735, and 0.795.

In spite of the good agreement observed between R and R^* , the validity of the correlations expressed by the Eq. (18) was also investigated for all the 128 distinct

Fig. 2 Comparison between thermal resistances R and R^*



operating cases listed by the technical catalog of a manufacturer [16]. The tested cases lie in the following range of values: $T_{a,in}$ from -15 to 20 °C; $T_{w,in}$ from 45 to 110 °C; \dot{V}_w from 0.425 to 3.42 m³ h⁻¹; and \dot{V}_a from $2,000$ to $4,300$ m³ h⁻¹. The comparison between the heating coil capacity given by the manufacturer, \dot{Q} , and the capacity predicted by the proposed methodology, \dot{Q}^* , is depicted in Fig. 3. An acceptable agreement is observed between both variables. The maximum deviation between \dot{Q} and \dot{Q}^* is of $2,190$ W, and the RMSD value is 730 W. An excellent agreement is observed for $\dot{Q} < 40,000$ W. The agreement in the other range ($\dot{Q} > 40,000$ W) could be improved by adopting a linear correction as Fig. 3 suggests.

If the selection software of the manufacturer was available, another set of tests could be done by considering operating conditions at high altitude as well as with a greater value of the heating coil capacity to obtain an outlet air temperature greater than 100 °C. Nevertheless, the agreement observed in the results of the test conducted at sea level conditions shows that the simple approach, also used in Sect. 2.5, is promising.

To investigate the influence of the atmospheric pressure on the performance of the heating coil represented in Fig. 1, the simple approach is extended to operating cases with $\dot{V}_w = 1.85$ m³ h⁻¹, $T_{w,in} = 110$ °C, and $T_{a,in} = 20$ °C. The actual-volume airflow rates at the inlet of the heating coil range from $2,000$ to $4,300$ m³ h⁻¹, the maximum value adopted as a reference value for volume airflow rate ($\dot{V}_{a,ref} = 4,300$ m³ h⁻¹). The air density given by Eq. (9) was used to convert the volume airflow rate into dry air mass flow rate, adopting $\psi_{a,in}^* = 0.4$.

The predicted results showing the dependence of the effectiveness and of the heating capacity of the coil on the atmospheric pressure are presented, respectively, in Figs. 4 and 5.

Increases in the effectiveness of 15 and 33 % are observed when the atmospheric pressure drops from $101,325$ to $80,000$ Pa and to $60,000$ Pa, respectively. In spite of the increase in effectiveness, the heating capacity decreases 10 % when changing

Fig. 3 Comparison between the heating coil capacity \dot{Q} and \dot{Q}^*

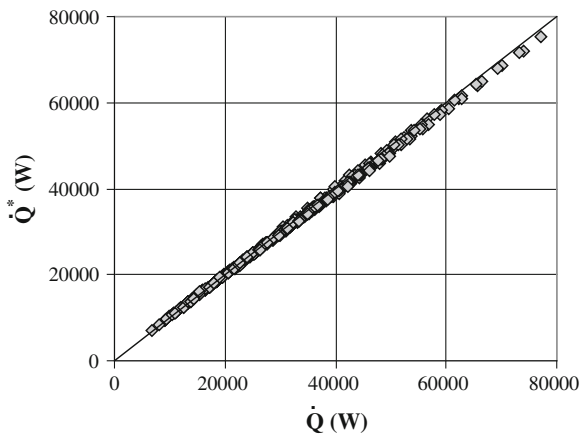


Fig. 4 Influence of the atmospheric pressure on the heating coil effectiveness

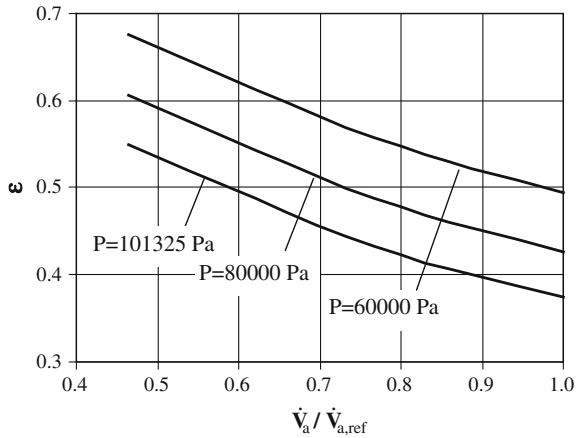
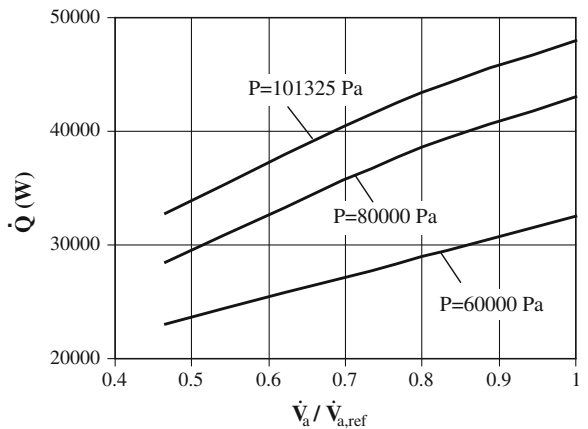


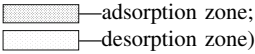
Fig. 5 Influence of the atmospheric pressure on the coil heating capacity



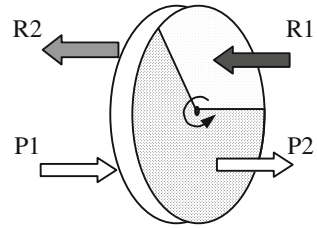
from 101,325 to 80,000 Pa and 28 % when changing from 101,325 to 60,000 Pa. So, this set of results demonstrates the importance of correcting the performance data usually available for sea level conditions. Assuming that a 5 % decrease in the heating capacity is a quite negligible value, it comes out that when the atmospheric pressure is higher than 90,000 Pa, no need of correction is required.

2.4 Desiccant Wheel at Altitude

A desiccant wheel is a rotating hygroscopic matrix submitted to a cyclic sequence of adsorption and desorption of water molecules in order to promote the air dehumidification of the process airflow (P). Heat and mass convection on the gas side, as well as heat and mass diffusion and water sorption on the solid side, are the

Fig. 6 Desiccant wheel (


 —adsorption zone;
 —desorption zone)



main important phenomena occurring in a desiccant wheel. The rotation speed is relatively low, and a hot airflow (R) is used to regenerate the matrix. The most simple desiccant wheel configuration is illustrated in Fig. 6. Process and regeneration airflows pass through the matrix in a counter-current configuration. The desorption zone is generally smaller than the adsorption zone in systems operating with relatively high regeneration temperature. The psychrometric evolutions of the process and regeneration airflows are sketched in Fig. 7.

The equilibrium relationship between water vapor present in the moist air and the desiccant at equilibrium is usually presented by a function, $X_\ell = f(\psi)$, relating the adsorbed water content in the desiccant X_ℓ to the ratio of water vapor pressures ψ in the moist air. The relation depicted in Fig. 8 by the functions $X_\ell = f(\psi)$ and $X_\ell = g(T, w_v)$ applies to the silica gel RD and has been used in detailed numerical modeling of the heat and mass transfer phenomena in hygroscopic matrices [9, 10, 12, 13].

The equilibrium relationship is not affected by altitude when it is represented by the sorption isotherm, function $X_\ell = f(\psi)$ shown in Fig. 8a. The inlet states of both airflows dictate the minimum and maximum theoretical values of the adsorbed water content in the desiccant, $X_{\ell, \min}$ and $X_{\ell, \max}$, respectively. These values can be used to define the corresponding isolines of maximum and minimum values of the ratio ψ in the psychrometric chart (see Fig. 7). The difference between the maximum and minimum values of the adsorbed water content, $X_{\ell, \max}$ and $X_{\ell, \min}$, is related to the theoretical maximum sorption capacity of the desiccant matrix,

Fig. 7 Typical psychrometric evolutions of the process and regeneration airflows in a desiccant wheel

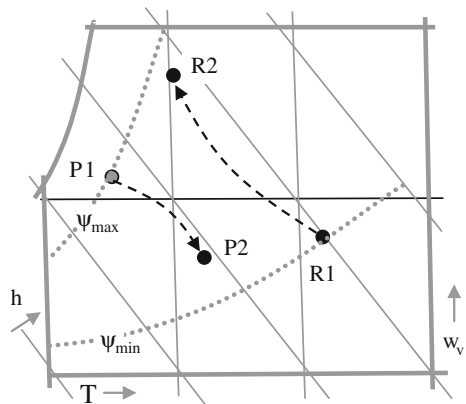
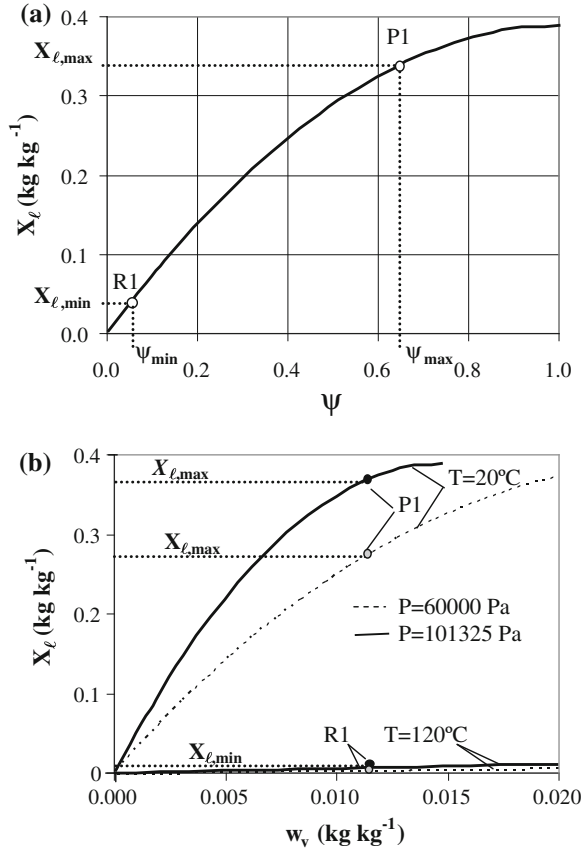


Fig. 8 Sorption equilibrium for silica gel RD: **a** $X_\ell = f(\psi)$ and **b** $X_\ell = g(T, w_v)$



which is not affected by atmospheric pressure changes when the inlet states of both airflows are specified by the pair (T, ψ) . On the contrary, when the inlet states are specified by the pair (T, w_v) , the theoretical maximum sorption capacity decreases with altitude, as illustrated in Fig. 8b, mainly due to the reduction verified on the $X_{\ell, \max}$. This reduction corroborates the decreasing in the predicted removal moisture capacity of desiccant wheel with increasing altitude [12, 13].

The moisture removal capacity of the desiccant wheel of the AHU represented in Fig 1 can exhibit significant time variations according to the load profile and weather conditions, a fact that must be taken into account at the design stage. Several capacity control alternatives can be adopted: (1) modulation of fans, (2) bypass of the process airflow or of the regeneration airflow, (3) modulation of the heating capacity of the heating coil, or (4) modulation of the rotation speed of the wheel. The modulation of fans is generally the strategy leading to better energy efficiency.

Different numerical modeling methods of solution have been used to predict the performance of desiccant wheels. One crucial aspect when using detailed numerical methods is the characterization of the hygroscopic matrix, namely the

knowledge of its thermal properties, diffusion coefficients, phase equilibrium laws, hysteresis effects. The validation of numerical models by comparison with accurate experimental data, which should necessarily cover a wide range of operating conditions, is missing and is a difficult task. In fact, some extensive experimental researches show significant mass and energy imbalances between the regeneration and the process air streams [3].

The application of the so-called effectiveness method to estimate the performance of the desiccant wheel represented in Fig. 6 requires two effectiveness independent parameters. One of the pairs that has been more used is the classical pair, (η_{F1}, η_{F2}) , based on the combined potentials or characteristic potentials $F1$ and $F2$ [18]. A more intuitive pair (η_ψ, η_h) based on the variations in the ratio ψ and of the specific enthalpy of moist air h was investigated in recent works [19]. The methods based on the effectiveness concept are simple and suitable to be integrated in dynamic simulation programs of air-conditioning systems, since appropriate correlations or calculation procedures are available. Some studies addressing specifically the characterization of the dependence of the effectiveness parameters on the operating conditions of a desiccant wheel have been conducted [20, 21]. Although considering different definitions of the effectiveness parameters, those studies are not as exhaustive as they should be regarding the range of the operating conditions. The recent investigation conducted by Ruivo et al. [19] demonstrated that important errors can result when constant values of the effectiveness parameters are assumed in the effectiveness method. So, the influence of the altitude on the behavior of the desiccant wheel is investigated by numerical modeling [9, 10, 12, 13]. A parametric study is conducted considering a desiccant matrix with the desiccant properties of silica gel RD, the B4-type cell, specific transfer area of $2,980 \text{ m}^2 \text{ m}^{-3}$, and porosity of 0.627 [10]. No purge sector is considered. The channel length of the matrix is 200 mm. The fractional frontal area of the regeneration sector is 33 % of total area. It is assumed that the effective cross-section of desorption sector has the same cross-sectional area of the heating coil, for which the estimated value is 0.37 m^2 . So, the effective cross-section of adsorption sector is approximately 0.7512 m^2 due to the assumed matrix split 67:33.

For fixed-volume airflow rate operation (FV), the face velocity of both airflows at the inlet of the matrix channels is assumed to be 2 m s^{-1} . For fixed-mass airflow rate operation (FM), a mass velocity of $1.8 \text{ kg s}^{-1} \text{ m}^{-2}$ for both airflows is imposed. Two modes of fixing the inlet states of both airflows are considered. The specifications in mode A are $T_{P1} = 30 \text{ }^\circ\text{C}$, $T_{R1} = 100 \text{ }^\circ\text{C}$, and $w_{v,P1} = w_{v,R1} = 0.010 \text{ kg kg}^{-1}$ and in mode B, $T_{P1} = 30 \text{ }^\circ\text{C}$, $T_{R1} = 100 \text{ }^\circ\text{C}$, $\psi_{P1} = 0.35$, and $\psi_{R1} = 0.015$. The atmospheric pressure values considered are 60,000, 70,000, 80,000, 90,000, and 101,325 Pa as well as two rotation speed values, 12 and 24 rpm.

The effect of a pressure decrease on the heat and mass transfer rates can be expressed through correction factors defined as $k_h = \dot{J}_h / \dot{J}_{h,\text{ref}}$ and $k_m = \dot{J}_m / \dot{J}_{m,\text{ref}}$, where \dot{J}_h and \dot{J}_m represent, respectively, the heat and mass transfer rates per unit of transfer area of the matrix at pressure P . At sea level condition, the reference values are represented by $\dot{J}_{h,\text{ref}}$ and $\dot{J}_{m,\text{ref}}$.

Table 2 Reference heat and mass transfer rates per unit of transfer area (sea level)

Operation	Rotation speed (rph)	Mode	$\dot{J}_{h,ref}$ ($W m^{-2}$)	$\dot{J}_{m,ref}$ ($kg s^{-1} m^{-2}$)
Fixed-volume flow rate	12	A	66.2	16.5×10^{-6}
		B	65.1	15.8×10^{-6}
	24	A	73.0	13.3×10^{-6}
		B	72.4	12.7×10^{-6}
Fixed-mass flow rate	12	A	54.6	12.7×10^{-6}
		B	53.7	12.1×10^{-6}
	24	A	59.4	9.2×10^{-6}
		B	61.4	11.8×10^{-6}

The predicted mass and heat transfer rates per unit of transfer area for the set of operating cases at sea level conditions ($P = P_{ref} = 101,325$ Pa) are indicated in Table 2.

The influence of atmospheric pressure on the correction factors is depicted in Fig. 9. It can be seen that the sea level performance data can be adopted directly for different altitudes when the inlet states are specified by mode A with fixed-mass airflow rates (FM-A). In other different situations of fixing the inlet conditions, the direct use of such information without any correction would lead to oversized or undersized equipment. For the operating situations FV-A, FV-B, and FM-B, the corrections required are greater for the mass transfer rate than for the heat transfer rate. When the atmospheric pressure is lower than about 95,000 Pa, the error in using sea level performance data is greater than 5 %.

When fixed-volume airflow rate operation is adopted (FV-A and FV-B), both the mass and heat transfer rates diminish as the atmospheric pressure decreases. This means a risk of undersizing the equipment if the appropriate corrections are not taken into account.

In case of fixed-mass airflow rates with inlet states specified by mode B (FM-B), the mass transfer rate increases significantly with altitude, meaning that a correction is needed to avoid oversizing of the desiccant wheel.

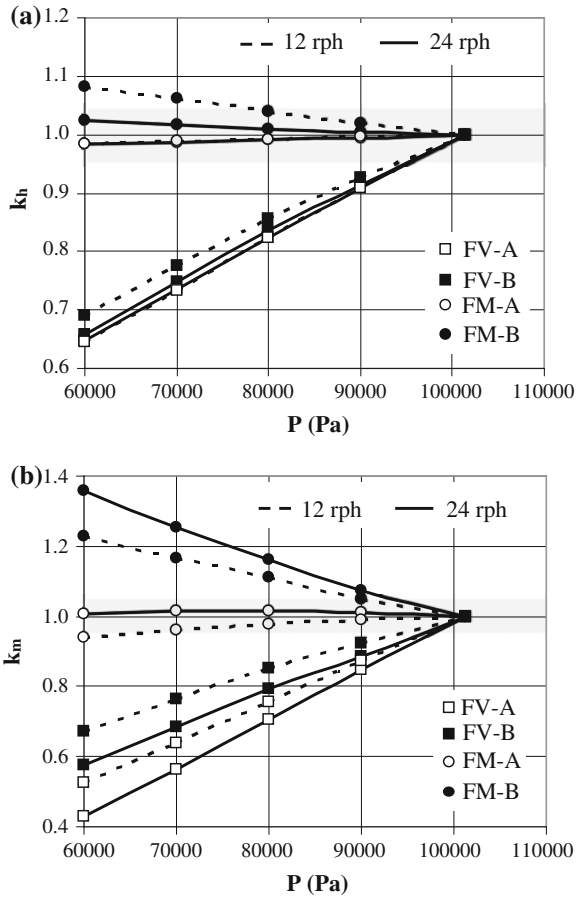
It should be noted that the influence of the rotation speed on the correction factors (k_m and k_h) is generally not negligible as demonstrated by Ruivo et al. [13].

The conclusions drawn in the present section obtained from a limited number of simulations cannot be generalized to other cases. Moreover, the research studies considering fixed-mass airflow rate operation [12, 13] demonstrated that the correction factors depend also on the values of the airflow rates.

2.5 Air-Handling Unit at Altitude

Another parametric study is conducted to investigate the influence of the altitude on the global behavior of the AHU represented in Fig. 1. The considered heating coil and desiccant wheel are those presented in the previous sections. Both airflows

Fig. 9 Correction factors for the performance of the desiccant wheel: **a** k_h and **b** k_m



entering the AHU consist of outside air; therefore, the corresponding inlet states are equal. The atmospheric pressure values considered are 60,000, 80,000, and 101,325 Pa. The same two rotation speed values, 12 and 24 rph, are considered.

The two ways of fixing the inlet air states (points $P1$ and $R0$ in Fig. 1) are assumed: $T_{P1} = T_{R0} = 30\text{ }^\circ\text{C}$ and $w_{v,P1} = w_{v,R0} = 0.010\text{ kg kg}^{-1}$ (mode A), and $T_{P1} = T_{R0} = 30\text{ }^\circ\text{C}$ and $\psi_{P1} = \psi_{R0} = 0.35$ (mode B).

For fixed-volume airflow rate operation, the actual-volume airflow rates of both process and regeneration air streams entering the AHU are assumed to be equal to 2,500 and 5,076 $\text{m}^3\text{ h}^{-1}$, respectively. For fixed-mass airflow rate operation, the dry air mass airflow rates of both process and regeneration air streams are 0.666 and 1.352 kg s^{-1} , respectively.

The assumed inlet hot water conditions in the coil are $\dot{V}_{W1} = 1.85\text{ m}^3\text{ h}^{-1}$ and $T_{W1} = 150\text{ }^\circ\text{C}$. The effect of a pressure decrease on the heating capacity of the coil can also be expressed through a correction factor defined as $k_{\text{coil}} = \dot{Q} / \dot{Q}_{\text{ref}}$, where

\dot{Q}_{ref} is a reference value at sea level condition. The corrections for the heating coil capacity in both modes of specifying the inlet air conditions can be considered equal.

The AHU was simulated by combining the effectiveness method to predict the performance of the heating coil and the detailed numerical model of the desiccant wheel [9, 10, 12, 13]. Twelve operating cases are simulated in this parametric study.

When dealing with fixed-volume airflow rate operation, the mass flow rate of each airflow is calculated by using the actual dry air density at the respective inlet condition at each AHU component. The temperature of the regeneration air is predicted by applying the effectiveness method to the heating coil. The same steps used in the last parametric study of the Sect. 2.3 are followed, namely for the assessment of the overall thermal resistance of the heating coil after Eq. (18). The water vapor content of the regeneration air (point *R1* in Fig. 1) is equal to the outdoor air due to the fact that only sensible heat is transferred by the heating coil to the airflow. Then, with the known inlet conditions of both airflows in the desiccant wheel (states and flow velocities), the detailed numerical model is used to predict the heat and mass transfer rates.

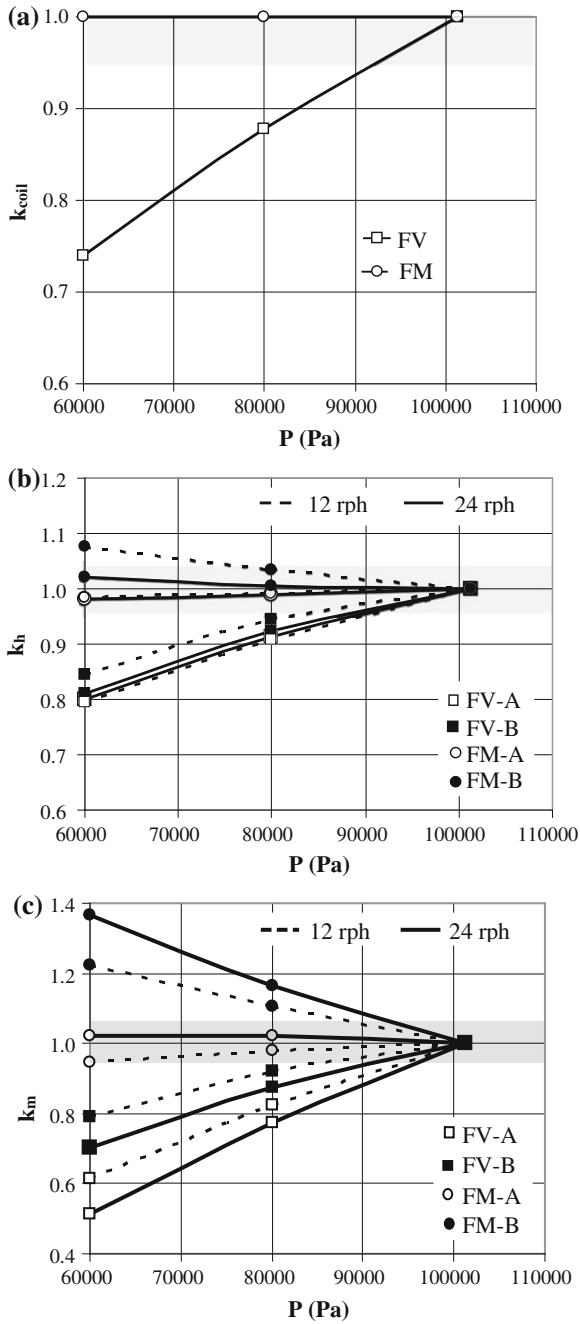
The achieved dependences of the correction factors (k_m and k_h) on the atmospheric pressure are plotted in Fig. 10. It is concluded that the data predicted for sea level can be used for fixed-volume airflow rate operation when the atmospheric pressure is lower than 95,000 Pa (error below 5 %). The correction for mass transfer rate is more important than the correction required for the heat transfer rates in the desiccant wheel and in the heating coil.

Like previously referred in Sect. 2.4, for fixed-mass airflow rate operation with inlet states specified by mode A (FM-A), sea level performance data of the heating coil can be used directly with no need for correction and the same applies to the whole AHU. For mode B (FM-B), a strong increase in the mass transfer rate with altitude is registered.

Comparing Figs. 9b and 10c, it is observed that for fixed-mass airflow rate operation, the same factors k_m and k_h apply to the desiccant wheel and to the AHU. In case of fixed-volume airflow rate, the required corrections for the AHU are smaller than those for the desiccant wheel.

These assessments are valid for the conditions considered in the present study. According to the results of Ruivo et al. [12, 13], additional research work must be carried out. Sea level performance data can be used to predict the performance of the AHU at any elevation since a correction procedure is available. Without any correction of performance of the main components of the AHU, the errors become significant for altitudes above 550 m, approximately, when fixed-volume airflow rate operation is adopted. For fixed-mass airflow rate operation with inlet states specified by T and w_v , the sea level data can be applied with reasonable accuracy for different altitudes, but if the pair (T, ψ) is adopted for the inlet air states, the direct use of sea level data will lead to an oversized installation.

Fig. 10 Correction factors for the performance of the AHU: **a** k_{coil} , **b** k_h and **c** k_m



Exhaustive parametric studies must be carried out to investigate a generic correction procedure to apply to different operating conditions. The use of numerical methods or other simplified methods is important to derive the required correction approach. Moreover, it is also imperative to validate the correction methodology by conducting a large number of experimental tests in an AHU specifically designed for that purpose and equipped with very accurate measurement systems.

3 Conclusions

A research was performed to investigate the influence of altitude on the performance of a simple open solid desiccant system operating as an air dehumidifier. The research involved the use of a detailed numerical model to simulate the behavior of a desiccant wheel and also the effectiveness method to predict the behavior of a heating coil. An innovative approach regarding the estimation of the overall thermal resistance of the heating coil, by using the capacity table presented in the technical catalog of the manufacturer, was presented, tested, and used in the conducted parametric studies. System simulations were performed considering fixed-volume and fixed-mass airflow rate operations at both inlet sections of the AHU and two different modes of specifying the respective air states. The atmospheric pressure ranged from 60,000 to 101,325 Pa. Correction factors for the heat and mass transfer rates were determined to account for the effect of the decreasing atmospheric pressure on the performance of heating coil and of the desiccant wheel as well as on the whole system. The results of the simulations showed that the sea level performance data are valid for altitudes below around 550 m. For greater altitudes and for fixed-volume airflow rate operation, an appropriate correction procedure must be adopted at the design stage of the system to avoid undersizing errors.

The need for correcting the sea level performance data for fixed-mass airflow rate operation depends on the mode of specifying the inlet states of both airflows. The use of a validated correction procedure would help the designers in the selection of equipment at altitude, as recognized by the ASHRAE Technical Committee TC 8.12 (call for proposals for the research project 1339-TRP, "Selection of Desiccant Equipment at Altitude," 2009).

References

1. Pesaran A, Heiden R (1994) The influence of altitude on the performance of desiccant-cooling systems. *Energy* 19:1165–1179
2. Dai Y, Wang H (2001) Parameter analysis to improve rotary desiccant dehumidification using a mathematical model. *Int J Therm Sci* 40:400–408
3. Cejudo J, Moreno R, Carrillo A (2002) Physical and neural network models of a silica gel desiccant wheel. *Energy Build* 34:837–844

4. Niu J, Zhang L (2002) Effects of wall thickness on the heat and moisture transfer in desiccant wheels for air dehumidification and enthalpy recovery. *Int Commun Heat Mass Transf* 29:255–268
5. Zhang L, Niu J (2002) Performance comparisons of desiccant wheels for air dehumidification and enthalpy recovery. *Appl Therm Eng* 22:1347–1367
6. Zhang XJ, Dai YJ, Wang RZ (2003) A simulation study of heat and mass transfer in a honeycomb rotary desiccant dehumidifier. *Appl Therm Eng* 23:989–1003
7. Sphaier L, Worek W (2004) Analysis of heat and mass transfer in porous sorbents used in rotary regenerators. *Appl Therm Eng* 47:3415–3430
8. Sphaier L, Worek W (2006) Comparisons between 2-D and 1-D formulations of heat and mass transfer in rotary regenerators. *Numer Heat Transfer, Part B Appl* 49:223–237
9. Ruivo C, Costa J, Figueiredo A (2007) On the behaviour of hygroscopic wheels: Part I—channel modelling. *Int J Heat Mass Transf* 50:4812–4822
10. Ruivo C, Costa J, Figueiredo A (2007) On the behaviour of hygroscopic wheels: Part II—rotor performance. *Int J Heat Mass Transf* 50:4823–4832
11. Chung J, Lee D, Yoon S (2009) Optimization of desiccant wheel speed and area ratio of regeneration to dehumidification as a function of regeneration temperature. *Sol Energy* 83:625–635
12. Ruivo C, Costa J, Figueiredo A (2011) Influence of the atmospheric pressure on the mass transfer rate of desiccant wheels. *Int J Refrig* 34:707–718
13. Ruivo C, Costa J, Figueiredo A (2011) Numerical study of the influence of the atmospheric pressure on the heat and mass transfer rates of desiccant wheels. *Int J Heat Mass Transf* 54:1331–1339
14. ASHRAE Handbook (2005) Fundamentals Volume, American Society of Heating, Refrigerating and Air-Conditioning, Inc., Atlanta
15. Qureshi B, Zubair S (2006) A comprehensive design and rating study of evaporative coolers and condensers. Part I. Performance evaluation. *Int J Refrig* 29:645–658
16. Wolf technical documentation, Air handling units KG/KGW Top 21-1000, <http://www.wolf-heiztechnik.de/en/pkp/produkte/klimatechnik/kgtop.html>. Accessed on 4 Jul 2012
17. Çengel Y (1998) Heat transfer—a practical approach. McGraw-Hill, New York
18. Stabat P, Marchio D (2008) Heat-and-mass transfers modelled for rotary desiccant dehumidifiers. *Appl Energy* 85:128–142
19. Ruivo C, Carrillo-Andrés A, Costa J, Domínguez-Muñoz F (2012) A new approach to the effectiveness method for the simulation of desiccant wheels with variable inlet states and airflows rates. *Appl Therm Eng* 58:670–678
20. Neti S, Wolfe E (2000) Measurements of effectiveness in a silica gel rotary exchanger. *Appl Therm Eng* 20:309–322
21. Mandegari M, Pahlavanzadeh H (2002) Introduction of a new definition for effectiveness of desiccant wheels. *Energy* 34:797–803
22. Kabeel A (2007) Solar powered air conditioning system using rotary honeycomb desiccant wheel. *Renew Energy* 32:1842–1857

The Performance of Desiccant Wheels for Desiccant Air-Conditioning

Mark Goldsworthy and Stephen White

List of Symbols

A	Desiccant channel area (m^2)
a_f	Friction factor (—)
Bi	Biot number (—)
c	Desiccant layer thickness (m)
c_p	Specific heat capacity ($\text{J kg}^{-1} \text{K}^{-1}$)
COP	Coefficient of performance (—)
D	Channel hydraulic diameter (m)
D_{eff}	Effective moisture diffusivity ($\text{m}^2 \text{s}^{-1}$)
D_K	Knudsen diffusivity ($\text{m}^2 \text{s}^{-1}$)
D_O	Ordinary diffusivity ($\text{m}^2 \text{s}^{-1}$)
DR	Dehumidification rate (—)
f	Fraction of desiccant in matrix (—)
Fo	Fourier number (—)
h	Heat transfer coefficient ($\text{W m}^{-2} \text{K}^{-1}$)
h_m	Mass transfer coefficient ($\text{kg m}^{-2} \text{s}^{-1}$)
H_{ads}	Differential enthalpy of adsorption (J kg^{-1})
H_{vap}	Enthalpy of vaporization (J kg^{-1})
k	Thermal conductivity ($\text{W m}^{-1} \text{K}^{-1}$)
L	Channel length (m)
Le	Lewis number (—)
Le_f	Lewis factor (—)
Nu	Nusselt number (—)
m	Air mass flow rate (kg s^{-1})
MRC	Moisture removal capacity (kg s^{-1})
NTU	Number of transfer units (—)
P	Perimeter (m), pressure (Pa)

M. Goldsworthy (✉) · S. White
Commonwealth Scientific and Industrial Research Organisation, Mayfield West,
Newcastle 2304, Australia
e-mail: mark.goldsworthy@csiro.au

R	Isotherm shape factor (–)
Re	Reynolds number (–)
RH	Relative humidity (%)
RPH	Revolutions per hour
S	Process to total face area ratio
Sh	Sherwood number (–)
T	Time (s)
T	Temperature (K)
u	Air channel velocity (m s^{-1})
W	Desiccant moisture content (kg water/kg desiccant)
x	Channel radial dimension (m)
Y	Air moisture content (kg moisture/kg air)
Z	Channel axial dimension (m)

Greek Letters

α	Thermal diffusivity ($\text{m}^{-2} \text{s}^{-1}$)
δ_c	Concentration boundary layer thickness (m)
δ_t	Thermal boundary layer thickness (m)
ε	Effectiveness (–)
φ	Porosity (–)
η	Dimensionless axial dimension (–)
κ	Dimensionless radial dimension (–)
θ	Dimensionless cycle time (–)
ρ	Density (kg m^{-3})
ζ	Tortuosity factor (–)
τ	Dimensionless time (–)
ω	Rotation rate (RPH)
Υ	Performance parameter (–)
Ω	Cycle rotational time (s)

Subscripts

a	Air
eq	Equilibrium
i	Process or regeneration
in	Inlet
l	Liquid
m	Mass, matrix
max	Maximum
out	Outlet
p	Process side
r	Regeneration side

<i>s</i>	Surface
<i>sat</i>	Saturation
<i>t</i>	Thermal, total
<i>th</i>	Theoretical

1 Introduction

Desiccant wheels are an established technology for removing moisture from an airstream. They are commonly used as either (1) a component of an air-conditioning system providing temperature and humidity control for indoor air quality, or (2) as a dehumidification or drying device for industrial or commercial processes. Here, the focus is on desiccant wheels for air-conditioning applications.

The benefits of desiccant-wheel-based air-conditioning systems include the ability to

1. replace electricity use with ‘free’ solar or waste heat energy, in order to reduce greenhouse gas emissions,
2. reduce peak electricity demand and so minimize electricity network infrastructure costs,
3. obtain better control of humidity and enhance human comfort,
4. reduce mildew and corrosion problems in humid areas,
5. reduce the size and loading of conventional air-conditioning equipment,
6. enable a greater fresh air fraction to be supplied to the building and so minimize ‘sick building syndrome,’
7. reduce the noise level associated with air-conditioning equipment.

The performance of the desiccant wheel is key to realizing these benefits from the complete air-conditioning system.

1.1 Desiccant Wheel Operation

The purpose of a desiccant wheel is to remove moisture from a process airstream. The operating principles of the desiccant wheel are illustrated in Fig. 1.

Process air flows from left to right through channels in the desiccant wheel. A very large number of small (~ 2 mm hydraulic diameter), axially aligned channels are contained in a typical desiccant wheel. The channels are lined with desiccant material which adsorbs moisture out of the passing airstream. The adsorption process releases heat, and as a result, air progressively becomes dryer and hotter as it traverses the channel. Warm dehumidified air exiting the channels is combined and passed on to further downstream processes before entering the building as conditioned supply air.

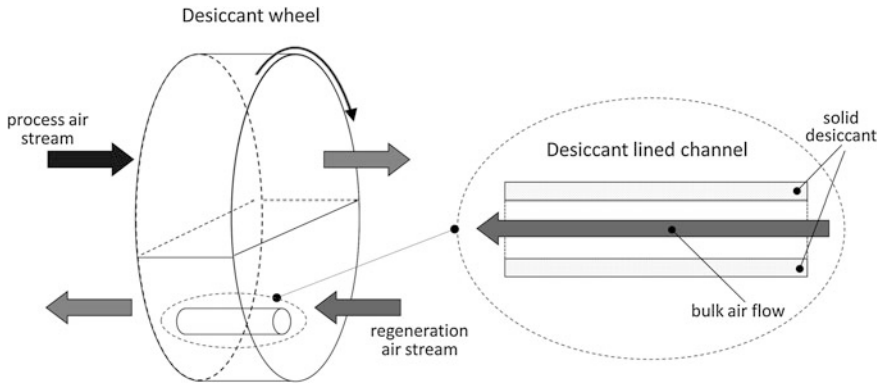


Fig. 1 Schematic of desiccant wheel operation

During the dehumidification process, the desiccant material progressively collects moisture. However, since there is a limit to how much moisture the desiccant material can hold, the rotating desiccant wheel sequentially transfers the channels between the dehumidification zone and a regeneration zone where the desiccant material is dried out. As the channels pass through the regeneration zone, the heated regeneration air flowing from right to left through the channels acts to strip moisture out of the desiccant material. The air flowing through the channels typically has a velocity in the range of 1–5 m/s and so is in the laminar flow regime (Reynolds number ~ 250). The wheel rotates at a comparatively low speed, commonly in the range of 5–50 revolutions per hour (RPH).

The wheel is enclosed in a duct with (1) end seals to prevent air leakage around the wheel and (2) face seals to prevent leakage between the process and regeneration airstreams. The ratio of process air face area to total face area is denoted by S . While Fig. 1 shows a wheel with 50% of the face area being used for dehumidification ($S = 0.5$), other common wheel designs use 75% of the wheel face area for dehumidification. The pressure drop across the wheel is significant (100–200 Pa) and can be arranged such that any air leakage, which might occur between streams, would not cause contamination of the dehumidified process airstream.

The regeneration airstream is typically supplied to the wheel at temperatures between 50 and 140 °C. The potential to use relatively low-temperature (<80 °C) air is particularly attractive for utilizing low-grade heat sources such as engine jacket coolant (in co/trigeneration applications) and hot water from low-cost flat-plate solar collectors.

In air-conditioning applications, a high-performance desiccant wheel should

1. achieve deep dehumidification and, consequently, low building supply air temperatures,
2. require minimal heat for regeneration, leading to high thermal coefficient of performance (COP_r) in the desiccant air-conditioning system and reduced equipment (e.g., solar collector) cost for supplying the regeneration heat,

3. require minimal parasitic electricity to drive the fans and pumps, such that the electrical coefficient of performance (COP_e) of the system is much higher than that of a conventional vapor compression system. Desiccant wheel pressure drop is therefore a key concern.

The characteristics of desiccant-wheel-based air-conditioning systems mean that there is a comparatively small range of operating parameters over which savings can be realized [40]. Hence, it is important to perform detailed system optimization of both COP_e and COP_t [12].

There have been continual efforts to develop improved wheels. More attention has been given to the development of new desiccant materials, with comparatively less emphasis placed on the complete wheel structure.

1.2 Desiccant Wheel Development

The earliest desiccant wheels were developed by Pennington in the 1950s [27] and were based on packed beds of LiCl, which, although having a very high affinity for moisture, tends to liquefy at high moisture content. These wheels were thus unstable, and contamination of the airstream with LiCl was also unsafe. Munters [25] reduced the pressure drop through the wheel by replacing the packed bed with parallel passages lined with desiccant material.

In the 1970s Type X, Y, and A, zeolite molecular sieves were identified as possible desiccant materials. However, these materials require relatively high regeneration temperatures due to the more extreme (Type 1) isotherm shape and have low equilibrium moisture capacity per unit heat capacity.

A non-deliquescing silica gel wheel was developed by Seibu Giken in the 1980s [20]. Jurinak [17] identified that adding heat capacity to the wheel reduced the total cooling capacity in the desiccant air-conditioning system and that the enthalpy of adsorption should be minimized (and in so doing, demonstrated why the previously developed zeolite wheels did not perform as well as expected). He also proposed that great performance improvements over that of microporous silica gel were not expected in the future for any optimization of desiccant properties.

In the late 1980s, the Gas Research Institute funded research at a number of US organizations with the aim of creating composite desiccant materials with an adsorption isotherm shape approximating that identified by Collier et al. [8] to be 'ideal' [29]. A number of different materials were investigated including polymers and hydratable salts. Polymeric materials were identified by [9] as possible desiccants with low enthalpy of adsorption ($\sim 2,500$ kJ/kg), high moisture capacity, high diffusivity, and low regeneration temperature. These materials were also stated to be cheap and stable. However, the work did not lead to the development of a commercial polymer wheel, perhaps due to degradation problems which were encountered [15].

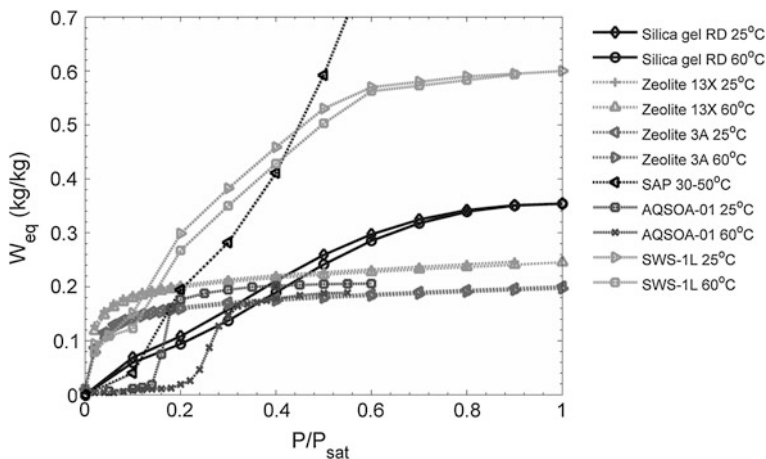


Fig. 2 Desiccant water vapor adsorption isotherms at specified temperatures

Researchers at the Borekov Institute of Catalysis continued the research into methods of creating a composite desiccant by impregnating a porous host structure such as silica gel with a hydratable salt. The aim was to overcome the lyolysis phenomenon, which leads to the loss of desiccant material and occurs after the desiccant salt forms a solid crystalline hydrate [16]. This work resulted in the development of the SWS-1L material, which combines silica gel with CaCl_2 [3]. While the SWS-1L material has a high equilibrium moisture capacity (see Fig. 2), it also has a high heat capacity such that the heat capacity per unit of total moisture capacity is similar to silica gel. High enthalpy of adsorption is also detrimental to performance [11].

A composite wheel with LiCl embedded in pores of silica gel was also tested [16]. They reported a 50 % improvement in moisture removal capacity (MRC) over a conventional silica gel wheel. However, the ‘conventional’ wheel used employed a particular silica gel with a Type 3 isotherm which is known to be inappropriate for desiccant wheels, and the performance was actually comparable to wheels constructed from regular density silica gel.

Renewed interest in zeolite molecular sieves with AIPO and SAPO structures has led to the development of commercially available wheels which require lower regeneration temperatures [18]. Molecular sieves are so named because they contain a regular repeating (crystalline) structure with defined micropores sizes, which selectively adsorb molecules based on their physical size. Although the heat capacitance of these materials is comparable to that of silica gel, the higher enthalpy of adsorption and lower overall moisture capacity may limit any performance benefits. Experimental testing has shown comparable performance to silica gel wheels for one selected material [36].

A new polymer-based desiccant was developed [34] by ion modification of polyacrylic acid impregnated with a hygroscopic sodium salt solution. This

material has a very high equilibrium moisture adsorption capacity (>1 kg/kg above 75 % relative humidity), and batch testing of the super-adsorbent polymer (SAP) desiccant wheel structure was found by Shim et al. to give a 30 % higher dehumidification rate (than a commercial silica gel wheel) at 30 °C and 70 % relative humidity. Further experimental testing [36] showed that the polymer wheel does lead to comparatively low rates of heat transfer between the regeneration and process streams (which should aid in dehumidification), but that the performance improvement was less than previously reported. Optimization of the SAP wheel construction parameters may potentially result in better performance.

Recent efforts to develop other composite desiccant materials (see, for example, references in [22]) have largely focused on improving the equilibrium moisture capacity of the desiccant material, which appears to be still considered the most important desiccant wheel parameter despite earlier works [6, 7, 17] providing evidence to the contrary.

1.3 Indicative Physical Properties of Desiccant Materials

Although there are numerous materials capable of acting as desiccants, only silica gel, molecular sieves (including zeolites), and lithium chloride have seen significant application in commercial wheels. The vast majority of experiments, monitoring results, and performance modeling studies have either used silica gel wheels for comparison or have been based on the performance of silica gel wheels, for which the material and construction parameters are most readily available.

Representative values for the (1) desiccant material apparent density ρ , (2) specific heat capacity c_p , (3) differential enthalpy of adsorption (also known as the isosteric heat of adsorption) H_{ads} , (4) thermal conductivity k , (5) effective moisture diffusivity D_{eff} , and (6) maximum equilibrium moisture capacity W_{max} are listed in Table 1 for conventional RD silica gel, a recently developed commercial zeolite molecular sieve material AQSOA-Z01 [18] and a composite desiccant combining CaCl_2 and silica gel referred to as SWS-1L [3]. These quantities are generally functions of temperature and/or moisture content and so their range of variation should be checked before use in calculations. The adsorption isotherm and the ratio of the differential enthalpy of adsorption to the enthalpy of vapourization of water H_{vap} , as a function of equilibrium moisture content W_{eq} , are shown in Figs. 2 and 3.

For the desiccant materials for which data are given here, there exist quite varied moisture adsorption isotherms and material properties. Silica gel wheels remain in widespread use because they provide consistently good performance and because of the scarcity of detailed data on new wheels. However, it is important to note that, as with zeolites and molecular sieves, there are a number of different types of silica gel, and not all are appropriate for desiccant wheels. In addition to the desiccant material, the design of the wheel (including the support structure and channel geometry) and the operating conditions all play an important part in determining the performance. These parameters are discussed in the following sections.

Table 1 Representative desiccant material parameters

Quantity	Silica gel (type RD)	Molecular sieve (AQSOA-Z01 SAPO-34)	SWS-1L (CaCl ₂ in mesoporous silica)
c_p (J/kg K)	921 ^a	805 (303 K) ^b	1,223 (303 K) ^c
ρ (kg/m ³)	700 ^a	600–700 ^b	800
H_{ads} (kJ/kg)	2,693 ^a	3,110 (298 K) ^b	3,030 above 15 g/kg ^e
k (W/m K)	0.198 ^a	0.11 (303 K) ^b	0.13–0.35 ^c
D_{eff} (m ² /s)	2×10^{-9} – 4×10^{-11} ^f		10^{-10} – 10^{-11} ^d
W_{max} (kg/kg)	0.45 ^a	0.2 ^b	0.6 ^e

^a [35]

^b [18]

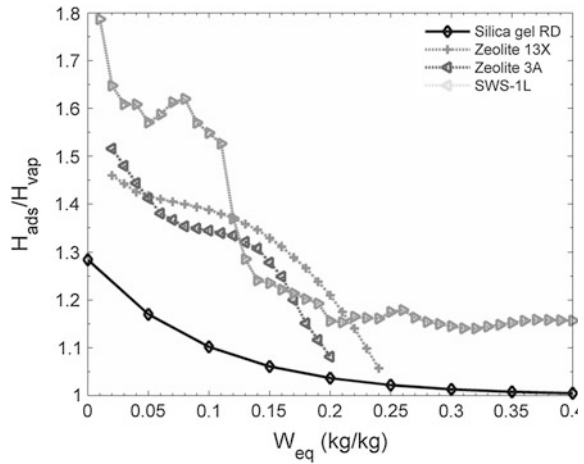
^c [37]

^d [2]

^e [3]

^f [26]

Fig. 3 Comparison of the enthalpy of adsorption of desiccant materials as a function of adsorbed moisture content



2 Dehumidification Transport Mechanisms and Simulation Equations

2.1 Transport Mechanisms

The key physical processes and transport mechanisms occurring in a desiccant wheel are illustrated in Fig. 4. A single desiccant channel is represented schematically in cross-section as (1) an airstream, (2) a desiccant surface layer, which exchanges moisture and energy with the airstream, and (3) the bulk desiccant material. The channel has length L , cross-sectional area A , perimeter P , wall thickness c , and hydraulic diameter D . The arrows, which indicated the process directions for the regeneration stage, are reversed for the dehumidification stage.

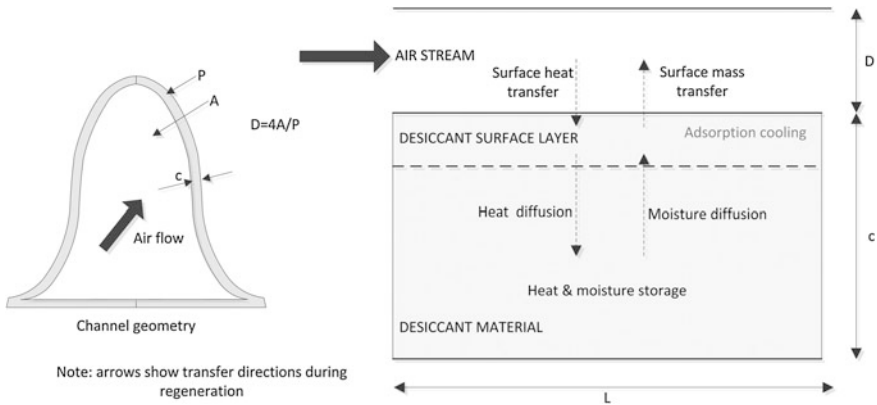


Fig. 4 Schematic of desiccant channel and physical processes during regeneration

In the dehumidification zone, moisture convects out of the air onto the surface of the desiccant material. The moisture then diffuses through the solid, and the average moisture content of the desiccant material increases. Enthalpy of adsorption is released at the surface of the desiccant material where it was initially adsorbed. This heat conducts into the desiccant material and also convects back into the air. Both the air and the desiccant material become progressively hotter in the dehumidification zone.

In the regeneration zone, heat from the hot dry regeneration air convects to the surface of the desiccant material and subsequently conducts into the material. The resulting elevated temperature of the desiccant material increases the partial pressure of water in the desiccant material, and a concentration gradient is established that causes moisture to convect back into the airstream. Moisture leaving the desiccant material takes adsorption enthalpy with it, with a resulting cooling effect on the desiccant surface.

A qualitative indication of the desirable relative magnitudes of these competing transport mechanisms is summarized in Table 2. During regeneration, convective heat transfer between the air and the desiccant surface should be fast so that the desiccant surface is heated rapidly by the regeneration air and the desired equilibrium partial-pressure driving force for regeneration is established. During dehumidification, high convective heat transfer also helps by cooling down the desiccant material to enable it to dehumidify.

It is desirable to have (1) fast mass transfer between the air and desiccant to maximize moisture transfer and (2) fast moisture diffusion through the solid to ensure all of the storage capacity is used. (Note that given the disparity of the cross-channel and axial dimensions, and the likely magnitude of the solid moisture diffusion rates, there is little chance that moisture diffusion in the axial dimension could be fast enough to negatively impact performance.)

Hot desiccant material leaving the regeneration zone and entering the dehumidification zone must first be cooled down by convective heat transfer before it

Table 2 Desirable qualitative magnitudes of various wheel parameters

Description	Quantity	Regeneration zone	Dehumidification zone
Rate processes	Heat convection	Fast	Fast, provided that thermal capacitance is low
	Mass convection	Fast	Fast
	Heat conduction	Slow	Slow
	Mass diffusion	Fast	Fast
Storage values	Thermal capacitance	Low	Low
	Equilibrium moisture content	Moderate	Moderate
Coupling parameter	Adsorption enthalpy	Low	Low

can begin adsorbing again. High thermal capacitance (of the combined desiccant material, backing material, and the adsorbed moisture) slows this cooling period down. The extra heat carried over into the dehumidification zone also leads to higher temperatures and reduced partial-pressure driving force for adsorption.

The adsorbed moisture may contribute a significant fraction of this thermal capacitance. For example, in a silica gel wheel, the adsorbed moisture may comprise up to 50 % of the thermal capacitance at 100 % relative humidity. Hence, the desiccant equilibrium moisture content should be large enough to enable a significant change in moisture content between the process and regeneration conditions, but not so high as to lead to a high overall wheel moisture content with resulting high thermal capacitance.

The detrimental effects of thermal capacitance are less pronounced if thermal conductivity is low because, in this case, heat does not penetrate the solid layer and only a relatively small layer of desiccant material (with correspondingly low thermal capacitance) will participate in the dehumidification process. Low conductivity will also change the temperature profile in the desiccant material with some resulting effects on the average moisture diffusivity.

The enthalpy of adsorption is released during the exothermic adsorption process. This heats the desiccant during the dehumidification stage and cools it during the regeneration stage. Hence, the higher the adsorption enthalpy, the higher the regeneration temperature will need to be and the warmer the process air will be when exiting the wheel. Consequently, a low adsorption enthalpy is desirable during both stages.

2.2 Key Dimensionless Parameters

A desiccant wheel transfers heat and moisture between two airstreams. The driving force for heat transfer is the temperature difference between the airstream in a channel and the desiccant material bounding that channel. The driving force for

moisture transfer is the difference between the partial pressure of water vapor in the channel (a function of humidity) and the equilibrium vapor pressure at the surface of the channel (a function of the desiccant temperature and moisture loading). The larger these two driving forces and the longer the time that the surface and air are in contact, the greater the heat and mass transfer between the streams.

For modeling the heat and mass transfer process in the desiccant wheel, it is instructive to define a series of dimensionless parameters. These parameters group collections of measurable properties into a single number, which can then be used to identify the relative importance or extent of different physical process. The dimensionless parameters are also helpful for characterizing different systems with varied material properties.

The dimensionless contact time numbers θ_i describe the relative time that desiccant spends in either the process or regeneration stream compared with the time taken for air traveling at speed u_i to traverse the channel of length L .

$$\theta_i = \frac{u_i \Omega_i}{L} \tag{1}$$

Here, Ω_i is the rotation time in a single stream, and the subscript ‘ i ’ refers to either the process or regeneration stream. A typical value of θ_i is 1,000 indicating that desiccant moisture loading processes are much slower than the air-side convective processes. If the values are too high, then the supply-side dehumidification is low because the channels approach equilibrium well before the channel switches airstream, and a fraction of air will pass through the wheel without significant dehumidification occurring. If the values are too small, then the dehumidification is also low because there is not enough time for loading and unloading the desiccant material with moisture.

The dimensionless Fourier number gives a representation of how close a particular heat or mass transfer process is to equilibrium. If the wheel process and regeneration-side rotational times are given by

$$\Omega_p = \frac{2\pi}{\omega} S, \quad \Omega_r = \frac{2\pi}{\omega} (1 - S) \tag{2}$$

where ω is the rotational speed (rad/s), then the heat and mass transfer Fourier numbers for the process and regeneration sides can be defined in directions both (1) parallel to the axis of the desiccant wheel

$$FO_{\eta,i} = \frac{k\Omega_i}{\rho_m c_{p,t} L^2}, \quad FO_{m,\eta,i} = \frac{D_{\text{eff}}\Omega_i}{L^2} \tag{3}$$

and (2) perpendicular to the airflow through the channel;

$$FO_{\kappa,i} = \frac{k\Omega_i}{\rho_m c_{p,t} c^2}, \quad FO_{m,\kappa,i} = \frac{D_{\text{eff}}\Omega_i}{c^2}. \tag{4}$$

Note that $c_{p,t}$ is the total specific heat capacity which includes the heat capacity both due to the dry solid material and due to the adsorbed water and is given by

$c_{p,t} = c_{p,m} + fWc_{p,l}$, where f is the desiccant material fraction (further defined in the Sect. 1.2.3).

The values of these Fourier numbers may be used to determine how heat and mass transfer processes should be modeled. If $Fo \ll 1$, then the solid-side kinetic process is slow in comparison with the storage capacity in the desiccant material. If the kinetic process is critical (i.e., there are no other transport mechanisms), then the solid-side kinetics would become the rate-limiting effect. Alternatively, if there are other transfer mechanisms, then the kinetic process may be safely ignored. If $Fo \gg 1$, then the kinetic process is fast in comparison with the storage capacity and the process is governed by equilibrium behavior. That is, a lumped parameter model may be appropriate. Finally, if Fo is intermediate in value, then both the kinetics and storage capacity (equilibrium behavior) are important and should be considered in the mathematical model.

For conventional desiccant wheels, the heat and mass transfer Fourier numbers in the axial direction are much less than one. Thus, axial diffusion of both heat and moisture is insignificant compared with transport occurring in the transverse direction (perpendicular to the channel wall). For transport in the transverse direction, $Fo_\kappa \gg 1$ and $Fo_{m,\kappa}$ is of order 1. Consequently, the temperature across the thickness of the desiccant layer is close to uniform and there will be a gradient of moisture concentration inside the desiccant material in the direction perpendicular to the channel wall.

The rates of convective heat and mass transfer from the bulk airstream to the solid surface in a desiccant channel are given by the heat transfer coefficient (h) and mass transfer coefficient (h_m), respectively. The dimensionless Biot number gives a measure of the relative magnitudes of the resistance to heat or mass transfer from the bulk gas to the solid as compared to the resistance to heat or mass transfer within the solid itself. The Biot number is thus a ratio of the gas-side to solid-side thermal or moisture transfer resistance and is given by

$$Bi = \frac{hc}{k}, \quad Bi_m = \frac{h_m c}{\rho_m f \mathcal{D}_{\text{eff}}}. \quad (5)$$

If $Bi \ll 1$, then the gas-side resistance is high in comparison with the solid-side resistance, and in the absence of other effects, the temperature or moisture concentration profile perpendicular to the surface will be close to uniform. If $Bi \gg 1$, then the overall heat or mass transfer is limited by the rate of conduction or diffusion from the surface in the desiccant. In the absence of other effects, there will be a strong temperature or moisture concentration profile perpendicular to the surface in the desiccant material. Finally, if Bi is of order 1, then both the gas-side and solid-side resistances will be important in determining the overall heat and mass transfer.

For conventional wheels, $Bi \ll 1$ and $Bi_m < \sim 10$. That is, gas-side heat transfer resistances are important, and both the solid-side and gas-side resistances are potentially important for moisture transport.

The heat and mass transfer analogy may be used to relate the relative rates of heat and mass transfer from the bulk airstream to the walls of the channel. Because

the first-order equations describing heat and mass transfer via diffusion are of identical form, it is hypothesized that the heat and mass transfer rates may be related by a function which describes the relative thermal and moisture boundary layer thicknesses denoted δ_t and δ_c , respectively. The Lewis number is a material parameter (a function of temperature) and is the ratio of the thermal to moisture diffusivity. Assuming that for laminar boundary layers $\delta_t/\delta_c = Le^{1/3}$ [14], it follows that the Lewis factor (a flow parameter) is given by

$$Le_f = \frac{h}{h_m c_{p,a}} = Le^{2/3}. \quad (6)$$

Values of $Le_f < 1$ indicate enhanced mass transfer relative to heat transfer. For air at standard temperature and pressure, $Le = 0.88$ [24] giving $Le_f = 0.92$.

Whereas the Fourier numbers describe the approach to equilibrium of heat and moisture diffusion processes, and the Biot numbers the relative magnitudes of gas- and solid-side heat and mass transfer resistances, the number of transfer units (NTU) is a dimensionless measure of the *potential* rate of heat or mass transfer from the air to the surface relative to the thermal capacitance or moisture holding capacity of the air, respectively. The heat transfer NTU is given by

$$NTU_i = \frac{h}{\rho_m c_{p,a}} \frac{P L}{A u_i} = 4 Nu \frac{\alpha_a L}{D^2 u_i}. \quad (7)$$

Here, Nu is the channel's Nusselt number. The higher the NTU, the more the heat or moisture that can be transferred for a given temperature or moisture differential between the airstream and surface layer. Typical values of NTU are between 3 and 20 for desiccant wheel channels.

2.3 Transport Equations and Boundary Conditions

For modeling heat and moisture transfer in a desiccant wheel, it is usual to neglect rotational effects given the typically large value of θ . If it is also assumed that each individual flow channel is identical and insulated from its neighbors and that the backing matrix is impermeable to water, then the entire wheel may be modeled by considering only the processes occurring in a single physical channel as it rotates through each wheel revolution. Such a channel is shown in Fig. 4.

Here, the solid layer is assumed to be composed of a homogenous mixture of desiccant material and backing material in the mass ratio f and with an equivalent overall dry specific heat capacity $c_{p,m}$. While this does not reflect the actual geometry which is most commonly a desiccant layer on an inert backing matrix, the approximation is reasonable for silica gel wheels, which typically have a thin backing layer (high value of f).

For calculating the overall wheel performance, it is sufficient to use a lumped parameter model for the moist airstream, whose components can be considered as

ideal gases under the conditions typically encountered. The channel's Reynolds number Re is typically much less than the transition Reynolds number, indicating that the flow is laminar. Nusselt number correlations assuming fully developed flow are readily available for a number of channel cross-sections, e.g., [33].

Energy and moisture conservation equations for the cross-section-averaged airstream moisture content Y_i and temperature T_i , and the desiccant moisture content W_i and matrix temperature T_{mi} can be written in partially dimensionless form using the parameters defined in Eqs. (1–7) and by making non-dimensional the time, axial distance, and desiccant wall thickness variables t , z , and x , according to

$$\tau_i = t_i/\Omega_i, \quad \eta = z/L, \quad \kappa = x/c. \quad (8)$$

Note here that the dimensional time is taken to reset at the beginning of each process and regeneration stage. Retaining dimensional representations of temperature and moisture content in the equations is convenient since it avoids the clutter associated with defining reference values, which add little extra meaning. Thus, assuming that convection is the dominant transport mechanism in the airstream and that the heat and moisture transport to the air is proportional to the difference between the cross-section-averaged air temperature or humidity and the matrix surface temperature T_s and surface air equilibrium humidity ratio Y_s , then the airstream energy and moisture conservation equations follow as

$$\begin{aligned} \frac{\partial T_i}{\partial \tau_i} + \theta_i \frac{\partial T_i}{\partial \eta} &= \theta_i NTU_i (T_s - T_i) \\ \frac{\partial Y_i}{\partial \tau_i} + \theta_i \frac{\partial Y_i}{\partial \eta} &= \frac{\theta_i NTU_i}{Le_f} (Y_s - Y_i) \end{aligned} \quad (9)$$

For the solid desiccant material, heat and moisture transport occurs via diffusion, and according to the Fourier number analysis, axial conduction and diffusion may be neglected and transverse conduction is very rapid. Assuming that the moisture stored in the gas phase in the pores of the desiccant is small compared to the moisture stored in bound form, the conservation equations in the bulk of the desiccant thus become

$$\begin{aligned} \frac{\partial T_m}{\partial \tau_i} &= Fo_{\kappa,i} \frac{\partial^2 T_m}{\partial \kappa^2} \approx 0 \\ \frac{\partial W}{\partial \tau_i} &= Fo_{m,\kappa,i} \frac{\partial^2 W}{\partial \kappa^2} \end{aligned} \quad (10)$$

Here, the mass transfer Fourier number is evaluated with an overall effective diffusivity, with, in the most general case, contributions from two terms;

1. a surface diffusion along the walls of the pores driven by the gradient of adsorbed moisture content and proportional to the surface diffusivity D_s and
2. a porous diffusion arising from combined ordinary and Knudsen diffusion inside the pores of the desiccant material driven by the gradient of the

equilibrium gas phase humidity in the pores and proportional to the combined ordinary D_O and Knudsen D_K diffusivities.

Assuming that $\partial^2 T_m / \partial \kappa^2$ is very small, the overall effective diffusivity is given by

$$D_{\text{eff}} = \frac{1}{\zeta} \left[D_s + \frac{\rho_a}{f \rho_m} \varphi \left(\frac{1}{D_O} + \frac{1}{D_K} \right)^{-1} \frac{\partial Y}{\partial W} \right] \tag{11}$$

where ζ is the tortuosity factor of the pores and φ is the porosity of the desiccant material. According to [28], for the case of type RD silica gel, surface diffusion is the dominant mechanism and the gas phase diffusion terms may be neglected.

Equations (1–11) thus form a set of coupled parabolic partial differential equations. The airstream inflow boundary condition alternates between the process and regeneration inlet state according to the wheel rotational position. Thus, the channel reaches a cyclically steady state, which is independent of the initial condition. The air inlet boundary temperature and humidity are given by

$$\left. \begin{aligned} \eta = 0, & \quad \left. \begin{aligned} T_p &= T_{p,\text{in}} \\ Y_p &= Y_{p,\text{in}} \end{aligned} \right\} \quad \text{for } 0 < \tau_p < 1 \\ \eta = 1, & \quad \left. \begin{aligned} T_r &= T_{r,\text{in}} \\ Y_r &= Y_{r,\text{in}} \end{aligned} \right\} \quad \text{for } 0 < \tau_r < 1 \end{aligned} \right\} \tag{12}$$

The desiccant material is modeled as insulated and impermeable at the backing between channels. Combined with the non-dimensional temperature and moisture concentration gradient at the desiccant surface as given by Bi and Bi_m , this allows the desiccant boundary conditions to be written as

$$\left. \begin{aligned} \frac{\partial W}{\partial \kappa} \Big|_{\kappa=0} &= 0, \quad \frac{\partial T_m}{\partial \kappa} \Big|_{\kappa=0} = 0 \\ \frac{\partial W}{\partial \kappa} \Big|_{\kappa=1} &= Bi_m (Y_s - Y_i), \\ \frac{\partial T_m}{\partial \kappa} \Big|_{\kappa=1} &= Bi \left[(T_s - T_i) + \frac{1}{Le_f c_{p,a}} (Y_s - Y_i) \right] \end{aligned} \right\} \tag{13}$$

where the component of the temperature gradient due to the difference in temperature of the sorbed water has been assumed to be small and the adsorption energy is assumed to be released onto the desiccant surface.

Equations (1–11) together with the boundary conditions may be solved numerically using any appropriate finite difference method. In some cases, it may be appropriate to assume fixed (non-temperature and humidity dependent) values for Fo , Bi , and Le and this simplifies the solution procedure significantly by allowing implicit numerical solvers to be used such as the ADI method [32].

Given the channel’s Reynolds number Re , the air-side pressure drop through the desiccant channels can be computed assuming an overall average friction

coefficient in the fully developed channel flow, a_f , and with a loss factor to account for the channel entrance and exit pressure drops:

$$\Delta P = 0.5 \rho_a u_i^2 \left(1 + \frac{4c}{D} \right)^2 \left[\frac{a_f L}{Re D} + 1.5 \right] \quad (14)$$

3 Desiccant Wheel Performance Indicators

In a desiccant-wheel-based air-conditioning system, the most important wheel performance parameters are (1) the process air dehumidification rate, (2) the outlet humidity of the process airstream, and (3) the energy efficiency (e.g., power required to pass air through the wheel). All three parameters are required to provide a proper comparison between different wheels because, for example, higher dehumidification rates can be achieved by increasing air velocity, but this is likely to be achieved at the expense of increased outlet humidity (with a corresponding increase in building supply air temperature) and higher pressure drop. Similarly, outlet humidity could be reduced by increasing the length of the wheel, although this would most likely come at the expense of increased fan power requirements.

3.1 Dehumidification Rate Indicators

A number of parameters have been used to quantify desiccant wheel performance [30, 31]. The MRC is the rate of moisture removal (kg moisture/s) of the process stream and is defined by

$$\text{MRC} = \dot{m}_p (Y_{p,\text{in}} - Y_{p,\text{out}}). \quad (15)$$

The MRC gives a dimensional measure of the rate of moisture removal by a particular wheel. A more useful version of this parameter, which can be used for comparing different wheel configurations, may be defined by normalizing MRC by the total (process and regeneration) airflow rate. For equal process and regeneration air face velocities, the scaled dehumidification ratio (DR) may be defined as

$$\text{DR} = S(Y_{p,\text{in}} - Y_{p,\text{out}}). \quad (16)$$

This is the dehumidification amount per unit of total pumped flow rate and so accounts for the fact that the pumping energy of the system is proportional to the combined process and regeneration airflow rate. Typical values of DR are in the range 2–5 g water per kg *total* airflow.

3.2 Humidity Reduction Indicators

The ability of a desiccant wheel to reduce humidity is sometimes represented by the desiccant wheel dehumidification effectiveness, a form which is analogous to heat exchanger effectiveness,

$$\varepsilon = \frac{Y_{p,\text{in}} - Y_{p,\text{out}}}{Y_{p,\text{in}}}. \quad (17)$$

This equation assumes that, in the ideal case ($\varepsilon = 1$), the process stream leaves the wheel completely dry, which is not thermodynamically possible. An alternative thermodynamically feasible dehumidification effectiveness would take into account the theoretical limiting process air dryness Y_{th} that could be obtained from a given regeneration airstream,

$$\varepsilon_{\text{dehumid}} = \frac{Y_{p,\text{in}} - Y_{p,\text{out}}}{Y_{p,\text{in}} - Y_{\text{th}}}. \quad (18)$$

However, determining an appropriate value for Y_{th} is not obvious.

The isotherms shown in Fig. 2 suggest that, for a number of desiccants (with the notable exception of the AQSOA desiccant), the equilibrium moisture loading is mainly dependent on relative humidity and is fairly insensitive to temperature over the likely range of temperatures the desiccant will encounter.

Consequently, the theoretical minimum moisture content that the desiccant material can be dried to in the regeneration zone corresponds to equilibrium at the relative humidity of inlet regeneration air. This can be expressed as an effectiveness based on relative humidity, the definition of which has some attraction because $\text{RH}_{r,\text{in}}$ is generally known:

$$\varepsilon_{\text{RH}} = \frac{\text{RH}_{p,\text{in}} - \text{RH}_{p,\text{out}}}{\text{RH}_{p,\text{in}} - \text{RH}_{r,\text{in}}}. \quad (19)$$

Experimental data suggest that values of ε_{RH} are generally above 0.9 across a reasonably wide range of air velocities and regeneration air conditions for wheels with $S = 0.5$. These high efficiencies suggest that the rate of heat and mass transfer is quite good in modern desiccant wheels.

However, it should be noted that Eq. (19) does not fully describe how good the performance of the desiccant wheel is at achieving absolute dehumidification, because the reduction in relative humidity can be caused by either increasing temperature or reducing humidity. Clearly, reducing humidity is the useful function, while increasing temperature serves no purpose.

To overcome the ambiguity of the relative humidity effectiveness definition (with respect to differentiating between humidity and temperature effects), it is possible to define theoretically feasible ideal outlet humidity at a condition where (1) relative humidity is equal to the inlet regeneration air and (2) temperature is equal to the inlet process air:

$$\varepsilon_{\text{dehumid}} = \frac{Y_{p,\text{in}} - Y_{p,\text{out}}}{Y_{p,\text{in}} - Y_{\text{th}}(T_{p,\text{in}}, \text{RH}_{r,\text{in}})}. \quad (20)$$

That is, $\varepsilon_{\text{dehumid}} = 1$ corresponds to an isothermal dehumidification process where the process air exits the wheel with a relative humidity equal to the regeneration inlet relative humidity.

3.3 Energy Efficiency Indicators

It is also useful to define parameters which give a measure of the electrical consumption and thermal regeneration energy use of the wheel in a manner somewhat analogous to the electric and thermal COP of a desiccant-wheel-based air-conditioning system. Using the ratio of dehumidification amounts to pressure drop and regeneration energy usage, non-dimensional electrical and thermal efficiency parameters may thus be defined as

$$\Upsilon_e = \frac{\text{DR} \cdot h_{fg}}{\Delta P / \rho_a}, \quad \Upsilon_t = \frac{\text{DR} \cdot H_{\text{vap}}}{c_{p,a} \Delta T_r} \quad (21)$$

where it has been assumed that the pressure drop and face velocity are the same across both sides of the wheel.

4 Impact of Desiccant Material Properties

4.1 Sensitivity to Physical Properties (Conductivity, Diffusivity, Thermal Capacitance, and Moisture Capacity)

The physical properties of the desiccant material, the conductivity (k) and diffusivity (D_{eff}), determine how fast heat and moisture diffuse through the material, while the specific heat capacity ($c_{p,m}$) and equilibrium adsorption capacity (W_{eq}) determine how much heat and moisture can be stored per unit mass of the material.

As discussed above, it is desirable for k to be low, D_{eff} to be high, $c_{p,m}$ to be low, and W_{max} to be moderate to high. The relative importance of conduction and diffusion in the transverse (cross-channel) direction as a limiting factor in the heat and mass transfer between the air and desiccant may be evaluated using the Biot numbers defined in Eq. (1.5). For a silica gel wheel, this analysis indicates that transverse conduction is not a critical factor but that, depending on the diffusivity and layer thickness, the transverse diffusion may be a critical factor. For conduction and diffusion in the axial direction, the Fourier numbers indicate that both these processes are not critical.

Fig. 5 Variation in DR with independent scaling of D_{eff} and k in the transverse (cross-channel) and axial directions. Inlet conditions of process/regeneration air 30/80 °C and 16.5 g/kg

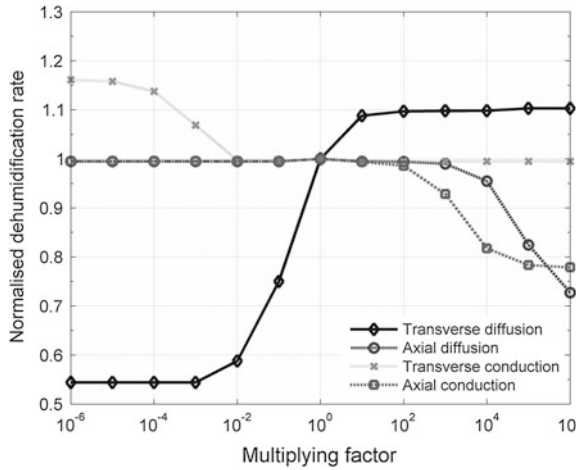


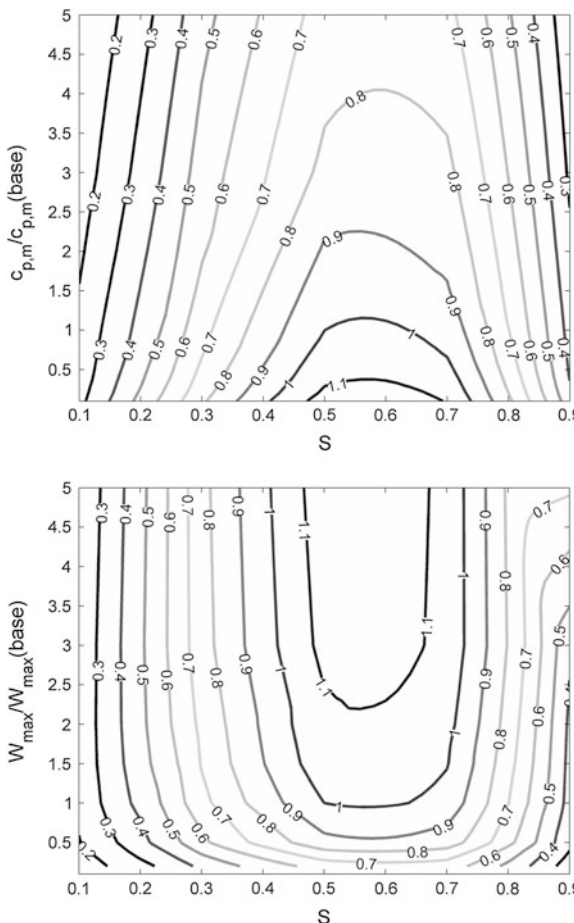
Figure 5 shows the variation in dehumidification rate DR, which results from independently varying the transverse and axial conduction and diffusion by scaling each by a multiplying factor, using a silica gel wheel as the base case. These results were obtained using a numerical model calibrated to experimental data [12] and with a desiccant layer thickness of 0.2 mm and the moisture diffusivity data of [28].

The results show that k must be increased or decreased by a factor of more than 100 before there is any significant change in DR. On the other hand, if D_{eff} is increased by a factor of 10, then DR increases by approximately 10 %. The thicker the desiccant layer, the greater the potential benefit from increasing D_{eff} .

The influence of independently varying the matrix heat capacity and the desiccant equilibrium adsorption capacity by scaling by a multiplying factor is shown in Fig. 6. (Note here that the increased heat capacity due to adsorbed moisture was included when the moisture capacity was scaled.) The influence of varying S is also included, and for each case, the optimum rotation rate was used. Reducing $c_{p,m}$ by half improves the performance by 5–10 % for S values near the optimum, while increasing $c_{p,m}$ by a factor of 2 results in close to a 10 % decrease in performance. Halving W_{eq} (that is, decreasing both the magnitude of the maximum uptake and the gradient of the adsorption isotherm) results in only a 15 % drop in dehumidification rate, while doubling the capacity leads to between 5 and 10 % improvement.

This result shows that the moisture isotherm is a relevant material parameter contributing to the overall wheel performance, but that minimizing the heat capacity of the matrix (both the desiccant and backing layer) is similarly important. For example, Collier [6] proposed that the ratio of the heat capacity of the matrix to the total moisture ratio cycled is a critical performance parameter. That is, similar results are obtained for materials where the ratio $\rho c_{p,m}/W_{max}$ is similar. They found that the cooling capacity always decreases as this ratio increases, with more effect at higher regeneration temperature. Similarly, Zheng et al. [38, 39]

Fig. 6 Variation in DR with scaling of $c_{p,m}$ (*top*) or W_{\max} (*bottom*) by a multiplying factor. Comparison with varying S with optimal rotational rate for each condition. Inlet conditions of process/regeneration air 30/80 °C and 16.5 g/kg



found that extra moisture capacity above $fW_{\max} = 0.2$ (or equivalent to multiplying factors above 1) does not result in significant additional dehumidification.

It is worthwhile to note that results shown in Fig. 6 do not consider variations in the enthalpy of adsorption, moisture diffusivity, or conductivity which may occur as the equilibrium moisture capacity is increased. If, for example, increasing W_{\max} coincided with a decrease in H_{ads} and an increase in D_{eff} , then the performance improvement may be higher.

4.2 Sensitivity to Isotherm Shape and Enthalpy of Adsorption

In the previous section, the influence of the maximum desiccant material moisture capacity W_{\max} on the dehumidification performance was found to be

comparatively small for $W_{\max} > 0.3\text{--}0.4$ kg/kg. A number of studies have investigated the influence of the isotherm shape for a fixed value of W_{\max} . For example, [8] investigated theoretical isotherm shapes with Type 1 (concave down), Type 3 (concave up), and linear forms. They found that a moderate concave-down ('Type 1M') shape gave the best compromise between efficient dehumidification and regeneration processes.

Collier et al. described the influence of the isotherm shape in terms of whether it tends to result in a 'sharpening' or a 'broadening' of the concentration and thermal gradients as they traverse the wheel.

During regeneration, the desiccant is subjected to an increase in temperature as the regeneration air passes over it. For the Type 3 profiles, this increase in temperature corresponds to an extremely rapid reduction in the equilibrium moisture capacity and a comparatively sharp thermal and concentration 'front' in the regeneration zone. This front is advantageous because it means that the maximum possible difference between inlet and outlet regeneration air conditions is contained within the length of the wheel. However, during dehumidification, adsorption enthalpy is released and the desiccant material rises in temperature. The rapid increase in the saturation vapor pressure with temperature exhibited by the Type 3 profile therefore leads to a very broad, gradual dehumidification process. As a result, the full dehumidification potential of the wheel is not realized over the course of a wheel cycle for any realistic wheel length.

Conversely, the general Type 1 shape leads to a sharp front on the outlet of the dehumidification zone and a broad front on the outlet of the regeneration zone. The sharp front is more important in the dehumidification zone, and consequently, the moderate Type 1 isotherm exhibits best performance.

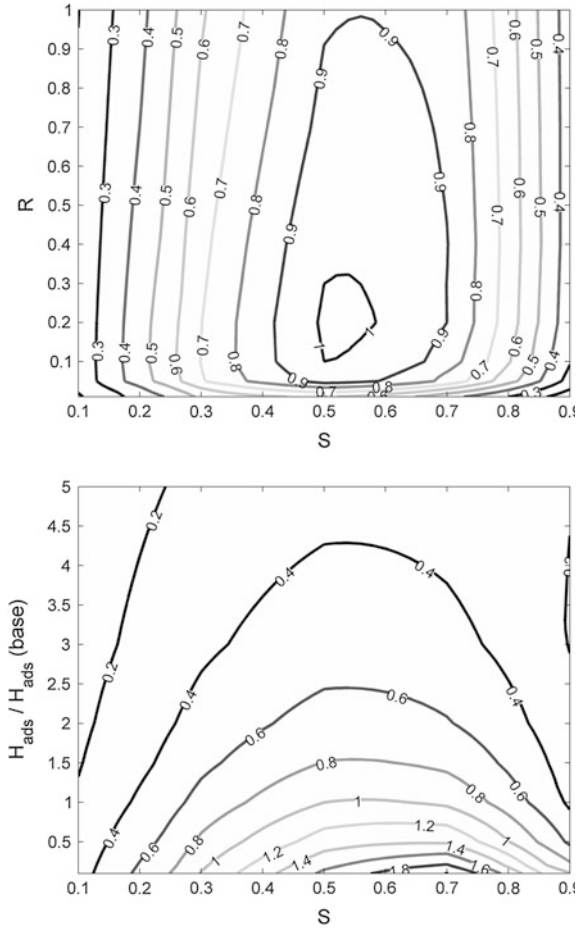
A numerical investigation was performed [4] using a gas-side resistance model (i.e., neglecting moisture diffusion and conductivity) to vary S and Ω for different regeneration temperatures and Type 1 (concave down) theoretical isotherm shapes defined by

$$\frac{W}{W_{\max}} = \frac{P/P_{\text{sat}}}{R + (1 - R)P/P_{\text{sat}}} \quad (22)$$

where $0 \leq R < 1$ is a parameter, which defines the shape. (Note that $R = 1$ corresponds to a linear isotherm and $R < 0.1$ represents an extreme Type 1 isotherm.) MRC was used as the performance metric. The highest MRC at T_r , 80 °C was obtained for $R \sim 0.2$, but the MRC was found to be relatively insensitive to isotherm shape with little difference ($\sim 10\%$) for $0.05 < R < 1$.

The variation in DR with R and S and with optimum Ω as calculated here is shown in the top plot of Fig. 7 for inlet air conditions of 30/80 °C and 16.5 g/kg. These results confirm those of Chung and Lee, that is, that it is important that the isotherm shape is not too sharp (referred to as Type 1E or extreme) (i.e., $\sim 0.05 < R < \sim 0.1$) and that the variation in DR is only moderate for $0.1 < R < 1$. If the isotherm shape is too sharp, high regeneration temperatures are

Fig. 7 *Top* variation in DR with isotherm shape parameter R in Eq. (22), with area ratio S , and with optimum rotation rate for each case. *Bottom* variation in DR with scaling of the enthalpy of adsorption by a multiplying factor



required to obtain a low value of ϕ during regeneration and so to effectively remove the moisture from the wheel.

For low regeneration temperatures ($<80\text{ }^\circ\text{C}$), the optimal value of R is slightly higher, but there is still very little performance difference for $0.2 < R < 1$. Hence, the isotherm shape does not have large influence on performance, provided that it resembles the general Type 1M shape.

The preceding analysis of the influence of isotherm shape assumed that isotherm shape is independent of temperature. As shown in Fig. 2, this is a reasonable approximation for a number of desiccants such as silica gel and certain zeolites over the temperature ranges commonly encountered. However, in practice, these isotherms also have a temperature dependence, which is determined by the variation in H_{ads} with W .

The Clausius–Clapeyron relation may be used [5] to relate the enthalpy of adsorption to the isotherm data assuming a thermodynamically reversible process

and that the sorbate acts as a perfect gas whose volume in the liquid phase is much less than in the vapor phase:

$$\left(\frac{\partial \ln P}{\partial \ln P_{\text{sat}}} \right)_W = \frac{H_{\text{ads}}}{H_{\text{vap}}} \quad (23)$$

The variation in $H_{\text{ads}}/H_{\text{vap}}$ with W is shown in Fig. 3 for a number of desiccant materials. The shape is determined by the nature of the physical adsorption processes occurring on and within the surface of the desiccant, more details of which can be found in texts on surface chemistry such as [1]. Generally, H_{ads} decreases as W increases and tends toward H_{vap} as the sorption approaches multi-layer condensation.

The influence of the magnitude of H_{ads} on DR is shown in the bottom plot of Fig. 7. Here, a fixed value of H_{ads} was employed and its magnitude was scaled by a multiplying factor for a range of S and with Ω optimized for each case.

Doubling H_{ads} leads to close to a 40 % drop in DR at the optimum S ratio, while in theory, halving H_{ads} would lead to a 40 % improvement. Although such a large decrease in H_{ads} may not be physical, the magnitude of these changes reflects the fact that the dehumidification process is strongly limited by heating of the process stream, which occurs due to both the release of the adsorption enthalpy and the carryover of stored heat from the regeneration stream.

5 Impact of Wheel Design and Operating Parameters

In addition to the desiccant material properties, the wheel configuration and operational parameters can influence the overall performance.

5.1 Rotational Speed

For a given wheel with fixed air face velocities, wheel length, regeneration to process face area ratio, and channel geometry, there exists a rotational speed leading to the maximum possible process air dehumidification for each set of inlet air conditions. Faster rotational speeds lead to insufficient penetration of the dehumidification front into the process stream before the airstreams are reversed and regeneration begins. Slower rotational speeds result in the desiccant and air approaching vapor and thermal equilibrium, which reduces the overall rate of moisture transfer. Since the rotational speed is an external parameter which may be independently adjusted, it is possible to choose the correct speed for any given condition, and although the precise optimum speed may vary with conditions (Zheng et al. 1995a), the influence of this variation on the performance is relatively small over a broad range of speeds.

5.2 Supply Air Face Area Fraction

Dehumidification effectiveness increases as S decreases. However, the resulting low absolute humidity of the outlet process air comes at the expense of a comparatively low flow rate that can be supplied to the building. A balance exists between increasing flow rate and reducing absolute humidity, with maximum DR occurring with S generally slightly larger than 0.5 as shown in the figures above. For theoretical isotherm shapes defined by Eq. (22) with $R = 0.1-1$, Chung and Lee [4] present results showing that the optimum value of S is in the range 0.52–0.54 for $T_r = 50$ °C increasing to 0.59–0.61 for $T_r = 90$ °C. These values are relatively insensitive to wheel parameters, though they require the optimum rotational speed to be employed.

5.3 Channel Geometry

The NTU can be increased to ensure that convective rate processes do not limit the performance. NTU can be increased by designing the wheel for increased Nusselt and Sherwood numbers, increasing the channel length or reducing the channel hydraulic diameter.

The influence of increasing NTU on the performance of a generic gas-side resistance wheel model with a theoretical Type 1M isotherm shape was investigated (Zheng et al. 1995a). They found that the performance increases with increasing NTU but that there is little additional benefit for $NTU > 12$.

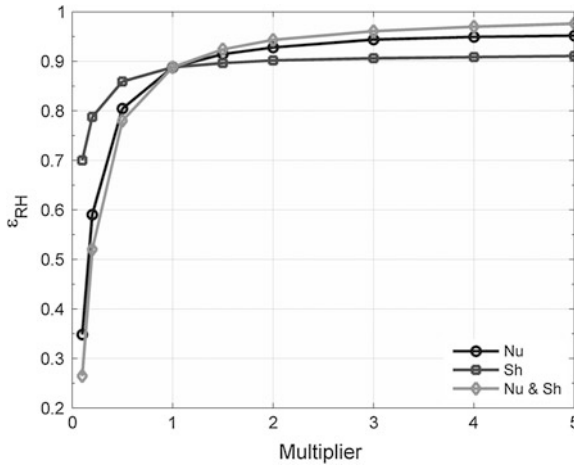
A comparison of the variation in relative humidity effectiveness with independent scaling of Nu and Sh by a multiplier, and with a combined variation in Nu and Sh , is shown in Fig. 8. The base case corresponds to $NTU \sim 8$ and $\varepsilon_{RH} = 0.89$. Hence, there is less than 10 % improvement in relative humidity effectiveness (or 20 % improvement in DR) possible for $NTU > 12$.

5.4 Wheel Length, Air Velocity, and Channel Hydraulic Diameter

Unlike the desiccant material parameters and the rotational speed, supply area fraction and channel geometry, which have defined optimal values or ranges for best dehumidification performance, the choice of wheel length, airflow velocity, and air channel size (hydraulic diameter) reflects a trade-off between wheel performance, electrical power consumption to operate fans or motors, and the physical size of the wheel.

This trade-off is explored in Figs. 9 and 10 through the presentation of lines of constant: (1) dehumidification rate DR (dashed dot); (2) electrical power

Fig. 8 Comparison of variation in ϵ_{RH} with independent scaling of the channel Nusselt number, Sherwood number, and combined scaling of both



consumption based on the channel air pressure drop (dashed); (3) specific DR or dehumidification per unit of electrical power consumption (solid lines), and (4) wheel face area (solid lines in Fig. 9 and right-hand vertical axis in Fig. 10). Each of these parameters is normalized against the respective base case result at $L = 0.2$ m, $D = 1.5$ mm, $u = 2.5$ m/s. Regions where the influence of turbulent flow, axial conduction, and laminar entrance length effects becomes significant are also shown.

In all simulations, Nu and a_f were taken to be independent of D and the optimum rotation speed was chosen for each case. The required face area of the wheel was calculated solely as a function of D , reflecting the reduced area taken up by channel walls when D is increased. Although material parameters for silica gel are assumed, the same trends are expected for other wheel materials.

In Fig. 9, the effect of varying air velocity and channel size at fixed wheel length is presented. In Fig. 10, the effect of varying wheel length and channel size at fixed air face velocity is presented. A number of variations can be observed. For example, a lower face velocity with the same channel size leads to a larger wheel face area and greater dehumidification, while a larger channel size can be combined with a slightly smaller wheel to obtain a higher dehumidification per unit pressure drop at the same face velocity. Alternatively, a longer wheel can be combined with a slightly larger channel size to give the same total dehumidification but higher dehumidification per unit pressure drop.

In general, the largest wheel area, which can be employed in any particular application, will give the best specific dehumidification performance. Larger channel hydraulic diameters and shorter wheels will also give better specific dehumidification performance (provided the larger wheel area is acceptable and the channel flow remains laminar).

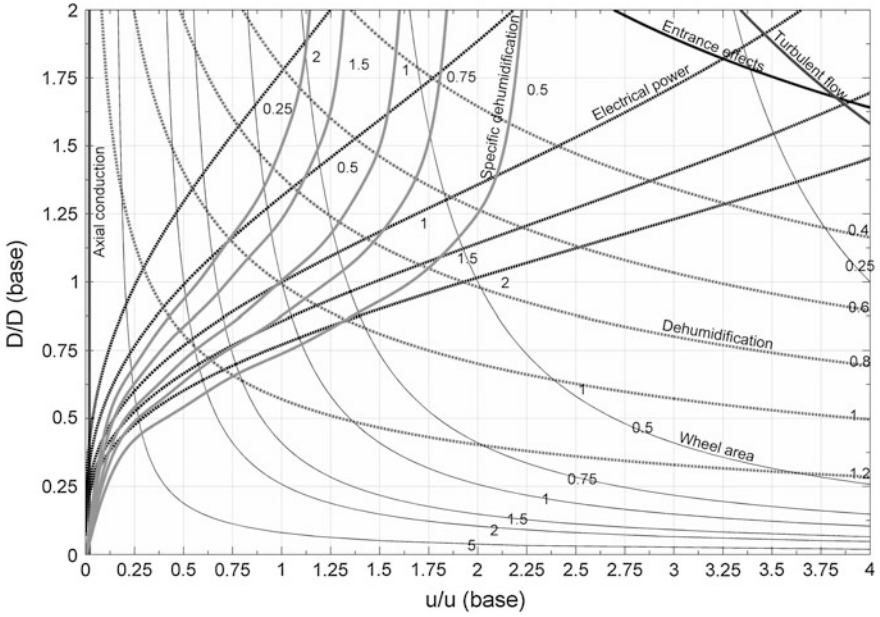


Fig. 9 Comparison of dehumidification performance with varying channel diameter and air face velocity for fixed length $L_o = 0.2$ m

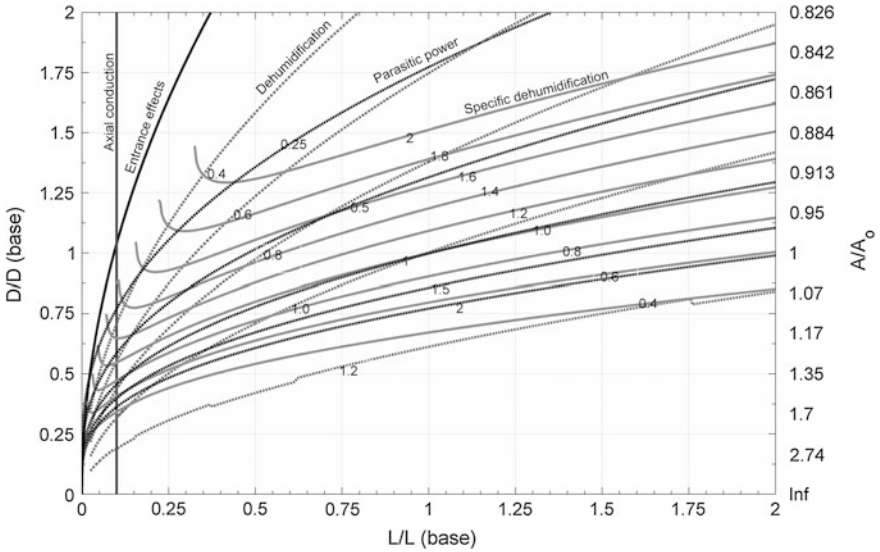


Fig. 10 Comparison of dehumidification performance with varying channel diameter and length for fixed air face velocity $u_o = 2.5$ m/s

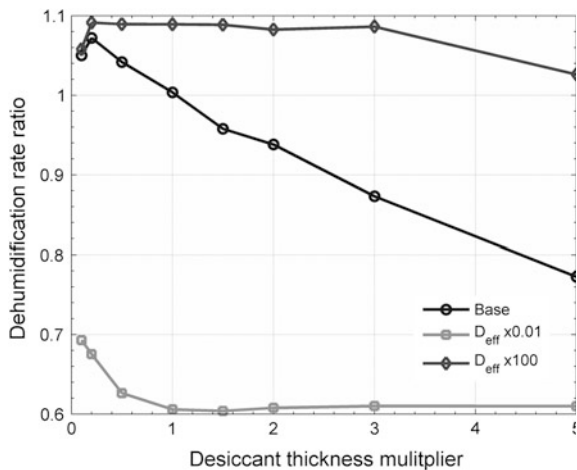
5.5 Desiccant Layer Thickness

The thickness of the desiccant layer influences both the total moisture capacity of the wheel and the total heat capacity. Since the dehumidification performance is determined by the rate of moisture transfer between the process and regeneration streams, increasing the layer thickness does not necessarily lead to a performance improvement. In fact, the additional heat capacity has a negative effect on the overall performance due to carryover of heat as discussed above, while the additional moisture capacity can only be used if the moisture can diffuse into the desiccant rapidly enough.

The influence of layer thickness on the dehumidification amount was investigated [30, 31]. They found that the dehumidification amount increased marginally when the thickness was reduced from 0.1 to 0.05 mm. The process outlet air temperature also decreased by almost 10 °C. The optimum rotation rate increases as the thickness decreases as less time is required for the moisture to diffuse through the layer.

The variation in DR as the thickness is scaled from the base value of 0.2 mm by a multiplying factor is shown in Fig. 11 for the base material moisture diffusion rate and with diffusion rates scaled by $\times 100$ and $\times 0.01$. Up to 10 % higher dehumidification is obtained when the layer thickness is decreased or when the diffusion rate is increased such that a greater portion of the layer can be used to adsorb moisture.

Fig. 11 Comparison of the variation in DR (normalized) with scaling of the desiccant layer thickness for three different moisture diffusivity rates



6 Alternative Wheel Designs

A number of alternative desiccant wheel designs have been proposed to further improve performance. These include

1. inclusion of a third ‘purge’ stage in the wheel in addition to the process and regeneration stages,
2. incorporating internal cooling in the process air stage,
3. splitting the single regeneration stage into multiple stages with different regeneration temperatures,
4. having multiple consecutive supply and regeneration stages in the wheel.

6.1 Purge Section

The simplest method of decreasing the process outlet air humidity and temperature is to incorporate a small third ‘purge’ stage in the wheel after the regeneration stage. This arrangement is shown in Fig. 12a. This works by removing the hottest and wettest section of the process air outlet stream, which exits from the channels immediately after the regeneration stage when the desiccant material is still too hot for effective adsorption. Purge air exiting the desiccant wheel can be either

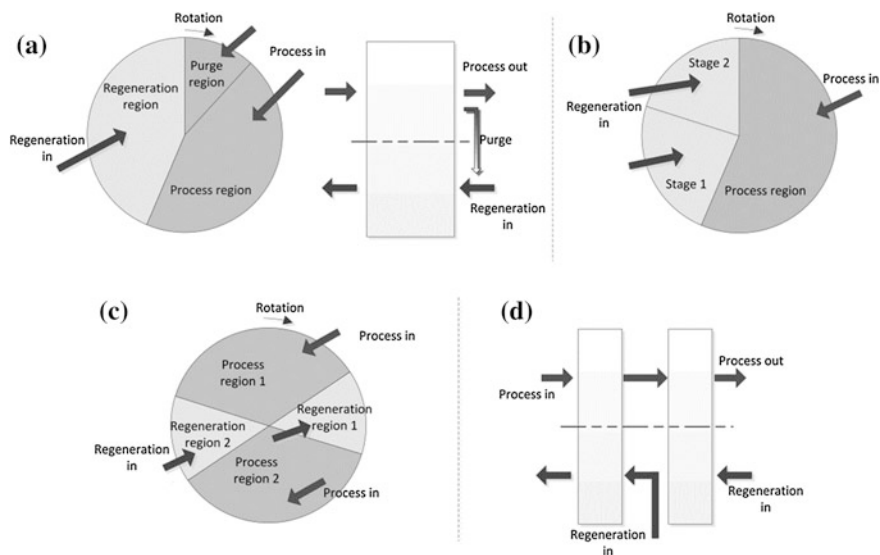


Fig. 12 Schematic diagrams of alternative desiccant wheel designs. **a** Wheel with process air purge. **b** Wheel with internal staged regeneration. **c** Multiple process and regeneration stages (single wheel). **d** Multiple process and regeneration stages (2 wheels)

redirected to the regeneration inlet (to recycle heat from the regeneration section), or exhausted to atmosphere. The decrease in average process outlet air humidity is off-set by the reduced total delivered air volume.

For example, Golubovic et al. [13] numerically investigated the influence of varying purge area fraction for different values of S , T_r , and L . For a regeneration temperature of 140 °C and a molecular sieve 3A wheel, 8–10 % higher dehumidification was obtained for $S = 0.5$ – 0.66 with a reduction in delivered air of approximately 20 %. The regeneration energy used per unit of dehumidification was found to always be lower with a purge section. Hence, a purge section is most appropriate when low outlet humidity is required, or when lower regeneration energy consumption is desired and an increase in electrical power consumption is deemed tolerable.

6.2 Internal Process Air Cooling

As identified above, it is highly desirable to minimize the heating of the process air, with optimal performance corresponding to isothermal dehumidification. This can be achieved by passing a cooling stream, for example air or water at ambient conditions, near to the process air stage. For example, Kodama et al. [19] designed and tested a prototype device incorporating both process air cooling and regeneration air heating in the walls of the wheel. While process air cooling is known to improve dehumidification performance, the complexity of such a design, and of similar designs, is a significant limitation to the development of a commercial wheel.

6.3 Internal Staged Regeneration

The idea of using staged regeneration is to divide the regeneration into multiple separate regions through which regeneration airstreams with different temperatures pass, so as to reduce the regeneration heating required. This is shown schematically in Fig. 12b. As discussed by Collier and Cohen [7], this increases the thermal COP of the system but reduces the amount of dehumidification of the process stream. However, the thermal COP can also be increased by increasing S without using staged regeneration, and the corresponding dehumidification rate is higher than for the staged regeneration case.

6.4 Multiple Process and Regeneration Stages

The conventional desiccant wheel design consists of a single process air and regeneration air stage. A modification of this design is to divide the wheel face into two (or more) process air and regeneration air stages as shown in Fig. 12c or, alternatively, to use two desiccant wheels operated in series as shown in Fig. 12d. In the latter case, the length of each wheel can be reduced to minimize any increase in pressure drop.

Dividing the process into two more stages allows interstage reheating of the regeneration air and/or interstage re-cooling of the process air [10]. This allows the process to act more like an isothermal process with resulting increase in thermodynamic equilibrium driving force for moisture adsorption.

In another multi-staged arrangement, Li et al. [23] designed and tested a system which used the outlet air from the first process stage as the inlet air for the second process stage, but with a single source of high temperature regeneration air feeding both desiccant wheels. In this case, a greater dehumidification of the process air can be obtained, with a corresponding decrease in the required building supply air volume. The operating performance was measured with a full desiccant A/C system installed in a building over a day. The average COP_t of 0.95 and average COP_e of 5.8 obtained are comparable or better than conventional systems, though no direct comparisons were made.

A multi-staged wheel A/C system is more complex than a conventional system, although the modifications to the desiccant wheel itself are only minor. Whether such a system is cost-effective or not is still to be determined.

7 Conclusions and Future Research Directions

The ideal desiccant wheel would enable a complete transfer of moisture between the process and regeneration airstreams without any heat transfer. In a real wheel, it is only possible to limit this heat transfer and maximize the rate of moisture transfer between the desiccant solid and airstreams.

The relative importance of optimizing specific desiccant material and wheel construction parameters is summarized in Table 3. The ranking is made considering plausible variations, which could be employed, and the resultant influence that these changes would have on the overall dehumidification rate. These conclusions assume parameter variations in the range examined and that the optimum wheel rotational rate is chosen.

The most important parameters relate to the generation and transfer of heat in the wheel. That is, the enthalpy of adsorption of the desiccant material and the matrix (overall) heat capacity should be as low as possible. These parameters are more important than the isotherm shape, which only needs to be of a general Type 1 (concave down) form. Since the job of the desiccant material is to act as a

Table 3 Desirable qualitative magnitudes of various wheel parameters

Importance ^a	Parameter	Specification
Highest	Enthalpy of adsorption	As low (close to H_{vap}) as possible
	Matrix heat capacity	As low as possible
	Isotherm shape	Type 1M, R between 0.1 and 0.3
	Moisture capacity	Max. of around 0.3–0.4 kg/kg
	Process face area fraction	0.5–0.6
	Desiccant layer thickness	Thin layer (e.g., <0.2 mm depending on D_{eff})
	Moisture diffusivity	As high as possible
Lowest	Channel shape	High Nu/a_f . (Small Nu can be compensated for by a longer channel, lower velocity, or small diameter) Increasing NTU above 12 leads to <20 % extra dehumid performance
	Thermal conductivity	As low as possible

^a Assuming that the rotation rate is optimized and considering plausible parameter variations

temporary holding point for moisture in transit between the two airstreams, the overall storage capacity is only moderately important, such that it is large enough to allow a slow rotation rate to minimize the overall heat transfer for a realistic size wheel.

Having a greater quantity of desiccant material in the wheel can actually be detrimental to the performance, as this adds thermal capacitance and only increases the moisture storage capacity, all of which may not be usable depending on the moisture diffusivity.

While the channel shape, which defines the non-dimensional heat and mass transfer gradients and the friction coefficient, is an important parameter, the variation that exists between different channel shapes with moderate aspect ratios is comparatively small. Furthermore, it is only the relative rates of heat/mass transfer and friction loss which are important, since low values of the non-dimensional heat/mass transfer parameter may be compensated for by a longer wheel, slower air velocity, or small channel diameter. The dehumidification is more limited by thermal effects as the heat transfer efficiency increases.

It is important to re-emphasize that for the desiccant wheel to perform well as part of a complete A/C system, the parasitic fan power required to overcome the pressure drop through the wheel must be small. This requirement drives the selection of the wheel length, face velocity, channel diameter, and wheel area, parameters which are independent of the desiccant material and so should be able to be optimized for any material.

The simplest and by far the most effective method of improving the performance of desiccant-wheel-based A/C systems that suffer from high electrical power consumption is to increase the wheel area and lower the face velocity and wheel rotation rate.

While much of the current research focuses on improving the isotherm characteristics of desiccant materials, the comparisons above have shown that the thermal properties generally play a more important role. Whether it is practical to

develop new materials with lower enthalpy of adsorption and thermal capacitance is unclear, though the best application for materials with very high equilibrium moisture capacity (for example, the composite SWS-1L or 'SAP') is in using these to create very thin desiccant layers, which minimize the overall heat capacity of the wheel. This, combined with further work in selecting wheel parameters to minimize the pressure drop, is likely to be the most promising avenues for future wheel developments.

References

1. Adamson A, Gast A (1997) Physical chemistry of surfaces. Wiley, New York
2. Aristov Y, Glaznev I, Freni A, Restuccia G (2006) Kinetics of water sorption on SWS-1L (calcium chloride confined to mesoporous silica gel): influence of grain size and temperature. *Chem Eng Sci* 61:1453–1458
3. Aristov Y, Tokarev M, Cacciola G, Restuccia G (1996) Selective water sorbents for multiple applications, 1. CaCl_2 confined in mesopores of silica gel: sorption properties. *React Kinet Catal Lett* 59(2):325–333
4. Chung L, Lee D-Y (2009) Effect of desiccant isotherm on the performance of desiccant wheel. *Int J Refrig* 32:720–726
5. Close D, Banks P (1972) Coupled equilibrium heat and single adsorbate transfer in fluid flow through a porous medium-II predictions for a silica gel air drier using characteristic charts. *Chem Eng Sci* 27:1157–1169
6. Collier R (1989) Desiccant properties and their affect on cooling system performance. *ASHRAE Trans* 1:823–827
7. Collier R, Cohen B (1991) An analytical examination of methods for improving the performance of desiccant cooling systems. *J Sol Energy Eng* 113:157–163
8. Collier R, Cale T, Lavan Z (1986) Advanced desiccant materials assessment. Gas Res Inst, Chicago
9. Czanderna A, Neidlinger H (1988) Polymers as advanced materials for desiccant applications, report 255–3443. Solar Energy Research Institute, Colorado
10. Ge T, Li Y, Dai Y, Wang R (2010) Performance investigation on a novel two-stage solar driven rotary desiccant cooling system using composite desiccant materials. *Sol Energy* 84:157–159
11. Goldsworthy M, White S (2012) Limitationing heat and mass transfer mechanisms in desiccant wheels. *Int J Refrig*, Under review
12. Goldsworthy M, White S (2011) Optimisation of a desiccant cooling system design with indirect evaporative cooler. *Int J Refrig* 34:148–158
13. Golubovic M, Hettiarachchi M, Worek W (2007) Evaluation of rotary dehumidifier performance with and without heated purge. *Int Commun Heat Mass Transfer* 34:785–795
14. Incropera F, DeWitt D (2002) Fundamentals of heat and mass transfer. Wiley, New Jersey
15. Lee J, Lee DY (2012) Sorption characteristics of a novel polymeric desiccant. Submitted to *Int J Refrig*
16. Jia C, Dai Y, Wang R (2006) Experimental comparison of two honey-combed desiccant wheels fabricated with silica gel and composite desiccant material. *Energy Convers Manage* 47:2523–2534
17. Jurinak J (1982) Open cycle solid desiccant cooling: component models and system simulations Ph.D Thesis. University of Wisconsin, Madison

18. Kakiuchi H, Iwade M, Shimooka S, Ooshima K, Yamazaki M, Takewaki T (2004) Novel zeolite adsorbents and their application for AHP and desiccant system. Proceedings of the IEA expert meeting. Kizkalesi, Turkey
19. Kodama A, Watanabe N, Hirose T, Goto M, Okano H (2005) Performance of a multipass honeycomb adsorber regenerated by a direct hot water heating. *Adsorption* 11:603–608
20. Kuma T, Okano H (1988) Patent No. 4911775. USA
21. La D, Li Y, Dai YJ, Ge TS, Zhang RZ (2002) Development of a novel rotary desiccant cooling cycle with isothermal dehumidification and regenerative evaporative cooling using thermodynamic analysis method. *Energy* 44:778–791
22. La D, Dai Y, Li Y, Wang R, Ge T (2010) Technical development of rotary desiccant dehumidification and air conditioning: a review. *Renew Sustain Energy Rev* 14:130–147
23. Li H, Dai Y, La D, Wang R (2011) Experimental investigation on a one-rotor two-stage desiccant cooling/heating system driven by solar air collectors. *Inst Refrig Cryogenics* 31:3677–3683
24. Lide D (ed) (2009) *Handbook of chemistry and physics*. CRC Press/Taylor and Francis, Boca Raton
25. Munters C (1961) Patent No. 3009540. USA
26. Ni C, San J (2002) Measurement of apparent solid-side mass diffusivity of a water vapor-silica gel system. *Int J Heat Mass Transf* 45:1839–1847
27. Pennington N (1955) Patent No. 2700537. USA
28. Pesaran A, Mills A (1986) Moisture transport in silica gel packed beds I. Theoretical study. Solar Energy Research Institute, Colorado
29. Pesaran A, Penney T, Czanderna A (1992) Desiccant cooling: state-of-the-art assessment. National Renewable Energy Laboratory, Golden, Colorado
30. Ruivo C, Cost J, Figueiredo A (2012a) Heat and mass transfer in matrices of hygroscopic wheels. In: Delgado J (ed) *Heat and mass transfer in porous media*. Springer, Berlin, pp 245–263
31. Ruivo C, Costa J, Figueiredo A, Kodama A (2012b) Effectiveness parameters for the prediction of global performance of desiccant wheels: an assessment based on experimental data. *Renew Energy* 38:181–187
32. Schilling R, Harris S (2000) *Applied numerical methods for engineers*. Brooks/Cole, Pacific Grove
33. Shah R (1975) Laminar flow friction and forced convection heat transfer in ducts of arbitrary geometry. *Int J Heat Mass Transfer* 18:849–862
34. Shim J, Song G, Lee D (2008) Dehumidification and regeneration of a polymeric desiccant. International sorption heat pump conference, Seoul
35. Wang X, Zimmermann W, Ng K, Chakraborty A, Keller J (2004) Investigation on the isotherm of silica gel+water systems. *J Therm Anal Calorim* 76:659–669
36. White S, Goldsworthy M, Reece R, Spillman T, Gorur A, Lee D-Y (2011) Characterisation of desiccant wheels with alternative materials at low regeneration temperatures. *Int J Refrig* 34(8):1786–1791
37. Yu I, Aristov Y, Tokarev M, Cacciola G, Rectucci G (1997) Properties of the system calcium chloride–water confined in pores of the silica gel; specific heat, thermal conductivity. *Russ J Phys Chem* 71(3):391–394
38. Zheng W, Worek W, Novosel D (1995a) Effect of operating conditions on optimal performance of rotary dehumidifiers. *Trans ASME* 117:62–66
39. Zheng W, Worek W, Novosel D (1995b) Performance optimisation of rotary dehumidifiers. *Trans ASME* 117:40–44
40. Ziegler F (2011) The phenomenon of solar cooling. International Congress of Refrigeration. IIR, Prague

Separate Sensible and Latent Cooling

Jiazhen Ling, Yunho Hwang and Reinhard Radermacher

List of Symbols

a	POD coefficient
A	Area (m^2)
AC	Alternating current
BLDC	Brushless DC
COP	Coefficient of performance
D	Diameter (m)
DW	Desiccant wheel
EA	Exhaust air
EC	Evaporative cooling
EW	Enthalpy wheel
f_{cl}	Clothing factor
h	Heat transfer coefficient/enthalpy ($\text{kW/K m}^2/\text{kJ/kg}$)
HX	Heat exchanger
I	Solar incidence (W)
M	Metabolic rate (W)
N	Fan rotation speed (RPM)
P	Pressure lift (Pa)
Pa	Water vapor partial pressure (Pa)
PR	Pressure ratio
Q	Air flow rate (m^3/s)
RH	Relative humidity (kg/kg dry air)
SHF	Sensible heat factor
SSLC	Separate sensible and latent cooling
t	Air temperature ($^{\circ}\text{C}$)
UA	Overall heat transfer conductance (kW/K)
v	Velocity or temperature (m/s or $^{\circ}\text{C}$)

J. Ling · Y. Hwang (✉) · R. Radermacher
Center for Environmental Energy Engineering, University of Maryland,
4164 Glenn L. Martin Hall Bldg, College Park, MD 20742, USA
e-mail: yhhwang@umd.edu

W	Work output (W)
WVR	Water removal rate (g/s)

Subscripts

a	Air
c	Convective
cl	Clothing
comp	Compressor
d	Diffusive
D	Direct
disp	Displacement
g	Glass
i	Inside
in	Inlet
ise	Isentropic
o	Operative/outside
out	Outlet
r	Radiative
vol	Volumetric

Greek letters

α	Absorptivity
φ	POD basis
ΔP	Pressure drop
Δt	Superheat/subcooling
η	Compressor efficiency
ρ	Density

1 Introduction

During the operation of a conventional air-conditioning (AC) system, two kinds of cooling, i.e., sensible cooling and latent cooling are usually simultaneously provided to a conditioned space. Cold air from the evaporator reduces the temperature of the conditioned space and therefore provides sensible cooling. When the refrigerant temperature in the evaporator is below the dew point of room air, it causes water vapor in moist air to condense on the evaporator and consequently reduces the humidity ratio of air. The drier supply air removes the latent load in the space. Figure 1 shows the psychrometric process of two aforementioned types of cooling, where points A, B, and D refer to return air from the space, the dew point of space air, and supply air, respectively.

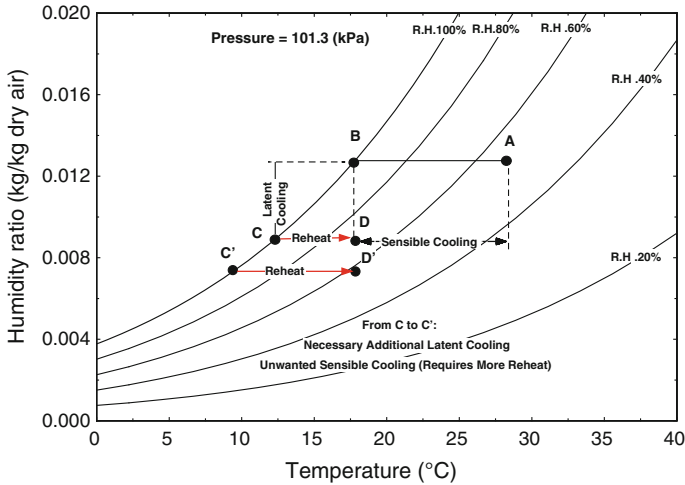


Fig. 1 Psychrometric process of conventional AC operation

There are two limitations related to the operation of conventional AC systems:

- Reheat process reduces system COP

Theoretically, the process of supply air flowing through the evaporator can be assumed to follow the path that is composed of a horizontal sensible load removal part (point A to point B) and a latent load removal part along the 100 % relative humidity (RH) line from B to C. In general, the temperature of point C is too low if occupants’ thermal comfort is considered; therefore, a reheat process, typically adapted in commercial buildings, is added to increase the temperature of point C to the temperature of point D. The reheat process, usually carried out by electric heaters, requires extra energy input and increases the total net energy input (Eq. 1). Hence, the reheat process reduces the COP [25]

$$COP = \frac{\text{useful refrigerating effect}}{\text{net energy input}} \tag{1}$$

- Conventional AC systems lack the independent control of sensible and latent cooling.

The reheat process in conventional systems is in fact caused by the lack of independent control of sensible and latent cooling. The path from point B to point C along the 100 % RH line reveals that the amount of latent cooling and the amount of sensible cooling are interdependent on each other and relevant to the slope of the 100 % RH line. That is to say, removing a certain amount of water vapor requires an accompanying ratio of temperature reduction. Therefore, when the system requires more latent cooling, it is more likely that the conditioned space becomes

sensibly over-cooled. Such a dependent relationship not only costs a reheat stage but also causes a control issue in a conventional AC system's operation. For example, when more people enter the room, extra latent cooling is required. In such case, the supply air point moves downward to point C'. Meanwhile, an unnecessary amount of sensible cooling (the horizontal blue arrow pointing leftward) has to be added to the room as well. This requires more reheat power input to increase temperature for thermal comfort and further reduces the COP.

In order to overcome the two limitations of conventional systems, the separate sensible and latent cooling (SSLC) approach is hereby proposed as a solution. Figure 2 plots the psychrometric process of one kind of SSLC systems, which consists of one vapor compression system (VCS) and one solid desiccant wheel (DW). In this system, the VCS provides only sensible cooling (point A to point B) required by the conditioned space at both elevated air temperature leaving the evaporator (point B in Fig. 2 versus point C in Fig. 1) and a higher air mass flow rate (MFR). The reason for a higher air MFR requirement is to compensate for the reduced enthalpy difference of air across the evaporator and hence maintain the capacity of sensible cooling. Since the evaporating temperature of the VCS is above the dew point temperature of air, the DW is used to reduce the water vapor content in part of the air leaving from the sensible evaporator. The dry air from the DW mixes with the rest of the air from the evaporator and is delivered to the conditioned space (point D).

DWs absorb water vapor in air and provide latent cooling, but they generate an amount of heat of adsorption during the process and increase the dry air temperature. Theoretically, the amount of latent cooling is equal to the amount of sensible heat generation. Hence, the operation of DWs follows an isenthalpic line, which is from point B to point C in Fig. 2.

The SSLC systems have two following features during their operations:

- No reheat process is needed

Since the VCS used in an SSLC system operates above the dew point temperature, the supply air temperature (see point D in Fig. 2) is thermally comfortable enough to be sent to the conditioned room directly. No reheat is necessary in the SSLC systems.

- Independent control on sensible and latent cooling

The SSLC system uses a VCS to provide sensible cooling. In consequence, any fluctuations of sensible cooling demand can be simply met by changing the capacity of the VCS. The control method to deal with the fluctuation of latent cooling demand is a little bit more complicated. Of course, the rotation speed of DW can be adjusted to meet the fluctuation of latent cooling demand within a certain range. Any latent cooling demand change beyond the reach of rotation speed adjustment can be met by either increasing the regeneration temperature or increasing the air MFR through a DW. It should be noted that although a DW is a stand-alone device providing latent cooling, any amount of the latent capacity change would theoretically lead to the same amount of change in the sensible heat

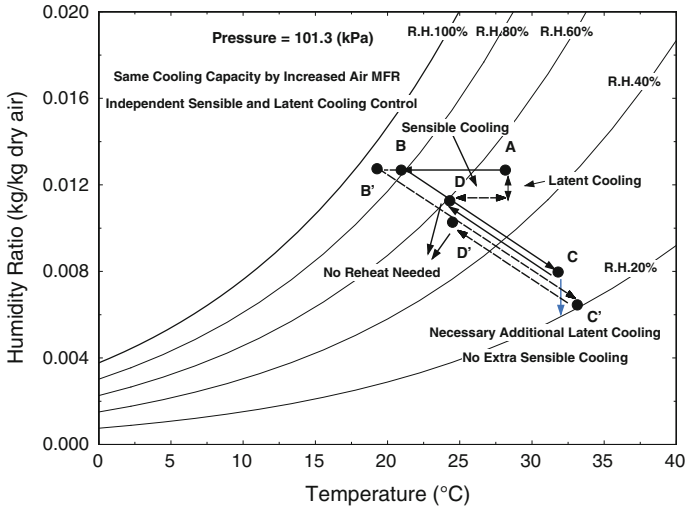


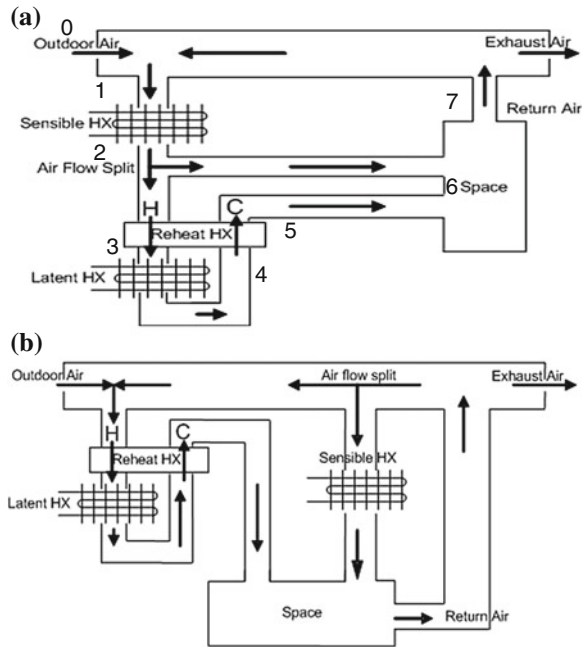
Fig. 2 Psychrometric process of one kind of SSLC system (VCS + DW)

generation. Therefore, the VCS must increase the cooling capacity to cover the extra heat. However, such an increase will not lead to overcooling because the VCS still operates above the dew point temperature.

2 SSLC Using Two Vapor Compression Cycles

In this section, the SSLC systems using two VCS are introduced. The systems use one VCS to provide sensible cooling and a second VCS to provide latent cooling. Two schematic drawings are demonstrated in Fig. 3: one is the SSLC system in a serial configuration and the other is the SSLC system in a parallel configuration. In both configurations, a counter-flow heat exchanger (HX) is used in the system to utilize the cooling from the latent evaporator for pre-cooling of the incoming air. The sensible and latent HXs are arranged in series along the process airflow direction in the serial configuration. Return air from space is mixed with outdoor fresh air before flowing into the sensible evaporator. The airflow is divided into two streams after passing through the sensible evaporator. While one stream, as in Fig. 3a, is sent to the reheat HX for pre-cooling before being processed through the latent evaporator, the other stream bypasses the reheat HX. After exiting the latent evaporator, the air stream is reheated through the reheat HX and is finally mixed with the other stream. The mixed stream supplies to space. In the second configuration, the sensible and latent HXs are arranged in parallel. Its only difference compared to the serial configuration is that the return flow is split into two streams, and one stream passes through the sensible HX, while other stream is mixed with outdoor fresh air.

Fig. 3 Schematic diagram of an SSLC system (the numbers represent air state points in the system which are the same as in Fig. 4, C and H refer to cold and hot streams through the reheat HX) [23]. **a** Serial configuration, **b** Parallel configuration



2.1 Modeling Approach and Results

Engineering equation solver (EES) [16] was used to model SSLC systems. A conventional combined cooling system, which serves as a comparison baseline, was also simulated in the EES. Assumptions used in the modeling are as follows:

Refrigerant side:

- Refrigerant: R410A
- Degree of subcooling: 5 K [27]
- Degree of compressor superheating: 10 K [27]
- Isenthalpic expansion
- Condenser pressure drop: 100 kPa [12]
- Evaporator pressure drop: 50 kPa [14]
- Isentropic efficiency is calculated as a function of the pressure ratio [17]
($\eta_{iso} = 0.9 - 0.0467 \times PR$)
- Volumetric efficiency is calculated as a function of the pressure ratio [17]
($\eta_{iso} = 1 - 0.04 \times PR$)
- Compressor motor efficiency: 0.95 [8]

Air side:

- No pressure drops and heat losses in the ducts and pipes.
- Return air and outdoor fresh air are well mixed.
- All the air mixing process is adiabatic.

Heat exchanger UA values:

- Total UA value of all HXs (exclude the internal HX) in the SSLC systems is 50 kW/K.
- Total UA value of all HXs in the baseline system is 50 kW/K.

Initial conditions:

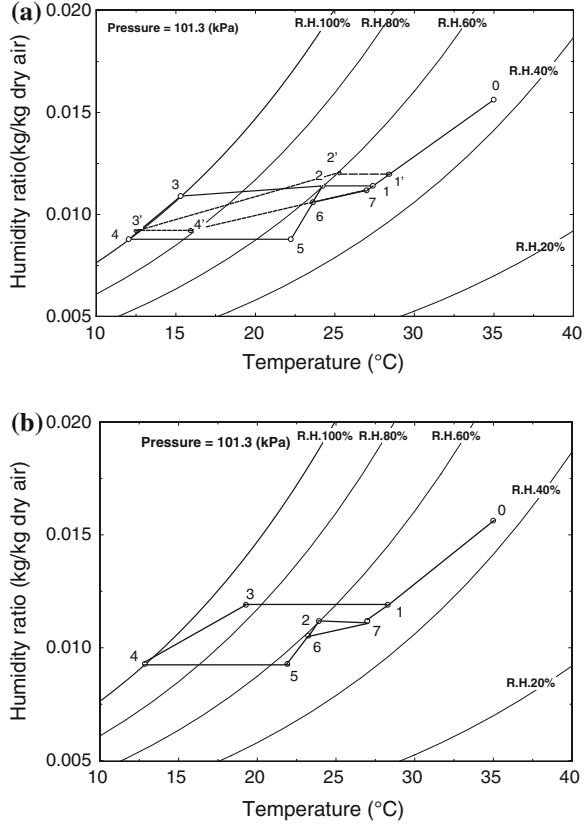
- Outdoor air temperature is under AHRI standard 210/240 [2]: 35 °C, 44 % RH.
- Outdoor air mass flow rate is set to be 1 kg s⁻¹ (ANSI/ASHRAE standard 62.1, 2004) 5.
- Space air condition is under AHRI standard 210/240 [2]: 27 °C, 50 % RH.
- Space load is 100 kW.
- Sensible heat factor (SHF) of the space is 0.7.
- For the baseline system, the mass flow rate of air is set to be 5 m³/s based on the space load of 100 kW (ASHRAE standard 140, 2004) [6].

Range of conditions studied in the later parametric study:

- Outdoor temperature: 15–37 °C
- Outdoor humidity ratio: 5.8 g/kg dry air (15 °C, 55 % RH) ~ 28 g/kg dry air (37 °C, 70 % RH)

Figure 4 indicates the psychrometric process of the two aforementioned SSLC systems (solid line) and the conventional reheat system (baseline system) (dotted line) on a psychrometric chart. For the baseline system, in order to meet the 30 kW latent cooling demand (calculated from SHF = 0.7), air temperature exiting the evaporator is 12.8 °C (from airflow rate 5 m³/s), which is much lower than the dew point temperature 16.7 °C. Based on the size of the evaporator used in the model, the refrigerant temperature is 6.0 °C. Decreasing the temperature of the return air below the dew point temperature consumes much power in the VCC. The COP of the baseline is 3.9. The total refrigerant mass flow rate in the system is 0.712 kg s⁻¹. For the SSLC system using serial configuration, the sensible heat load is removed separately at first. It can be simply achieved by decreasing the air temperature by 3 °C (the reason of choosing 3 °C will be discussed later) and increasing the airflow rate (AFR) to maintain the total sensible load. In order to do a fair comparison to the baseline system, the same AFR is used for the latent heat removal cycle. It is cooled down to approximately the same temperature as in the baseline system, which is 12.0 °C. The power consumption of the SSLC system is 30 % lower, and the COP of the SSLC is 5.45, which is 39 % higher than that of the baseline system. For the SSLC system using parallel configuration, the sensible

Fig. 4 Comparison of psychrometric process of SSLC systems and baseline system in psychrometric chart [23]. **a** Psychrometric process of the serial SSLC configuration and the baseline system. **b** Psychrometric process of the parallel SSLC configuration (SSLC: 0 outdoor condition, 7 indoor condition, 1 mixing point, 2 after sensible HX, 3 after pre-cooling, 4 after latent HX, 5 after reheat, and 6 supply air; Baseline: 1' mixing point, 2' after pre-cooling, 3' after evaporator, and 4' after reheat and supply air)



heat load is removed through decreasing the air temperature of return air by 3 °C. The same AFR is used for latent heat removal cycle as in the baseline system. It is cooled down to 12.8 °C. The COP of the SSLC using parallel configuration is 5.50, which is 41 % higher than that of the baseline system. The total refrigerant mass flow rates in the sensible cycle and the latent cycle are 0.38 and 0.32 kg s⁻¹, respectively.

The reasons for these energy savings are explained as follows. The baseline VCC consumes 20 and 10.5 kW to meet the sensible and latent cooling loads by assuming they are proportional to their respective cooling capacities which are 78.3 and 41.3 kW, respectively. However, in the SSLC system, the refrigerant evaporating temperature of the sensible cycle is increased to 19.1 °C due to the higher air temperature. The corresponding evaporating pressure is increased from 1.0 to 1.4 MPa, and therefore, the sensible cycle compressor pressure ratio is decreased from 2.93 (baseline system) to 2.00 (SSLC system). The power consumptions of the sensible and latent cycles of the SSLC system are estimated to be 9.7 and 12.3 kW, respectively. This means that the sensible cycle saved 10.3 kW power as compared to the baseline system, while the latent cycle consumes 1.8 kW

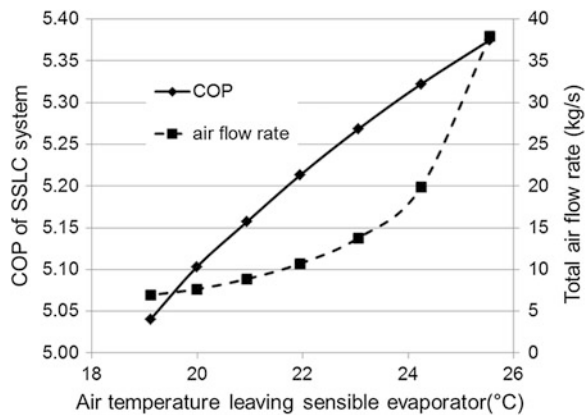
more power. The similar latent cycle power consumption is an expected outcome since both the baseline system and the SSLC system remove the same amount of water vapor (16 g s^{-1}). The lower refrigerant mass flow rate in the SSLC system (0.700 kg s^{-1}) than the one in the baseline system (0.712 kg s^{-1}) also contributes to the power savings. One thing should be noted is that all the power consumptions calculated above are compressor power inputs only.

Since there are two evaporators in the SSLC system which account for higher UA value than the one in the baseline system, a higher condensing approach temperature is expected in the SSLC system, which slightly increases the power consumption for the latent cycle. However, the SSLC system still consumes 8.6 kW lower than the baseline. There are also other benefits resulting from the SSLC system. In the sensible cycle, the pressure ratio of the compressor reduced from 2.93 (baseline) to 2.00, which leads to a 6.6 % isentropic efficiency improvement (0.76–0.81). Better compressor efficiency and reduced power inputs also reduce the total displacement volume of the two compressors in the SSLC system, which can be 25 % smaller than that in the baseline system. However, it should be noted that the SSLC system requires a higher AFR from 5 to 15.9 m³/s. This is due to the smaller air enthalpy difference in the sensible cycle. More air is required to meet the sensible cooling load. This raises a question whether the increased power consumption of the fan will offset the power savings from compressors. This question is addressed in the later subsections (Sects. 2.3, 2.4).

2.2 Parametric Studies

Figure 5 can be used to clearly demonstrate the previously mentioned high AFR issue. The air temperature leaving the sensible evaporator changes from 19 °C, which is close to dew point temperature, to 25.5 °C. The COP of the SSLC system increases with the increase in the air temperature leaving sensible evaporator. However, the highest COP coincides with the highest air mass flow rate, which is

Fig. 5 COP and total airflow rate of SSLC system under different air temperature leaving sensible evaporator [23]



almost five times as high as the baseline system. If both the COP benefit and the higher air mass flow rate penalty are considered simultaneously, the temperature leaving the sensible evaporator can be set between 22 °C (70 % RH) and 24 °C (60 % RH). Since the higher temperature condition (24 °C, 60 % RH) shows a higher COP, that condition is selected for the rest of the study.

Figure 6 shows different power saving potentials of the SSLC system under different ambient conditions. The ambient temperature is set to be 37 °C, and the RH ranges from 20 to 70 %. This result demonstrates the feature of distributing the sensible and latent cooling load depending on the ambient condition. While the sensible load of the system was kept roughly constant between 60 and 66 kW, the latent load varied from 42 to 88 kW. Therefore, the ratio of the sensible load to latent load decreases with the increase in RH, which is shown on the secondary y-axis. It is also observed that the power savings decrease when the ambient RH increases. This is because more power is required for the latent cycle, which makes the savings from the sensible cycle less significant. However, even under the highest RH condition, the power savings are over 17 % as compared to the baseline system.

Fig. 6 Power savings under different ambient relative humidity [23]

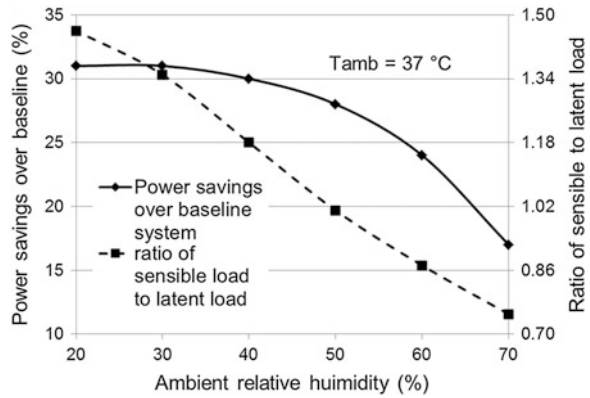


Fig. 7 Power savings under different ambient temperatures [23]

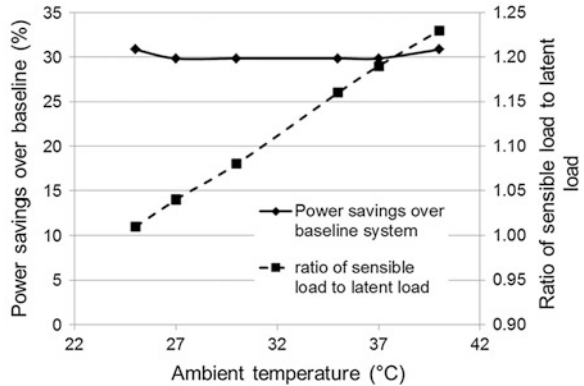


Fig. 8 Six zones on the psychrometric chart (clockwise from the top right: hot and humid; standard; hot and dry; cool and dry; cool but humid and humid) [23]

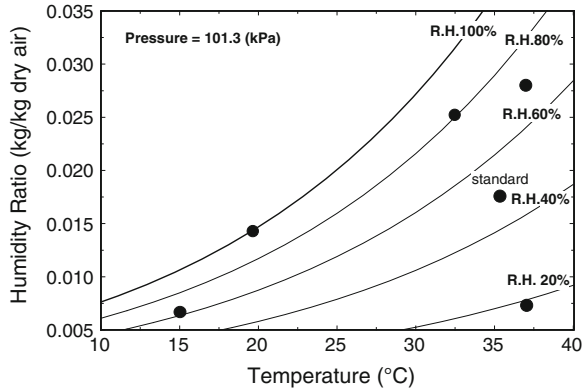


Table 1 Power savings under different climate conditions [23]

Zone	Standard	Cool and dry	Cool but humid	Hot and dry	Hot and humid	Humid
Condition	35 °C/44 % RH	15 °C/55 % RH	20 °C/100 % RH	37 °C/15 % RH	37 °C/70 % RH	32 °C/80 % RH
Power savings	30 %	50 %	33 %	32 %	17 %	22 %

Figure 7 shows the power savings under different ambient temperatures. The ambient humidity ratio is set to be constant at 15 g/kg dry air, while the temperature ranges from 25 to 40 °C. The ratio of the sensible to latent cooling increases load with the ambient temperature. Meanwhile, the power savings remain almost constant. This trend indicates that the power savings of the system are greatly affected by the latent load of the system but not much affected by the sensible load. Detailed discussion is provided in the later chapter.

To evaluate the performance of the SSLC system over a wide ranging envelop of the ambient conditions, the system performance was modeled under five different climatic conditions shown on the psychrometric chart in Fig. 8. The power savings over the baseline system are calculated for different climate conditions. The results are summarized in Table 1. While the maximum power savings are achieved in the cool and dry conditions, the minimum power savings are achieved in the hot and humid conditions. It has been observed that under hot and humid conditions, the power of the latent cycle accounts for 70 % of the total power consumption and affects the total power savings of the SSLC system.

2.3 Air Distribution Method

The duct design and calculation of the fan power consumption were compared for the baseline system and the SSLC system. In the baseline system, the total air-side pressure drop in the system is around 285 Pa, including 100 Pa from the evaporator coil (calculated from the model above), 160 Pa from the duct and fittings, and

25 Pa from the filters [7]. Therefore, the fan motor was chosen based on the necessary pressure lift of 285 Pa and the volume flow rate of $5 \text{ m}^3 \text{ s}^{-1}$. The total power consumption of the conventional evaporator fan motor at $5 \text{ m}^3 \text{ s}^{-1}$ is 3.875 kW [17], which is 12.9 % of the compressor power. Compared to the baseline system, the SSLC system has significantly high AFR through the sensible HX, depending on the choice of exit air temperature. Thus, the duct–fan arrangement used for the baseline air distribution is not suitable for the SSLC system. In order to maintain the fan motor power consumption as low as possible while providing a high enough AFR through the system (to keep the COP high), one possible solution is minimizing the pressure lift of the fan. Kopko [21] presented a concept using an entire suspended ceiling called “a plenum” to distribute a large AFR. The air in the plenum is transported slowly so that there is a much smaller pressure drop than the typical duct design. In light of this, a propeller fan, which produces a relatively high AFR at a low pressure head, can be utilized. A new air distribution method consisting of the sensible HX(s) and the plenum is proposed for the SSLC system, as shown in Fig. 9. The sensible HXs are arranged around the fans in the plenum. Taken from the bottom by propeller fans, air flows through the sensible HXs and is then distributed to the space through openings placed along the entire plenum. It has been demonstrated in the previous subsection that the total air-side pressure drops of the evaporator can be reduced to 62.5 Pa. Since the air moves very slowly in the plenum, the pressure drop in the plenum can be neglected. According to this new design, the fan motor can be chosen to provide a large AFR, which is $15.9 \text{ m}^3 \text{ s}^{-1}$ (corresponding to $24 \text{ }^\circ\text{C}$ exit temperature) and a low pressure lift of 62.5 Pa for the SSLC system. Fan laws [9] in Eqs. (2)–(4) were used to compare the fan motor power consumptions of the two systems. The requirements of the two fans are listed in Table 2.

Fig. 9 Air distribution method for the SSLC system [23]

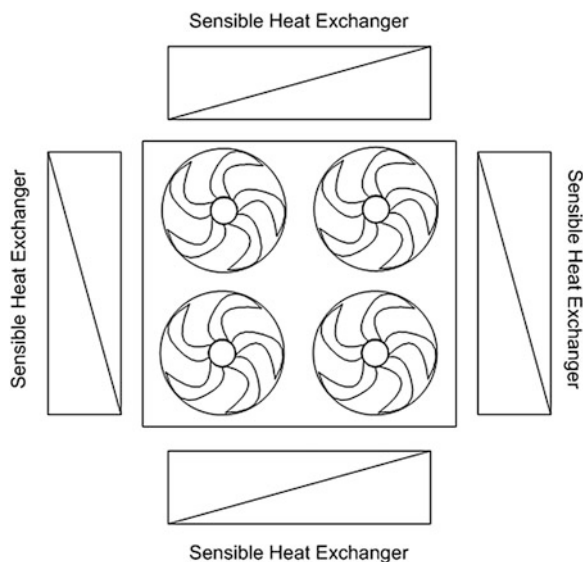


Table 2 Pressure lift and airflow rate requirements for fans [23]

System configuration	Pressure lift (Pa)	Airflow rate at the pressure lift (m ³ /s)
Baseline system	$P_2 = 285$	$Q_2 = 5$
SSLC system	$P_1 = 62.5$	$Q_1 = 15.9$

Fan laws [8] are used to compare the fan power consumptions of the two systems. The requirements of the two fans are listed in Table 2.

$$Q_1 = Q_2 \left(\frac{D_1}{D_2} \right)^2 \left(\frac{P_1}{P_2} \right)^{\frac{1}{2}} \left(\frac{\rho_2}{\rho_1} \right)^{\frac{1}{2}} \quad (2)$$

$$N_1 = N_2 \left(\frac{D_2}{D_1} \right) \left(\frac{P_1}{P_2} \right)^{\frac{1}{2}} \left(\frac{\rho_2}{\rho_1} \right)^{\frac{1}{2}} \quad (3)$$

$$W_1 = W_2 \left(\frac{D_1}{D_2} \right)^2 \left(\frac{P_1}{P_2} \right)^{\frac{3}{2}} \left(\frac{\rho_2}{\rho_1} \right)^{\frac{1}{2}} \quad (4)$$

By substituting Eq. (2) and the data in Table 2 into Eq. (3) to cancel out the ratio of diameters and neglecting the density difference, the ratio of RPMs becomes Eq. (5):

$$\frac{N_1}{N_2} = \left(\frac{Q_2}{Q_1} \right)^{\frac{1}{2}} \left(\frac{P_1}{P_2} \right)^{\frac{3}{4}} = 0.18 \quad (5)$$

By substituting Eqs. (2) and (5) to Eq. (4) and using the data in Table 2, we obtained the ratio of power consumptions:

$$\frac{W_1}{W_2} = \left(\frac{N_1}{N_2} \right)^{\frac{4}{3}} \left(\frac{Q_1}{Q_2} \right)^{\frac{5}{3}} = 0.70 \quad (6)$$

Equation (6) shows that it is theoretically possible for the SSLC system to save 30 % fan power consumption from the baseline. The reason is that the rotation speed of the fan in the SSLC system could be reduced to only 18 % of the baseline. By plugging in the data from Table 2 into Eq. (2), we found that the diameter of fan in the SSLC system was 2.6 times larger than that in the baseline system.

2.4 SSLC HXs Design (Conventional Design)

This subsection introduces one design of SSLC HX. It still uses conventional fin-and-tube HX as design candidates. In the later section, radiative HX provides an alternative choice. As described before, the SSLC system needs 3–4 times higher AFR than the conventional one. The higher the AFR through the HX, the larger pressure drop it may cause. One possible solution is to increase the frontal area of

the HX, meanwhile to decrease the number of banks. However, the single-bank design may have a negative impact on the heat transfer when compared to a multi-bank HX design. It is necessary to conduct a parametric study to find out an optimum design and compare it with conventional design in terms of total heat transfer area. The total heat transfer area is the sum of primary heat transfer area (tubes) and secondary heat transfer area (fins).

First, a conventional evaporator rated at 119.8 kW was modeled and its performance was compared to manufacturer's source [26]. The detailed specifications used in the model are listed as follows:

- Tube arrangement: Staggered divergent
- Number of tubes per bank: 84 ea.
- Number of tube banks: 3 ea.
- Number of circuits: 18 ea.
- Tube length: 0.889 m
- Tube outer diameter: 0.0127 m
- Tube thickness: 0.381 mm
- Tube horizontal spacing: 19 mm
- Tube vertical spacing: 25.4 mm
- Fins per Inch: 12.33 ea
- Fin type: Slit fins
- Fin thickness: 0.0011 m
- Coil face area: 1.90 m²
- Primary heat transfer area: 8.46 m²
- Secondary heat transfer area: 77.59 m²
- Total heat transfer area: 86.05 m²

Figure 10 shows the pressure drop as a function of AFR listed in the manufacturer source. It shows that the pressure drop at the design point (5 m³ s⁻¹) is 100.8 Pa. The model gave the pressure drop at design point to be 101.45 Pa. The relative error of the simulation is less than 0.6 %. Table 3 compares the modeling results and catalog data in terms of capacity and SHF. The average relative error of

Fig. 10 Pressure drop under different airflow rates through the evaporator [23]

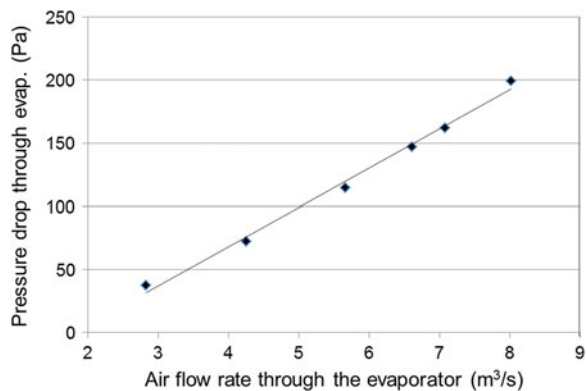


Table 3 Capacity and SHF comparison [23]

Wet-bulb temp.	16 °C				23 °C			
	Mfg. data	Model data	Mfg. data	Model data	Mfg. data	Model data	Mfg. data	Model data
Temp. (°C)	Capacity (kW)	Capacity (kW)	SHF	SHF	Capacity (kW)	Capacity (kW)	SHF	SHF
24	98	92.5	0.85	0.8	117.5	118	0.4	0.4
27	101	93	1	0.92	117.8	118.23	0.52	0.49
29	106.5	97.5	1	0.98	117.8	118.8	0.65	0.58
32	112	108	1	1	118.4	119.3	0.78	0.65

capacity is 2.89 %, and the average relative error of SHF is 6.13 %. Since the errors are in acceptable range, it is concluded that the model can be used to design baseline evaporator.

The total load of condenser is divided into four subcondensers. The design is conducted in the same manner as for the evaporator. Each of the four condensers is identical to each other and described as follows:

- Tube arrangement: Staggered divergent
- Number of tubes per bank: 60 ea.
- Number of tube banks: 1 ea.
- Number of circuits: 8 ea.
- Tube length: 3.7 m
- Tube outer diameter: 0.0127 m
- Tube thickness: 0.65 mm
- Tube horizontal spacing: 22.9 mm
- Tube vertical spacing: 25.4 mm
- Fins per inch: 20
- Fin thickness: 0.002 m
- Coil face area: 5.64 m²
- Primary heat transfer area: 7.46 m²
- Secondary heat transfer area: 157.27 m²
- Total heat transfer area: 164.73 m²

An in-house coil design software, CoilDesigner [19], was used to design the optimum SSLC HXs. The objective of the optimization is to minimize the total heat transfer area of evaporators and condensers. The constraints are capacity, air-side pressure drop, refrigerant-side pressure drop, and superheat/subcool temperature.

$$\text{Objective: } \min(\text{Total heat transfer area}); \quad (7)$$

$$\text{Constraints: } \text{Capacity} \geq \text{requirement}$$

$$\Delta P_{\text{air}} \leq 50 \text{ Pa};$$

$$\Delta P_{\text{ref}} \leq 50 \text{ kPa}; \Delta T \geq 2 \text{ K}.$$

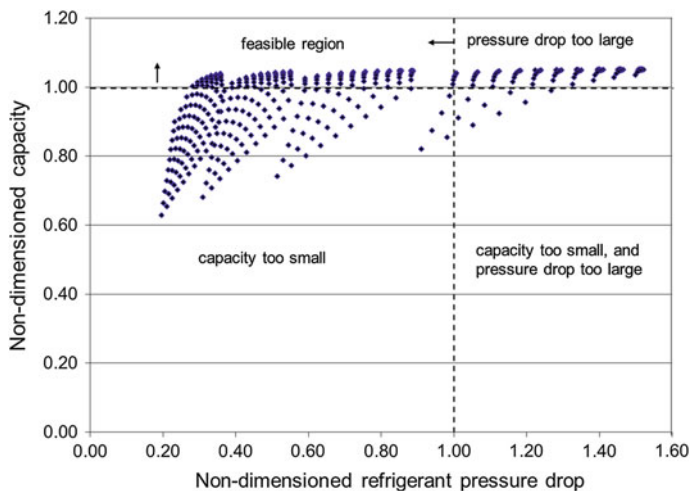


Fig. 11 Data screening for sensible HX design: 1 bank, 24 tubes/bank [23]

The optimization procedure is described as follows: a basic HX is simulated at first. Parametric studies are then conducted by changing the tube length, tube outer diameter, and fin pitch. All the possible optimization data from parametric studies are screened by capacity (denominator of the non-dimension data is 15 kW) and refrigerant-side pressure drop (denominator of the non-dimension data is 50 kPa) requirements as shown in Fig. 11. Then, superheat/subcooling temperature requirements are applied to the screened data, and the one with the smallest total heat transfer area in the feasible region is considered to be optimum point as long as the air-side pressure drop is within 50 Pa (Fig. 12).

The final design of SSLC HXs design is listed in Table 4. The sum of the total heat transfer area of the four HXs is 647.16 m², which is 13 % smaller than that of the baseline system, which is 744.97 m². The comparison shows the potential of obtaining the energy savings in the SSLC system without increasing the cost of HXs.

3 Desiccant-Assisted SSLC Systems

In this section, the SSLC systems using one VCS and one desiccant wheel (DW) are introduced. As mentioned in the previous chapter, one VCS is used for latent cooling. Consequently, the VCS in the sensible cycle cannot remove the entire sensible cooling in the space because a small amount of sensible cooling has to be removed associated with the latent cooling. From that point of view, the sensible cooling and latent cooling are not fully separated. The need of a complete cooling separation motivates the integration of DW into the SSLC system. The new SSLC

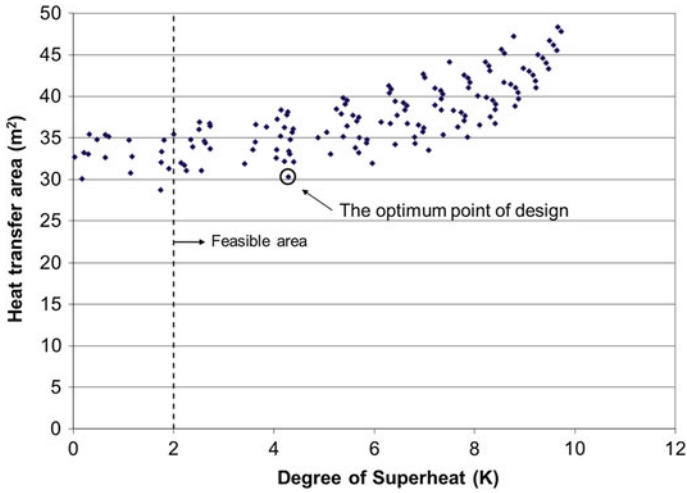


Fig. 12 Heat exchanger heat transfer area optimization [23]

Table 4 The optimization results of SSLC HXs [23]

Heat exchangers	Required number (ea)	Configuration (-)	Tube outer diameter (mm)	Capacity (kW)	Total heat transfer area (m ²)
Sensible evaporator	4	1 bank/24 tubes per bank	9	15.33	30.39
Latent evaporator	1	1 bank/48 tubes per bank	11.5	58	66.36
Sensible condenser	1	2 banks/84 tubes per bank	12.7	73.26	228.86
Latent condenser	1	3 banks/84 tubes per bank	12.7	68.14	228.86

system utilizes a DW to remove the entire amount of latent load from the space and a VCS to remove the entire sensible load. The benefit to the VCS is therefore similar to the previous system; however, since the separation is complete this time, the power saving potential of the DW-assisted SSLC is expected to be larger than that of the previous system. For the DW, the electric power consumption is very small compared to the compressor power input; however, heat is continuously required to regenerate the desiccant material. As the desiccant material technology improves, low-regeneration-temperature-driven DWs are available. When applying such DWs to the SSLC system, waste heat rejected from VCS is used to regenerate the DW which eliminates any need of extra heat or electricity input to provide the proper regeneration temperature. A test facility was built to examine the energy-saving potential of the DW-assisted SSLC system.

3.1 Test Facility

Figure 13 shows the schematic diagram of the experimental setup. The experimental setup consisted of a VCS and two wind tunnels. The two wind tunnels were constructed by polypropylene boards in order to simulate an indoor condition (upper closed duct) and an outdoor condition (bottom open duct). The two operating conditions were chosen based on the AHRI standard 210/240 (2008) test condition, which are 27 °C, 50 % RH for the indoor condition and 35 °C, 44 % RH for the outdoor condition. No ventilation air was added to the air stream inside the closed loop. The outdoor tunnel was a straight both-ends-open duct and built adjacently to the aforementioned closed loop. The outdoor condition was controlled by an environmental chamber, where the entire experimental setup was installed. The indoor condition was controlled by a heater and humidifier listed in Fig. 13. A 305 × 102 mm gap was cut between the two tunnels so that a 300 × 100 mm DW could fit inside of it. In the VCS, two pairs of compressors, evaporators, a condenser, and a gas cooler were prepared for the R410A and CO₂ tests. The two variable-speed rotary compressors provided the same cooling capacity, which was set to be 3.5 kW. The two evaporators and condenser (gas cooler) were almost identical to each other, except that the tube thickness of the R410A HXs was much thinner than that of the CO₂ HXs (0.3 mm vs. 1.0 mm). All the HXs were made with copper tubes and aluminum fins. An electronic expansion valve (EXV) was used to control the pressure ratio and mass flow rate of the

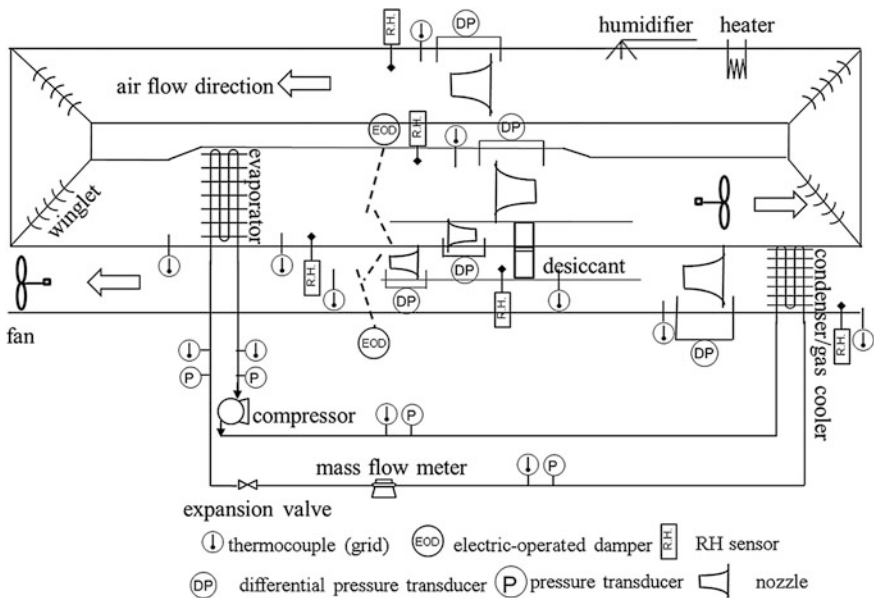


Fig. 13 Schematic diagram of the experimental setup [22]

refrigerants. The DW, which was cylindrical in shape with honeycomb-shaped cells, slowly rotated as it continuously dehumidified the incoming process airflow. Both the indoor and outdoor tunnels were separated into two subtunnels in the vicinity of the DW. The cooled air from the evaporator was divided into two parts. A large portion of the cooled air bypassed the DW and is assumed to be directly supplied to a space, while the rest moved through the DW. The distribution of the two airflows was decided based on the required latent capacity (0.7 kW). For the open duct, the same amount of airflow as used in the process duct was sent to regenerate the DW, while the rest was directly exhausted out of the system. Table 5 lists the specifications of measuring instruments and components used in the experiment.

Table 5 Specifications of experimental component and instrument [22]

Component/instrument	Specification
Closed-loop airflow range	Up to 2,100 kg h ⁻¹ , inverter controlled
Open-duct airflow range	Up to 1,000 kg h ⁻¹ , inverter controlled
DW	Diameter: 300 mm, axial width: 100 mm Rotation speed: 10–25 revolutions per hour (RPH)
Compressors	(CO ₂) rotary compressor: 3.9 cm ³ (displacement per revolution) (R410A) rotary compressor: 13.2 cm ³ (displacement per revolution)
Evaporators	Frontal area: 704 mm (H) × 699 mm (W) 4 banks, 32 tubes per bank, 4 parallel circuitry Fin pitch: 2.0 mm, fin thickness: 0.2 mm (CO ₂) tube outer diameter: 7.94 mm, thickness 1.00 mm, bare tube (R410A) tube outer diameter: 7.94 mm, thickness 0.31 mm, bare tube
Condensers/gas coolers	Frontal area: 484 mm (H) × 622 mm (W) 4 banks, 22 tubes/bank, 2 parallel circuitry Fin pitch: 2.0 mm, fin thickness: 0.2 mm (CO ₂) tube diameter: 7.94 mm, thickness 1.00 mm, bare tube (R410A) tube diameter: 7.94 mm, thickness 0.31 mm, bare tube
Nozzles	DW, size: 7.6 cm diameter, range: 280–660 kg h ⁻¹ Condenser/gas cooler, size: 12.7 cm diameter, range: 790–1,800 kg h ⁻¹ Evaporator, size: 17.8 cm diameter, range: 1,500–3,600 kg h ⁻¹
Relative humidity sensors	Duct mount-type (uncertainty: ±2 % RH, range: 0–100 % RH)
Thermocouples	Type T (uncertainty: 0.5 K, range: –200 to 350 °C)
Pressure transducers	Capacitive pressure transducer (uncertainty: ±0.11 % FS, FS: 7 and 21 MPa)
Differential pressure transducer	Capacitive differential pressure transducer (uncertainty: 1 % FS, range: 0–250 Pa and 0–1,250 Pa)
Refrigerant mass flow meter	Coriolis flow meter (uncertainty: 0.05 %, reset range: 0–60 g s ⁻¹)
Power transducer	AC watt transducer (uncertainty: 0.2 % FS, range: 0–4 kW)

Table 6 Test conditions [22]

Parameter	Setting	Description
Space cooling capacity	3.5 kW	Effective cooling capacity delivered by evaporator to space
Latent capacity	0.7 kW	Sensible heat factor (SHF) = 0.8
Indoor condition	27 °C, 50 % RH	Fixed at the inlet of evaporator
Evaporator outlet temperature	18 °C, 20 °C, 22 °C	DW process side inlet temperature
Outdoor condition	35 °C, 44 % RH	Fixed at the inlet of condenser/gas cooler
Condenser/gas cooler outlet temperature	45 °C, 50 °C, 55 °C	DW regeneration side air temperature
Airflow rate through the DW	300 kg h ⁻¹ , 350 kg h ⁻¹	Same airflow rate for both dehumidification and regeneration
DW rotation speed	0 rph, 10–25 rph	

As described above, the temperature and humidity ratio of the indoor and outdoor conditions were decided based on the AHRI standard 210/240 (2008). The sensible cooling capacity, latent capacity (which was provided by the DW), and the compressor power consumption were measured. The AFR passing through the DW was set to be 300 and 350 kg h⁻¹ for the different regeneration temperatures of 55 and 50 °C, respectively. The EOD dampers listed in Fig. 13 were used to control the distribution of airflows into subtunnels. The regeneration temperature was set to be in the range of 45–55 °C, and the condenser (gas cooler) was the only heat source. The cooling capacity of the VCS was set to be 3.5 kW, and the required latent capacity was 0.7 kW. Charge optimizations were conducted for both refrigerants at the condition of maintaining air leaving the condenser (gas cooler) at 50 °C and air leaving the evaporator at 20 °C. Table 5 lists the specifications including the uncertainties of components and instruments in the tests. The detailed information of test conditions is included in Table 6.

3.2 Experimental Results

Figure 14 depicts the psychrometric process of the SSLC test where point 1 to point 4 represent the condition change of indoor air loop and point 5 to point 7 represent the condition change in the outdoor air duct. All the condition points are corresponding to the locations numbered in Fig. 13. The refrigerants' pressure and temperature profiles in the tests were plotted from Figs. 15, 16, 17, and 18. Different series of lines represent different test conditions. The numbers listed in the figures are either the highest pressure (temperature) or the lowest pressure (temperature) during the tests. The evaporating pressure and temperature changed with different supply air temperatures, which varied between 18 and 22 °C. At the same supply air temperature, several different VCS conditions which delivered the same amount of cooling were created by simultaneously adjusting the opening of the

Fig. 14 Psychrometric process of the SSLC system [22]

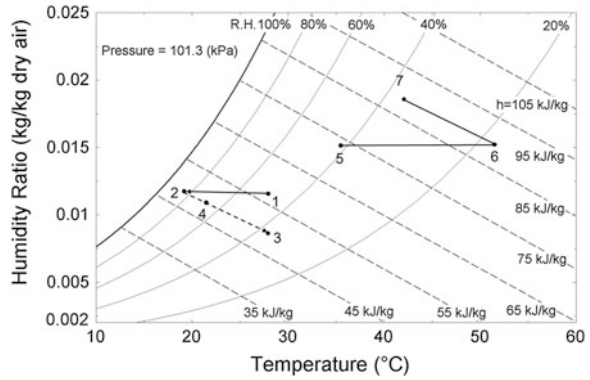


Fig. 15 Pressure variation along the cycle for R410A SSLC test [22]

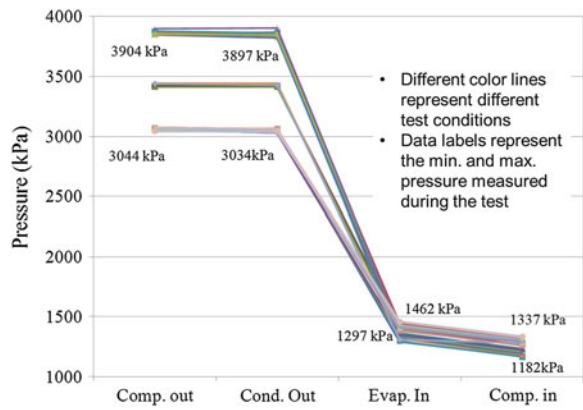


Fig. 16 Temperature variation along the cycle for R410A SSLC test [22]

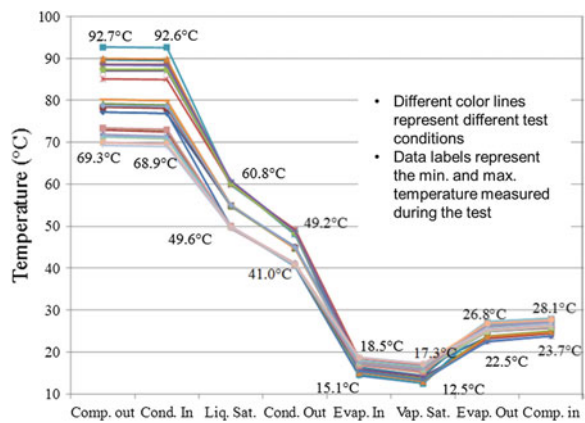


Fig. 17 Pressure variation along the cycle for CO₂ SSLC test [22]

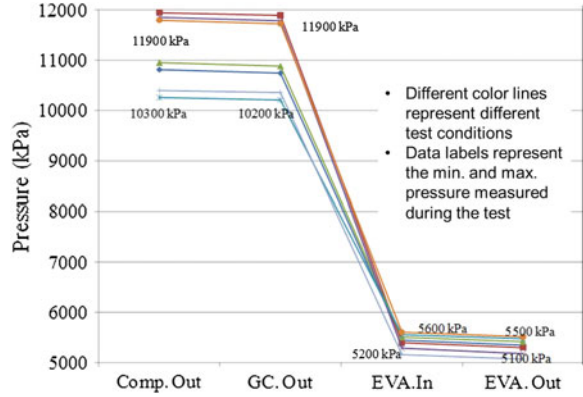
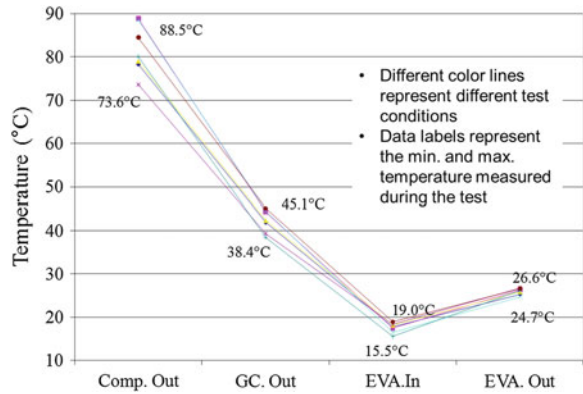


Fig. 18 Temperature variation along the cycle for CO₂ SSLC test [22]



EXV and the frequency of the variable-speed compressor. The purpose of such adjustment was to find the maximum COP at the given condition. Such adjustment also affected the high side pressure and temperature. The other factors causing the different high side conditions were the different regeneration air temperature requirements, which varied between 45 and 55 °C. The numbers listed in the graph represent the upper and lower boundaries of the aforementioned ranges. Uncertainties of measured data were calculated based on the instruments’ system error, which was listed in Table 5, and the random error was taken from a standard deviation of a set of measured data.

The COP profiles of both refrigerants’ SSLC tests were summarized in Figs. 19 and 20. Each test condition, which is defined by one supply air temperature (T_{evap}) and one regeneration air temperature (T_{reg}), is represented by a cluster of points, which were created by different compressor frequencies and different EXV openings. An additional dry condition was tested for the condition of $T_{reg} = 50$ °C and $T_{evap} = 20$ °C. The dry condition was created by turning off the chamber’s humidifier, which made the humidity ratio inside the chamber less than 5 g kg^{-1}

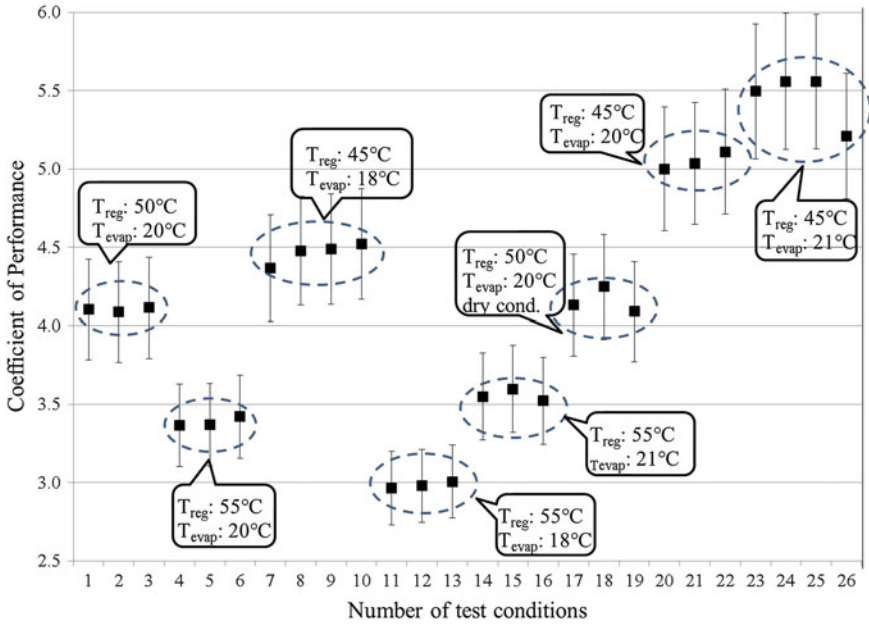


Fig. 19 COP profile of R410A SSLC tests with error bars [22]

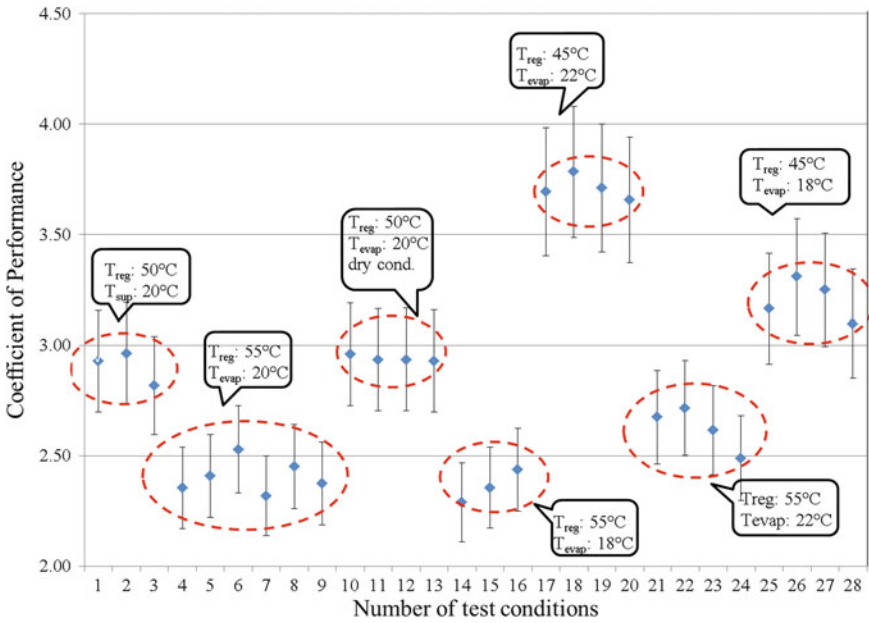


Fig. 20 COP profile of CO₂ tests with error bars [22]

dry air. The purpose of creating such condition is to test the performance of the DW. It was found that the DW performed better in the dry ambient condition than in the standard condition, but basically, it had no effect on improving the VCS' COP. It is because the role of DW in the entire system was found to be independent from the VCS, which is discussed in the following chapter.

The general role of a DW in an SSLC system is to remove the latent load by absorbing water vapor from the process air and dumping it to regeneration air. The dehumidification performance of a DW is mostly affected by air frontal velocity, regeneration temperature, and DW rotation speed [9]. To be more specific, a high regeneration temperature, a low air frontal velocity, and a fast-rotating DW have a positive effect on dehumidifying a unit rate of airflow. In the tests, in order to maintain the same latent capacity (0.7 kW) at different regeneration temperatures, different amounts of air were sent to the DW and the rotation speed of the DW were carefully adjusted. Based on these characteristics, it was concluded that in an SSLC system, a DW can independently control latent load from a vapor compressor cycle. An improved dehumidification performance over a unit rate of air under a fixed latent capacity only brings the benefit of a reduced amount of air required by the DW. Alternatively, a reduced dehumidification performance can be compensated through providing a larger amount of air. Furthermore, operation of DWs has only a limited effect (heat of adsorption) on a VCS. Most DW operates closely along an isenthalpic line, which makes such operation basically convert the same amount of latent cooling to sensible cooling. This means that as long as the latent capacity is fixed, no matter how the DW operates, for example, at different regeneration temperatures, the VCS deals almost the same amount of sensible cooling. This made the further study of SSLC systems focus on comparing the performance of VCS only. The current DW, which had a diameter of 300 mm and an axial width of 100 mm, was not able to deliver the required latent capacity at 45 °C regeneration temperature. A larger diameter rotor is required so that a larger amount of airflow can be dried at the same unit rate of dehumidification performance. However, because of the independent role of DW in the SSLC system, the VCC was still tested in the condition of delivering 45 °C regeneration temperature with the assumption that a larger diameter rotor had removed the required amount of latent capacity. Table 7 provides the DW's rotation speed, Ω , and air frontal velocity, V_{frontal} , under different regeneration temperatures.

From Figs. 19 and 20, it can be found that the regeneration temperature and supply air temperature significantly affected the COP. The higher the regeneration temperature, the lower the COP, and the higher the supply air temperature, the higher the COP. Such a trend could be explained by the following: In order to

Table 7 DW operating conditions [22]

T_{reg} (°C)	V_{frontal} (m/s)	Ω (rph)	Q_{lat} (kW)
55	2.11	15	0.7
50	2.46	25	0.7
45	N/A	N/A	N/A

obtain high regeneration temperature, the condensing pressure (high side pressure) of refrigerant had to rise. Such a rise led to two effects: an increased pressure ratio across the compressor and an increased temperature of refrigerant leaving the condenser (gas cooler). Both effects resulted in an increase in compressor power input. On the other hand, an increased air supply temperature raised the evaporating pressure of refrigerant, which reduced the pressure ratio across the compressor, and led to a reduction in compressor power input. The pressure and temperature profiles in Figs. 15 through 18 support the aforementioned statements by demonstrating wide ranges of high side pressure and evaporating pressure.

A computer model was written in the EES platform to simulate the performance of VCS using parameters such as compressor efficiency, DW dehumidification capacity, and UA values of HXs. The HX was modeled in a multi-segment UA-LMTD method, with the UA values adjusted so that the refrigerant inlet and outlet conditions calculated from the code matched the experimental results. The compressor module was modeled based on a three-efficiency method, and the three efficiencies were obtained from the tests. Performance of the baseline systems, which represented conventional AC systems using evaporators to remove both latent and sensible loads, was calculated by the model based on the same UA values as the SSLC systems, which was used later for the COP comparison on the basis of the same sizes of HXs. The compressors in the baseline systems had the same displacement volumes as those in the SSLC systems. The rate of airflow through the evaporator and the evaporator outlet air temperature were calculated to meet the sensible and the latent capacities of the evaporator with the SSLC system capacity. Table 8 shows the comparison results calculated by the model. Since the experimental results demonstrated the low COP performance of VCC at 55 °C regeneration temperature, the comparison focused only on the conditions of 50 and 45 °C.

Several observations can be made from Table 8. First of all, all R410A systems outperform their CO₂ counterparts in terms of COP, which again proves the low COP behavior of CO₂ systems. Regarding the improvement from the application of SSLC technology, two refrigerants behave very similar to each other. When the regeneration temperature was around 50 °C, the COP improvements of both refrigerants were only 7 %. When the regeneration temperature was around 45 °C, the COP improvements were 32 % for CO₂ and 34 % for R410A, respectively. But setting the regeneration temperature at 45 °C is the lowest operating limit for the

Table 8 COP comparison between baseline and SSLC systems [22]

Refrigerant	System	Evaporating temperature (°C)	High side pressure (MPa)	Regeneration temperature (°C)	COP (improvement %)
CO ₂	Baseline	13.9	10.37	47.3	2.58 (100)
	SSLC	17.6	10.91	51.0	2.76 (107)
		17.7	10.26	45.5	3.40 (132)
R410A	Baseline	14.3	3.16	47.3	3.64 (100)
	SSLC	18.3	3.42	50.7	3.89 (107)
		18.5	3.03	45.7	4.89 (134)

300-mm-diameter DW. Both maximum AFR of the fan and maximum DW rotation speed of the DW had to be used, so not as many different conditions can be tested as in the 50 °C case. Moreover, the higher the regeneration temperature possible by the VCC, the smaller the DW rotor requires. Therefore, conducting a further study is worthwhile to explore new DW-assisted SSLC systems, which can have a better VCS efficiency meanwhile provide as high regeneration temperature as possible.

4 Exploration of Energy-Enhancing Options for SSLC Systems

As mentioned in the previous section, a major challenge for DW-assisted SSLC system is to balance the regeneration temperature which affects the performance of the DW and the COP of the VCS. As a solution to such challenge, Ling et al. [23] applied divided condensers (gas coolers) in the VCS. Instead of heating the entire amount of air to a required temperature, only a portion of air is heated by a high-temperature section of divided HXs to the temperature required by the DW regeneration. The other sections of divided HXs (HXs) work as heat sinks, and the temperature of discharge air can be much lower than the regeneration temperature. In this section, further energy-enhancing options such as evaporative cooling and enthalpy wheel (EW) were also added to the DW-assisted SSLC systems using divided HXs.

CoilDesigner was utilized to model all the HXs used in the VCS. EES (F chart 2011) gathered the calculation results from CoilDesigner and was used to model other components of the VCC (compressor and expansion device) and EW. Both CO₂ and R410A SSLC systems were modeled. For CO₂ systems, a suction line HX (SLHX) was also modeled in the CoilDesigner since it is a common approach to increase CO₂ system's COP. However, no significant improvement was found when applying a SLHX to R410A systems and therefore no SLHX modeling for R410A systems. The compressor was modeled using the same three-efficiency method in the previous section. The expansion device was modeled based on an isenthalpic expansion assumption. The dehumidification performance of the DW was assumed to be a function of DW rotation speed, regeneration temperature, and air velocity through the wheel, as well as the inlet humidity ratio of the regeneration side. The enthalpy of air in the process side of the DW was calculated as a function of DW rotation speed, regeneration temperature, and air velocity. The EW was modeled as an air-to-air HX using the efficiency-based method. The maximum possible enthalpy difference between two air streams was first calculated, and then the actual enthalpy exchange between the two streams was assumed to be the product of the maximum enthalpy difference and the efficiency. The efficiencies of EW used in the model are 0.82 for sensible heat transfer and 0.65 for latent heat transfer, respectively. All of the input data

described above were obtained from experimental data [22]. In addition, fan power consumptions were modeled based on two scenarios: one with all AC motor-driven fans and the other with all brushless DC (BLDC) motor-driven fans. The fan efficiency was assumed to be the product of the motor efficiency and the fan blade efficiency.

4.1 Layout of Divided HX and Optimization

Since the DW has to be continuously regenerated, it requires hot air discharged from the condenser as the heat source. For the entire system, such requirement leads to a design issue: how to provide enough hot air to the DW while maintaining a high system COP. As the AFR through the conventional condenser is usually 2–4 times higher than the amount required by the DW, the condenser outlet air temperature is usually not high enough for DW regeneration. Consequently, less air has to be circulated through the condenser than that of the conventional system in order to provide high enough air temperature to the DW. However, it may increase the heat rejection pressure and reduce the system COP [22]. To address this issue, a divided HX is hereby proposed as a solution. To promote better understanding, only R410A divided HX is discussed in detail in this chapter. The design of CO₂ divided HX is similar to the R410A one. However, when applying the divided HX to the systems, COP improvement is quite different between R410A and CO₂ systems; therefore, in the next section, both systems are discussed. In a divided HX, there is one section (the first section) dedicated to supplying DW regeneration air, and the other sections are for the usual heat rejection. The first section produces only the required amount of regeneration air by utilizing high-temperature discharge refrigerant from the compressor. The other sections have no requirement of regeneration air production, and therefore, the entire condenser can still have the same amount of air and approach temperature as those of the conventional condenser. Moreover, for the heat rejection sections, it is now possible to apply evaporative cooling to further reduce the condensing pressure. While the design of the divided HXs can involve various aspects, this subsection deals with two issues: the layout of the divided HXs and the exploration of low-cost condenser design. For the layouts, the first section of the divided condenser, which is used to provide hot air for DW regeneration, can be either placed behind the other sections so that air flows in series from the other sections to the first section and forms a counter-flow HX configuration with the refrigerant circuit, or it can be placed parallel to the other sections so that the air flows parallel to all the sections. The benefit of the serial layout is that the total height of the HX can be reduced and air can be heated more effectively because it flows through most banks than in the parallel design. However, the air-side pressure drop may accordingly be high. The benefit of the parallel layout is to reduce the air-side pressure drop. Table 9 shows the details of three HX layouts for comparison. All three HX layouts have the same tube geometries, fin geometries, and tube spacing.

Table 9 HX layouts of baseline HX and divided HXs in parallel layout and serial layout

HX Layout	Baseline HX	Divided HXs in parallel layout		Divided HXs in serial layout	
	Single condenser	Divided condenser I	Divided condenser II	Divided condenser I	Divided condenser II
Number of tube bank	4	4	4	4	4
Number of circuit	2	2	2	2	2
Number of tube/bank	22	12	10	6	16

Hence, the three HXs have the same primary and secondary heat transfer areas. The only difference among the three is how the tubes and air streams are divided into different sections. Figures 21, 22, and 23 show the air outlet temperature profiles of the three HX layouts. It is clear that the baseline HX’s profile has two separate parts of high-temperature discharge air, which makes it difficult to collect enough hot air for DW regeneration. In contrast, both divided HX designs make hot air concentrate on the top part of the HX for DW regeneration. From that point of view, both divided HXs are successful. However, the serial layout has less frontal area than the parallel layout, which leads to a higher air velocity. Moreover, the serial design directs part of the airflow through eight banks of tubes and consequently leads to a much larger air-side pressure drop. The parallel layout has an air-side pressure drop of only 47 Pa, while the serial layout, which is subject to the double penalties of larger air velocity and more banks, has an air-side pressure drop of 164 Pa. Since too much of an air-side pressure drop can consume too much fan power, the serial layout of divided HXs is not preferred.

The current dimension of the divided condenser is based on the commercial product described in Ling et al. [22]. To explore the potential of any material cost savings of the condenser, a parametric study was conducted to investigate different designs of condensers by varying the tube length, tube vertical and horizontal

Fig. 21 Discharge air temperature profile of the baseline single HX design

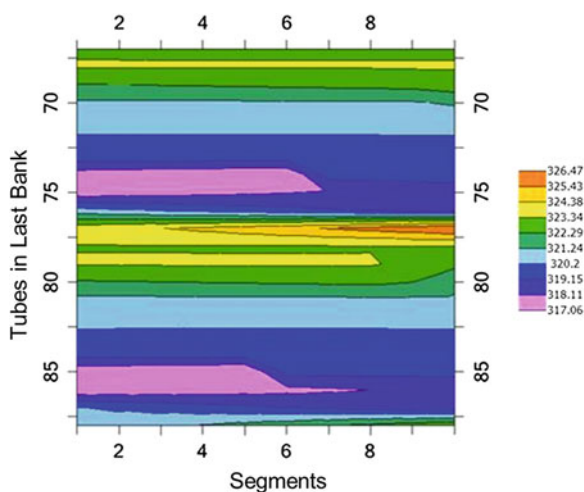


Fig. 22 Discharge air temperature profile of the divided HXs in parallel layout

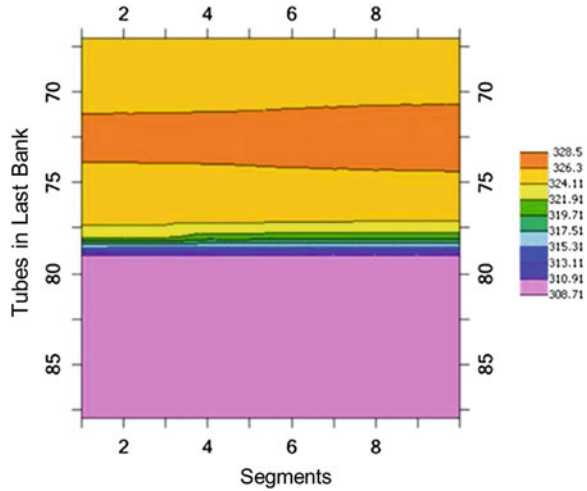
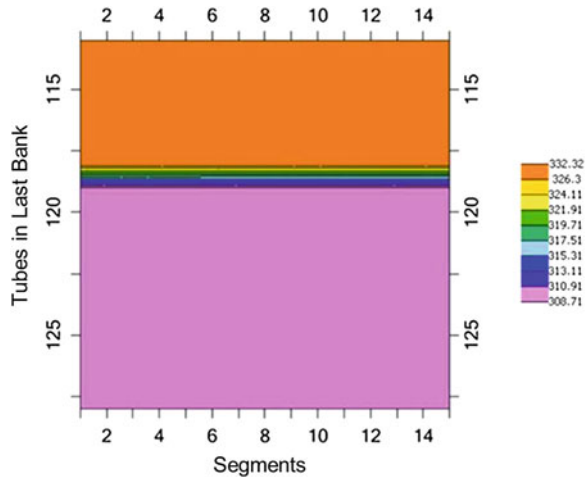


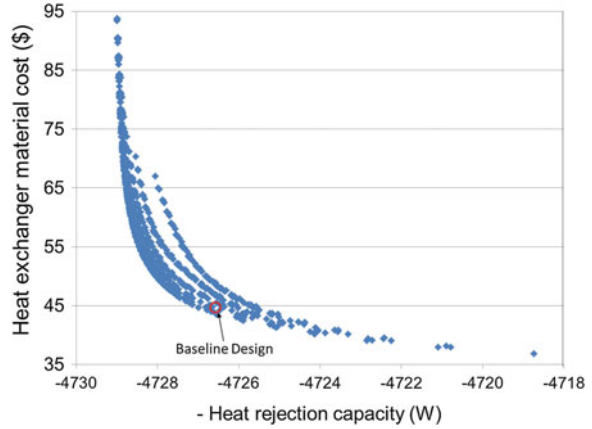
Fig. 23 Discharge air temperature profile of the divided HXs in serial layout



spacings, and fin density. Air-side and refrigerant-side pressure drops are the two constraints which are specified as $PD_{air} < 50 \text{ Pa}$ and $PD_{R410A} < 1 \text{ }^\circ\text{C}$ saturation temperature, respectively. All the feasible designs are plotted in Fig. 24 in the form of HX material cost versus minus condenser capacity. The commercial product aforementioned is marked by a red dot and used as the baseline design. The black arrow indicates the direction toward better HX designs. A pareto frontier represents the best possible designs. As shown in the figure, the design at the right corner has the least material (16 % less than the baseline design) and the smallest capacity (but only 0.2 % less than the baseline design).

The cost savings come from 12 % of tube length reduction and 22 % of the fin density reduction compared to the baseline design. On the other hand, the design

Fig. 24 Parametric study of divided condenser designs



on the top left indicates the largest capacity condenser (0.06 % larger than the baseline) at the highest cost (93 % higher than the baseline). The largest capacity design requires 12.5 % longer tube, 36 % larger tube vertical spacing, 26 % larger tube horizontal spacing, and 27.5 % larger fin density than those of the baseline HX. After reviewing the two extreme design points, it is concluded that the baseline HX is oversized, and the least cost design obtained from the parametric study provides a similar capacity but saves 16 % material cost.

4.2 DW-Assisted SSLC Systems Integrated with Evaporative Cooling and EW

In this section, several integrated system configurations were selected as candidates for a detailed study in order to explore an SSLC system with highest COP. For each configuration, both R410A and CO₂ were simulated. The conventional four-component VCC was considered as the baseline system (Fig. 25). Additionally, four SSLC systems were considered. Figure 26 shows components layout

Fig. 25 Four-component baseline system

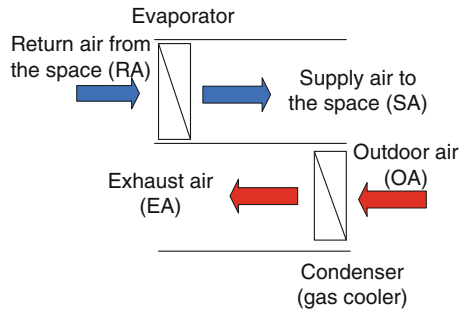
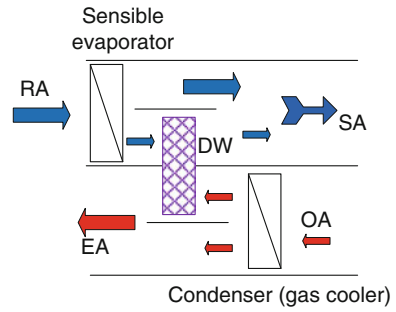


Fig. 26 DW-assisted SSLC system with single HX



in the air streams of the DW-assisted SSLC system with a single, undivided condenser. Both Figs. 27 and 28 describe DW-assisted SSLC systems using divided condensers. The SSLC option 1 is a zero-ventilation system, with the condenser divided into two parts. In this option, the incoming air to the second part of the condenser may or may not flow through evaporative cooling. The SSLC option 2 has the required amount of fresh air mixed with return air from the space, and the condenser is divided into three parts. Each part may face different air conditions, such as the ambient air condition, the ambient air condition after the evaporative cooling process, and the exhaust air from the space after the evaporative cooling process. The SSLC option 3 is the DW-assisted SSLC system with

Fig. 27 DW-assisted SSLC system (Option 1)

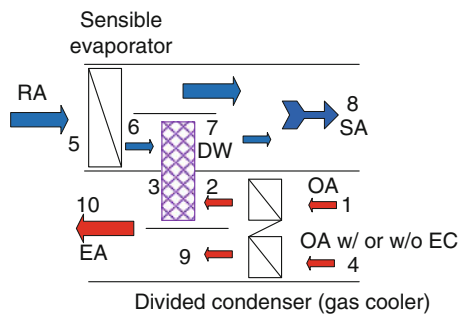


Fig. 28 DW-assisted SSLC system (Option 2)

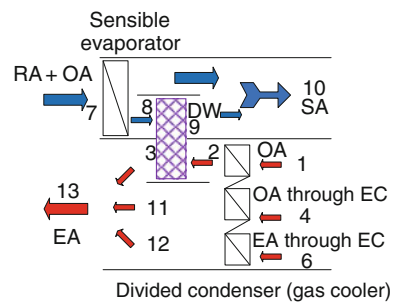
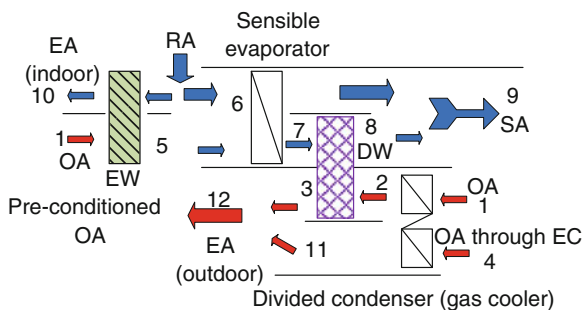


Fig. 29 DW-EW-assisted SSLC system (Option 3)



an added EW (Fig. 29). The working principle of the EW can be simply described as follows: hot and humid ambient air flows through the EW, transferring the sensible heat and water vapor to the relatively cold and dry return airstream from the conditioned space. The heat and mass transfer between the two air streams, via the EW, helps recover both the sensible and latent cooling from the space.

The COPs of different SSLC options are compared with the conventional systems. The system COP is defined as the ratio of the space cooling capacity (3.5 kW) to the total electric power input, including the compressor power input and the power inputs of all fans. For the baseline systems, the system COP could be considered the same as the COP of the VCC when neglecting the heat load of fans, which is defined as the ratio of the evaporator air-side cooling capacity to the total power input. However, for the DW-assisted SSLC system, the VCC provides extra cooling capacity to compensate the difference between the heat of adsorption and heat of evaporation. It consequently causes a smaller system COP than that of the VCC. In order to search for the optimum operating condition of VCC in which the COP is maximized, a genetic algorithm built in EES [13] was adapted to maximize the system COP by varying the evaporating and condensing pressures. The optimization problem is formulated as follows:

$$\text{Min}(f) = -(\text{COP of the system}) \quad (8)$$

$$\text{s.t. system capacity} \geq Q_{\text{req}} \quad (9)$$

$$\text{Air discharge temperature off the condenser} \geq 50^\circ\text{C} \quad (10)$$

Equation (8) shows the objective of the optimization followed by two constraints in Eqs. (9) and (10), which represent that the required system cooling capacity should be at least 3.5 kW and the minimum regeneration temperature should be 50 °C, respectively. Figures 30 and 31 show the system COP improvement by applying aforementioned performance-enhancing options for R410A system and CO₂ system, respectively, while Tables 10 and 11 provide the system COP, COP improvement, and respective baseline system of each system option. From Fig. 30, it can be seen that the improvement resulting from the application of divided condenser (option 1) to the SSLC system with single

Fig. 30 COPs of R410A baseline system and different SSLC options

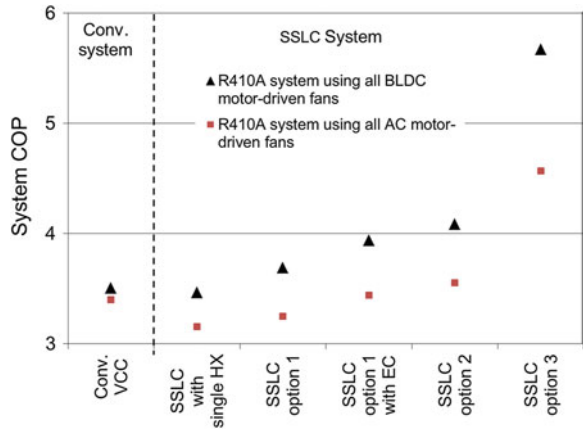


Fig. 31 COPs of CO₂ baseline system and different SSLC options

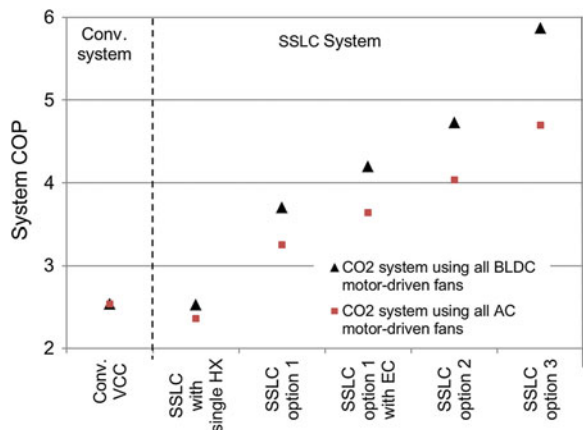


Table 10 Detailed R410A system COP, COP improvement over respective baseline systems

System option	System COP (AC/BLDC motors)	COP improvement [%] (AC/BLDC motors)	Respective baseline system
Conventional system	3.40/3.50	N/A	N/A
SSLC with single HX	3.15/3.46	-7/-1	Conventional system
SSLC option 1	3.25/3.69	3/7	SSLC with single HX
SSLC option 1 w evaporative cooling	3.44/3.94	6/7	SSLC option 1
SSLC option 2	3.55/4.08	3/4	SSLC option 1 w evaporative cooling
SSLC option 3	4.57/5.67	33/39	SSLC option 1 w evaporative cooling

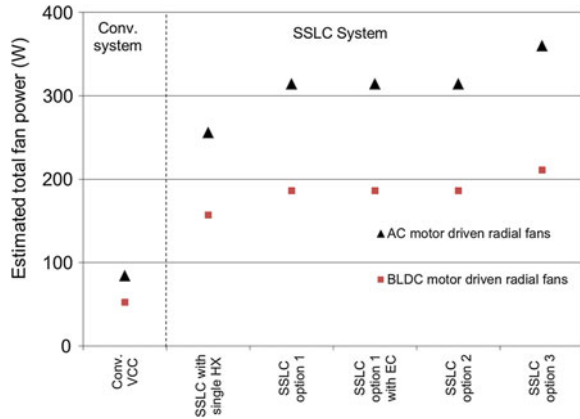
Table 11 Detailed CO₂ system COP, COP improvement over respective baseline systems

System option	System COP (AC/BLDC motors)	COP improvement [%] (AC/BLDC motors)	Respective baseline system
Conventional system	2.54/2.59	N/A	N/A
SSLC with single HX	2.36/2.53	-7/-3	Conventional system
SSLC option 1	3.26/3.69	38/46	SSLC with single HX
SSLC option 1 w evaporative cooling	3.64/4.19	12/14	SSLC option 1
SSLC option 2	4.03/4.73	11/13	SSLC option 1 w evaporative cooling
SSLC option 3	4.70/5.87	29/40	SSLC option 1 w evaporative cooling

condenser is 3 and 7 % for systems using AC motors and BLDC motors, respectively. The application of evaporative cooling to the lower part of the condenser in the R410A SSLC option 1 system resulted in 6 and 7 % COP improvement for systems using AC motors and BLDC motors, respectively. The application of evaporative cooling reduces the actual ambient temperature to the condenser and therefore helps reducing the condensing pressure. The SSLC option 2 divides the condenser into three parts, and the evaporative cooling of return air provides the lowest possible temperature to further cool down the refrigerant. In the SSLC option 2, the COP had 3 and 4 % improvement over the SSLC system option 1 with evaporative cooling for systems using AC motors and BLDC motors, respectively. The DW-EW-assisted SSLC system (option 3) demonstrates the highest COP. Application of the EW provides “free” sensible and latent cooling and reduces the sensible cooling requirement of the VCC by 29 % (3.8–2.7 kW).

The HXs were modeled in reduced sizes in proportion to the reduced capacity. The compressor power input was reduced to a minimum with this option. The COP reached 4.6 and 5.7 for systems using AC motors and BLDC motors, respectively, and the improvement over the SSLC system option 1 with evaporative cooling is 33 and 39 %, respectively. It is also observed from the simulation results that it is important to apply high-efficiency motor for the SSLC systems. Because of the reduced air temperature difference across the evaporator, AFR through the evaporator has to be increased to match the required cooling capacity. The increased AFR can lead to an excessive fan power, and an example of it can be found from the COP decrease when the SSLC is applied with single HX. Therefore, BLDC motors are suggested for the SSLC systems. The CO₂ system has a similar trend of improvement as the R410A system, but the improvement magnitude is larger. Such a larger improvement is a result of the fact that the COP of a CO₂ system tends to decrease quickly under high ambient temperature conditions, whereas the applications of evaporative cooling and divided HX either lower the actual operating conditions of the system or reduce the approach temperature of the HX. Figure 32 compares the total fan power consumptions for SSLC options investigated. The fan power consumptions of the SSLC system are almost tripled that of the conventional system. The increase is partly due to aforementioned increased

Fig. 32 Fan power estimation for different systems



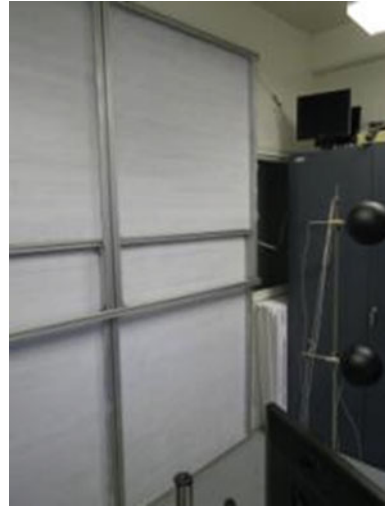
AFR, and moreover, it is also due to the increased pressure lift requirement from the DW and EW. However, the cases utilizing BLDC-motor fans save around 50 % power consumption compared to the AC-motor fan cases. Such savings are the result of high efficiency of BLDC motor.

5 Indoor Heat Exchanger Design for SSLC System and Thermal Comfort Evaluation

Despite the encouraging energy savings reported in the previous chapter, the design of the indoor HX in the SSLC system remains a challenge. For the sensible cycle in an SSLC system, the refrigerant evaporating temperature increases, so the supply air temperature usually increases for a given HX. Consequently, the air mass flow rate has to increase to maintain the system capacity. The increased AFR leads to an increased fan power consumption and may offset the power savings by the compressor. In short, how to design an indoor HX that minimizes the fan power demand is the challenge. In the previous section, it has been concluded that SSLC systems using conventional fin-and-tube HXs, under careful design, can still keep the HX cost comparable to conventional systems. However, are there any other, probably better, options to design an indoor HX?

Chilled ceiling panels and heated floor systems are in fact good examples. For both products, the heat transfer mechanism between the working fluid and indoor air is natural convection and radiation, and therefore, the fan power demand is almost zero. Moreover, the enlarged heat transfer area of those products provides radiant cooling or heating to the occupants so that both products may provide better thermal comfort than conventional indoor HXs. However, the installation of the two systems normally requires an overhaul of the existing ceiling and floor and hence should preferably be done during the constructions of new houses. For the purpose of designing a similar product with easy installation, a novel radiative HX

Fig. 33 Picture of the radiative HX installed in an office setting



is introduced. The radiative HX has a similar structure to the chilled ceiling panels, which includes serpentine-shaped tubes fixed on metal sheets. The tubes filled with working fluid such as water serve as heating/cooling source and conduct heat to the metal sheets. The metal sheets condition the space air through both natural convection and radiation. An attractive feature of the radiative HXs is that instead of installing them over the ceiling or under the floor, the HXs can be simply installed against walls (see Fig. 33). Such installation method has a twofold benefit: easy installation and capability of providing both heating and cooling. This section discusses the modeling of the radiative HXs so that it can be used as a tool to evaluate the thermal comfort in a zone equipped with such HXs.

5.1 Radiative HX Thermal Comfort Modeling

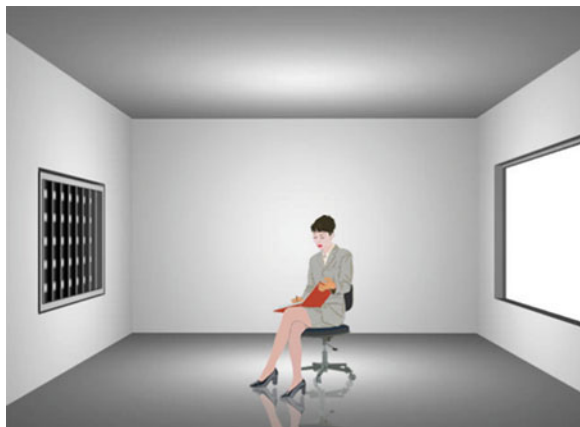
The objective of the simulation tool development is to evaluate the thermal comfort condition of the entire space conditioned by the radiative HX. In the modeling, the radiative HX is assumed to control the temperature of the entire wall being installed. The modeling includes two major efforts: the simulation of operative temperature (OT) field and the evaluation of ASHRAE's thermal comfort criteria. According to the ASHRAE standard 55 [1], OT is a combination of mean radiant temperature (MRT) and air temperature. In the case of applying the radiative HX, OT calculation can be simplified as the arithmetic mean of MRT and air temperature (Eq. 11). In the same standard, two important indices are defined to quantify the thermal comfort criteria: predicted mean vote (PMV) and predicted percentage dissatisfied (PPD). The following subsections provide detailed discussions of the two aforementioned modeling efforts.

$$\begin{aligned}
 t_o &= (h_c t_a + h_r t_r) / (h_c + h_r) \quad \text{for high air velocity} \\
 t_o &= (t_a + t_r) / 2 \quad \text{for low air velocity}
 \end{aligned}
 \tag{11}$$

As mentioned above, OT is the combination of MRT and air temperature. Figure 34 describes the radiation model adopted in the study. The room is assumed to be rectangular in shape with four walls (front wall is not shown), a ceiling, and a floor. One wall is assumed to have the radiative HX (left wall in the Fig. 33). It is assumed that the HX covers the entire wall and maintained a constant temperature. It should be noted that the later experiment demonstrated a 2 K temperature difference between inlet and outlet water flow [20]; therefore, the assumption of a constant temperature profile is a simplified one compared to the real case. Other walls, ceiling, and floor may have different temperatures. Window usually has a different temperature compared to the wall where it is located, which is mainly due to the solar radiation. Equation (12) [10] is then applied to calculate the window temperature. It should be noted that the solar incidence in the equation varies with solar angles and window orientation. Therefore, local solar angles such as solar azimuth angle and solar altitude angle should be identified beforehand. As all surface temperatures (wall temperatures, ceiling and floor temperatures, window temperature, etc.) are obtained, the MRT can be evaluated by the summation of the view factors between the occupant and individual surfaces multiplied by the surface temperature. For simplification, the occupant in the room is assumed to be a sphere. Dunkle [15] defined the equivalent sphere radius of both a standing person and a sitting person. However, since the sphere’s radius is infinitesimal compared with the room dimension, the sphere was further simplified to be a dot. As occupants can move inside the space, the evaluation of their thermal comfort requires calculation of MRT everywhere inside the space, which means that an MRT field has to be obtained.

$$A_{sun} \alpha_D I_D + A \alpha_d I_d = A [h_i (t_g - t_i) + h_0 (t_g - t_0)]
 \tag{12}$$

Fig. 34 Adapted model for radiant temperature field



The other component of OT calculation is the air temperature simulation. The technique of computational fluid dynamic (CFD) is utilized for air temperature field simulation inside the space. A commercially available CFD [3, 4] package was chosen for the modeling. As an example to facilitate initial research, 2D square was assumed to represent the vertical middle inter-section plane of the space. It has one cold side (left side) of 20 °C which can be assumed as a case of the radiative HX filled with cold water to provide cooling and one hot side (right side) of 35 °C which can be assumed as a case of hot window by direct solar radiation. The square has a mesh of 240 by 240 quad cells with enhanced mesh density in the boundary layer to capture the complicated flow characteristics. To be specific, the boundary layer has the first row of 1 mm and the growth of 1.15, i.e., the entire depth of the boundary layer is 20 mm. The turbulence model used in the model is $k-\omega$ SST model. The velocity (streamline) and temperature field are demonstrated in Fig. 35.

Although the example proves that the CFD simulation can be applied to simulate the air temperature field, the computation cost is high. It would be better to develop a reduced-order modeling method, allowing a good compromise between the accuracy and the computation cost. The proper orthogonal decomposition (POD) was chosen as the reduced-order model to replace the above CFD simulation. The POD method was first introduced by John Lumley [11]. In other disciplines, the same method was called as Karhunen–Loève decomposition or principal components analysis. It has several advantages as pointed out by Berkooz et al. [11]: (1) It is statistically based on extracting data from experiments and simulations. (2) Its analytical foundations supply a clear understanding of its capabilities and limitations. (3) It permits the extraction of the results.

The flow chart of the POD method is shown in Fig. 36. In short, the method seeks to decompose a large degree of freedom system into a series of expansion as shown in Eq. (13).

$$v(x, t) = \sum_{i=1}^m a_i(t) \varphi_i(x) \quad (13)$$

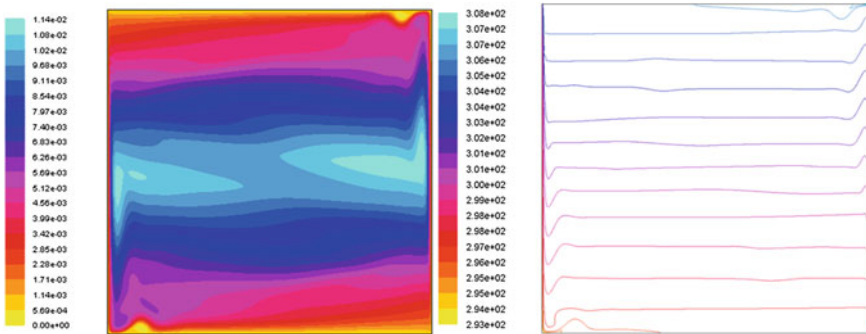
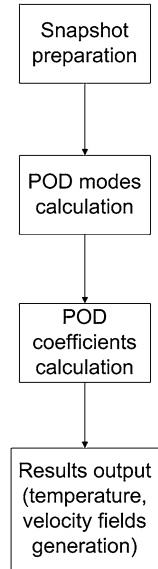


Fig. 35 The streamline (velocity, *left*) and air temperature (*right*) fields in the studied place

Fig. 36 Flow chart of POD method



After skipping the detailed extreme computing, it turns out that the basis functions (φ) are the eigenfunctions of the integral equation [24]:

$$\int C(x, x')\varphi(x')dx' = \lambda\varphi(x) \tag{14}$$

where the kernel C is given by:

$$C(x, x') = \frac{1}{N} \sum_{i=1}^N V_i(x)V_i(x') \tag{15}$$

For the current problem, in order to obtain the POD modes for the air temperature field, a technique called “snapshot” was applied to form the matrix C by utilizing the existing CFD simulation results. Nine sets of temperature fields and velocity fields were chosen to form the snapshot. The difference among each snapshot is the different Rayleigh numbers. The CFD software package is used to calculate the eigenvalues of the kernel matrix C . The built-in singular value decomposition (SVD) function was applied to return the eigenvalues and the corresponding eigenvectors. If the eigenvalue is zero meaning that it poses no impact on the system anymore, then its corresponding eigenvector is neglected. The POD provides the basis of the expansion series. The next step is to find the coefficients in the expansion (Eq. 13). A method called Galerkin projection is considered to be a standard approach to obtain the coefficients. The method projects the governing equations on the modal subspace and then solves the governing equations, usually in the form of ODE or arithmetic equations to obtain the coefficients.

5.2 Operative Temperature Validations

In order to verify the correctness of the POD simulations, two cases of POD calculation results were compared to those from CFD simulations. Case 1 is solving for air temperature inside a 3 m by 3 m square enclosure with the Rayleigh number of 10^6 . Case 2 is solving for the same problem with the Rayleigh number of 10^9 . Figure 37 demonstrates the comparison results. The 3 m by 3 m enclosure is divided into 225 cells. The x-axis represents the 225 cells. For example, the top left cell is number 1, the rightmost cell of the top row is number 15, and the right bottom cell is number 225. The temperature results in each cell were compared to those from the CFD simulation. Both POD cases show good agreement with the CFD simulations. In Case 1, the maximum deviation is only 0.04 K, while in Case 2, the maximum deviation is around 0.1 K. It demonstrates that the POD calculation provides enough accuracy compared with CFD calculation. Considering the fact that it takes only several minutes for the POD codes to solve all the ODE functions and to output the results, the benefit of using POD is very clear. However, the fast speed depends on the existence of snapshots. The first preparation of snapshots may take a week, and then, the POD calculation can solve any problem within the range of snapshots.

The simulated OT field was then compared to experimental data. Figure 38 shows the comparison results. The OT-measuring facility was located in the center of the room with four OT sensors installed at different heights. The average deviation between the two results is only 0.4 K. It demonstrates that the reduced-order model and the radiation model together provide a good prediction of the OT field inside the cubic office room setting.

5.3 PMV and PPD Field Simulation

The previous subsection discusses the simulation of both MRT and air temperature. By simply averaging those two, one can obtain the OT field. However, it is not straightforward to use OT as a thermal comfort criterion. Therefore, the PMV

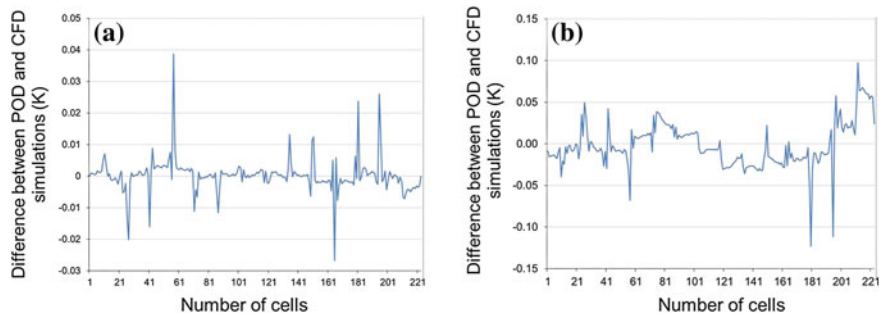
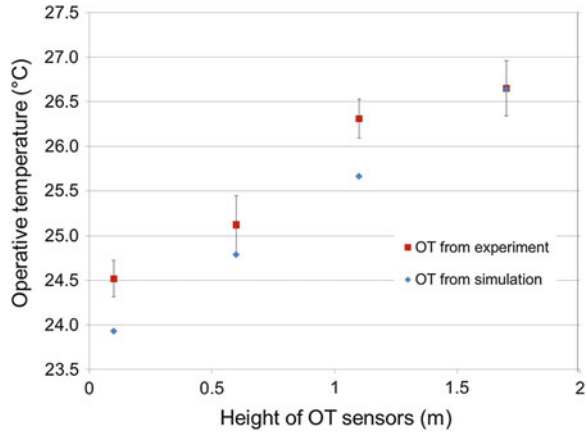


Fig. 37 Difference in air temperature from POD and CFD simulation

Fig. 38 Comparison of OT from experiment and simulation



and PPD fields should be simulated by the software tool. The PMV is a seven-scale system to describe occupant’s thermal sensation from very hot (+3) to very cold (−3). The PPD is its derivative to statistically show how much percentage of occupants feel uncomfortable at different PMV scale. Table 12 and Fig. 39 describe the PMV and PPD, respectively, in more detail. To calculate the PMV, Equation 16 is used. Although including many parameters, most of which in the equation can be obtained from the ISO Standard 7730 [18]. The air temperature and MRT can be calculated by methods summarized in the previous section. The PPD can be calculated based on the Eq. 17. Figures 40 and 41 demonstrate sample outputs of PMV and PPD from the tool, respectively. As shown, both left and right sides are affected by the hot wall and hot window as well as larger vertical air velocity than that in the middle, so the PMV indices near the walls are between slightly warm and warm. Due to the density difference of air, the cold air remains at the bottom and the hot air remains at the top of the space. Consequently, the PMV field shows negative numbers at the bottom and positive numbers at the top of the space. Although there are differences in PMV values inside the space, most of which are between −1 and +1 meaning thermal comfort to the occupants. This is supported by the PPD output, which shows that only 5 % thermal discomfort rate is predicted for most of the space.

Table 12 PMV scale (ISO 7730, 2005)

PMV scale	Thermal sensation
+3	Hot
+2	Warm
+1	Slightly warm
0	Neutral
−1	Slightly cool
−2	Cool
−3	Cold

Fig. 39 PPD as a function of PMV (Koepko [20] created based on ISO 7730, 2005)

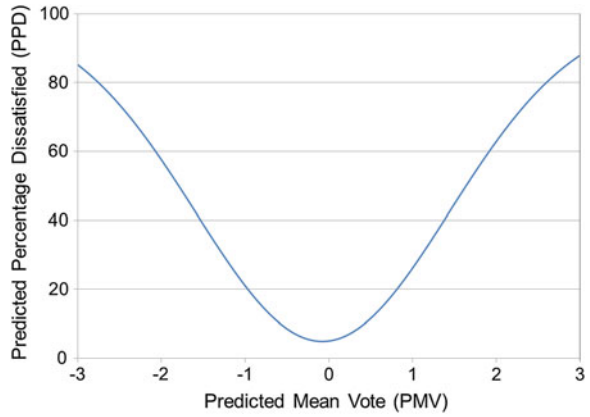


Fig. 40 Snapshots of sample PMV output (axis scales represent segment)

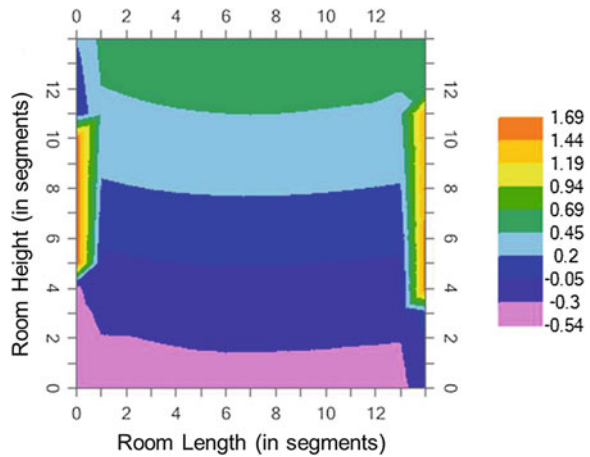
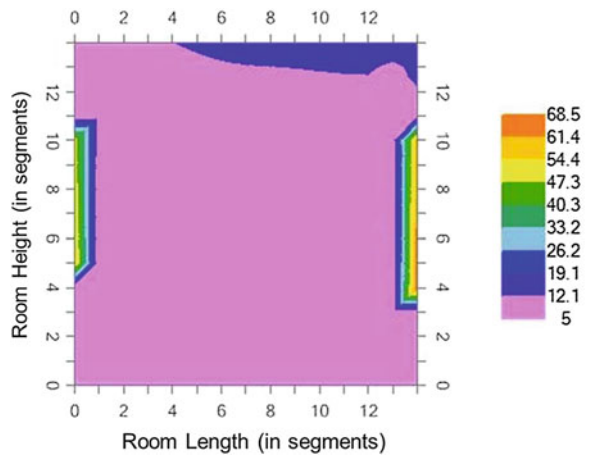


Fig. 41 Snapshots of sample PPD output (axis scales represent segment)



$$\begin{aligned}
 PMV = & \left[0.303 \cdot e^{(-0.036 \cdot M)} + 0.028 \right] \cdot \{ (M - W) - 3.05 \times 10^{-3} \\
 & \cdot [5733 - 6.99 \cdot (M - W) - p_a] - 0.42 \\
 & \cdot [(M - W) - 58.15] - 1.7 \times 10^{-5} \cdot M \cdot (5867 - p_a) - 0.0014 \cdot M \\
 & \cdot (34 - t_a) - 3.96 \times 10^{-8} \cdot f_{cl} \cdot \left[(t_{cl} + 273)^4 - (t_r + 273)^4 \right] - f_{cl} \cdot h_c \cdot (t_{cl} - t_a) \}
 \end{aligned} \tag{16}$$

$$PPD = 100 - 95 - \exp(-0.03353 * PMV^4 - 0.2179 * PMV^2) \tag{17}$$

6 Conclusions

Different configurations of the SSLC systems are introduced in this chapter. The technology of SSLC improves the COP of a sensible VCC by elevating its refrigerant evaporating pressure. The latent cooling can be provided by either a stand-alone vapor compression cycle or desiccant device. The SSLC systems using two VCCs are discussed at first. The system using R-410A as working fluid has been theoretically investigated. Under the AHRI standard test condition for AC application (35 °C, 44 % RH), a 30 % energy saving was calculated for the SSLC system as compared to the conventional AC system. It was also found that the energy savings of the SSLC system varied depending upon ambient conditions. The hot and dry climate tends to have the maximum energy savings potential. The total displacement volumes of the compressors in the SSLC system were estimated to be 25 % smaller than that in the baseline system. In order to address the larger AFR requirement in the SSLC system, a new air distribution method with a single-bank evaporator design was proposed to replace the conventional designs. The simple estimation using fan laws demonstrated that the SSLC system could save the fan motor power by 30 % as compared to the baseline system. In order to compare the HX cost, in-house HX design software was used to optimally design the HXs of the SSLC system and to estimate its total heat transfer area. The design result shows that the HXs of the SSLC system can have 13 % smaller total heat transfer area than that of the baseline. This design example means that the SSLC system can save energy without increasing HX cost.

Later, DW-assisted SSLC system was discussed in detail. The experimental results of the SSLC system with a single condenser (gas cooler) demonstrated a limited COP improvement, which was 7 % for both R410A and CO₂ systems, when the DW regeneration temperature was set at 50 °C. Although bigger improvement was recorded at the 45 °C regeneration temperature case, which were 32 % for CO₂ and 34 % for R410A, such improvement could not be provided by the DW. Two problems, heat of adsorption and excessive high side pressures, were identified as the reasons causing the reduction in COP of SSLC systems.

To address the issue of excessive heat rejection pressure, different efficiency-enhancing options for the DW-assisted SSLC AC system are discussed. The design of divided HX has been investigated in terms of HX layout and the potential of HX material cost savings. It is concluded that the parallel layout of the divided HX is suitable for the SSLC system. Other options such as evaporative cooling and EW can further improve the system performance. To better demonstrate the energy savings of the SSLC system, high-efficiency BLDC motors are recommended for the system.

Finally, the indoor HXs used in the SSLC systems are redesigned using radiative HXs. As an improved version of the sensible heat exchanger, the radiative HX utilizes both natural convection and radiation to provide better thermal comfort at virtually no cost of fan power. The thermal comfort conditions created by radiative HXs and a conventional HX (from a fan coil unit) were compared in terms of OT during the heating season. The conventional HX shows the problems of large temperature stratification from head to feet and low OT at the lower body; however, the radiative HX design solves both problems. A tool was developed to measure the thermal comfort created by such HXs, and the simulation results were validated by experimental data.

References

1. AHRI (2004) ANSI/AHRI standard 55-2004: thermal environmental conditions for human occupancy. Air-Conditioning and Refrigeration Institute, Arlington, VA
2. AHRI (2008) ANSI/AHRI standard 210/240 for performance rating of unitary air-conditioning and air-source heat pump equipment. Air-Conditioning and Refrigeration Institute, Arlington, VA
3. ANSYS Inc. (2006) Fluent version 6.3.26
4. ANSYS Inc. (2011) Gambit version 2.3.16
5. ASHRAE (2004a) ANSI/ASHRAE standard 62.1, 2004 ventilation for acceptable indoor air quality, ASHRAE, Atlanta, GA, USA
6. ASHRAE (2004b) ANSI/ASHRAE standard 140, standard method of test for the evaluation of building energy analysis computer programs, ASHRAE, Atlanta, GA, USA
7. ASHRAE (2005) Fundamentals, Chapter 35, American Society of Heating, Refrigerating and Air-Conditioning Engineers, Inc., Atlanta, GA
8. ASHRAE (2008a) Handbook-HVAC systems and equipment Chapter 20, American Society of Heating, Refrigerating and Air-Conditioning Engineers, Inc., Atlanta, GA
9. ASHRAE (2008b) Handbook-HVAC systems and equipment Chapter 23, American Society of Heating, Refrigerating and Air-Conditioning Engineers, Inc., Atlanta, GA
10. Arora CP (2000) Refrigeration and air conditioning. 2nd edn, Chapter 17, pp 571–615
11. Berkooz G, Holmes P, Lumley J (1993) The proper orthogonal decomposition in the analysis of turbulent flows. *Annu Rev Fluid Mech* 33:539–575
12. Casson V, Cavallini A, Cecchinato L, Col D, Doretto L, Fornasieri E, Rossetto L, Zilio C (2002) Performance of finned coil condensers optimized for new HFC refrigerants. *ASHRAE Trans* 108(2):517–520
13. Charbonneau P, Knapp B (2002) The genetic algorithm, Pikaia optimization program (version 1.2)

14. Domanski P, Yashar D, Kim K (2005) Performance of a finned-tube evaporator optimized for different refrigerants and its effect on system efficiency. *Int J Refrig* 28:820–827
15. Dunkle R (1963) Configuration factors for radiant heat transfer calculations involving people. *J Heat Transfer* 85:71–76
16. F Chart Software (2011) Engineering equation solver, Version 8.874
17. Hwang Y (2004) Potential energy benefits of integrated refrigeration system with microturbine and absorption chiller. *Int J Refrig* 27:816–829
18. ISO (2005) ISO standard 7730: 2005, ergonomics of the thermal environment—analytical determination and interpretation of thermal comfort using calculation of the PMV and PPD indices and local thermal comfort criteria. International Organization for Standardization, Geneva
19. Jiang H, Aute V, Radermacher R (2006) CoilDesigner: a general-purpose simulation and design tool for air-to-refrigerant HXs. *Int J Refrig* 29(4):601–610
20. Koepke M (2011) Experimental investigations on the thermal comfort of an office setting conditioned by low ΔT HXs, Bachelor thesis, University of Maryland, College Park and Technische Universität Berlin
21. Kopko WL (2002) High-efficiency air-conditioning system with high-volume air distribution. US Patent, US 6,405,543 B2
22. Ling J, Kuwabara O, Hwang Y, Radermacher R (2011) Experimental evaluation and performance enhancement prediction of desiccant assisted separate sensible and latent cooling air-conditioning system. *Int J Refrig* 34(4):946–957
23. Ling J, Hwang Y, Radermacher R (2010) Theoretical study on separate sensible and latent cooling air-conditioning system. *Int J Refrig* 33(3):510–520
24. Ly HV, Hein TT (2001) Modeling and control of physical processes using proper orthogonal decomposition. *Math Comput Model* 33:223–236
25. McQuiston FPJ (2005) Heating, ventilation, and air conditioning: analysis and design. Wiley
26. Trane (2009) Packaged rooftop air conditioners: IntelliPak™ Rooftops 20–130 Tons—60 Hz, Literature order number: RT-PRC010-EN, Trane Inc., Piscataway, NJ, USA
27. Whitman B, Johnson B, Tomczyk J (2004) Refrigeration and air conditioning technology. 5th edn, Delmer Cengage Learning, pp 627, 957

Adsorption/Desorption Characteristics of Solid Particles in Desiccant Bed for Different Design Configurations

Ahmed M. Hamed

List of Symbols

A	Cross section area of the bed, m^2
B	The bed characteristic constant
c_p	Specific heat, $kJ/kg.K$
C_{Ai}	Concentration of gas A, kg/m^3
k_1, k_2	Constants for equilibrium correlation (3)
L_m	Length of the static bed, m
t	Time, s
T	Temperature, $^{\circ}C$ or K
T	Dimensionless time
u	Velocity, m/s
w	Water content, kg/kg

Greek Symbols

ε	Porosity
φ	Sphericity
ρ	Density, kg/m^3

A. M. Hamed (✉)

Mechanical Power Engineering Department, Faculty of Engineering,
Mansoura University, Mansoura, Egypt
e-mail: amhamed@mans.edu.eg

Present Address:

A. M. Hamed
Mechanical Engineering Department, Faculty of Engineering,
Taif University, Taif, Saudi Arabia

Subscripts

b	Bed
e	Exit
f	Fluidized bed
g	Gas
i	Inlet value
o	Initial value
p	Particle
s	Silica surface or static
m	Fixed bed

Superscripts

- * At equilibrium conditions

1 Introduction

For improving the performance of desiccant dehumidification systems, new approaches are highly welcome. An attempt to improve the performance of desiccant bed using sorbent should include an investigation on the performance of new system configurations. In the present chapter, different bed design configurations will be presented and discussed. Different bed configurations including solid particles of burned clay impregnated with liquid desiccant in packed bed, vertical fluidized bed, and inclined fluidized bed will be covered in this chapter. Summary of the theoretical and experimental results obtained for the presented configurations will be demonstrated.

Several objectives are formulated to address the overall goal of the present chapter: the development and analysis of solid desiccant system, in different configurations, for air dehumidification purpose. These objectives are to:

1. study and discuss the transient variation of air exit parameters (humidity and temperature) as well as the thermo-physical properties of the desiccant bed (water content, temperature, and vapor pressure) during adsorption and desorption tests.
2. assess the effect of the inlet parameters of air stream (*mainly the humidity ratio*) on the adsorption characteristics.
3. evaluate and discuss the experimental values of mass transfer coefficient during transient operations.
4. evaluate the isothermal model for both adsorption and desorption, through the comparison between the theoretical solution and experimental data.
5. compare the performance results of different bed configurations.

2 Porous Bed Impregnated with Calcium Chloride

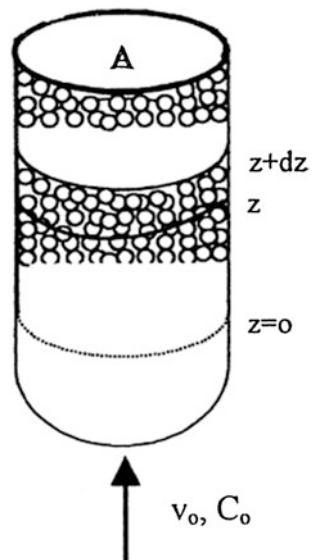
The performance of adsorption column of porous bed impregnated with calcium chloride as the desiccant is investigated [1, 2]. The experimental part of this study was based on application of inert material (porous granules of burned clay) as desiccant carrier. Also, the transient mass transfer process through the bed layers is discussed through the presented mathematical model. In the theoretical model, it is assumed that desiccant sorption properties are not affected by the inert material.

2.1 Analysis of Packed Porous Bed

The physical system considered in this analysis is illustrated in Fig. 1. The packed bed of granulated (porous) solid contacting a binary gaseous mixture, one component of which selectively adsorbs onto and within the solid material. The granules of the packed bed are impregnated with liquid desiccant to form the porous adsorbing surface. If the gas stream to be processed is dilute in the adsorbable fluid (ambient air, for example), then heat effects are usually ignorable, so isothermal conditions can be assumed. Also, the following assumptions will be considered in theoretical analysis of the mass transfer process [1]:

1. The physical process of adsorption is so fast relative to other slow steps (diffusion within the solid particle), that in and near the solid particles, local equilibrium exists.

Fig. 1 Packed porous bed
[1]



2. A single-film mass transfer coefficient controls the transfer rate between flowing and solid phase. However, when intra-particle diffusion is important, it is possible to replace the film coefficient with an effective coefficient. Thus, the model can be made to have wide generality.

2.2 The Adsorption Material

Grains of burned clay were used as a desiccant carrier to form the adsorption porous surface. The average diameter of used grains was about 9 mm. The grains were impregnated with calcium chloride solution with a concentration of 33.86 % by submersion of dry grains in the liquid solution for a period of more than 24 h. Porous grains impregnated with desiccant, are strained to remove the excessive liquid and avoid dropping of liquid from the bed. The mass of solution in the bed is then evaluated. By knowing the solution initial concentration and mass of solution in the bed, the mass of salt in the bed can be evaluated and assumed constant during experiments. To facilitate measurements of the transient distribution along the vertical column, the packed bed is divided into seven layers (see Fig. 2).

2.3 Transient Performance of Packed Porous Bed

The assumption used in the implementation of the simplified analytical solution is that the variation of solute concentration in the fluid with time is negligible compared with its variation in the adsorbent bed. The validity of this assumption can be proved by the results shown in Fig. 3, which illustrate the variation of humidity ratio of stream flowing through the bed for different layers. As shown in figure, the maximum change of air humidity is about 1 g/kg air and occurs only at start of adsorption during a small period of time. Also, except for the first layer, the humidity is nearly constant for most of the adsorption period.

The accumulated mass of water in the bed layers are presented in Fig. 4. As shown in figure, the higher value of mass of water is collected in the first layer. It is

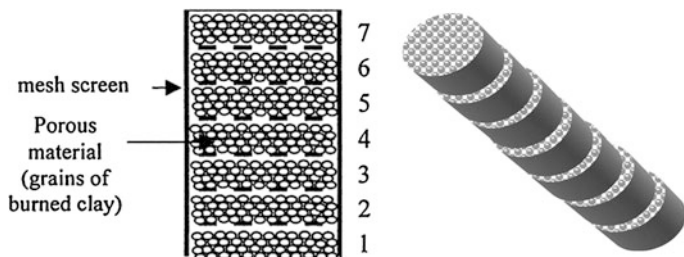


Fig. 2 Experimental packed bed consisting of seven separate layers [1, 2]

Fig. 3 Air inlet humidity ratio for different layers versus time [1]

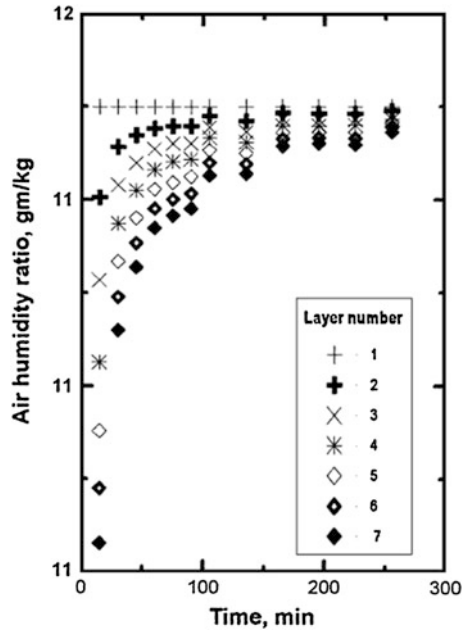
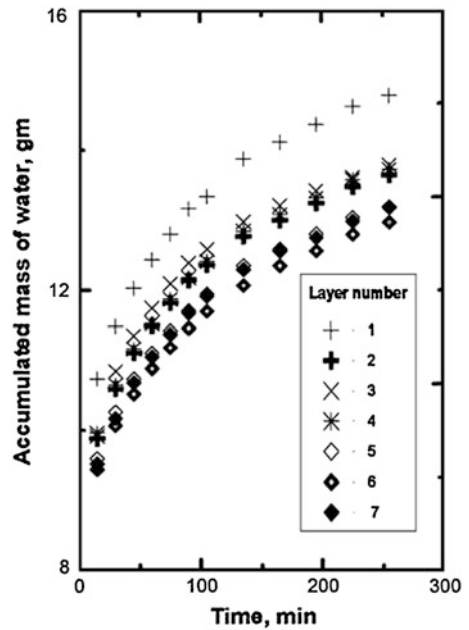


Fig. 4 Accumulated mass of water versus time [1]



seen that the mass of water in different layers decreases with increase in height Z from the entrance of the bed. Also, when comparing any two adjacent layers, it can be found that the difference between the first and second layer is nearly higher than

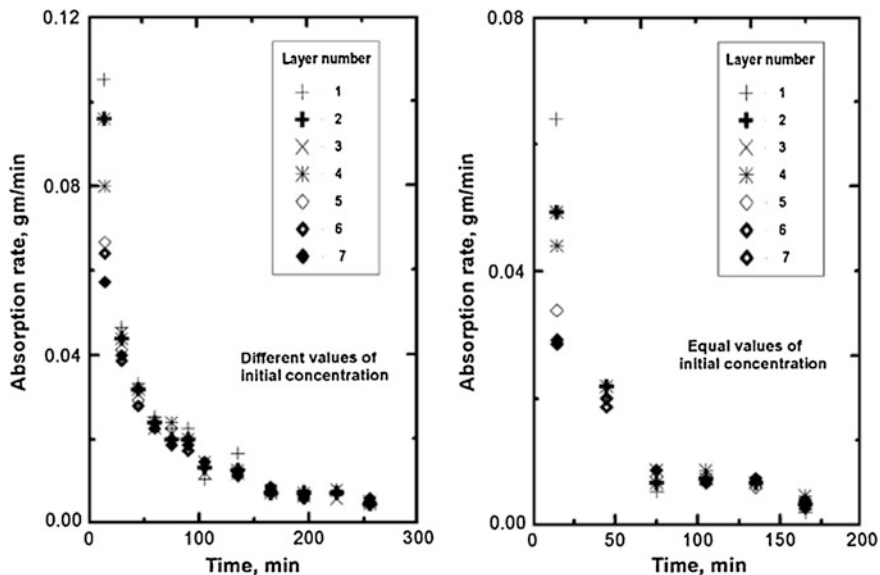


Fig. 5 Absorption rate versus time [1]

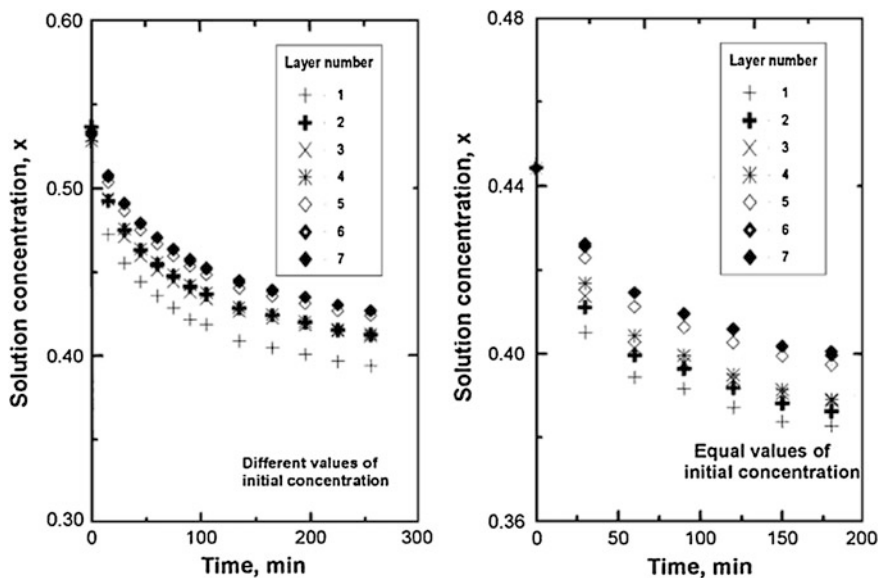
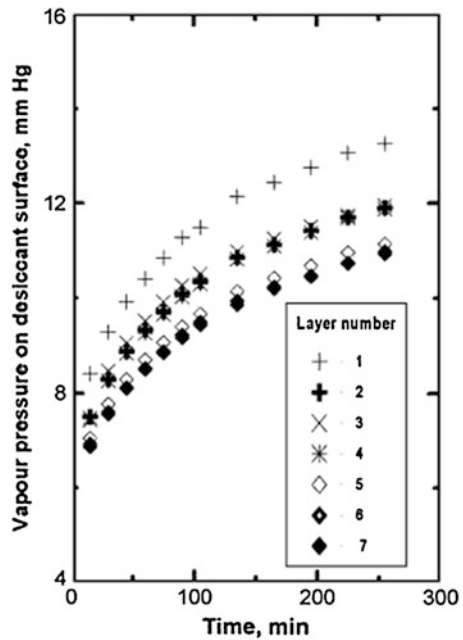


Fig. 6 Desiccant concentration versus time [1]

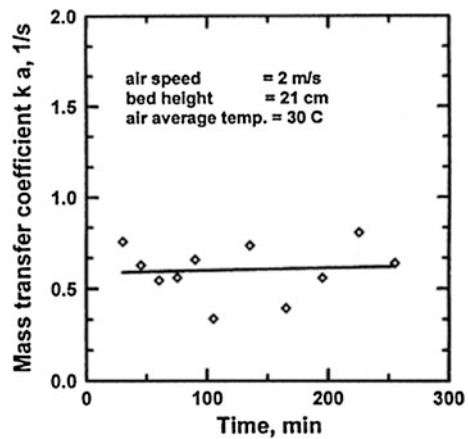
Fig. 7 Vapor pressure versus time [1]



that between the second and the seventh layer. This means that rising the bed height will lower the mass of water absorbed per unit bed volume. Therefore, bed thickness is a design factor which must be properly selected.

Transient variation of the rate of adsorption of water vapor for bed layers is presented in Fig. 5. It can be noticed that the adsorption rate decreases in an exponential nature. The maximum rate occurs at start of adsorption and its value depends on the initial concentration of desiccant in the bed. Transient values of solution concentration and vapor pressure on desiccant surface are shown in

Fig. 8 Mass transfer coefficient versus time [1]



Figs. 6 and 7, respectively, for the two groups of experiments. Comparing the experimental results of Figs. 5 and 7, it can be observed that the rate of adsorption decreases with increase in vapor pressure on the desiccant surface. This because the potential for mass transfer process depends on the difference between vapor pressure in air stream (nearly constant) and that on the desiccant surface. This potential difference is also expressed as the difference between vapor concentration in air stream, C , and that value existing at equilibrium with solution in the bed, C^* .

From the analysis of experimental data, mass transfer efficient for the bed is potted with time as shown in Fig. 8. The average value of k_a is about 0.52, which is presented by the solid line.

3 Vertical Fluidized Bed

The problem of solute concentration gradient in the fixed bed adsorber for both adsorption and desorption modes has been investigated [3–13]. In packed bed adsorbers, it has been found that the concentration of solute for a certain time during adsorption decreases with the increase in distance from the entrance of the bed. This concentration gradient greatly influences the operation of the fixed bed. Figure 9 illustrates the time-dependent concentration of the solute in the fixed bed. In the sketch, the relative density of the vertical lines is meant to indicate the relative concentration of adsorbate. It can be observed that as gas continuous to

Fig. 9 Concentration profile along fixed bed [10]

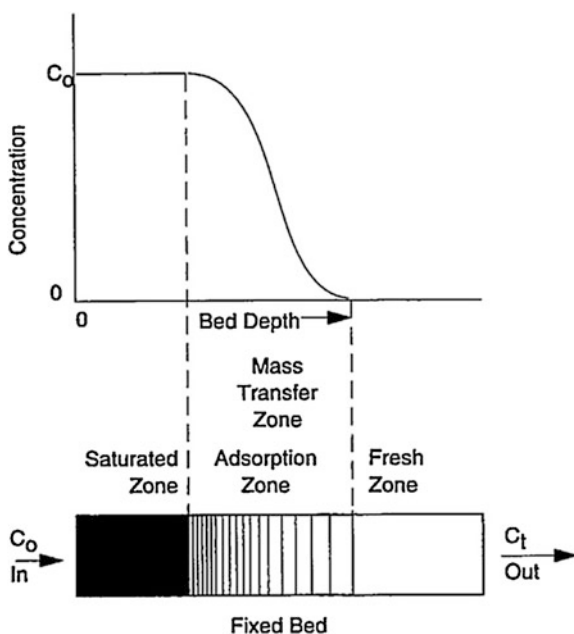
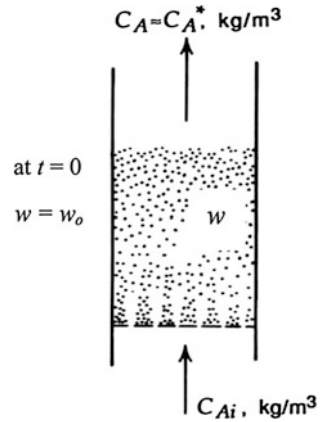


Fig. 10 Adsorption of vapor by a batch of solids [14]



flow, the adsorption zone moves far from the entrance of the bed as a wave, at a rate ordinarily very much slower than the linear velocity of the fluid through the bed [10]. As expected, desiccant layers at the bed inlet adsorb moisture faster than the successive layers and this may result in non-homogeneous distribution of moisture in the bed and consequently the adsorption efficiency, in general, decreases.

Preliminary adsorption/desorption tests are performed for both fixed and fluidized bed conditions at nearly constant conditions of the air inlet parameters and bed initial conditions [14]. These tests emphasized, to some extent, the existence of performance differences between the fixed and fluidization conditions of operation.

The physical system of the fluidized bed is illustrated in Fig. 10. The system contains a batch of solids fluidized with an inert carrier gas containing dilute A of mass concentration $C_{Ai} \text{ kg/m}^3$, which is adsorbed, by the solids. Let w be the weight fraction on a dry basis of adsorbed vapor (adsorbate) on the solids, and let C_A^* be the vapor concentration of A in equilibrium with solids having a moisture fraction (w).

3.1 Mass Transfer Analysis

It is well known that physical adsorption is always coupled with some heat generation. In many cases, this thermal effects have no significant influence on the adsorption dynamics and the process could be handled as isothermal one [12]. In case of fluidized adsorption bed, it is important to examine the validity of isothermal model, under equilibrium condition.

The following assumptions will also be considered in the theoretical analysis of the mass transfer process.

1. There are no radial or axial moisture content gradients within the fluidized bed particles.
2. The mass transfer process can be modeled using the bulk mean moisture concentration of air.
3. The exiting gas can be considered in equilibrium with the solids in the bed [13].

However, when non-equilibrium condition between exit stream and the bed particles is attained, it is possible to assume a certain degree of mass transfer effectiveness. This value could be evaluated from the analysis of experimental data.

Material Balance about the Whole Bed Gives

$$(\text{Vapor lost by gas}) = (\text{Vapor adsorbed by solids})$$

In symbols,

$$A_t u_o (C_{Ai} - C_A^*) dt = A_t L_m (1 - \varepsilon_m) \rho_s dw \quad (1)$$

where A_t is the cross-sectional area of the tube, u_o denotes the superficial fluid velocity (velocity that would exist in an empty tube), and ε_m denotes the fractional void volume. Hence, $(1 - \varepsilon_m)$ denotes the fractional volume taken up by the solid phase. L_m is the static head length and ρ_s is the density of silica gel particles. Separating the variables and integrating for an initial moisture content on the solids w_o gives

$$\int_{w_o}^w \frac{dw}{C_{Ai} - C_A^*} = \frac{u_o t}{\rho_s L_m (1 - \varepsilon_m)} \quad (2)$$

The relationship between the adsorbate concentration C_A^* and w for applied material depends on the thermo-physical properties of the solid adsorbent–adsorbate pair. For the condition of silica gel–water vapor as adsorbent and adsorbate, respectively, linear relation can be expressed for a given temperature range. The relation between C_A^* and w can be expressed in linear function as

$$C_A^* = k_1 + k_2 w \quad (3)$$

where k_1 and k_2 are constants depending on the temperature range.

Substituting Eq. (3) in Eq. (2) and solving gives

$$\frac{w_i^* - w}{w_i^* - w_o} = \text{Exp} \left[- \frac{k_2 u_o t}{\rho_s L_m (1 - \varepsilon_m)} \right] \quad (4)$$

For a given adsorbent–adsorbate system with a specific porosity, density, and bed length, the transient adsorption characteristics can be expressed as

$$\frac{w_i^* - w}{w_i^* - w_o} = \text{Exp}(-B\bar{T}) \quad (5)$$

$$B = \frac{k_2}{\rho_s(1 - \varepsilon_m)} \quad (6)$$

$$\bar{T} = \frac{u_o t}{L_m} \quad (7)$$

where the constant B is the bed characteristic constant and \bar{T} is the dimensionless time. Analysis of Eq. (5) shows that the theoretical time required for the bed to reach an equilibrium condition with the inlet gas is infinity. Actual values of \bar{T} could be evaluated from the experimental measurements and its values depend on the deviation of the theoretical solution from the actual data. Similar analysis for desorption of the bed gives

$$\frac{w_i^* - w}{w_i^* - w_o} = \text{Exp} \left[\frac{k_2 u_o t}{\rho_s(1 - \varepsilon_m) L_m} \right] \quad (8)$$

which is the same expression given in Eq. (4). Also, Eq. (5) can be applied for desorption process.

3.2 Heat Transfer Analysis

Consider a batch of solids originally at temperature T_{po} fluidized by a gas entering at temperature T_{gi} . Due to the rapid movement, the temperature of the bed particles can be considered independent of location in the bed. Assuming plug flow for the gas stream and a quasi-steady-state condition for the gas temperature with height [12], the heat balance gives

$$\text{Heat given by the gas} = \text{heat gained by solids} \quad (9)$$

Applying Eq. (9) to the whole bed during a short-time interval dt gives

$$\rho_g C_{pg} u_o (T_{gi} - T_p) dt = \rho_s C_{ps} (1 - \varepsilon_f) L_f dT_p \quad (10)$$

Solving this heat balance equation with the initial condition

$$T_p = T_{po} \text{ at time } t = 0 \quad (11)$$

gives

$$\frac{T_{gi} - T_p}{T_{gi} - T_{po}} = \text{Exp} \left[- \frac{\rho_g C_{pg}}{\rho_s C_{ps}} \frac{u_o}{(1 - \varepsilon_f) L_f} t \right] \quad (12)$$

where C_{pg} and C_{ps} are the specific heats of gas and solid in the bed, respectively. L_f and ε_f are the height of bubbling fluidized bed and void fraction in a fluidized bed as a whole, respectively. ρ_g and ρ_s are gas density and density of solid, respectively. This expression shows that the time needed to heat the solids to a given temperature is proportional to the static bed height and inversely proportional to the gas velocity.

3.3 Experimental Study of Desiccant Fluidized Bed

An experimental system has been built to operate the desiccant bed in the adsorption and regeneration modes, respectively. Air is supplied to the system through an air tank connected to a reciprocating air compressor (see schematics in Figs. 11 and 12). Air heater is connected through a by-pass between air tank exit and fluidized bed inlet. To adjust the air to a proper level of humidity, humidifier is designed and located in the adsorption system. Water is injected to the humidifier from the water tank through an injection pump. A packed bed dehumidifier is used to reduce the ambient air humidity during the experiments. The system piping diagram and control valves are designed to facilitate the operation in adsorption and regeneration phases. Details of the experimental unit are given in [14].

Preliminary test is carried out to evaluate the differences between packed and fluidized bed adsorption characteristics. Two beds with identical operating conditions of flowing air stream and initial water content in silica gel are tested in packed and fluidized conditions. Air parameters at bed exit are recorded for the two tests. Also, transient values of mass transfer coefficient are evaluated for purpose of comparison. The transient variation of humidity and temperature of air at bed exit for the two cases is presented in Figs. 13 and 14, respectively. Reducing the humidity of air is the major function for the adsorption bed, and therefore, the lower the humidity of exit air stream the better is the performance of the bed. Under fluidization condition, the humidity of the exit air decreases by about 20 % than that attained with packed bed. On the other hand, accumulation of the heat of adsorption in the packed bed results in increase in the bed temperature when it is compared with that of fluidized bed.

As shown in Fig. 14, the maximum temperature of exit air is about 46 °C for packed bed condition, whereas this value is around 40 °C for fluidization condition.

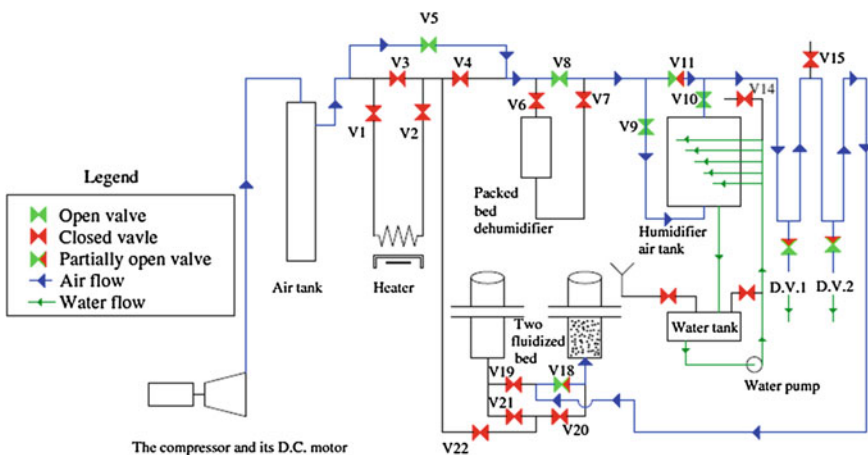


Fig. 11 State of control valves during the adsorption test [14]

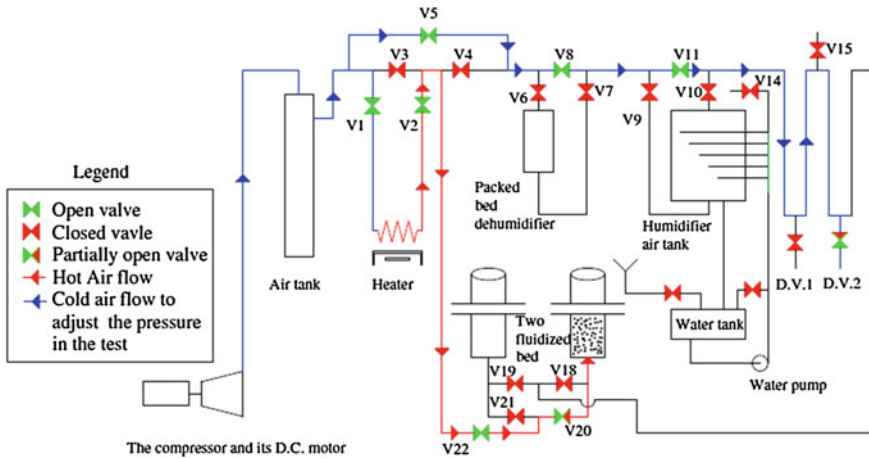


Fig. 12 State of control valves during the regeneration test [14]

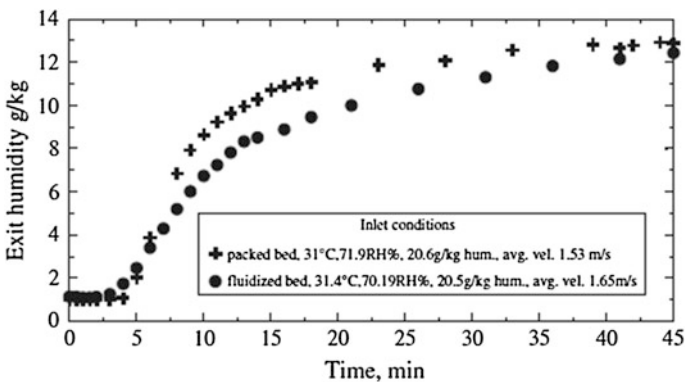


Fig. 13 Exit humidity versus time for packed and fluidized bed adsorption tests [14]

Values of volumetric mass transfer coefficient for packed and fluidized bed show that the mass transfer coefficient is higher during fluidization compared with that of packed bed, see Fig. 14. This preliminary test shows that the adsorption process can be improved by fluidization. Also, it can be expected that the desorption characteristics can be improved with fluidization of silica gel particles.

3.4 Adsorption Tests

Figure 15 shows the variation of the specific humidity (g/kg) of air stream as well as the exit temperature. The relative humidity at bed inlet for the four-presented

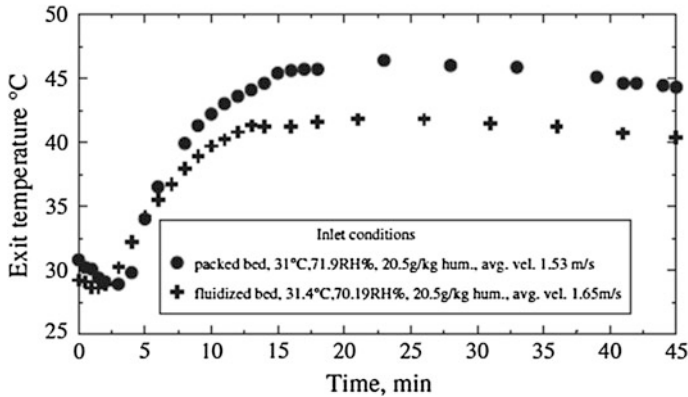


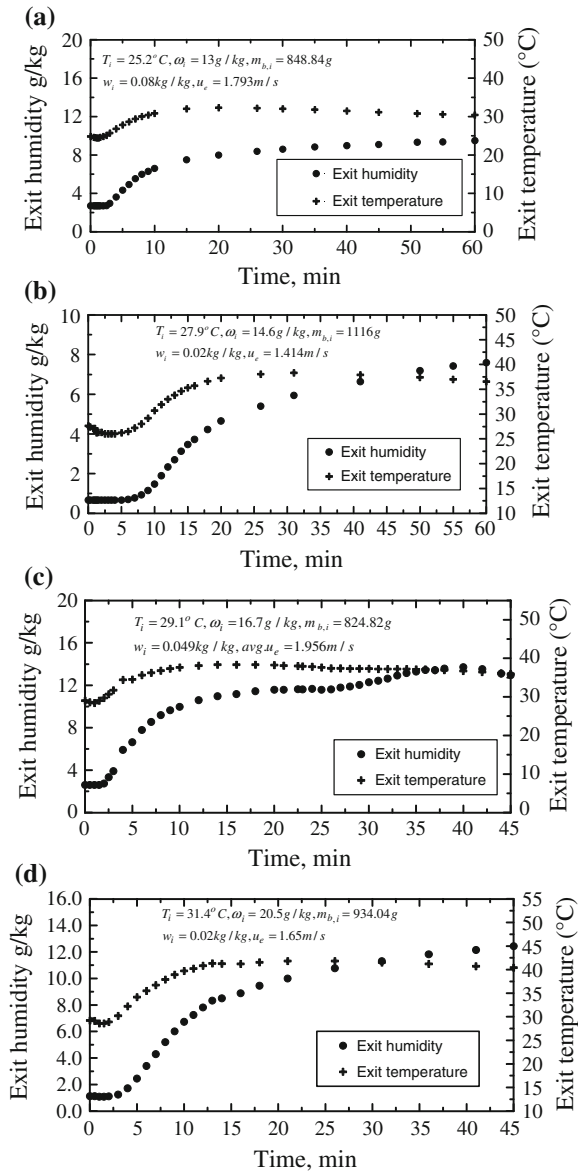
Fig. 14 Exit temperature versus time for packed and fluidized bed adsorption tests [14]

runs varies from 61.8 to 70.2 %. The transient variation of air humidity at bed exit shows a gradual increase in humidity with time from a minimum value attained within 2–7 min from the start of the process. The trend of humidity curve for different tests is nearly the same irrespective of the inlet parameters. Analysis of the measured values of humidity shows that the maximum rates of vapor transfer from air stream to the bed occur during the starting period of adsorption. As the water content in the bed increases with time, the vapor pressure on the surface of silica gel particles also increases and the potential for mass transfer decreases. The temperature of exit air stream also rises from a minimum value, which is nearly equal to the inlet temperature, to a nearly constant value. The trend of temperature rise is approximately similar to that of humidity increase. This can be explained as follows: when adsorption starts, bed temperature has its lower value and consequently, the vapor pressure difference between air stream and bed surface is the maximum. The heat of adsorption rises the temperature of the bed at a rate equal to that of moisture transfer. Subsequent increase in bed temperature results in increase in vapor pressure on the bed surface and consequently decreases in mass transfer potential. As the vapor transfer from air decreases, the rate of generation of adsorption heat also decreases. Also, the flowing air cools the heated bed, which results in a nearly constant bed temperature as shown in figure.

3.5 Adsorption Rate

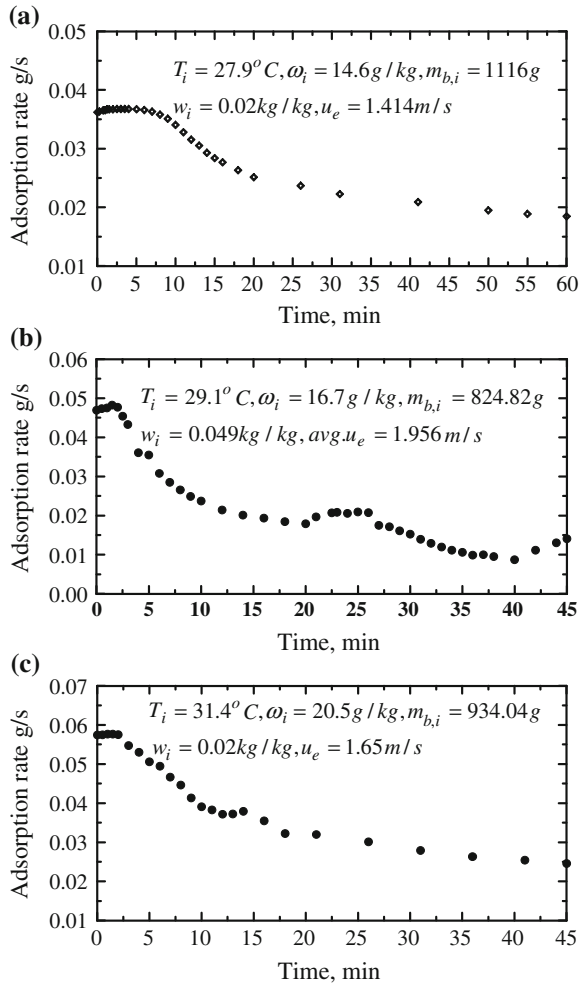
The rate of vapor adsorption for the different runs is depicted in Fig. 16. As expected, the maximum rate occurs at the first few minutes of the adsorption process, and then, the adsorption decreases gradually with time. The maximum value of the adsorption is found dependent on the initial humidity of air.

Fig. 15 Exit humidity and temperature with time [14]



For example, its value is about 3.46 g/min when the inlet humidity equals 20.5 g/kg, while this rate decreases to 2.07 g/min for air inlet humidity equal 13.0 g/kg. However, this adsorption rate is also affected by the initial mass of the bed and airflow rate.

Fig. 16 Water adsorption rate with time [14]



3.6 Water Content of the Bed

One of the most effective parameters on the bed performance is the water content in silica gel. Bed temperature and water content determine the equilibrium relative humidity of air with the bed. Figure 17 shows the variation of water content in the bed for different runs.

Also, Fig. 18 shows the variation of bed mass with time. It can be noted that the adsorbed mass of water for each bed depends on the bed initial mass, initial water content, and the air inlet conditions. For the same period of adsorption, an increase in initial mass of the bed and inlet humidity and/or decrease in operating temperature and initial water content results in increase in the total mass of water adsorbed in the bed.

Fig. 17 Water content in silica gel with time [14]

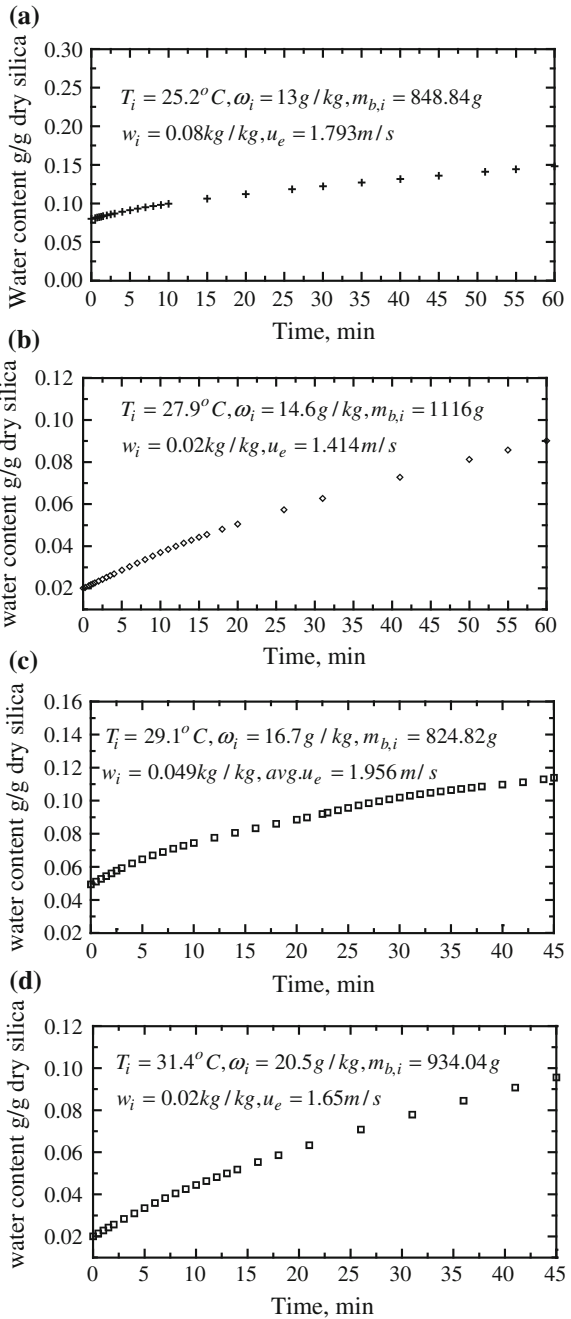
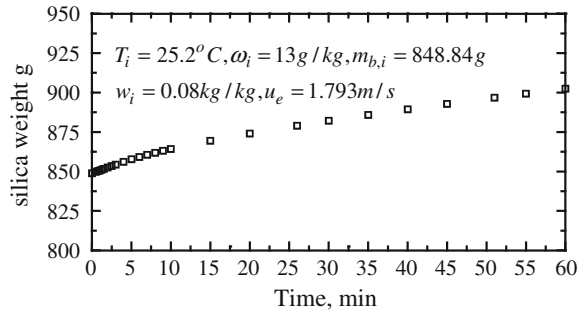


Fig. 18 Increase in silica mass with time [14]



3.7 Vapor Pressure on Desiccant Surface

The mass transfer potential can be expressed in terms of vapor pressure difference or vapor density difference between flowing air and the desiccant bed. Therefore, values of vapor pressure in the air stream at bed inlet and exit as well as on the bed surface are evaluated and plotted in Fig. 19. Water content is assumed constant in both axial and radial direction in the bed. The vapor pressure varies along the bed due to temperature change. Vapor pressure is then used to evaluate the vapor density, which is used as the mass transfer potential to evaluate the mass transfer coefficient.

3.8 Mass Transfer Coefficient

The volumetric mass transfer coefficient for the different adsorption tests is presented in Fig. 20. It can be seen that the mass transfer coefficient has higher values at the beginning of adsorption and decreases to nearly constant value. As the flow rate is constant during various runs, Reynolds number is also constant. The variation in Schmidt number for each run will be due to the transient change in the thermo-physical properties (ν, D). For most cases, this variation in Schmidt

Fig. 19 Vapor partial pressure with time [14]

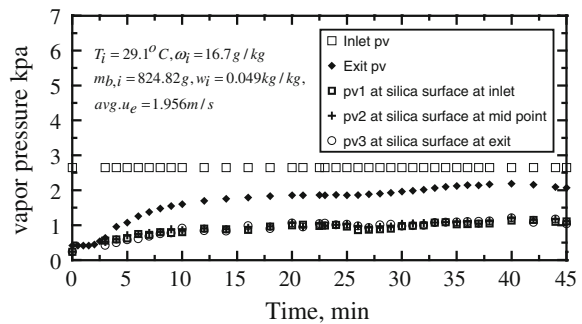
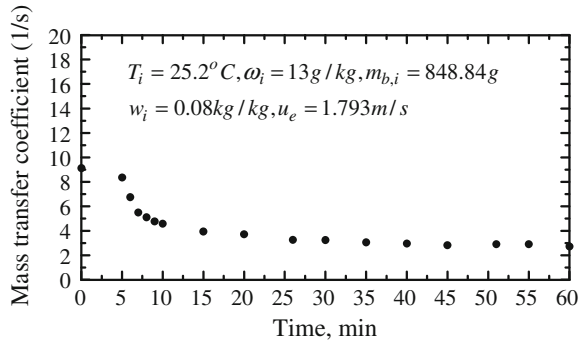


Fig. 20 Mass transfer coefficient with time [14]



number is small and consequently Schmidt number can be assumed constant. Therefore, the significant change in the mass transfer coefficient during the process must be explained in the light of the bed operating characteristics. From the visual observations of the particle movements, the lower zone of the bed is close to the packed bed conditions and fluidization or particles movements increase gradually in the axial direction. This results in homogenous adsorption during the first few minutes. The water content in the lower layers successively increases in a rate higher than that of the upper layers. As the lower layers adsorb excessive amount from the air, their mass transfer potential decreases in comparison with the upper layers. Therefore, the actual effective adsorption volume of the bed decreases with time until the major portion of the adsorption is carried out in the moving particles. When the lower portion of the bed particles has a lower adsorption rate, after a small period, the decrease in the effective bed volume is not considered in calculations of mass transfer coefficient and consequently it seems to be decreased.

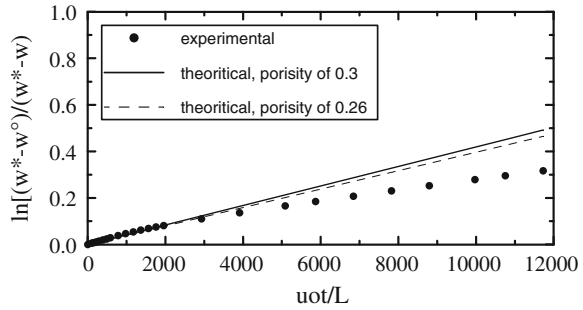
Regression constants of Eq. (3) are evaluated from the linear fitting of physical properties of silica gel. Equilibrium relative humidity is calculated from the physical properties of silica gel at constant temperature, and then, the specific humidity ω (kg_v/m^3 air) is evaluated by knowledge of temperature and relative humidity of air stream. Values of regression constants are dependent on the air inlet temperature during adsorption. Table 1 shows values of k_1 and k_2 with the corresponding temperatures.

Exact geometrical definition of the porosity of silica gel particles is rather difficult. In the present analysis, the so-called effective porosity will be considered which is based on the communicating portion of a pore [13]. The total porosity, of course, is very large compared with the effective one. However, spherical particles

Table 1 Evaluated values of k_1 and k_2 with the corresponding temperatures [14]

Temperature °C	k_1	k_2
25.2	-0.000483	0.0330948
27.9	-0.000556	0.0397986
28.8	-0.000582	0.0422896
31.4	-0.000663	0.0502858

Fig. 21 Comparison between the experimental measurements and theoretical calculations [14]



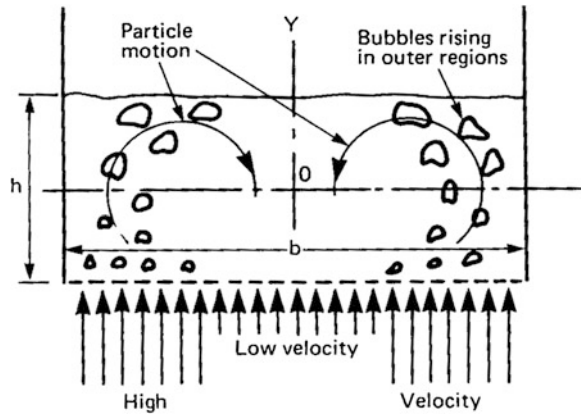
may be arranged in different ways. They may have a loose packing (cubic arrangement) or dense packing (hexagonal arrangement). Therefore, the porosity of silica gel particles depends on the type of arrangement rather than on the particle radius. With a cubic arrangement, $\varepsilon = 47.46\%$, and with the hexagonal arrangement, $\varepsilon = 25.95\%$. Moreover, with a hexagonal arrangement, every particle is in contact with 12 neighboring ones and pores may be of two shapes, namely tetrahedral and rhombohedral. For tetrahedral arrangement, the calculated value of ε is 0.2595 whereas the experimentally evaluated value is 0.302. Also, for octahedral arrangement, calculated value of $\varepsilon = 0.2595$ and the experiments give 0.33 [13].

The approximate analytical solution obtained from the model is plotted with the values obtained from the experimental measurements as shown in Fig. 21, which is presented for two values of ε (0.26 and 0.3). It can be observed that the lower value of ε decreases the deviation of the theoretical values from the experimental ones. Also, agreement between the theoretical and experimental results is better for the first period of time. As the adsorption time increases, the difference between model and experiments increases. This can be explained as follows: the isothermal equilibrium assumption is more close to reality at beginning of adsorption and deviation from reality increases with increase in bed temperature. As the bed temperature actually increases with time due to vapor condensation, the equilibrium state between the inlet air stream and silica gel particles can be attained with continuous cooling during the process.

4 Inclined Fluidized Bed

The motion of solid particles in a fluidized bed can be influenced by arranging for an uneven distribution of gas flow through the distributor plate. Thus, Merry and Davidson [8] introduced gross circulation of particles in both two- and three-dimensional beds by supplying more gas to the outer region of the distributor than the central area (see Fig. 22). In this way, an excess of particles was moved upwards in the bubble wakes in the outer regions while in the center of the bed, due to the relative scarcity of bubbles in that region, particles were moved

Fig. 22 ‘Gulf Stream’ circulation [8]



predominantly downwards. With this arrangement, particles were introduced to circulate continuously in a steady pattern in two circulation cells—the so-called Gulf Stream circulation. This type of motion is favored particularly in relatively shallow beds. The induced circulation of large particles has been studied by Rios et al. [16], using a device known as a ‘whirling bed,’ shown in Fig. 23. In this system, the perforated plate distributor is covered by a 45° angle wedge which serves to return particles, which are effectively de-fluidized in the upper region of the bed, to the grid where they are again carried upwards by the entering air.

For increasing adsorption and desorption efficiency, new approaches are highly welcome. An attempt to improve the performance of solid desiccant should include an investigation on the performance of new bed configurations.

An investigation on the operation of an inclined bed of silica gel in adsorption and desorption modes of operation has been presented in [16]. In this respect, the article is concerned mainly with the mass transfer aspect to evaluate the effect of air velocity on the adsorption and desorption rates.

The experimental test unit was designed to:

- study the adsorption and desorption operation of an inclined fluidized bed for different values of air velocity.
- evaluate the effect of bed inclination on the moisture concentration in the bed through the color gradient (the color is blue when the particles are regenerated).

The setup used in the adsorption–desorption experiments for the tilted bed of silica gel is depicted in Fig. 24. The apparatus mainly consists of (1) air blower, (2) air heater, (3) glass tube of 600 mm length and 31 mm diameter (4), (5) inlet and outlet screen, (6) stand to support the inclined bed. The metal screens have holes about 1 mm², where the particles are about 3 mm in diameter. The bed is inclined during the experiments at an angle of 45° (Figs. 25, 26, 27).

The maximum regeneration temperature used in this study was about 90 °C; therefore, the results of this study apply to low-temperature applications (waste

Fig. 23 Whirling bed apparatus [8]

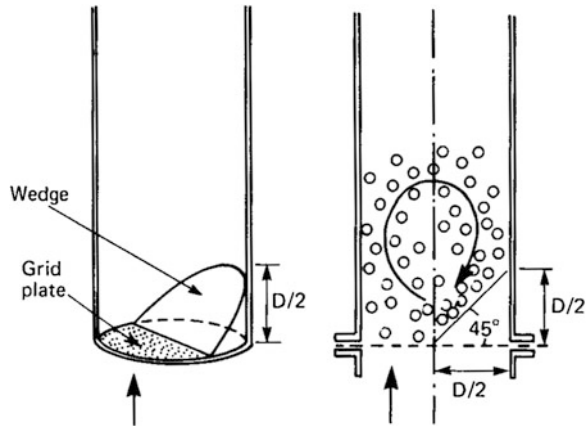
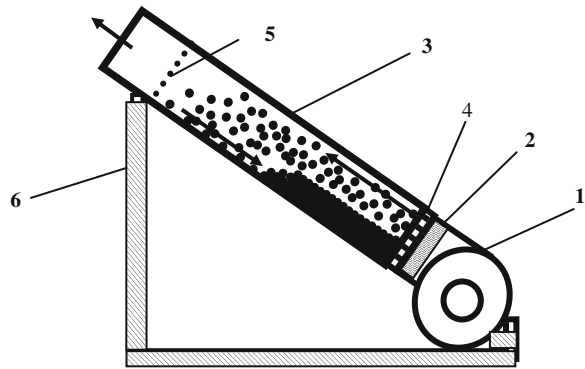


Fig. 24 Experimental inclined fluidized bed [15]



heat and low-temperature solar-regeneration). Operating conditions and parameters are reported in Table 2.

The most important property of a desiccant used in humidification and cooling applications is its ability to remove water vapor. This is usually quantified in terms of equilibrium isotherm, i.e., moisture capacity (kilograms moisture removed/kilograms dry desiccant) as a function of relative humidity at a constant temperature. The moisture capacity of the bed was measured by a gravimetric technique. To measure the adsorption capacity, desiccant sample was loaded in the test tube and the moisture gain (during adsorption) or removed (during regeneration) was obtained from the difference of initial and final weight of the desiccant. Measurements were carried out at nearly constant conditions of process and regeneration air (temperature and humidity). The inlet condition of the process air for different values of air velocity is fixed at 27 °C dry-bulb temperature and 66 % relative humidity. The mass of the bed is recorded with time using a digital balance of 0.02-g resolution and 600-g scale range.

Fig. 25 Effect of air velocity on the adsorption rate [15]

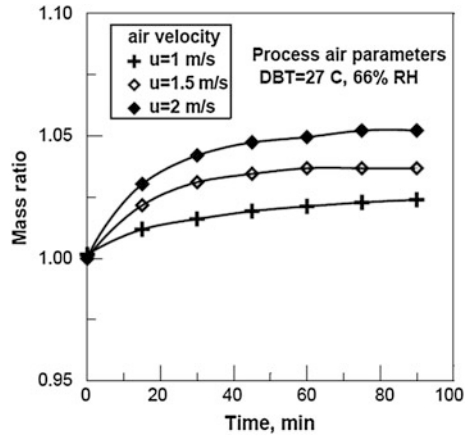


Fig. 26 Effect of air velocity on the desorption rate [15]

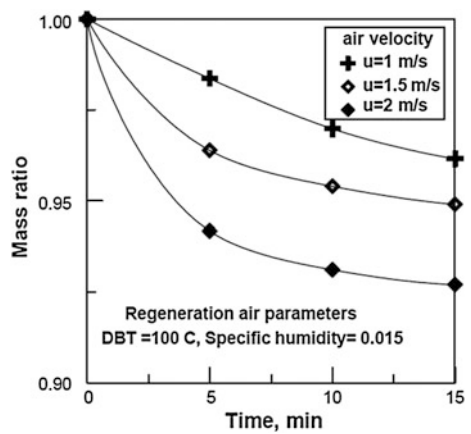


Fig. 27 Change of process air humidity with time for different values of air flow rate [15]

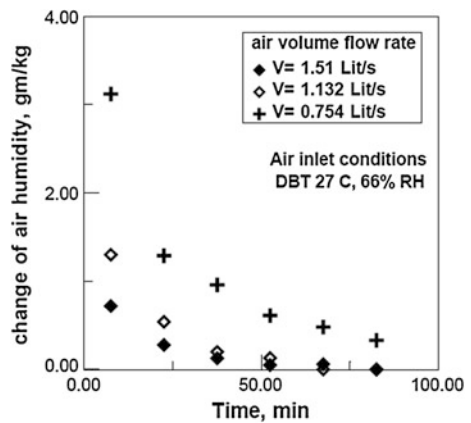


Table 2 Operating conditions for different values of air velocity during adsorption and desorption operations [15]

Air velocity, m/s	Bed volume, cm ³	Packed bed length, cm	Total mass adsorbed, g/kg	Total mass regenerated, g/kg
2.0	43.54	5.77	52.2	76.6
1.5	81.19	10.75	36.8	52.8
1.0	279.26	37	22.2	39.3

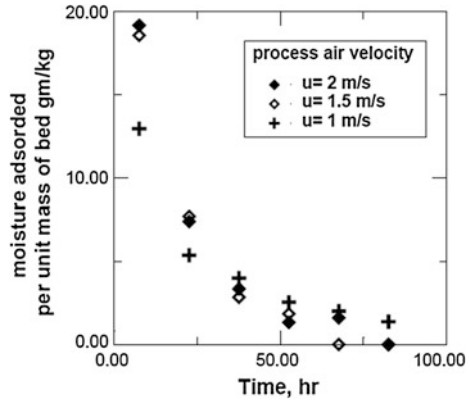
The motion of particles in the bed is influenced by the inclination of the tube. With inclination of the tube, uneven distribution of the effect of bed weight on the inlet area is attained. As a result, the bed pressure on the inlet section increases in a downward direction, and consequently, the resistance to air flow is higher in the lower part of the inlet section of the tube. When the process air is introduced, the upper layers of the particles along the bed is moved upwards with the flowing air stream while in the lower region, due to the effect of gravity, particles move predominately downwards. In this way, silica gel particles are introduced to circulate continuously. The bed in this condition can be divided into two regions: the upper region moves upward in fluidized manner, while the lower region can be described as packed bed moving downwards.

To evaluate the effect of process air velocity on the adsorption rate, mass ratio of the bed is plotted versus time as shown in Fig. 4. The mass ratio is defined as the ratio of the instantaneous mass of the bed to the initial mass. As shown in figure, higher rate of adsorption is attained at air velocity of 2 m/s. The inlet condition of the process air for different values of air velocity is fixed at 27 °C dry-bulb temperature and 66 % relative humidity. The average bed temperature during the adsorption period is about 35 °C. As the desiccant bed was near the saturation condition, the increase in the initial mass is limited to about 5 %. Cooling of desiccant bed during adsorption could increase this value. The desorption process was carried out at the end of adsorption using regeneration air of 15-g/kg specific humidity and about 100 °C inlet temperature, while the average bed temperature is about 90 °C. The desorption period was limited to 15 min for different values of air velocity. Figure 5 shows that the regeneration rate is highly affected by the air velocity. It can also be expected that more moisture could be removed by increasing the regeneration period, which means that the mass transfer potential for the specified regeneration condition is higher compared with adsorption.

The change in air humidity during adsorption is evaluated from the experimental measurements and plotted versus time as shown in Fig. 6. The drop in air humidity rapidly decreases with time and reaches zero at the end of adsorption. As the mass of desiccant was not equal, the specific humidity of process air has a significant change for lower values of flow rate of air. This of course is due to increase in bed capacity and the increase in bed to air mass ratio.

To eliminate the effect of bed mass, the specific moisture adsorbed from air is plotted in Fig. 28. The specific value of moisture adsorbed is defined as the ratio of the drop of the air humidity to the bed mass in $\text{g}_v/\text{kg}_{\text{air}}\cdot\text{kg}_{\text{bed}}$. It can be observed

Fig. 28 Transient variation of relative value of moisture adsorbed per unit mass of bed material for different values of air velocity [16]



that the specific moisture adsorbed rapidly decreases with time and reaches zero in shorter time for higher values of air stream velocity.

At the specified operating conditions of the experimental tests, the cooling capacity of the system is depicted in Fig. 29. This cooling capacity is evaluated from the mass of water vapor adsorbed into the bed. As shown in figure, higher values of cooling rate could be obtained at start of adsorption. This value rapidly decreases with time for all the tested values of air speed. However, complete evaluation of system performance must include the fan power consumed, this power is expected to be higher for higher values of process air velocity. It is also expected that increasing the regeneration temperature can enhance the cooling capacity of the bed.

The color of silica gel during experiments gives a good indication to the rate of mass transfer to/from the bed (the silica gel used in this investigation is of indicating type, the color is blue when regenerated). The degree of darkness in the bed during

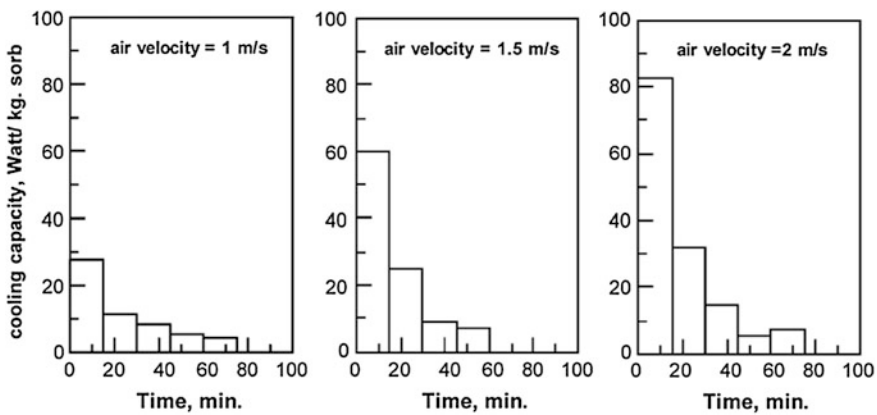


Fig. 29 Average value of cooling capacity versus time during adsorption at different values of process air velocity [16]

regeneration increases with time of exposure to the hot air stream. With packed bed operation, a drastic change in color at inlet section can be observed. Also, the gradient of color darkness decreases with bed height, which explains the degree of reactivation (regeneration) in the bed. In inclined bed operation, well mixing and distribution results in homogenous distribution of the color through the bed.

From the mass transfer analysis different configurations of the desiccant bed, it is evident that the process is transient for all configurations presented in this chapter. The application of inert material carrying the liquid desiccant shows a possibility to regenerate and absorb water vapor in packed bed, relatively lower regeneration temperature. However, the major problem in such case is the concentration gradient in the vertical direction of the bed. The concentration of solute for a certain time during adsorption decreases with the increase in distance from the entrance of the bed. This concentration gradient greatly influences the operation of the fixed bed. Desiccant layers at the bed inlet adsorbs moisture faster than the successive layers, and this may results in non-homogenous distribution of moisture in the bed and consequently the adsorption efficiency, in general, decreases. Also, an average value of the mass transfer coefficient for the bed is evaluated as 0.6 s^{-1} .

Fluidizing a bed of solid particles with a gas provides a means of bringing the two into intimate contact, and this can be very useful in improvement of the adsorption/desorption characteristics of the desiccant column. Its most important advantage stem from the fact that the solid particles in contains are in continuous motion and are normally very well mixed; the result is that 'hot spots' are rapidly dissipated and bed operates in an essentially isothermal manner. Moreover, the fluid-like properties of the gas–solid mixture enable the solid to be transferred without difficulty from one vessel to another a useful feature in cases where the solid is required to take part in two different reactions as part of the same overall process.

5 Conclusions

For all configurations, the relative mass of adsorbed water increases with the increase in the humidity of inlet air and the maximum value of air exit humidity during desorption (regeneration) is dependent on the regeneration temperature. Due to the transient operation of the system, vapor generation rate increases gradually with the increase in bed temperature and consequently the mass transfer potential. When water content in the bed decreases with time, a successive increase in bed temperature has small effect on the rate of vapor generation. Visual observation of the movement of the particles and color change of the silica gel during adsorption show that homogenous water content in the particles can be expected in the bed layers, which has higher degree of fluidization. Experimental measurements indicate that the regeneration and adsorption rates are highly dependent on the air stream velocity.

References

1. Hamed AH (2002) Theoretical and experimental study on the transient adsorption characteristics of vertical packed porous bed. *Renew Energy* 27:525–541
2. Hamed AM (2003) Desorption characteristics of desiccant bed for solar dehumidification/humidification air conditioning systems. *Renew Energy* 28:2099–2111
3. Van der Wiel JP, Wesselingh JA (1988) Continuous adsorption in biotechnology. In: Rodrigues AE et al *Adsorption: science and technology*. Kluwer Academic publishers, Portugal
4. Pesaran AA, Mills AF (1992) Moisture transport in silica gel packed beds-I. Theoretical study. In: *Desiccant cooling and dehumidification*. ASHRA Technical Committee
5. Dupont M, Celestine B, Merigoux J, Brandan B (1994) Desiccant solar air conditioning in tropical climate: dynamic experimental and numerical studies of silica gel and activated alumina. *Solar Energy* 52(6):509–517
6. Chaul SS, Fan LS (1998) Heat transfer in packed and fluidized beds. In: Rohsenow WM et al *Handbook of heat transfer*, 3rd edn. McGraw-Hill, New York
7. Pesaran AA, Mills AF (1992) Moisture transport in silica gel packed beds-II experimental study. In *desiccant cooling and dehumidification*, ASHRA Technical Committee
8. Dupont M, Celestine B, Beghin B (1994) Desiccant solar air conditioning in tropical climate: II-field testing in Guadeloupe. *Solar Energy* 52(6):519–524
9. Kim S, Biswas P, Mills AF (1985) A compact low pressure drop desiccant bed for solar air conditioning applications. *ASME J Solar Energy Eng* 127:107–120
10. Treybal RE (1980) *Mass-transfer operations*, 3rd edn. McGraw-Hill, New York
11. Pentchev I, Paev K, Seikova I (2002) Dynamic of non-isothermal adsorption in packed bed of biporous Zeolites. *Chem Eng J* 85:245–257
12. Kunii D, Levenspiel O (1991) *Fluidization engineering*, 2nd edn. Butterworth-Heinemann, Boston
13. Luikov AV (1978) *Heat and mass transfer*. Mir Publishers, Moscow
14. Hamed AM, Abd-elrahman WR, El-Emam SH (2010) Experimental study of the transient adsorption/desorption characteristics of silica gel particles in fluidized bed. *Energy* 35(6):2468–2483
15. Hamed AM (2005) Experimental investigation on the adsorption/desorption processes using solid desiccant in an inclined-fluidized bed. *Renew Energy* 30:1913–1921
16. Yates JG (1983) *Fundamentals of fluidized-bed chemical processes*. Butterworths

Desiccant Dehumidification Integrated with Hydronic Radiant Cooling System

A. Z. Zainal and A. S. Binghooth

1 Introduction

Solid desiccant wheel is a main part of desiccant dehumidification system, while chilled ceiling panel is a main part of hydronic radiant cooling system in the present study. Desiccant is compatible with a conventional air-conditioning system in which the desiccant deals with latent heating load, while the air conditioner deals with sensible heating loads. Desiccants materials which have an ability to absorb and/or adsorb water vapor from the surrounding is a unique approach that can overcome unwanted humidity. The common desiccants used in dehumidifier are silica gel in solid form and calcium chloride in liquid form. Reduction in energy consumption was achieved when assisted by desiccant dehumidification. In attaining an acceptable thermal comfort, controlling indoor air quality, temperature, relative humidity, and ventilation is essential. The humidity of an air-conditioned space can be reduced by removing the moisture via desiccant dehumidification [1, 2]. Desiccant dehumidifiers normally comprise of a singular desiccant; however, compound desiccants have also been used [3–5]. Hot humid climates in the tropics have relative humidity in the range of about 70–80 % and require significant refrigeration capacity to reduce the temperature below the dew point to remove the moisture in the air. Using desiccant dehumidification in these climatic locations will reduce the electrical power consumption. In general, the advantages of employing desiccant have encouraged many researches to extend their investigations experimentally and numerically on the performance of the desiccant and improving indoor air quality [6, 7]. More advance dehumidification system integrated with a membrane-based total heat exchanger would enhance the performance of the air-conditioning system [8]. Conventional air-conditioning is a system designed to generate indoor cool air by counterbalancing two types of loads: latent and sensible heat loads. The

A. Z. Zainal (✉) · A. S. Binghooth
School of Mechanical Engineering, Universiti Sains Malaysia, Engineering Campus,
14300 Penang, Nibong Tebal, Malaysia
e-mail: mezainal@eng.usm.my; mezainal@yahoo.com

system's goal is to preserve temperature and humidity for thermal comfort and set it within acceptable range. But this is difficult to achieve in tropical areas, such as Malaysia, as converting the hot humid air into a dry cool air to attain thermal comfort is a challenging task, although vapor compression cycle systems have been widely used for this purpose [9]. The first use of hydronic radiant cooling (HRC) system using chilled ceiling panels was recorded in the 1990s in Europe [10]. Dehumidification prior to cooling reduces the condensation risk in hot and humid countries [11]. HRC provides the comfortable air environment and energy cost-effective solution for moderate climate regions; however, its performance is affected for humid hot climates due to the condensation issues. Computerized models have been developed to understand the effect of chilled ceiling system on the properties of indoor air quality, thermal comfort, and concentration distribution, and to compare chilled ceiling system with conventional air-conditioning system in terms of energy consumption [12, 13]. Applying a ventilation system has many benefits, such as attaining better air quality, more control over the airflow, and improved comfort [14]. According to ASHRAE (2005) Standard, ventilation process involves achieving equilibrium air pressure, such that the amount of exchanged air to the outside is equal to the amount of air entering/circulating inside the target space. This equilibrium is one of the most important objectives for maintaining acceptable indoor air quality in buildings. When this optimum condition is met, the air is then called "ventilation air," which is the one that provides an acceptable indoor air quality. In humid climates, much energy is required to remove excess moisture from ventilation air. The principal targets of any ventilation system in internal closed space environment are removal of pollutants from the space air to preserve occupant's health [15] and thermal conditioning to provide space occupants with comfort [16]. Therefore, ventilation system must be designed to provide an adequate fresh air for respiration, minimize the exposure of occupants to pollutants (such CO₂ and odors), and regulate the temperature within the space. Simulation studies have been carried out on the applications of radiant cooling system and thermal comfort assessment comparing with naturally ventilated classrooms and air conditioning offices [17]. Displacement ventilation mode is the highest quality mode of ventilation as it provides fresh air and shows higher ventilation efficiency.

Adequate amount of fresh air into an air-conditioned space depends on the ventilation system, in particular the location and either natural or forced convection [18, 19]. High fresh air composition is required, for example, in hospitals where contaminated air is removed and also to replenish oxygen supply. However, this requires a much higher refrigeration capacity to cool the higher amount of incoming hot and humid air especially for conventional air-conditioned system that uses a cooling coil with an air blower. Integrating chilled ceiling with dehumidified ventilated air presents many advantages related to thermal comfort, absence of condensation, and energy saving [20]. In the desiccant dehumidifier, incoming humid air passes through a rotating wheel of desiccant. When the desiccant wheel is saturated with moisture, it must be reactivated with energy supplied via an electrical heater. Therefore, to determine the required time for the desiccant

to be saturated, it is necessary to control relative humidity and reduce energy consumption. Undesirable condensation on chilled ceiling panels' surfaces normally occurs in hot humid climates like Malaysia and can be prevented by controlling the chilled ceiling surface temperature and relative humidity of the incoming air or ventilated air. Investigation on controlling the desiccant operation time at various airflow rates to reduce power consumption while maintaining the relative humidity and the dehumidification capacity is investigated.

2 Methodology

Bry-Air compact dehumidifier Fluted Flat Bed (model-FFB-600) with high-performance metal-silicate-fluted and desiccant-synthesized rotor was used in the present study. Figure 1 shows the main processes of the desiccant dehumidifier. Hydronic radiant cooling system consists of three main components: chilled ceiling panel, water circulation system, and environmental chamber. Chilled ceiling panel is made from aluminum sheet and has a size of $1.70 \times 0.5 \times 0.02$ m.

Chilled water from a chiller passes through copper tubes of 0.01 m diameter embedded into the panel as shown in Fig. 2. There are 12 chilled ceiling panels installed below the ceiling of the environmental chamber. The environmental

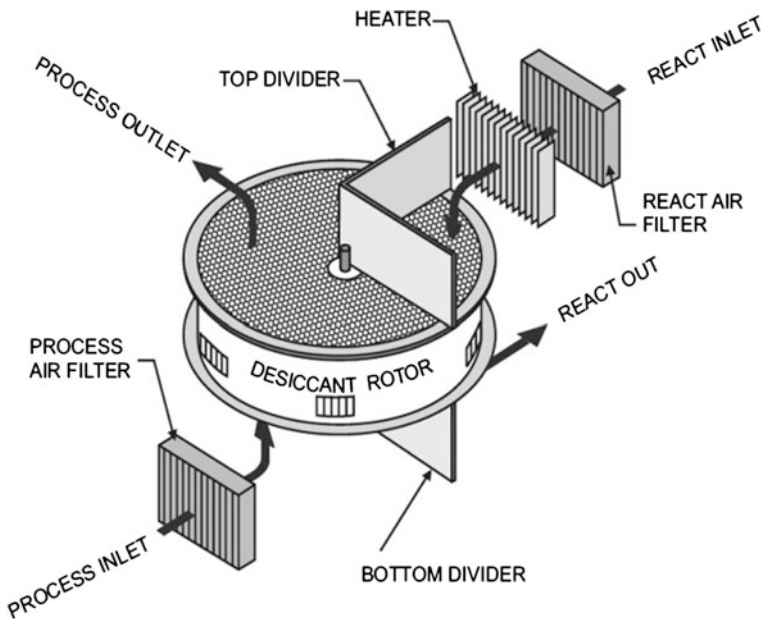


Fig. 1 Main process of the dehumidifier

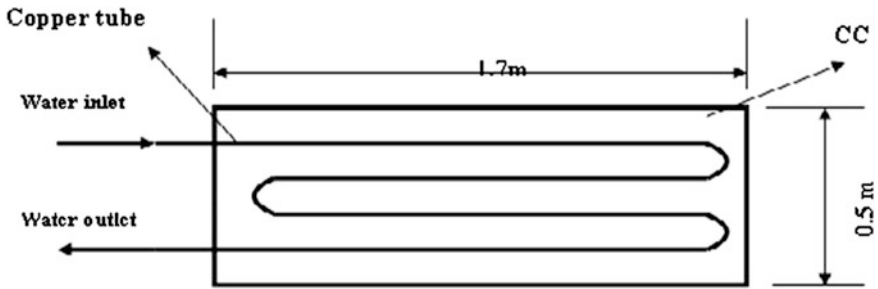


Fig. 2 Schematic of chilled ceiling panels with copper tubes

chamber wall thickness is 100 mm, constructed with demountable clip-lock-type insulated panels. The insulated panels are made of galvanized steel sheets laminated with the insulation core of polyurethane with the dimension of $4.25 \times 3.75 \times 3$ m. An inlet into the chamber is located at the bottom right, and the exit is located at the left top directly opposite to the air inlet. These air vents are of the same diameter of 11 cm.

Figure 3 shows the photograph of environmental chamber with chilled ceiling panels. The room temperature measurement (T_R) is taken 1 m above the floor.

The performance of the desiccant dehumidification was evaluated by determining the minimum relative humidity, the saturation time for dehumidification, and the dehumidification capacity. Two experiments were conducted on the desiccant dehumidifier. The first experiment was conducted by switching off the electrical heater and then running the desiccant with different airflow rates of 81, 162, and 243 L h^{-1} as soon as the desiccant reaches its active temperatures. The dehumidification capacity was determined by using the following equation:

$$Dc = m_{\text{air}}^{\bullet} * (w_{\text{in}} - w_{\text{out}}) \quad (1)$$

where m_{air}^{\bullet} is the mass flow rate of air (kg/s) and $(w_{\text{in}} - w_{\text{out}})$ is the difference in the humidity ratio (g water/g dry air).

The relative humidity was measured at the air inlet and outlet by a relative humidity meter (model BSU102). Psychometric probe sensor was connected to a data acquisition instrument (model BABUC/A). The relative humidity of the inlet air process was 86 %. While in the reactivation sector, the second experiment was conducted by running the desiccant for 60 min, with and without electrical heater to control the relative humidity. The desiccant was run with electrical heater with airflow rates of 81, 162, 243 L h^{-1} for about 30, 20, and 15 min, respectively, to maintain minimum relative humidity, and then, the electrical heater thereafter was switched off for the next 30, 40, and 45 min, respectively. Chilled ceiling chamber was subjected to three experiments. The first experiment was carried out by measuring the chilled water inlet temperature (T_{CWI}), chilled water outlet temperature (T_{CWO}), chilled ceiling temperature (T_{CC}), and room temperature (T_R) at steady state. The second experiment was carried out by varying the height of



Fig. 3 Environmental chamber with installing chilled ceiling panels

chilled ceiling panels (H_{CC}) of 2, 2.5, and 3 m and the chilled ceiling temperature T_{CC} of 14–18 °C. The third experiment was carried out by varying the relative humidity in the desiccant dehumidifier while observing condensation on the chilled panel's surfaces. The dew-point temperature of occupied zone was measured using data acquisition instrument (BABUC version 5.07 LSI). Numerical study was carried out using Fluent 6.3 CFD program. The purpose of the simulation is to determine the ventilation configuration performance for selecting the optimum thermal comfort configuration. However, different ventilation configurations with respect to chilled ceiling positions were associated with the HRC system simulated to select the optimum configuration for thermal comfort condition via evaluating its performance.

2.1 Computational Domain

An environmental chamber accommodates four occupants, one fluorescent light, and twelve chilled ceiling panels. Air inlet, outlet configurations, and chilled ceiling height (H_{CC}) are the most important factors needed to be considered. Nine ventilation configurations were simulated by varying four vents. Two vents were set up at the bottom of the chamber as air inlets, while the other two vents were installed at the top of the opposite side as exhausts. The ventilation configurations were achieved by opening and closing air inlets and exhausts. In each configuration, three positions of chilled ceiling panels of 2, 2.5, and 3 m height were varied with surface panel temperature design in the range of 14–18 °C. Twenty-seven cases were studied to determine the configuration performance for optimum ventilation configuration. The configuration performance was evaluated by considering the most important indicators: fresh air distribution, air age, path line size inside the environmental chamber, air velocity, and ventilation effectiveness. Thus, the optimization was carried out among nine configurations based on the configuration performance. Airflow rates through the right and left inlets were taken from the actual measurement experimental data of 0.03 kg/h. The optimum configuration was selected by dividing the optimization process into two steps. The first step is achieved with each configuration separately by considering air distribution observation inside the environment chamber. However, the optimum case was selected among three chilled ceiling positions. The second step was carried out among nine configurations, which have already been selected from the first step. The air age, path line size, air velocity, and ventilation effectiveness are the major indicators considered for the second step optimization to govern the last stage simulation for the optimum configuration. Geometry drawing needs to be built in independent software, which is a gambit. Figure 4 shows the model geometry of the environmental chamber, while the ventilation configuration arrangement is summarized in Table 1.

2.2 Mathematical Models for Simulation

The following assumptions were considered in Fluent 6.3 mathematical models for heat transfer:

- Incompressible Newtonian three-dimensional flow.
- Steady state without slip at the walls and without heat transfer by conduction between the chamber and the environment was used.
- Airflow is turbulent.

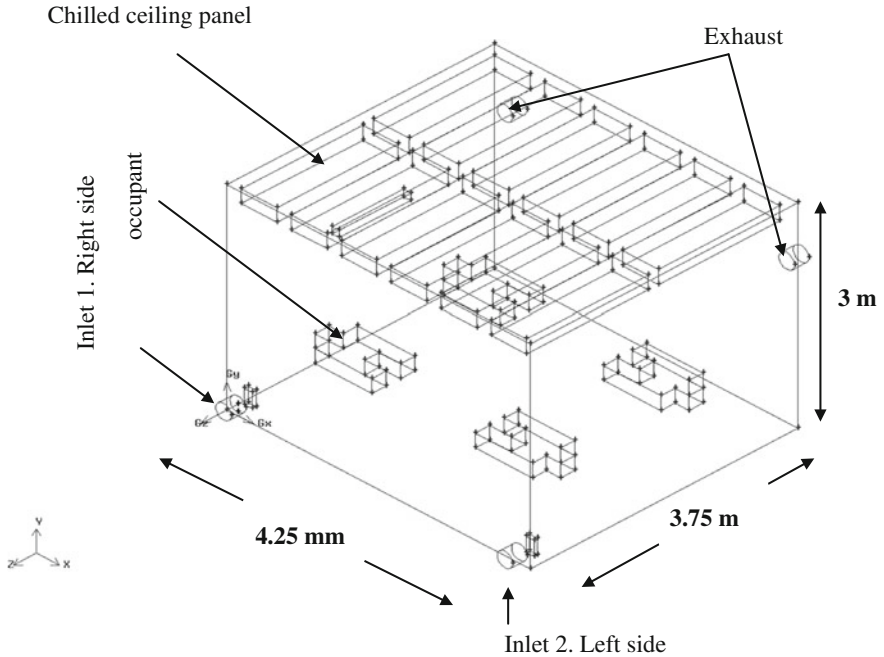


Fig. 4 Model geometry of environmental chamber

Table 1 Ventilation’s configuration

Location of vents	Ventilation’s configuration								
	1	2	3	4	5	6	7	8	9
Inlet 1	✓	✓	✓				✓	✓	✓
Inlet 2	✓	✓	✓	✓	✓	✓			
Outlet 3	✓		✓	✓	✓			✓	✓
Outlet 4	✓	✓		✓		✓	✓	✓	

2.3 Grid Independency

Mesh spacing sizes of 0.06, 0.07, 0.08, 0.09, 0.1, and 0.15 have been selected to create mesh cell number. The mesh cell number has to subject to the different simulation run tests in order to improve the result quality. When no difference is noticed in the simulation results, the acceptable mesh spacing was chosen for the comparison between the different geometries. Figure 5 shows the calculated final residence time average for exhausting fresh air (fresh air age) for different mesh numbers of 352,589, 301,457, 382,277, 420,140, 468,500, and 500,000 cells by

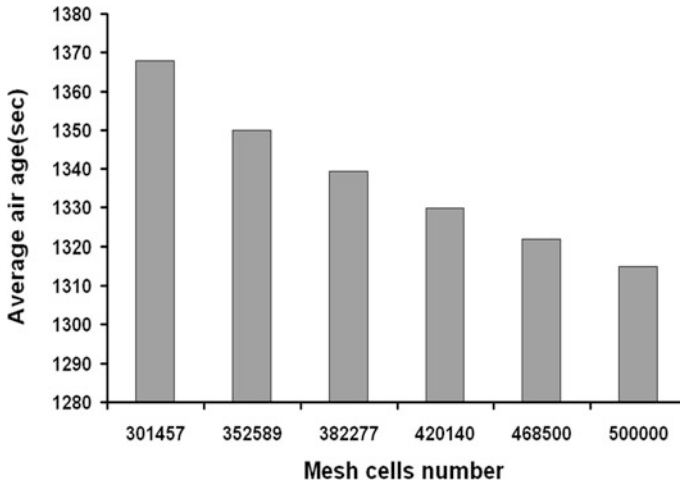


Fig. 5 Mesh cell numbers versus air age average

applying the maximum 200,000 steps, and the time was calculated through writing to the file. The model with mesh number of 382,277 is sufficient for the present study in order to save time.

2.4 Flow Analysis Inside the Environmental Chamber

The simulation modeling for the environmental chamber was based on a three-dimensional, viscous model with K-omega model. The K-omega model was used due to its excellent predictive abilities for a wide range of turbulent flows and the simplicity of its formulation in the viscous sublayer. Moreover, the redundancy of damping functions leads to stability in numerical calculation and it is ideal for modeling flows over complicated geometries with turbulent flows K-omega model which was used with the default Fluent constant values while applying the following options:

- K-omega model.
- Transitional flows.
- Viscous heating.

For flow analysis, the effect of ventilation configuration varies with air distribution, age, path length, and air velocity inside the environmental chamber were investigated.

2.5 Operating and Boundary Conditions

The environmental chamber was set to operate with pure dry air at atmospheric pressure. Environmental chamber boundary conditions were set as follows:

1. Constant temperature walls were set as follows:
 - (a) Six environmental chamber walls as default.
 - (b) Chilled ceiling panels with five temperature values ranged from 287 to 291 K.
 - (c) Four occupants at 305 K.
 - (d) One fluorescent light at 333 K.
 - (e) Two diffusers as default.
2. Right and left inlets set as mass flow rate of 0.03 kg/s with the temperature of 300 K.
3. Two exhausts set as flow out with the expected flow rate of 0.03 kg/s.

2.6 Experimental Work

Experimental work was implemented in an environment chamber to determine room air temperature for thermal comfort conditions. Twelve aluminum panels with a dimension of $1,700 \times 500 \times 200$ mm were designed to allow the chilled water circulation through embedded copper tubes. Ventilation displacement mode is chosen in the current study due to its better efficiency than mixed ventilation. Thermal comfort sensation satisfactoriness is considered for 28 occupants to enhance the optimum result. Experiments were carried out with different H_{CC} heights of 2, 2.5, and 3 m and T_{CC} in the range of 14–18 °C to optimize the comfortable environment chamber temperature. In addition, the optimization was carried out using design of experiment (DOE) to select the optimum T_C . Psychometric probe sensors were connected to data acquisition (model: BABUC version 5.07 LSI) instrument that was developed for the dry bulb temperature recording.

3 Result and Discussion

3.1 Desiccant Dehumidifier

3.1.1 Performance

Performance of a desiccant dehumidifier is its ability to reduce relative humidity within a period of time. Figures 6 and 7 show the minimum relative humidity and saturation state of the desiccant dehumidifier with varying air mass flow rates at

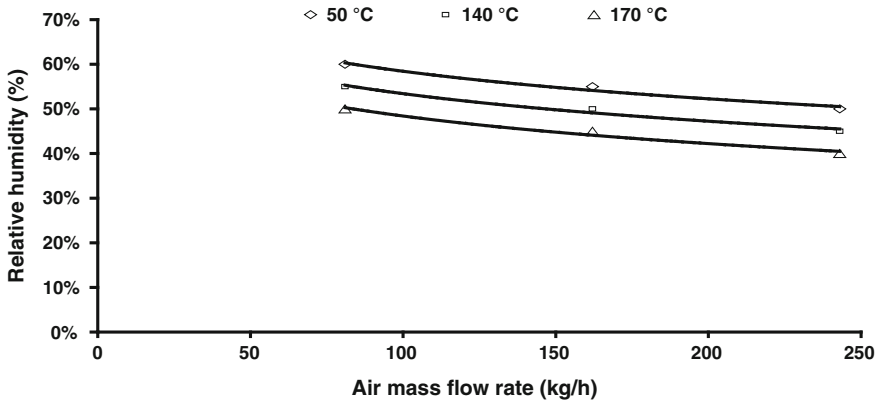


Fig. 6 Minimum relative humidity

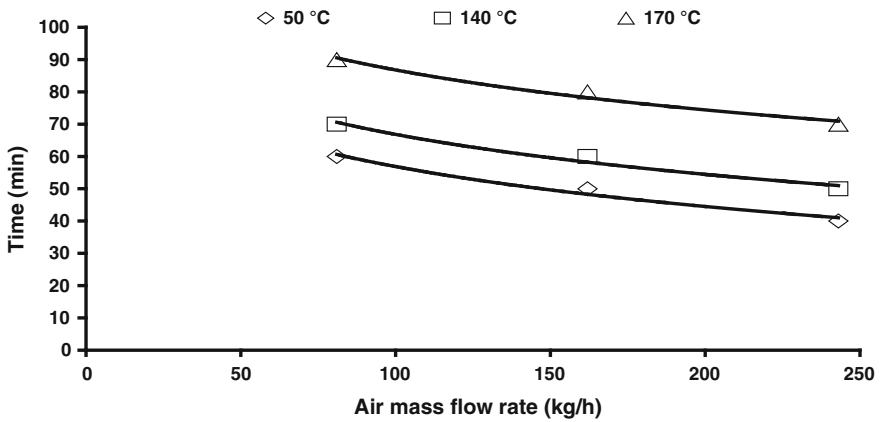


Fig. 7 Saturation time for desiccant dehumidifier

different desiccant active temperatures, respectively. The desiccant is able to reduce the relative humidity to 40, 45, and 50 % with respect to the airflow rates.

Figure 8 shows the dehumidification capacity of the desiccant wheel with varying air mass flow rates of air. The dehumidification capacity is almost linearly proportional to airflow rates since mass flow rate is always a dominant factor. The maximum dehumidification capacity was 2.673 kg h^{-1} at air mass flow rate of 243 L h^{-1} .

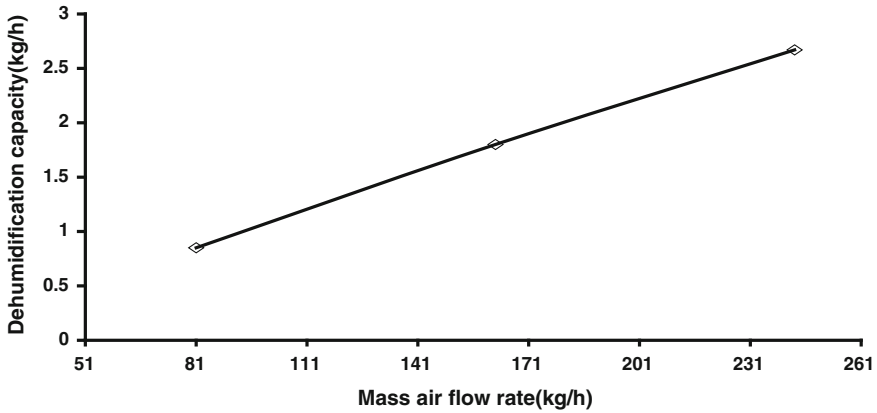


Fig. 8 Dehumidification capacity

3.2 Hydronic Radiant Cooling System

3.2.1 Performance

Figure 9 shows the response of T_{CC} (3 m above the floor), T_R , and $T_{C.W.O}$ with varying $T_{C.W.I}$. The minimum temperature of $T_{C.W.I}$ was 6 °C provided via a chiller. The T_{CC} , T_R , and $T_{C.W.O}$ are linearly proportional to $T_{C.W.I}$. T_R is high because $T_{C.W.I}$ affects the room air temperature due to heat gain inside the room and the position of the chilled ceiling. It was observed that when $T_{C.W.I}$ is stabilized at 6 °C, the differences in T_{CC} , T_R , and $T_{C.W.O}$ were 14, 24, and 10 °C, respectively. Thus, the following Eqs. 2a, b, and c at steady-state condition are derived.

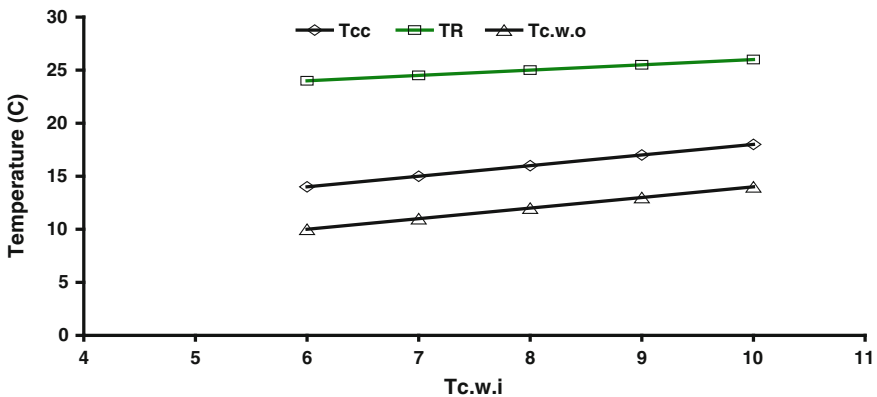


Fig. 9 The response of T_{CC} , T_R , and $T_{C.W.O}$

$$T_{CC} = T_{C.W.I} + 8 \tag{2a}$$

$$T_R = T_{C.W.I} + 18 \tag{2b}$$

$$C_{C.W.O} = T_{C.W.I} + 4 \tag{2c}$$

When $T_{C.W.I}$ increases by 1° above the minimum value of steady state, the T_{CC} , T_R , and $T_{C.W.O}$ increased by 1, 0.5, and 1° , respectively. Thus, the following Eqs. 3a, b, and c at steady-state condition are derived.

$$T_{CC+1} = T_{C.W.I} + 1 \tag{3a}$$

$$T_{R+1} = T_{C.W.I} + 0.5 \tag{3b}$$

$$C_{C.W.O+1} = T_{C.W.I} + 1 \tag{3c}$$

where T_{CC+1} , T_{R+1} , and $C_{C.W.O+1}$ are the different values related to the $T_{C.W.I}$ beyond 6°C steady state. Thermal comfort condition can be evaluated by determining the comfortable room temperature (T_C). Optimization was carried out based on lower power consumption for economical reason.

Figure 10 shows the effect of varying T_{CC} at different H_{CC} on T_R . T_R of $24\text{--}24.5^\circ\text{C}$ can be provided at different T_{CC} and H_{CC} . Points 1, 2, 3, 4, and 5 are within the thermal comfortable condition. Minimum H_{CC} of 2 m is the most economical, with a low power consumption of 2 kWh. However, for H_{CC} values higher than 3 m, the power consumptions were 3 and 3.5 kWh at T_{CC} of 14 and 15°C , respectively.

Dew-point temperature is an important factor to be considered in order to avoid condensation on the chilled panel surface. The effect of increasing relative humidity on the chilled panel surface was observed by the occurrence of condensation on the panel's surface. Figures 11, 12, and 13 show the effect of increasing relative humidity on room dew-point temperature at different H_{CC}

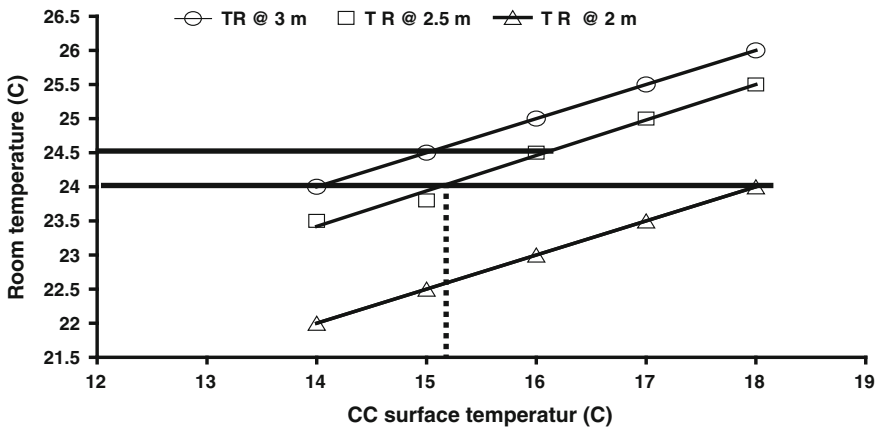


Fig. 10 Thermal comfort temperature condition

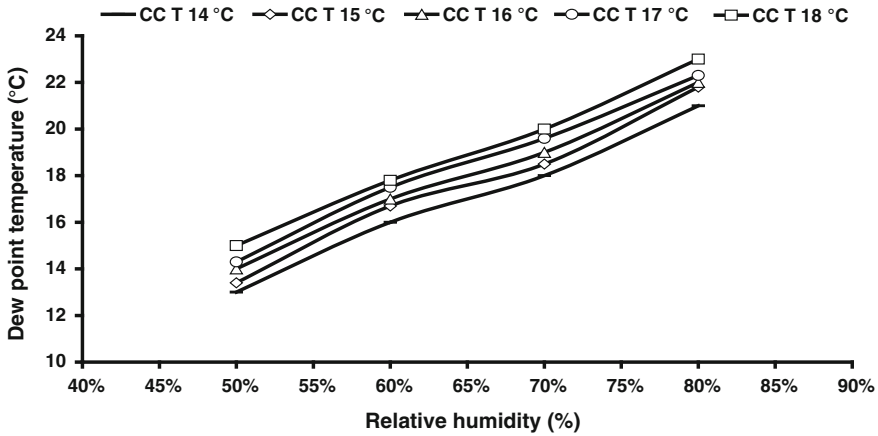


Fig. 11 The effect of RH on room dew-point temperature within H_{CC} of 3 m

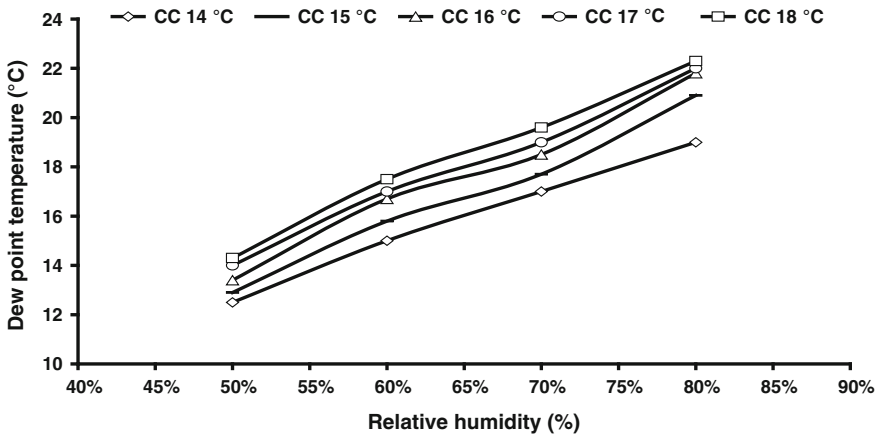


Fig. 12 The effect of RH on room dew-point temperature within H_{CC} of 2.5 m

positions of 3, 2.5, and 2 m above the floor by varying T_{CC} . It was observed that at 50 % RH, condensation does not occur at all H_{CC} and T_R due to the room dew-point temperatures being lower than the T_{CC} . Thus, the chilled ceiling is safe to operate without condensation at 50 % RH. Condensation occurred significantly at all room temperatures at all H_{CC} when relative humidity ranges between 70 and 80 %. Therefore, to operate chilled ceiling for the hydronic radiant cooling in Malaysian climate, it is preferred to control relative humidity to be about 50 % or below with T_{CC} of 14–18 °C, regardless of chilled ceiling height. However, for 60 % relative humidity, only H_{CC} of 2 m for all T_{CC} is possible.

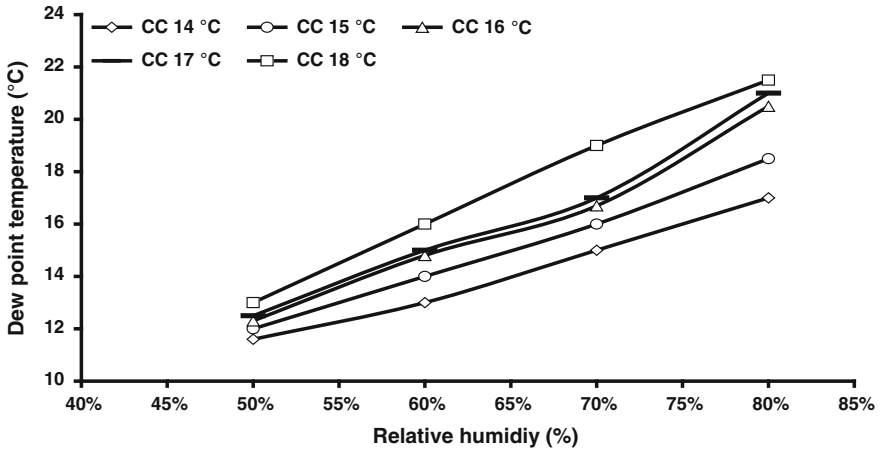


Fig. 13 The effect of RH on room dew-point temperature within H_{CC} of 2 m

3.3 Thermal Comfort

3.3.1 Numerical Study

Primary Optimization

Three H_{CC} values were varied with nine ventilation configurations. Fresh air distribution, stagnation zones, and air circulation are the most important parameters observed inside the environmental chamber to select the optimum configuration performance for thermal comfort condition, by applying path line option, velocity contours, and velocity vector. The optimum configuration was determined by achieving high ventilation quality in terms of homogenous air concentration, low stagnation zones, and air circulation. The air concentration inside the environmental chamber was determined by applying path line option to identify the ability of the fresh air concentration to be homogenous inside the environmental chamber. The study focused on the ventilation quality by observing traces of fresh air concentration. Figures 14 and 15 show 3D modeling of the airflow pattern, showing the contours of velocity magnitude in terms of stagnation zone that existed around the occupants for X and Y views for H_{CC} of 3 m. The plan location is chosen as it is representative of the occupied zone and hence the most focused location for the people. Large range of the stagnation zones, i.e., dead zones, actually exists when the ventilation design system provides poor quality. Therefore, in the current option, the air velocity distribution in the occupied zone ranges between 0.08 and 0.12 m/s, which falls in the standard acceptable range [21]. It seems that the spread of dead zones is concentrated in small areas at several locations. But the situation is better at the occupied zone. In contrast, high velocity



Fig. 14 Contours of velocity magnitude (m/s) at H_{CC} of 3 m, Z-Y, X = 3 m

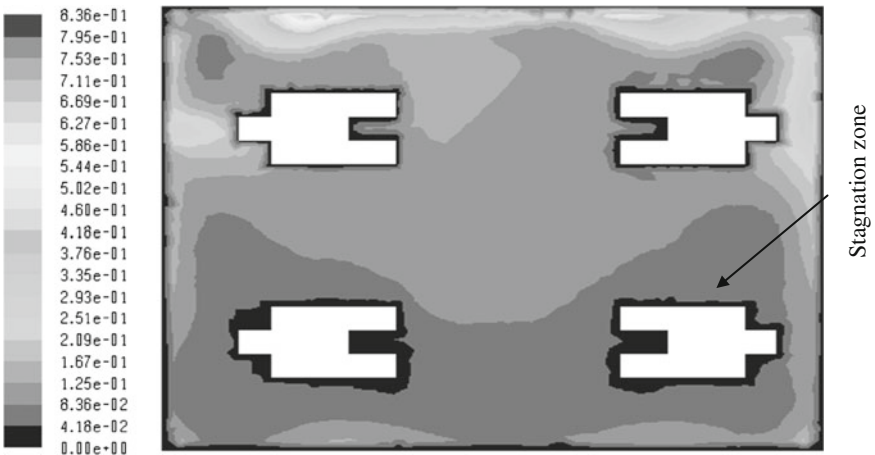


Fig. 15 Contours of velocity magnitude (m/s) at H_{CC} of 3 m, X-Z, Y = 0.6 m

is achieved at the entrance followed by the extreme right side, which also is not affecting the occupants.

Figure 16 shows the contours of velocity magnitude for Y views for H_{CC} of 2.5 m. The stagnation zones that exist around the occupants are concentrated on the right side due to the distant from the location of the air inlet entrance. Therefore, the ventilation quality is poor, which makes this option unsuccessful.

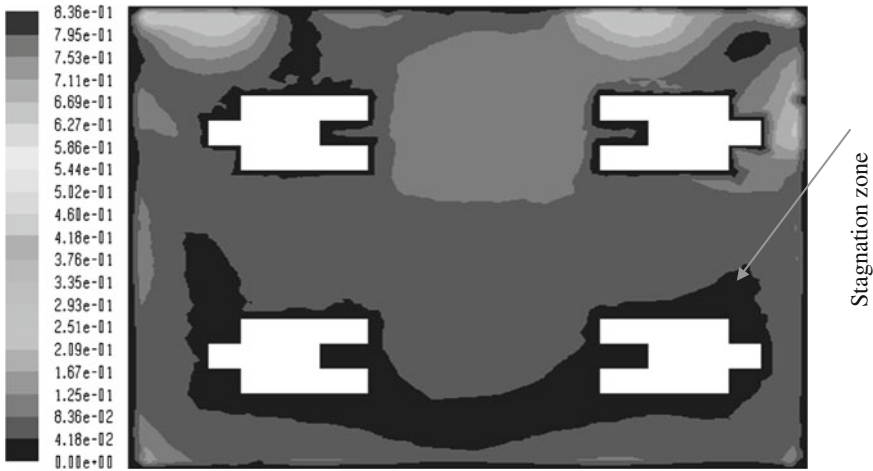


Fig. 16 Contours of velocity magnitude (m/s) at H_{CC} of 2.5 m X-Z, Y = 0.6 m

Figure 17 shows the contours of velocity magnitude for Y views for H_{CC} of 2 m. The stagnation zones exist in all occupied zones, especially around the occupants. This is caused by the low level of the chilled ceiling position. In addition, stagnation zones spread in large areas and occupied about 40 % of the total area.

Air circulation is an important indicator showing the air movement inside the environmental chamber and around human occupants. Figure 18 shows the air velocity vector that describes air movement for Y views for H_{CC} of 3 m. The air



Fig. 17 Contours of velocity magnitude (m/s) at H_{CC} of 2 m X-Z, Y = 0.6 m

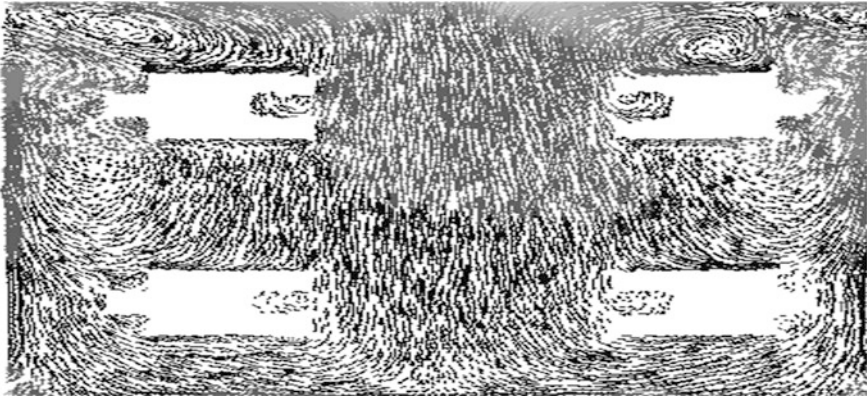


Fig. 18 Velocity vector at H_{CC} of 3 m X-Z, Y = 0.6 m

movement in the occupied zone appears practically low with good circulation to create comfortable condition. The formation of eddies does not exist in the occupied zone but exists in the upper zones. The circulation of the air is strong and moves from the upper zones downward. Good air mixing is observed in this plane that may be conditional for comfort as expected in the occupied zone.

Figure 19 shows the air velocity vector that describes air movement for Y views for H_{CC} of 2.5 m. The air circulation is slightly strong in the occupied zone with the formation of number of the stagnation zones on the right and left sides. The downward airflow from the upper zones is slightly weak due to relatively higher T_C for H_{CC} of 3 m, indicating slight discomfort.

Figure 20 shows the air velocity vector that describes air movement for Y views for H_{CC} of 2 m. The air movement in this plane seems to be low along the

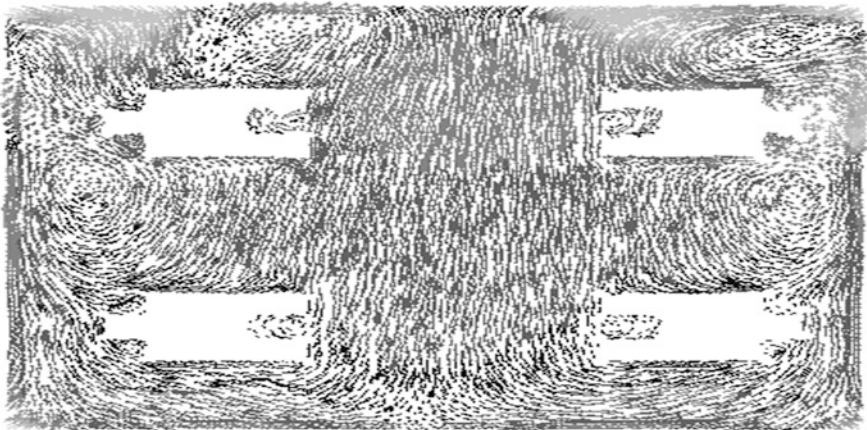


Fig. 19 Velocity vector at H_{CC} of 2.5 m X-Z, Y = 0.6 m

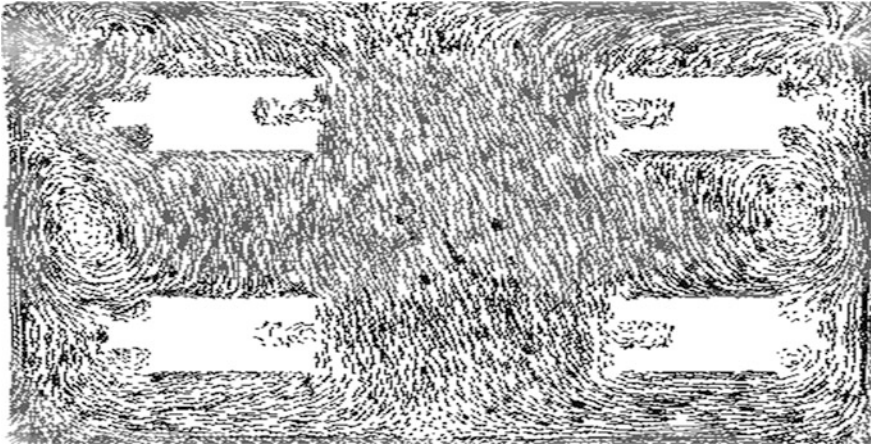


Fig. 20 Velocity vector at H_{CC} of 2 m X-Z, Y = 0.6 m

occupied zone except near the exit. The low level of H_{CC} creates several “pockets” of eddy. Since the air velocity and circulation in the occupied zone appear to be high, occupants would probably experience some draft.

According to the result, the higher ventilation quality is achieved with configurations with H_{CC} of 3 m.

Secondary Optimization

Based on the optimum nine configurations, which had already been selected from the primary optimization, the averages of path line size, air age, air velocity, and ventilation effectiveness are the main parameters evaluated for selecting the final optimum configuration. Path line size is a path length from the main entrance surface to the exhausting vent outlet by choosing path line option. It can be drawn by using XY plot options with particle variables: particle ID for y-axis and path length for x-axis. Sandberg, Chuan and Xin [22] have explained that the air age is a flow residence time for air distribution starts rushing from the youngest or zero age to the old age under path line option using XY plot option with particle variables: particle ID for y-axis and time for x-axis [22–24].

A. Path line size

Figure 21 shows the concluding average for path length against ventilation configuration. In the first configurations 1, 2, and 3, the path length increased gradually, because the outlet vent was unlocked in a different manner. In addition, the continuously operated florescent light and its location at right side of the air stream affect the airflow by making the close layers very thin and move forward

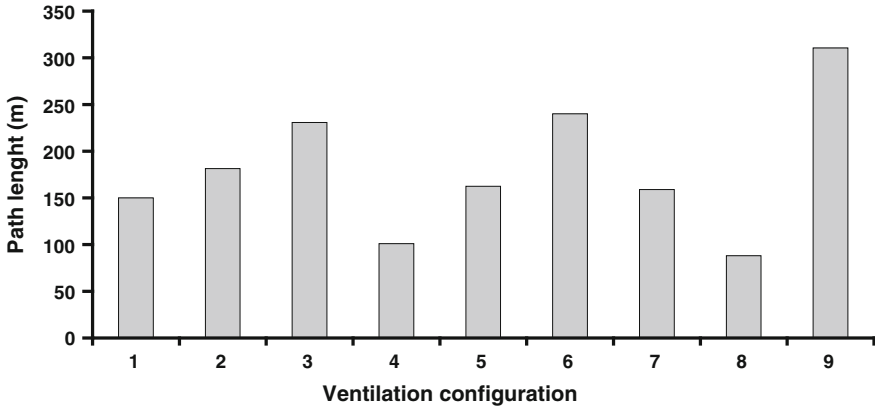


Fig. 21 Path length average

upper level which exhausts in the same air stream as in configuration 1. The absence of the same heat source on the left side of the air stream makes the path slightly longer than the other side. Configurations 4 and 8 indicate the shortest path length. Configurations 5 and 7 have a difference of 2.15 % of path length. This indicates that varying inlet vents while keeping the outlet constant neither causes the path line length to increase nor to decrease. Therefore, the air age will be the governing factor for configurations 5 and 7. Ventilation configurations 6 and 9 achieve larger path length since the one inlet and outlet were varied diagonally, the outlet vent distance from inlet and has dissimilar air streams. Moreover, in the ventilation configuration 9, the inlet at the right side where heat source is absent (florescent light) with chilled ceiling, the heavy layers of air tend downward rather than exhaust that makes the path line the longest.

B. Air age

The shortest residence time with superior distribution is the most appropriate configuration. Figure 22 shows the final average of air age against ventilation configuration. In Fig. 22, the air age difference percentage is varied between 4.7 and 30 % in seven configurations except configurations 7 and 9. Comparison in the air age is achieved by dividing the configurations into four groups with respect to the similar number of the inlet opened with outlet configurations and with respect to the path line length. Therefore; configurations 1, 2, and 3 were taken as first group, while 4 and 8 were taken as second group, 6 and 9 were taken as third group, and 5 and 7 were taken as fourth group. In the first group, configurations 1, 2, and 3 have different residence times. When the residence time is coupled with the path line, configuration 2 has a higher residence time but has a shorter path length than configuration 3 and a higher path length than 1, which caused configuration 2 to be ignored. In view of the fact that configuration 3 has additional path length, while the air age difference between configurations 3 and 1 is 5 %; consequently,

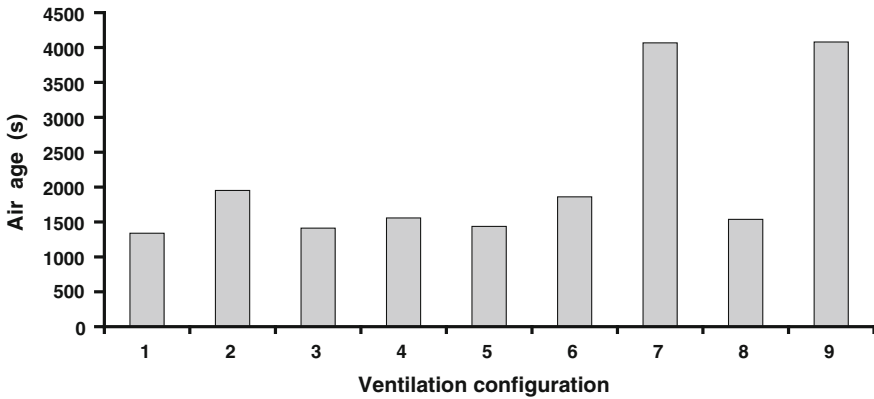


Fig. 22 Air age average

configuration 3 is better than configuration 1. Configurations 4 and 8 have difference of 20 % in the path length, while have the difference of 4 % in the residence time; hence, configuration 4 is preferable than configuration 8. Configurations 5 and 7 have the difference of 2.15 % in path length, while have a huge difference of 64.7 % in the residence time ; thus, configuration 5 is better than configuration 7. In the case of the fourth group configuration 6 and 9, although configuration 9 has 70% additional lengths than configuration 6 in path length, the difference in residence time is 54.4 % , therefore, configuration 6 is better than configuration 9.

C. Air velocity and ventilation effectiveness

Air velocity can be determined by two ways: using mathematical calculation as a ratio of path length to the residence time and by displaying data using both options velocity vector and velocity magnitude. Ventilation effectiveness can be defined as a ratio of chamber volume to mean air age and ventilation rate [25]. Thus, the comparison will be carried out among configurations 6, 5, 4, and 3. Table 2 summarizes the air velocity and ventilation effectiveness result.

3.3.2 Experimental Work

The thermal comfort experimental work was conducted in order to optimize comfort condition in terms of room air temperature. Environmental chamber

Table 2 Air velocity and ventilation effectiveness result for optimum configuration

Indicator	Configuration 3	Configuration 4	Configuration 5	Configuration 6
Air velocity (m/s)	0.14	0.09	0.11	0.12
Ventilation effectiveness	0.91	0.91	0.84	1

temperature is considered by varying H_{CC} and T_{CC} to select the optimum option experimentally by subjecting 28 occupants to the same experimental condition, to enhance the optimum result based on the optimum ventilation configuration. The optimum option was selected using Design-Expert software by the meaning of response surface methodology due to providing serious statistical analysis [26]. Three chilled ceiling positions of 3, 2.5, and 2 m and five chilled ceiling surface panels' temperatures varied. In each set, one H_{CC} was kept constant and T_{CC} varied. Room temperature at the occupied zone of 1 m above the floor has the single response. Therefore, optimization was carried out once more based on statistical analysis evaluation using Design-Expert software. The main steps of the software deal with experimental design, analysis of variance (ANOVA), and optimization.

Experimental Design

The relationship between H_{CC} , T_{CC} , and room temperature is presented. Figure 23 shows the Design-Expert response for thirteen runs via graphic columns from the Design-Expert software. The room temperature was varied between 22 and 26 °C. The temperature of 24 °C is the preferred thermal comfort temperature (T_c) determined from the point of view of majority of the occupants in the primary thermal comfort process. Hence, it was selected as a target value for optimization. Subsequently, the lower and higher values can be considered for demand by consumers. In case of H_{CC} of 2 m, the room temperature was 22 °C with T_{CC} of 14 °C, while for H_{CC} of 3 m, the room temperature was 24 °C associated with T_{CC} of 18 °C. The room temperatures of 24, 24.2, 24.5, 24.6, 24.7, 24.8, and 25 °C were achieved with H_{CC} of 2.5 m and T_{CC} of 16 °C, associated with replications for the same experiment as Design-Expert software recommended for assessing the pure error. A design summary is shown in Table 3.

Analysis of Variance (ANOVA)

The feasibility of the quadratic model for determining the room temperature was justified through the analysis of variance (ANOVA). Table 4 is a summarized report of the ANOVA for regression parameters of the predicted response surface quadratic model for room temperature. The Model F-value of 45.12 means the model is significant. There is only a 0.01 % chance that a large “Model F-value” could occur due to noise. Values of “Prob > F” less than 0.0500 indicate that the model terms are significant. A, B, and B2 are the model terms. “Values greater than 0.1000 indicate that the model terms are not significant.”

The “Lack of Fit F-value” of 0.65 means the Lack of Fit is not significantly relative to the pure error. There is a 75 % chance that a large “Lack of Fit F-value” could occur due to noise. Non-significant Lack of Fit is good requirement model to fit. Table 5 shows the statistical parameters for reduced model, and the

Fig. 23 **a** Room temperature response based on varying H_{CC} and T_{CC} . **b** Room temperature response based on varying H_{CC} and T_{CC} . **c** Room temperature response based on varying H_{CC} and T_{CC}

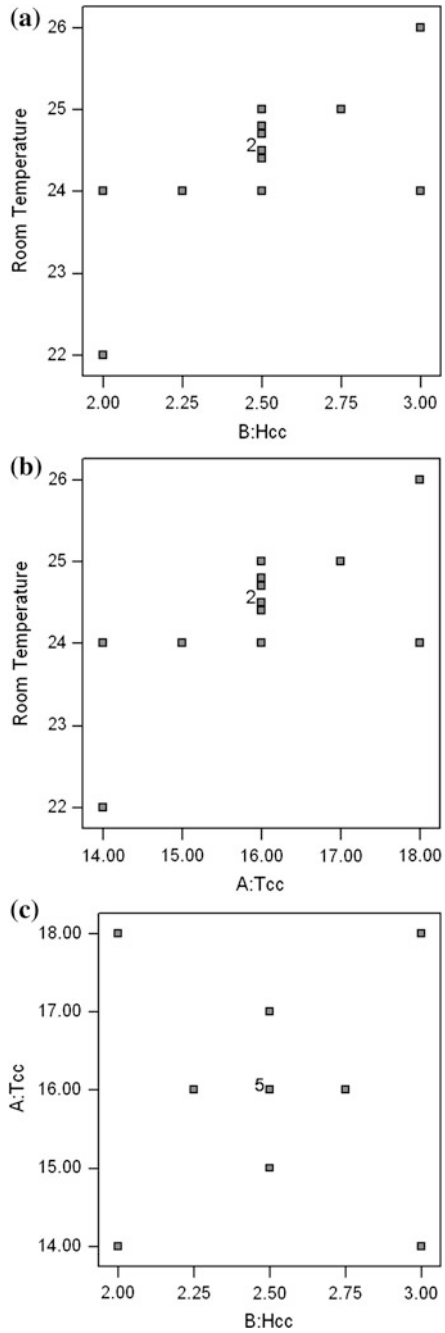


Table 3 Experimental design summary

Response	Name	Units	Obs	Minimum	Maximum	Trans	
Y1	Room Temp.	C	13	22.0	26.00	None	
Factor	Name	Units	Typ	Low Act.	High Act.	Low coded	High coded
A	T_{cc}	C	Numeric	14.00	18.00	-1.000	1.000
B	H_{CC}	m	Numeric	2.00	3.00	-1.000	1.000

Table 4 The analysis of variance (ANOVA)

Source	Sum of squares	DF	Mean square	F-value	Prob. > F	Remark
Model	9.29	3	3.10	45.12	>0.0001	Significant
A	4.01	1	4.01	58.48	>0.0001	
B	4.50	1	4.50	65.56	>0.0001	
B ²	1.78	1	0.78	11.31	0.00084	
Residual	0.62	9	0.069			
Lack of Fit	0.25	5	0.049	0.53	0.7500	Not sign.
Pure error	0.37	4	0.093			
Cor total	9.91	12				

Table 5 Statistical parameters of the reduced model equation for room temperature

Type of variables	Room temperature
Standard deviation (Std. Dev)	0.26
R-Squared	0.9377
Mean	24.37
Adjusted R-Squared (Adj-R-Squared)	0.9169
Predicted R-Squared	0.9041
Coefficient of Variance (C.V)	1.08
Predicted Error Sum of Squares (PRESS)	0.95
Adeq precision	26.760

R-Squared value = 0.9377

“predicted R-Squared” value of 0.9041 is in reasonable agreement with the “Adj-R-Squared” value of 0.9169. Adeq precision measures the signal-to-noise ratio that is described for values greater than 4. The ratio of 26.760 indicates an adequate signal. The final equation is expressed by the second-order polynomial Eq. (4). The final equation in terms of actual factors is expressed by the following second-order polynomial Eq. (5).

$$\text{Room Temperature} = +24.56 + 0.94 * A + 1.00 * B - 0.55 * B^2 \tag{4}$$

$$\text{Room Temperature} = -1.74132 + 0.47222 * T_{cc} + 12.99625 * CC_H - 2.19925 * CC_H^2 \tag{5}$$

Figure 24 shows the comparison between the predicted and actual responses based on the quadratic model equation. It is noticed that the models are perfect explanation of the experimental records, indicating previously that is successful in comparing the correlation between two variables such as T_{CC} and H_{CC} to room temperature. Moreover, there is an adequate correlation to the linear regression fit with the R-Squared value of 0.9377 for room temperature.

The effect of T_{CC} and H_{CC} on T_R was studied. For each plot, one variable was fixed to the minimum and maximum range, while the studied parameter was varied. Figure 25 shows the effect of T_{CC} on T_R as a default factor tool with constant H_{CC} of 2.50 m in the software. The effect of T_{CC} increased significantly from 14 to 18 °C, while T_R is varied from 23.5 to 25.5 °C. This result of the effect of T_{CC} on T_R strongly agrees with standard thermal condition as shown in Table 3. Figure 26 shows the effect of H_{CC} on T_R as a default factor tool with constant T_{CC} of 16 °C in the software. The effect of H_{CC} increased significantly from 2 to 2.75 m, while T_R is varied from 23 to 25 °C. The effect of H_{CC} on T_R strongly agrees with standard thermal condition as shown in Table 2.

Figures 27 and 28 show the contour plots and three-dimensional surface response of the quadratic model result of the room temperature with respect to H_{CC} and T_{CC} . Varying the H_{CC} from 2 to 3 m with T_{CC} resulted in decreasing the room temperature from 26 to 22 °C. These considerable decrease in room temperature present chilled ceiling as an alternative to conventional air conditioning system since it is capable of achieving thermal comfort conditions within the standard thermal conditions.

Fig. 24 Room temperature response comparison

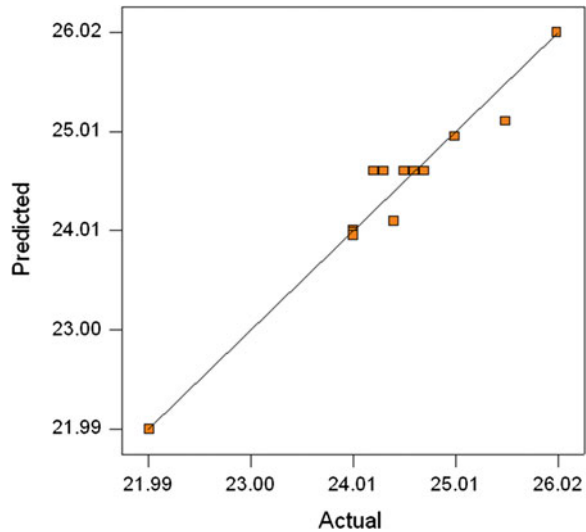


Fig. 25 Effect of T_{CC} on T_R

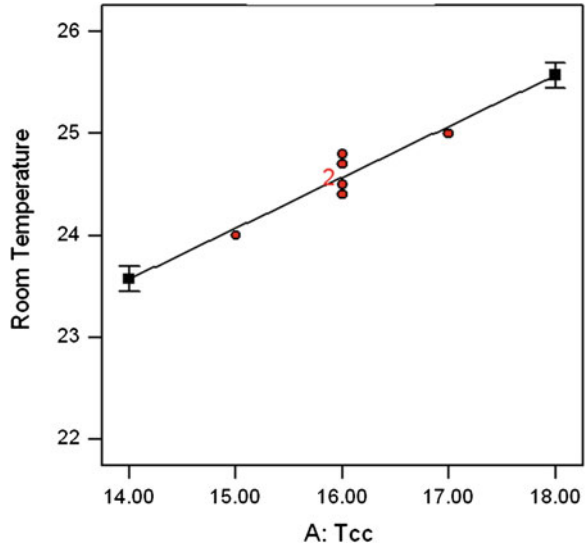
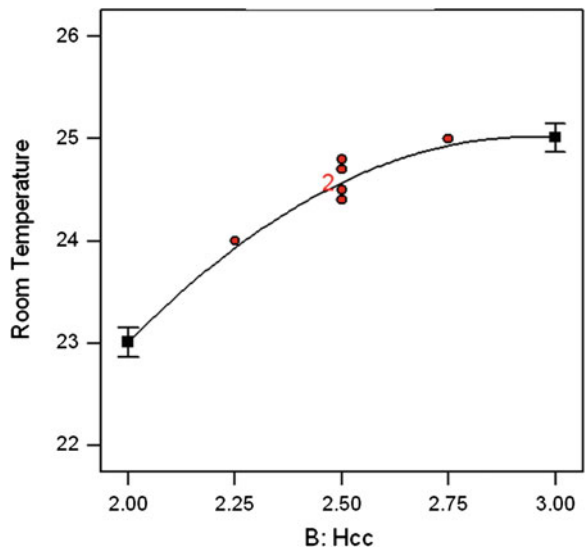


Fig. 26 Effect of H_{CC} on T_R



Optimization

Optimization process was carried out to determine the optimum value of room temperature using the Design-Expert 6.07 software. According to the software optimization step, the desired goal was chosen twice: H_{CC} within minimum, T_{CC} chosen within maximum, and the response room temperature set at target of 24 °C to achieve the T_C under numerical optimization as shown in Fig. 29. This criterion

Fig. 27 Contour plot

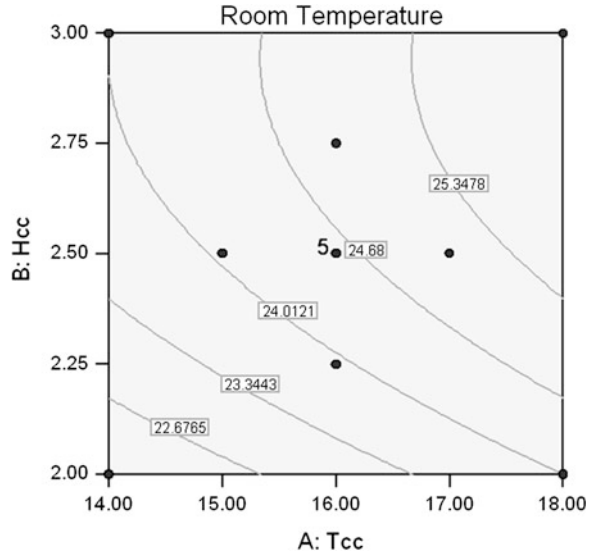
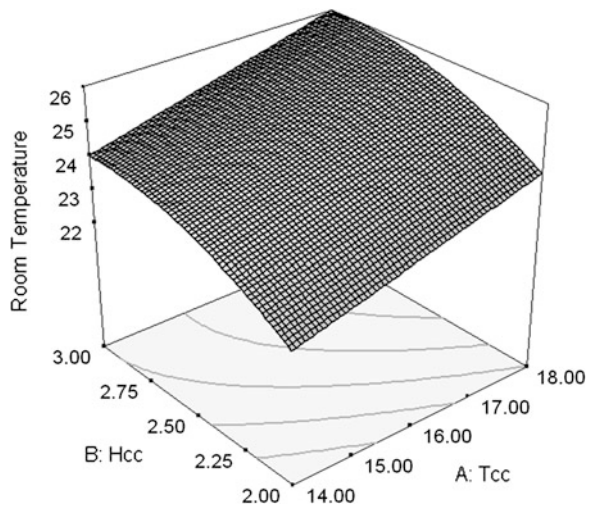


Fig. 28 3D response surface



was chosen based on economic value for saving energy consumption. The solution given by the software to meet the criteria proposed in Fig. 29 is summarized in Table 6. The 24.0 and 23.981 °C were predicted according to the model under optimized operating conditions (H_{CC} of 2.00 m and T_{CC} of 18.00 °C) as shown in Fig. 30. The predicted desirability was 0.996. Subsequently, another experiment was then carried out to confirm the optimum results. 24 °C was obtained from the laboratory experiment, which strongly agrees with the predicted response value.

Fig. 29 **a** Proposed H_{CC} criteria based on economic basis. **b** Proposed T_{CC} criteria based on economic basis. **c** Proposed T_R criteria based on economic basis

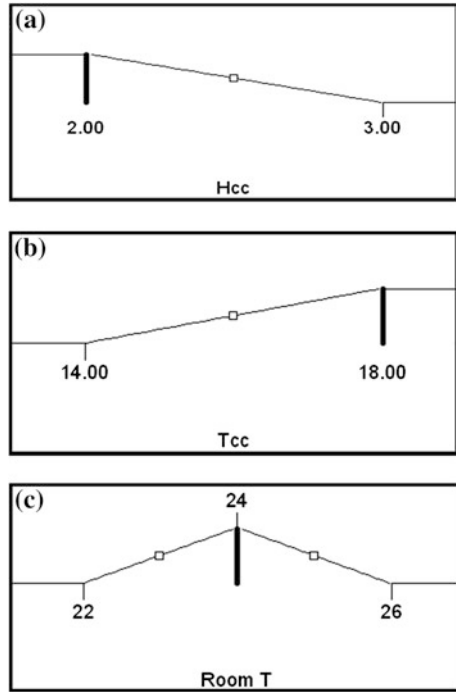


Table 6 Constrains of affected factors for room temperature optimization economic basis

Solution number	T_{CC}	H_{CC}	T_R	Desirability
1	18	2	24	0.996 (Selected)
2	18	2	23.9818	0.995

The second goal was achieved with proposed criteria for ventilation configuration H_{CC} of 3 m, T_{CC} of 14 °C, and T_R of 24 °C based on optimum ventilation configuration. Figure 31 shows the proposed criteria based on the optimum ventilation configuration.

The solution given by the software to meet the criteria proposed in Fig. 31 is summarized in Table 7. The room temperature value of 24.0 °C is merely selected according to the model under optimized operational conditions (H_{CC} of 3.00 m and T_{CC} of 14.00 °C) as shown in Fig. 32. The predicted desirability was 0.989. Subsequently, another experiment was then carried out to confirm the optimum results. 24 °C was obtained from the laboratory experiment, which strongly agrees with the predicted response value. Therefore, finally the preferable optimum room temperature was found to be 24 °C for both proposed criteria.

Fig. 30 Selected option for economic basis

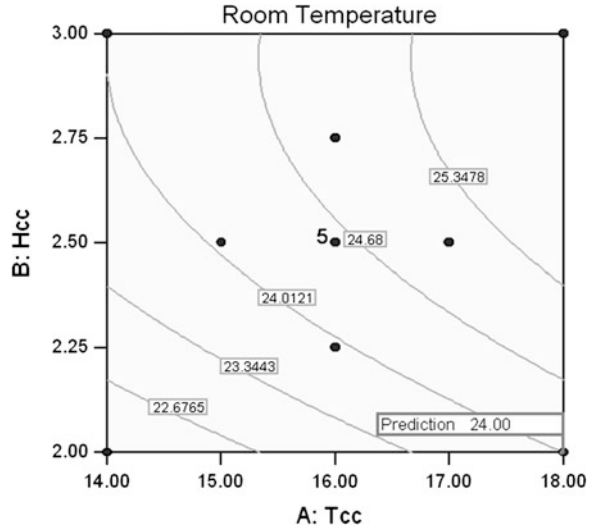


Fig. 31 a Proposed H_{CC} criteria based on optimum ventilation configuration. **b** Proposed T_{CC} criteria based on optimum ventilation configuration. **c** Proposed T_R criteria based on optimum ventilation configuration

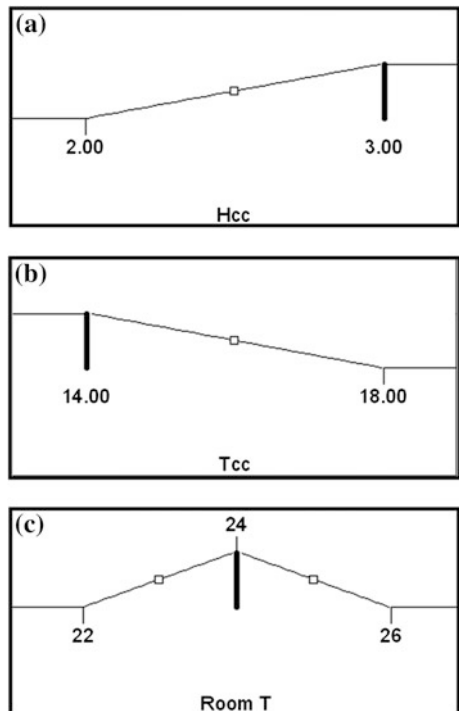
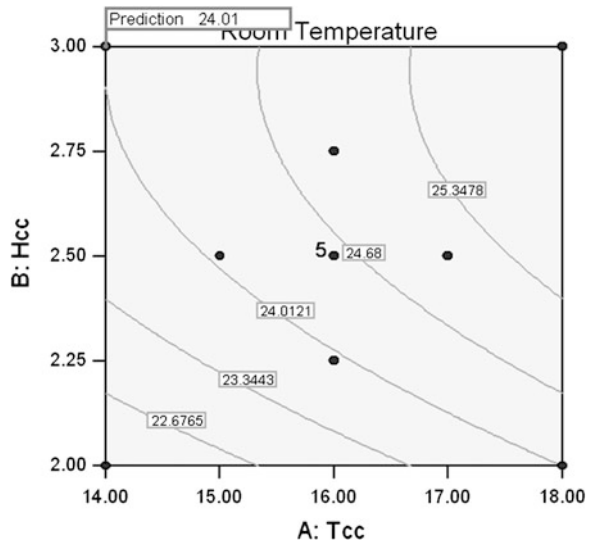


Table 7 Constrains of affected factors for room temperature optimization H_{CC} of 3 m basis

Solution number	T_{CC}	H_{CC}	T_R	Desirability
1	14	3	24.0143	0.989

Fig. 32 Selected optimum option



4 Conclusion

Desiccant dehumidification shows a good performance by reducing the relative humidity around 40 % with mass flow rate of air 243 L h^{-1} without heating for 10 min with dehumidification capacity of 2.673 kg h^{-1} . Chilled water temperature of 6–10 °C was able to maintain the chilled ceiling panel and room temperatures within the thermal comfort requirements. Chilled panels present its capability to operate at low temperature of 14 °C with relative humidity of 50 % without condensation occurring. The desired thermal comfort condition for this investigation was set between 24 and 24.5 °C, at H_{CC} of 2 m above the floor when T_{CC} is of 18 °C, H_{CC} of 2.5 m above the floor when T_{CC} is of 15 °C, and H_{CC} of 3 m above the floor when T_{CC} is of 14 °C. Minimum H_{CC} of 2 m provided the best value with low energy consumption. The thermal comfort condition was studied by both numerical and experiments. The numerical study focused on determining ventilation configuration performance, which is evaluated by the following parameters: fresh air distribution, stagnation zone, air movement, path line, air age, air velocity, and ventilation effectiveness to determine optimum ventilation configuration. The result shows that the diagonal location of inlet and outlet vents is the optimum configuration, which enables homogenous air distribution that overcomes stagnant zones with less air age and good air movement. Finally, the

optimum choice was found to be configuration 6. The response surface methodology (RSM) model was applied to achieve optimum room temperature by two proposed criteria. The results show that room temperature (T_R) based on 28 occupant's sensation satisfactoriness associated with the condition of economic basis and optimum ventilation configuration criteria was found to be 24 °C. This room temperature value is the optimum as far as the thermal comfort is considered.

References

1. Subramanyam N, Maiya MP, Murthy SS (2004) Application of desiccant wheel to control humidity in air-conditioning system. *Appl Therm Eng* 24(17–18):2777–2788
2. Waugaman D, Kini GA, Kettleborough CF (1993) A review of desiccant cooling system. *ASME Energy Resour Technol* 115(1):1–8
3. Ahmed CSK, Gandhidasan P, Al-Farayedhi AA (1997) Simulation of a hybrid liquid desiccant based air-conditioning system. *Appl Therm Eng* 17(2):125–134
4. Xiong ZQ, Dai YJ, Wang RZ (2010) Development of a novel two-stage liquid desiccant dehumidification system assisted by CaCl_2 solution using exergy analysis method. *Appl Energy* 87:1495–1504
5. Narayanan R, Saman WY, White SD, Goldsworthy M (2011) Comparative study of different desiccant wheel designs. *Appl Therm Eng* 31:1613–1620
6. Zhang LZ (2006) Energy performance of independent air dehumidification systems with energy recovery measures. *Energy* 31:1228–1242
7. Zhang LZ, Niu JL (2002) Performance comparisons of desiccant wheels for air dehumidification and enthalpy recovery. *Appl Therm Eng* 22:1347–1367
8. Zhang LZ, Zhu DS, Deng XH, Hua B (2005) Thermodynamic modeling of a novel air dehumidification system. *Energy Build* 37:279–286
9. Techajuntaa S, Chirarattannon RHB (1999) Excel Experiments in a solar simulator on solid desiccant regeneration and air dehumidification for air conditioning in a tropic humid climate. *Renew Energy* 17:549–568
10. Wilkins CK, Kosonen R (1992) Cool ceiling system. A European air-conditioning alternative. *ASHRAE J* 39(4):41–45
11. Zhang LZ, Niu JL (2003) A pre-cooling Munters environment control desiccant cooling cycle in combination with chilled ceiling panels. *Energy* 28:275–292
12. Mumma SA (2002) Chilled ceiling in parallel with desiccated outdoor air system addressing the concerns of condensation capacity. *ASHRAE Trans* 108:220–231
13. Imanari T, Omori T, Bogaki K (1999) Thermal comfort and energy consumption of the radiant ceiling panel system: comparison with conventional all air system. *Energy Build* 30(2):167–175
14. Hess D, Kacmarek R (2002) *Essentials of mechanical ventilation*, 2nd edn. McGraw-Hill, New York
15. Cheong KW, Chong KY (2001) Development and application of an indoor air-quality audit to air-conditioned building in Singapore. *Build Environ* 36:181–188
16. Coffey CJ, Hunt GR (2007) Ventilation effectiveness measures based on heat removal: part 2 application to natural ventilation flows. *Build Environ* 42:2249–2262
17. Rizwan AM, Surapong C, Prapaong V (2008) Thermal comfort assessment and application of radiant cooling: a case study. *Build Environ* 43:1185–1196
18. Evangelia H, Konstantinos P (2008) Natural ventilation of indoor spaces while minimizing heat losses: theoretical and experimental investigation. *Energy Build* 40:621–626

19. Wong LT, Mui KW (2008) A transient ventilation demand model for air-conditioning offices. *Appl Energy* 85:545–554
20. Loveday DL, Parson KC, Taki AH, Hodder SG (2002) Displacement ventilation environments with chilled ceilings: thermal comfort design within the context of the BS EN ISO7730 versus adaptive debate. *Energy Build* 34:573–579
21. ASHRAE (2005) ASHRAE handbook—fundamentals. American society of heating, refrigeration air-conditioning engineering, Inc, Atlanta
22. Sandberg M, Sjoberg M (1983) The use of moments for assessing air quality in ventilated rooms. *Build Environ* 18(4):181–197
23. Chuan KH, Wong YW, Bong YT, Teh SL (1999) Effectiveness of car parks ventilation. The Third International Symposium on Heating, Ventilation and Air Conditioning (ISHVAC99), Shenzhen, China, pp 245–254
24. Xing H, Hatton A, Awbi HB (2001) A study of the air quality in the breathing zone in a room with displacement ventilation. *Build Environ* 36(7):809–820
25. Chul NK, Chang HW, Myung DO (2008) Effect of the air flow rate of a ceiling type air conditioner on ventilation effectiveness in a lecture room. *Int J Refrig* 31:180–188
26. Ölmez T (2009) The optimization of Cr(VI) reduction and removal by electrocoagulation using response surface methodology. *J Hazard Mater* 162:1371–1378

Application of Liquid Desiccant System

Xiaohua Liu and Yi Jiang

1 Introduction

The control of indoor temperature and moisture is the main task of air-conditioning systems. Usually, outdoor air will be cooled and dehumidified in summer and heated and humidified in winter before being supplied into occupied spaces. In conventional HVAC systems, the process of dehumidifying air is implemented by condensing dehumidification method, in which the air contacts the surface of cooling coil (lower than the dew point of the air) so that moisture in the air will be condensed into water. Chilled water with a temperature of about 7 °C is usually adopted in conventional HVAC systems, which leads to the low COP of the chiller. Sometimes, the air passing the cooling coil is so cold that it has to be reheated before being supplied into occupied spaces. Furthermore, the condensed surface creates a suitable environment for bacteria, which will impair the indoor air quality. In winter, other electrical humidifier or steam humidifier has to be adopted to meet the humidification requirement.

Liquid desiccant air-conditioning systems have developed quickly in recent years. The air is dehumidified by contacting cold and concentrated liquid desiccant directly, and vice versa, it is humidified by contacting warm and diluted liquid desiccant. Compared with conventional HVAC systems, the advantages of liquid desiccant systems [1–6] can be summarized as follows: (1) the air can be dehumidified at a temperature higher than its dew point by contacting concentrated liquid desiccant; therefore, reheating is no longer needed; (2) liquid desiccant system can be driven by low-grade heat, such as solar energy, exhaust heat from condenser or other waste heat; (3) a number of pollutants will be removed by the system from the processed air; and (4) the air can be easily humidified in the same handling unit by contacting diluted liquid desiccant.

X. Liu (✉) · Y. Jiang
Department of Building Science, Tsinghua University, Beijing,
100084, People's Republic of China
e-mail: lxh@tsinghua.edu.cn

1.1 Basic Principles

The commonly used liquid desiccants are salt aqueous solutions, such as LiBr, LiCl, and CaCl₂ aqueous solutions. Of the three aqueous solutions, CaCl₂ solution is the cheapest but has the poorest absorption ability [7]. The status of liquid desiccants can be shown in the air psychrometric chart with the equilibrium status of humid air, as indicated in Fig. 1, where the physical properties of liquid desiccants are from Refs. [8] and [9]. When liquid desiccant is in equilibrium with the humid air, the temperatures and vapor pressures of the humid air and the liquid desiccant should be the same ($t_a = t_s$; $p_a = p_s$). Then, the equivalent humidity ratio of liquid desiccant ω_e can be determined with the equilibrium status of the air, as shown in Eq. (1), where B is the atmospheric pressure and p_s is the desiccant's vapor pressure.

$$\omega_e = 0.622 \frac{p_s}{B - p_s} \tag{1}$$

It can be seen from Fig. 1 that the desiccant isoconcentration line ($\xi = \text{const}$) almost coincides with the air iso-relative humidity line ($\varphi_e = \text{const}$). The absorption ability of liquid desiccant will be enhanced at lower temperature and in higher concentration. According to the crystal lines of LiBr and LiCl solutions, similar handling regions can be obtained for the two solutions and the air can be processed into very dry status.

Vaporization latent heat will release during the dehumidification process, and great amount of heat is required during the humidification or regeneration process. The cooling capacity in the dehumidification mode (or heating capacity in the regeneration mode) can be given to the air or to the liquid desiccant. Which mode can obtain better mass transfer performance and which kind of flow pattern can achieve the best mass transfer performance? To answer the above questions, two cases with the purpose of humidification [10] are taken as examples, as shown in Fig. 2. A heater is adopted to heat inlet air in mode 1 and to heat inlet liquid desiccant in mode 2. Conditions of the inlet air (point a₁) are 1 kg/s, 20 °C, and

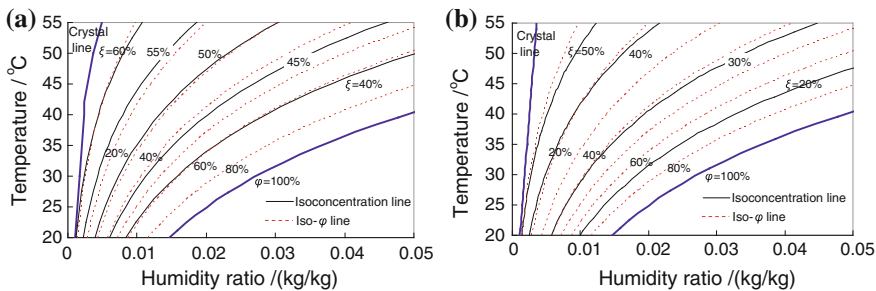


Fig. 1 Status of commonly used liquid desiccants shown in psychrometric chart. **a** Lithium bromide aqueous solution. **b** Lithium chloride aqueous solution [8, 9]

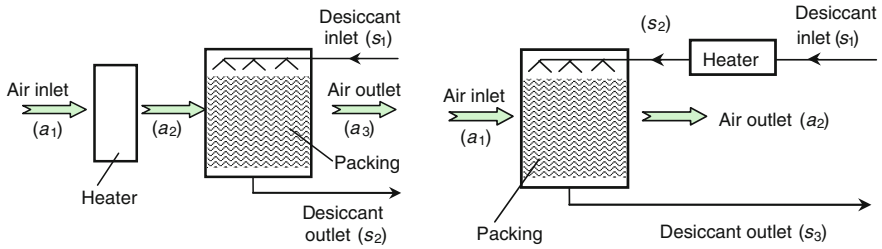


Fig. 2 Humidification of processed air. **a** Mode 1: heat inlet air. **b** Mode 2: heat inlet desiccant

Table 1 Inlet and outlet conditions of air and liquid desiccant through packed-bed devices as shown in Fig. 2 [10]

Mode	Flow pattern	Inlet conditions				Outlet conditions				Air humidity ratio variance (g/kg)
		$t_{a,in}$ (°C)	$\omega_{a,in}$ (g/kg)	$t_{s,in}$ (°C)	ζ_{in} (%)	$t_{a,out}$ (°C)	$\omega_{a,out}$ (g/kg)	$t_{s,out}$ (°C)	ζ_{out} (%)	
1	Parallel	47.7	8.0	20.0	40.0	33.8	10.4	26.8	40.2	2.4
1	Counter	47.7	8.0	20.0	40.0	33.1	10.0	28.2	40.1	2.0
2	Parallel	20.0	8.0	43.0	40.0	26.4	13.0	27.5	40.4	5.0
2	Counter	20.0	8.0	43.0	40.0	27.5	14.4	23.6	40.5	6.4

8 g/kg, and conditions of the inlet LiBr desiccant (point S_1) are 0.5 kg/s, 20 °C, and 40.0 %. The power of the heater in Fig. 2 is 28 kW. As indicated in Table 1, heating the desiccant (mode 2) has much higher humidification or regeneration capacity, 2–3 times as much as that of mode 1. In mode 2, humidification capacity of counterflow packed-bed regenerator is 28 % higher than that of parallel flow configuration. In the dehumidification process of air–desiccant direct contact system, similar conclusion can be drawn: liquid desiccant should be cooled rather than the air to obtain better mass transfer performance, and counterflow configuration is recommended. To sum up, in order to obtain better humidification performance, liquid desiccant should be heated rather than the air. Desiccant should be cooled rather than the air to obtain better dehumidification performance. These fundamental ideas will be applied in the design of liquid desiccant air-handling processes.

1.2 Basic Modules

Dehumidifier and regenerator, the most important components in liquid desiccant air-conditioning systems, can be divided into adiabatic type and internally cooled (or internally heated) type according to whether they have extra cooling fluid (or heating fluid) or not, as shown in Fig. 3. In the adiabatic module, only air and desiccant exchange heat and mass (moisture content). While in the internally cooled dehumidifier, extra cooling fluid, such as cooling water, cooling air, etc., is introduced to cool the desiccant. The internally cooled dehumidifier may have

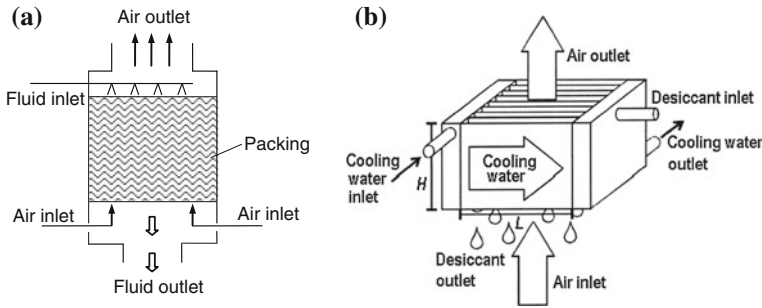


Fig. 3 Schematic of dehumidification/regeneration module. **a** Adiabatic packed-bed type. **b** Internally cooled type

better mass transfer performance than the adiabatic one, since the desiccant is cooled synchronously, as it contacts humid air, and thus maintains its low surface vapor pressure. The cooling fluid shown in Fig. 3b can also be used to heat fluid in the regeneration mode. The variance of air and desiccant parameters during the dehumidification experiments [2–4, 11–19] are shown in Table 2. The flow rate of liquid desiccant in the adiabatic dehumidifier is about an order of magnitude larger than that in the internally cooled one, so that the variance of desiccant's concentration is smaller in the adiabatic dehumidifier.

Although the internally cooled (or internally heated) type may have better mass transfer performance, some disadvantages appear in this module: (1) the configuration is more complex than the packed-bed module, and the leakage between the cooling side and liquid desiccant flow side must be confronted; (2) the material requirements of anticorrosive and wetting ability of the liquid desiccant conflict with each other; and (3) the desiccant distribution is more difficult under lower flow rate. Due to the complexity of the internally cooled type, a new fundamental module [6, 20] is then proposed as indicated in Fig. 4. In the dehumidification/regeneration module, desiccant is cooled/heated by external heat exchanger before coming into the sprayed module. There are two desiccant mass flow rates: one is the inside circulate mass flow rate that is at the same order of magnitude as the processed air, while the other is the outside circulate mass flow rate that is about one-tenth of the mass flow rate of the processed air.

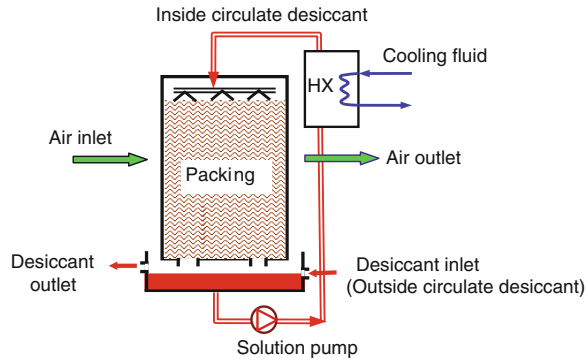
2 Liquid Desiccant Air-Handling Devices

As a new potential method for humidity control, liquid desiccant air-conditioning systems have drawn great public attention. Both latent and sensible heat recovery of indoor exhaust air can be realized by using liquid desiccant as the medium. Additionally, liquid desiccant systems can be driven by low-grade heat, for instance heat obtained from 65 to 80 °C hot water. Based on these benefits, many liquid desiccant air-handling devices have been developed.

Table 2 Parameters of air and liquid desiccant during dehumidification experiments [2-4, 11-19]

Reference	Type	Desiccant Cooling source Inlet conditions										$\xi_{in} - \xi_{out}$ (%)
		Desiccant	Cooling source	$\frac{\dot{m}_a}{\dot{m}_{d,in}}$	$t_{a,in}$ (°C)	$\omega_{a,in}$ (g/kg)	$t_{s,in}$ (°C)	ξ_{in} (%)	$\frac{\dot{m}_L}{\dot{m}_d}$	$t_{f,in}$ (°C)		
[2]	Adiabatic	LiCl	-	0.1-0.2	24-30	13-18	19-21	30-38	-	-	<0.1	
[3]	Adiabatic	LiBr	-	1.4-3.1	28-39	12-23	23-32	44-59	-	-	<0.7	
[4]	Adiabatic	LiCl	-	0.1-0.3	30-40	14-22	25-35	33-35	-	-	<0.2	
[11]	Adiabatic	LiCl	-	0.7	28-35	11-19	25-30	38-40	-	-	<0.2	
[16]	Adiabatic	LiBr	-	0.5-1.6	24-34	10-21	20-30	42-55	-	-	<0.5	
[17]	Adiabatic	CaCl ₂	-	0.2-1.7	40	38	35	45	-	-	<0.2	
[12]	Internally cooled	LiCl	Water	10.2-109	23-25	14-15	-	40	4.0-16	24	3.1-15.0	
[13]	Internally cooled	LiCl	Water	6.6-54	28-35	20-30	28-32	39-42	-	-	-	
[14]	Internally cooled	CaCl ₂	Air	0.9-7.9	26-31	15-21	27-33	41-45	-	-	-	
[15]	Internally cooled	CaCl ₂	Evaporative air	2.7-7.8	23-28	9-13	-	40	~1.0	23-28	~3.0	
[18]	Internally cooled	LiCl	Refrigerant	1.3-3.0	26-30	14-23	25-45	36-42	-	-	0.6-1.0	
[19]	Internally cooled	LiCl	Water	10.5	29-35	13-21	25	43	1.4	18-24	3.0-5.4	

Fig. 4 Schematic of fundamental module with external heat exchanger [6, 20]



2.1 Liquid Desiccant Total Heat Recovery Device

2.1.1 Operating Principle

As well known, fresh air-handling process consumes large amount (about 20–40 %) of the overall energy consumption of air-conditioning system. Therefore, decreasing the energy consumption during the fresh air-handling process is essentially important in improving system energy efficiency, and one of the promising methods is using heat recovery technique. Rotary wheel and plate-fin total heat recovery devices are commonly used, yet they cannot avoid cross-contamination between outdoor air and indoor exhaust air. Based on the absorption and desorption ability of liquid desiccant, such as LiBr, LiCl aqueous water solution, heat and mass transfer between the fresh air and indoor exhaust air can be completed in the liquid desiccant total heat exchanger [21].

The schematic of a typical single-stage total heat exchanger based on sprayed liquid desiccant is shown in Fig. 5a, which is composed of two direct contact heat exchangers (DCHE) and one self-circulation solution pump. Padding in the DCHE enhances the heat and mass transfer efficiency by increasing the efficient contact area between the liquid desiccant and the processed air stream. The shell of the total heat exchanger is mainly made by plastic in order to avoid the corrosion of the liquid desiccant. No anti-freezing measures are required due to the fact that the liquid desiccant has a relatively low freezing point. An added benefit of the liquid desiccant is the potential to remove a number of pollutants, and cross-contamination can also be avoided in this new type of total heat exchanger, which will improve indoor air quality.

According to the different operation conditions, the fresh air is cooled and dehumidified in summer, heated and humidified in winter by the indoor exhaust air. If taking the summer condition as an example, shown in Fig. 5a, liquid desiccant from the groove of the lower DCHE driven by the self-circulation pump flows into the distributor of the upper DCHE where liquid desiccant sprays and soaks the padding. After the heat and mass transfer between the exhaust air and

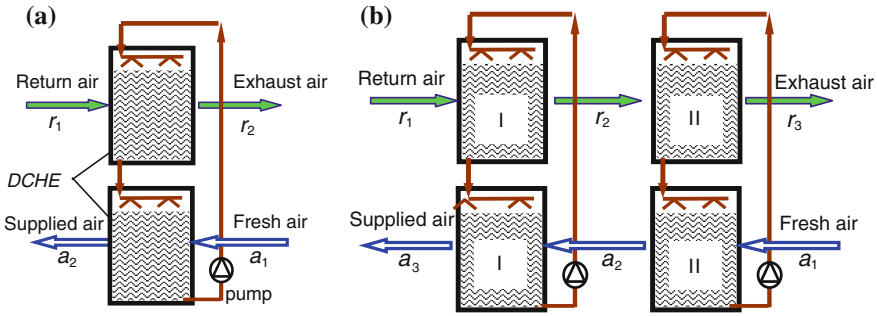


Fig. 5 Liquid desiccant total heat recovery device. a Single-stage. b Two-stage [21]

liquid desiccant in the upper DCHE, moisture is absorbed into the exhaust air from the liquid desiccant due to the vapor pressure difference. Then, the concentrated liquid desiccant enters the lower DCHE by gravity, where it contacts the fresh air. Since the liquid desiccant has lower temperature and surface vapor pressure than that of the fresh air, liquid desiccant is heated and diluted while the fresh air is cooled and dehumidified in the lower DCHE. Fresh air from the total heat exchanger will be further handled before being supplied to the occupied spaces. The liquid desiccant finally returns back to the groove of the lower DCHE and completes the cycle. The equilibrium parameters of the liquid desiccant in the total heat exchanger are determined by the status of both the fresh air and the exhaust air. The heat and mass transfer process of the liquid desiccant total heat exchanger in winter is similar to that in summer, except that the heat and mass transfer directions are different.

Several stages can be combined together to gain higher recovery efficiency compared with single-stage total heat exchanger. The schematic of a two-stage liquid desiccant total heat exchanger is shown in Fig. 5b, composed of two single-stage total heat exchangers where the upper and lower channels are for exhaust air and fresh air, respectively. The parameters of the liquid desiccant in each stage are determined by the parameters of the two air streams.

2.1.2 Performance Analysis

The serial numbers of fresh air and exhaust air in the liquid desiccant total heat exchanger can be seen in Fig. 5, where ‘a’ and ‘r’ stand for fresh air and exhaust air, respectively. The performance of the total heat exchanger can be described by η_h (overall transfer efficiency) and η_m (mass transfer efficiency). Here, η_h is the ratio of the larger energy gain of the two air streams to the maximal possible energy change, as shown in Eq. (2), where h is the air enthalpy, the subscripts ‘in’ and ‘out’ mean the input and output parameters, respectively, and the subscripts ‘1’ and ‘2’ stand for the fresh air and exhaust air.

Table 3 Comparison of multi-stage liquid desiccant total heat exchanger

	Exhaust air		Send air		Efficiency	
	t (°C)	d (kg/kg)	t (°C)	d (kg/kg)	η_h (%)	η_m (%)
Single-stage	29.2	0.0169	27.0	0.0164	53.9	51.6
Two-stage	30.5	0.0193	25.7	0.0140	70.1	67.9
Three-stage	31.1	0.0205	25.1	0.0128	77.9	76.0

$$\eta_h = \frac{(h_{\text{out}} - h_{\text{in}})_{\text{max}}}{h_{\text{in},1} - h_{\text{in},2}} \quad (2)$$

Mass transfer efficiency η_m is the ratio of the larger pressure change of the two air streams to the maximal possible pressure change, as shown in Eq. (3), where p is the vapor pressure of the air stream.

$$\eta_m = \frac{(p_{\text{out}} - p_{\text{in}})_{\text{max}}}{p_{\text{in},1} - p_{\text{in},2}} \quad (3)$$

The comparison results of different-stage total heat exchanger are shown in Table 3. The return air parameters are 24 °C, 0.0093 kg/kg (50 % relative humidity), and fresh air parameters are 32.0 °C, 0.024 kg/kg (80 % relative humidity); the air flow rate of the two air flows are the same. The overall transfer efficiency η_h are 53.9, 70.1, and 77.9 % for single-stage, two-stage, and three-stage total heat exchangers, respectively, and the corresponding mass transfer efficiency η_m are 51.6, 67.9, and 76.0 %, respectively. The air and liquid desiccant states changing processes for different stages are shown in Fig. 6, where broken lines I, II, and III stand for the status of liquid desiccant in each single stage. The detail comparison of different-stage liquid desiccant total heat exchanger can be seen in [21].

2.2 Heat Pump-Driven Liquid Desiccant Air-Handling Devices

2.2.1 Operating Principle

The liquid desiccant air-handling devices driven by heat pumps have quickly developed, where the exhaust heat from the condenser is used to regenerate the liquid desiccant and the cooling capacity from the evaporator is used to cool the liquid desiccant, as shown in Fig. 7. In the processor, a stream of outdoor fresh air (a_1) is dehumidified and cooled in the dehumidifier, and a stream of regeneration air (a_3) is adopted to regenerate the diluted liquid desiccant in the regenerator. In the regenerator, the air transfers heat and moisture with the hot and diluted liquid desiccant, and the water in the liquid desiccant evaporates into the air stream;

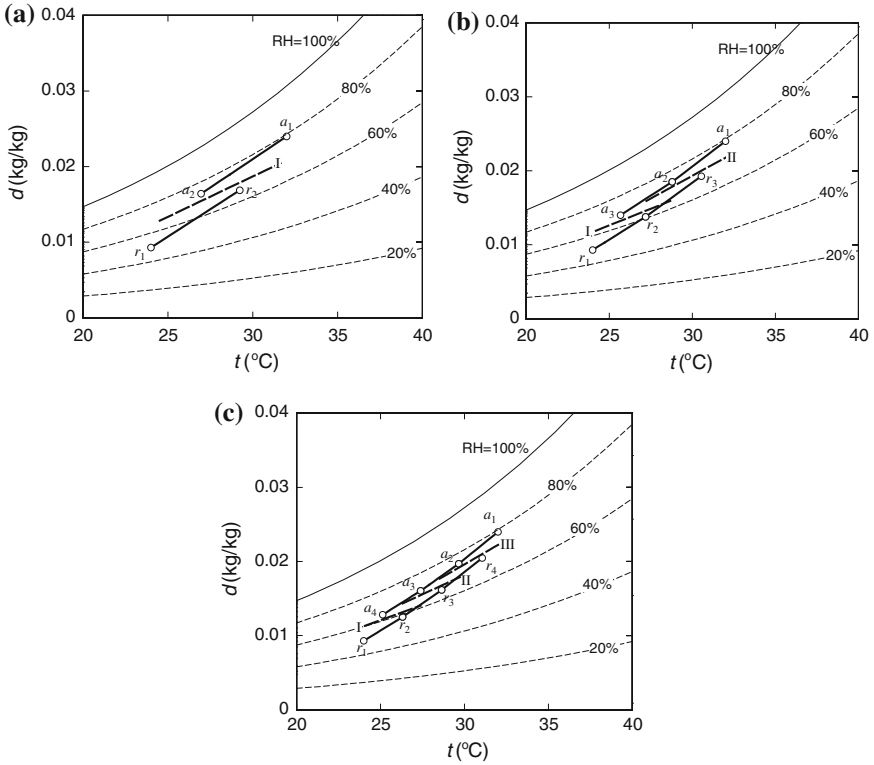


Fig. 6 Status changing process in multi-stage liquid desiccant total heat exchanger. a Single-stage. b Two-stage. c Three-stage

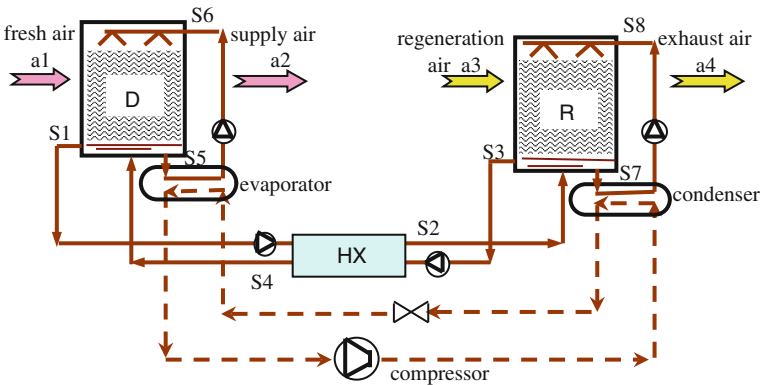


Fig. 7 Heat pump-driven liquid desiccant air-handling devices

hence, the desiccant is regenerated. In the dehumidifier, the moisture from the processed air is absorbed by the cool and strong liquid desiccant, and the air is cooled and dehumidified during the process. The solution (S_7) from the groove of generator is heated by the condenser and then supplied to the top of regenerator (S_8). The regenerated solution (S_3) exchanges heat in the heat exchanger with the cool and diluted solution coming from the dehumidifier (S_1), and then, it is supplied to the dehumidifier. Subsequently, the solution from the groove of the dehumidifier (S_5) is cooled by the evaporator and it is supplied to the top of the dehumidifier (S_6). The sprayed solution absorbs the moisture and becomes diluted. Then, the diluted solution exchanges heat with the hot and strong solution from the regenerator. Thus, a circulation is completed. There are three desiccant circulation flow rates in the liquid desiccant air-handling device, which are circulation in the dehumidifier (D, S_5 – S_6), circulation in the regenerator (R, S_7 – S_8), and circulation between the heat exchanger (HX, S_1 – S_2 and S_3 – S_4). The desiccant flow rate between the heat exchanger is about one order of magnitude smaller compared with the first two circulation flow rates.

Figure 8 shows a new type of fresh air processor [6, 22] composed of a two-stage total heat recovery device, two dehumidification modules, two regeneration modules, and a refrigeration cycle. Liquid desiccant total heat exchanger is adopted to recover the energy from exhaust air to decrease the energy consumption in the fresh air-handling process. The straight line and dashed line stand for liquid desiccant (LiBr solution) and refrigerant, respectively. The position of evaporator and condenser in summer is shown in Fig. 8. Fresh air first enters the two-stage dehumidification modules to be further cooled and dehumidified before being supplied into the occupied spaces. In winter, the refrigeration cycle is changed into ‘heat pump cycle’ by a four-way valve, and fresh air is heated and humidified before entering the occupied spaces.

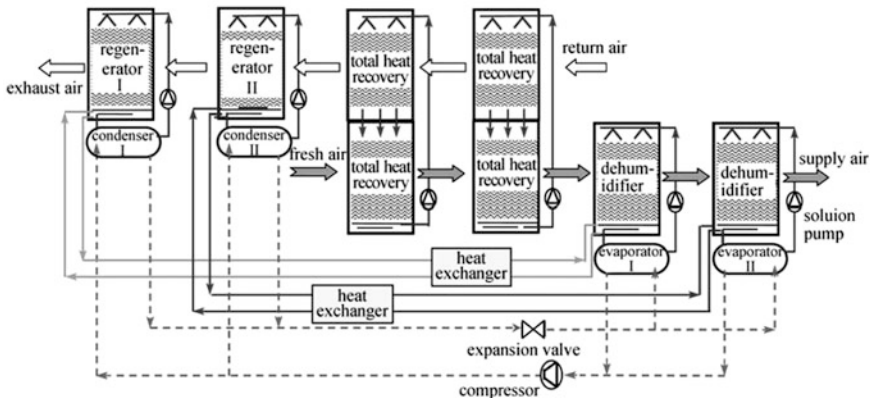


Fig. 8 Heat pump-driven liquid desiccant outdoor air processor [6, 22]

Liquid desiccant in the fresh air processor can be divided into two parts, one is accumulated in the middle solution groove for the purpose of total heat recovery and the other is accumulated in the left and right solution grooves. Mass transfer exists between the left and the right solution groove, and no mass exchange occurs between the middle solution groove and the left (or right) solution groove. Liquid desiccant from the right solution groove comes to the dehumidifier after been cooled by the evaporator, where it is heated and diluted by the fresh air. While liquid desiccant from the left solution groove comes to the regenerator after been heated by the condenser, where it is cooled and concentrated by the exhaust air. The diluted and concentrated liquid desiccants are connected by solution pipes, and plate heat exchanger is adopted to recover sensible heat of the solution.

2.2.2 Performance Analysis

The performance of the heat pump-driven outdoor air processor is shown in Table 4, where the flow rate of outdoor air is the same as that of indoor exhaust air. The outdoor air processor can operate in cooling and dehumidifying mode in summer, in total heat recovery mode in transition season, and in heating and humidifying mode in winter. The coefficient of performance COP_{air} is defined as the gained cooling capacity of outdoor air divided by the power consumption of the compressor and solution pumps, as shown in Eq. (4).

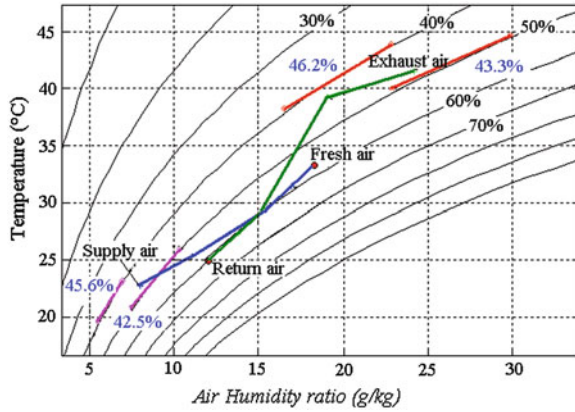
$$COP_{air} = \frac{\text{Cooling capacity of the outdoor air}}{\text{Power consumption of compressor and solution pumps}} \quad (4)$$

The air-handling processes as well as the liquid desiccant are shown in Fig. 9. The concentration of liquid desiccant in evaporator I and condenser I is about 43 %, and the concentration in evaporator/condenser II is about 46 %. As indicated in Table 4, the COP_{air} of the outdoor air processor can be as high as 5.0 both in summer and in winter operating conditions. The total heat recovery efficiency is higher than 60 %. The value of COP will be lower than 1 if electrical humidifier is adopted to humidify the outdoor air in winter.

Table 4 Testing performance of heat pump-driven liquid desiccant outdoor air processor [6, 22]

		Dehumidification mode in summer		Total heat recovery mode	Humidification mode in winter	
Fresh air	t (°C)	36.0	30.0	35.9	6.4	4.3
	ω (g/kg)	25.8	17.4	26.7	2.1	1.6
Supply air	t (°C)	17.3	17.3	30.4	22.5	25.6
	ω (g/kg)	9.1	9.6	19.5	7.2	10.7
Return air	t (°C)	26.0	26.0	26.1	20.5	22.1
	ω (g/kg)	12.6	12.7	12.1	4.0	5.1
Exhaust air	t (°C)	39.1	39.1	32.6	7.0	6.6
	ω (g/kg)	38.6	26.6	20.3	2.7	2.9
COP_{air}		5.0	5.9	62.5 %	6.2	4.6

Fig. 9 Air-handling process of heat pump-driven liquid desiccant outdoor air processor



2.3 Heat-Driven Liquid Desiccant Air-Handling Devices

2.3.1 Operating Principle

Heat-driven liquid desiccant air-conditioning system is consisted of a dehumidifier and a regenerator. Heat (with a temperature of 65–80 °C) is required in the regenerator. Based on the fundamental modules shown in Sect. 1.2, many air-handling processes using liquid desiccant can be proposed [6, 23, 24, 28]. The operating principle and performance of two types of multi-stage dehumidifiers and one type of multi-stage regenerator will be illustrated in this section.

- Dehumidifier

The operating principles of two types of outdoor air processors are shown in Fig. 10, and concentrated liquid desiccant will be introduced into the processors. Multi-stage dehumidification modules are utilized in the outdoor air processors. Outdoor air flows in the counterflow direction against the liquid desiccant, and in each stage, liquid desiccant is cooled first by either evaporative water or cooling water to enhance its absorption ability.

In type I, evaporative cooling capacity of the indoor exhaust air is used to cool the dehumidification process. In the upper heat and mass transfer units as shown in Fig. 10a, indoor exhaust air directly contacts the spraying water for evaporative cooling and then the cooling water produced is pumped into the middle heat exchanger to cool liquid desiccant on the other side. While inside the lower units, fresh air directly contacts the cooled spraying solution for the dehumidifying process. Strong solution, which is produced in the regenerator, is pumped in from the last stage of the lower unit (module C in Fig. 10a) and becomes diluted, stage by stage, and finally flows out as diluted solution. The air-handling processes as well as the liquid desiccant are shown in Fig. 11. In winter mode, the upper layer is shut down and no liquid desiccant is pumped into the lower modules, and hot

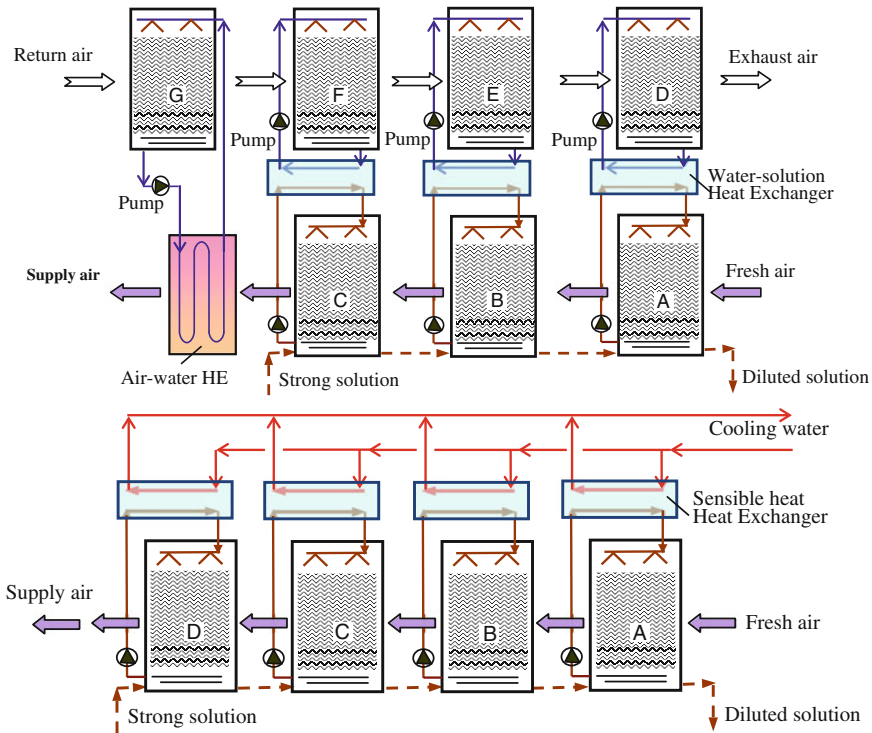


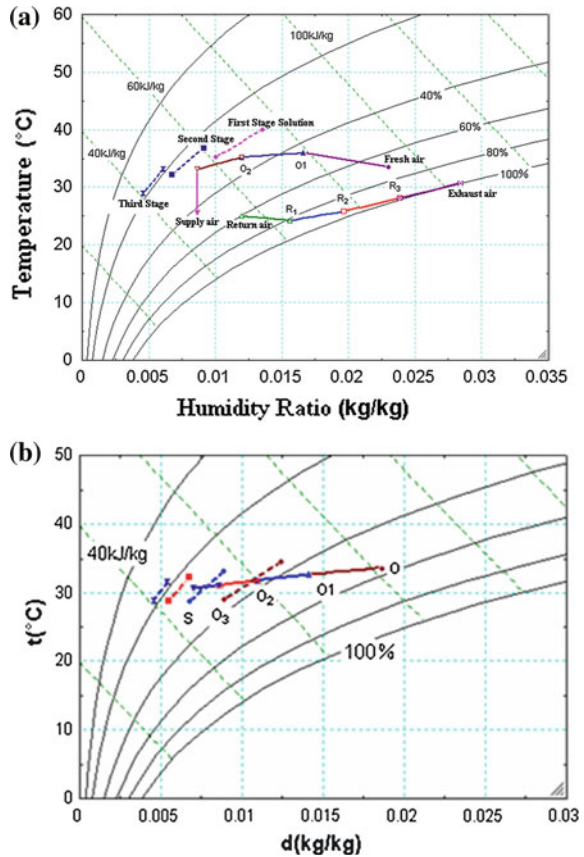
Fig. 10 Outdoor air processor or dehumidifier. **a** Type I, using evaporative exhaust air to cool the dehumidification process. **b** Type II, using cooling water to cool the dehumidification process [7]

water with a temperature of 35–40 °C is supplied into the middle heat exchangers to heat the spraying solution, which will then heat and humidify the dry and cold outdoor air.

In type II, cooling water from the cooling tower is adopted to cool the dehumidification process. It consists of four stages in series for fresh air dehumidifying or humidifying, as shown in Fig. 4. A small strand of strong solution, pumped in from the last stage (module D in Fig. 10b), flows as counter current against fresh air and flows out from the first stage (module A). This outdoor air processor is applied in buildings rich in low-grade heat and where no return air can be used for recovery.

Figure 12 shows the tested performance of the two types of outdoor air processors using liquid desiccant. During the test period, the outdoor air temperature was about 30 °C and humidity ratio of 0.013–0.015 kg/kg, the concentration of inlet liquid desiccant was 50–52 %, and the humidity ratio of the supplied air was about 0.007 kg/kg. The coefficient of performance COP_d is defined as the gained cooling capacity of outdoor air divided by the supplied latent heat of the liquid desiccant, as shown in Eq. (5). The COP_d was in the range of 1.5–1.8 for type I

Fig. 11 Air-handling process of dehumidifier shown in psychrometric chart. **a** Type I dehumidifier. **b** Type II dehumidifier



dehumidifier, and 1.0–1.2 for type II dehumidifier. The measured COP_d was higher than 1, due the utilization of the cooling capacity from indoor exhausted air or cooling water.

$$COP_d = \frac{\text{Cooling capacity of the processed air}}{\text{Latent heat of the processed air}} \quad (5)$$

In winter condition, hot water is imported instead of cooling water in summer, and fresh air can be heated and humidified for the indoor requirement. No extra liquid desiccant (dotted line shown in Fig. 10) is pumped into the modules, and a small amount of water is added into the module since the air is humidified during the process. The desiccant concentration inside the modules can be controlled according to the amount of adding water. The tested performance is shown in Table 5. The COP_{air} in winter is defined as the gained heating capacity of the outdoor air divided by the input heat of the hot water. The theoretical COP_{air} is 1, that is, all the heat from hot water is carried away by the processed outdoor air.

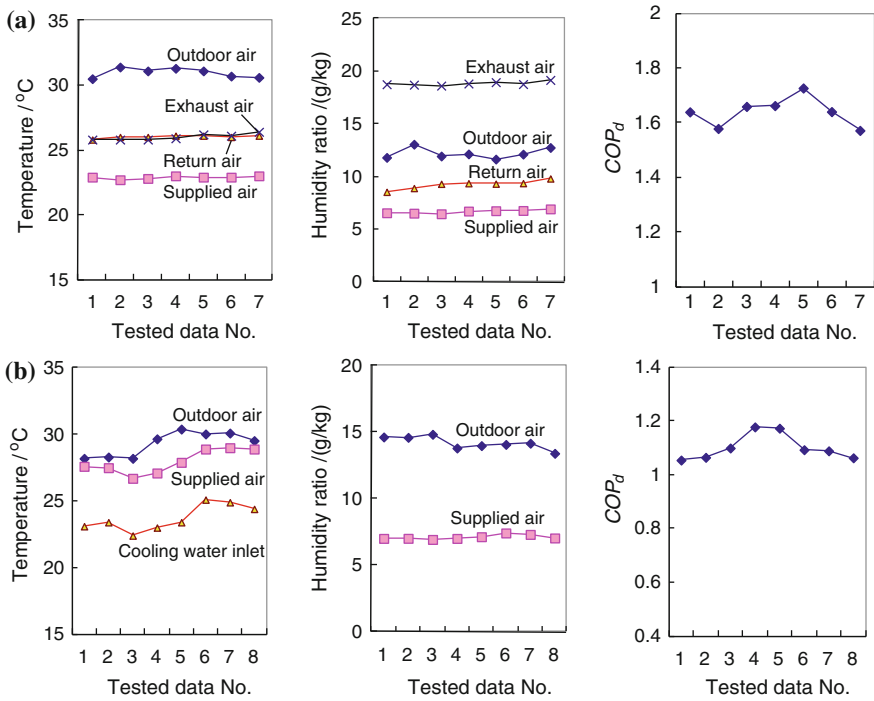


Fig. 12 Tested performance of the liquid desiccant dehumidifier. **a** Type I dehumidifier. **b** Type II dehumidifier

The tested COP_{air} results shown in Table 5 express the energy balance of the experiments, which are close to 1.

• Regenerator

The operating principle of the multi-stage regenerator is shown in Fig. 13. Using low-grade heat (65–80 °C hot water), waste heat or solar energy, as driving force, this regenerator produces strong solution and serves for heat-powered liquid desiccant fresh air processor (as shown in Fig. 13). In this regenerator, solution is first heated to increase its vapor pressure and then contacts with outdoor air directly to release moisture and becomes concentrated. Four stages are adopted and heat recovery devices are added in order to increase the regenerator’s performance. The regenerator operates only in summer and shuts down in winter. The tested performances of the multi-stage regenerator are shown in Table 6. The regenerator efficiency η_r is defined as the gained latent heat of the liquid desiccant divided by the supplied latent heat of the liquid desiccant, as shown in Eq. (6).

$$\eta_r = \frac{\text{Latent heat of the removed moisture}}{\text{Heat input of the regenerator}} \tag{6}$$

Table 5 Testing performance of liquid desiccant outdoor air processor in winter [24]

Fresh air flow rate (m ³ /h)	$t_{a,in}$ (°C)	$\omega_{a,in}$ (g/ kg)	$t_{a,out}$ (°C)	$\omega_{a,out}$ (g/ kg)	Hot water flow rate (t/h)	$t_{w,in}$ (°C)	$t_{w,out}$ (°C)	LiBr concentration inside the module (%)				COP _{air} (express energy balance)
								A	B	C	D	
1,914	1.0	2.7	17.3	10.1	1.6	28.3	14.2	35.6	33.2	29.8	–	0.86
1,914	4.4	3.1	18.2	11.1	1.6	28.6	14.9	34.2	30.9	29.8	–	0.85
1,955	12.1	5.1	23.2	14.6	1.8	35.5	22.0	43.9	40.7	34.5	26.6	0.82
2,010	7.1	2.2	22.3	12.7	2.2	32.2	21.5	46.0	43.8	38.9	29.9	1.03
2,056	0.8	2.7	17.8	7.4	1.6	27.3	16.1	48.9	47.8	45.0	42.1	0.95
2,056	3.4	3.4	21.8	11.6	1.7	39.1	22.7	49.8	48.7	44.0	38.8	0.82

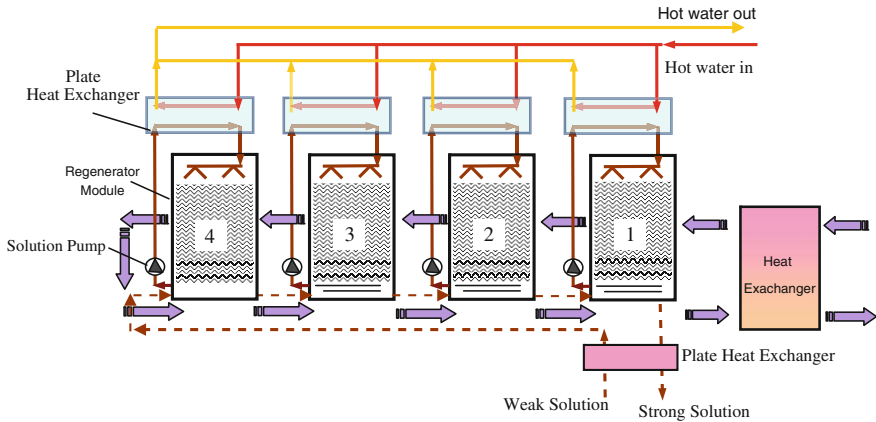


Fig. 13 Operating principle of a multi-stage regenerator

2.3.2 Performance Analysis

The performance of the heat-driven liquid desiccant air-conditioning system with the summer outdoor climate in Beijing is shown in Fig. 14. The regeneration temperature is fixed at 75 °C. The coefficient of performance COP_{air} is defined as the gained cooling capacity of outdoor air divided by the required regeneration heat, as shown in Eq. (7).

$$COP_{air} = COP_d \cdot \eta_r \tag{7}$$

The performance COP_{air} increases with the decrease in outdoor air relative humidity. The average seasonal performance of type I and type II air-conditioning system is 1.19 and 0.93, respectively. Due to the utilization of the cooling capacity from indoor exhaust air or cooling tower, the COP_{air} may be higher than 1.

3 Application of Liquid Desiccant Air-Conditioning Systems

In the conventional HVAC system that removes moisture by condensation, air is cooled and dehumidified simultaneously. In most cases, sensible load of building covers the majority part of the whole cooling load while the latent load (moisture load) takes only a small part. However, as the required cooling source temperature of dehumidification is much lower than that of cooling, the chilled water temperature has to be reduced to meet the demand for condensation dehumidification. Moreover, the ratio of sensible load to latent load varies largely due to the changes

Table 6 Tested performance of the multi-stage regenerator [23]

Working condition	Fresh air		Hot water		Solution in		Solution out		Moisture removal rate (kg/h)	Regenerator efficiency
	Dry bulb (°C)	Humidity ratio (g/kg)	Inlet T (°C)	Outlet T (°C)	Mass flow rate (m ³ /h)	Density (g/mL)	Mass flow rate (m ³ /h)	Density (g/mL)		
1	34.1	15.05	62.5	53.4	0.729	1.463	0.7	1.481	30.9	0.77
2	34.5	14.55	63	54.2	0.713	1.474	0.682	1.494	32.3	0.8
3	34.2	14.2	63.9	55	0.68	1.498	0.649	1.52	31.9	0.76
4	33.9	13.69	63.9	55.2	0.677	1.5	0.645	1.523	32.2	0.74
5	32.8	12.34	64.8	56	0.663	1.511	0.631	1.535	33.1	0.79
6	32.9	13.22	64.8	56.3	0.659	1.514	0.628	1.538	32.3	0.77
7	32.9	13.63	64.8	57.2	0.649	1.522	0.623	1.542	27.3	0.85

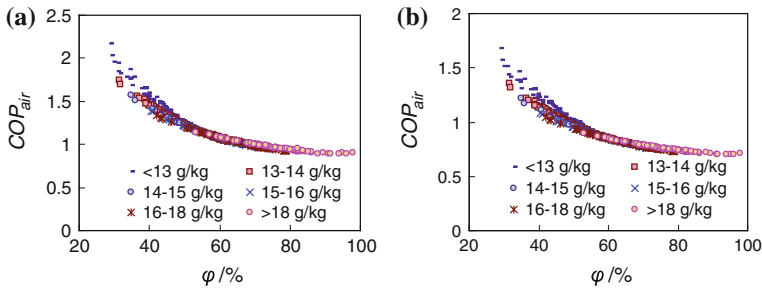


Fig. 14 Performance of hot water-driven liquid desiccant air-conditioning system. **a** Using type I dehumidifier. **b** Using type II dehumidifier

of outdoor climate, number variance of indoor occupants, indoor equipments, and lighting utilization mode and so on. Therefore, the indoor temperature and humidity, the two key parameters, can hardly be satisfied with condensation by the cooling coil only. In practice, the common reaction to the increased indoor humidity is to reduce the set-point temperature and then re-condition the air after passing the cooling coil to the proper temperature, which results in a plenty of energy wastefulness [25].

To avoid the aforementioned problems, temperature- and humidity-independent control (THIC) air-conditioning system stands out as an appropriate pattern that temperature and humidity can be regulated independently with temperature control subsystem and humidity control subsystem, respectively. As the humidity control subsystem, liquid desiccant air-handling processors can improve the indoor air quality and make it possible to utilize low-grade heat. Besides, the coil temperature for cooling in the temperature control subsystem can be considerably increased, e.g., from current 7 to 17 °C, so that improvement on the performance of chillers or even free cooling from ambient could be obtained. This section will investigate the real operating performance of some THIC air-conditioning systems, especially the performance of liquid desiccant air-handling devices.

3.1 Case 1: An Office Building in Shenzhen

The office building is located in Shenzhen, a modern metropolis in southern China of hot and humid climate. This system has been brought into operation in July 2008. In this THIC system, the liquid desiccant fresh air-handling units driven by heat pumps are employed to handle the outdoor air to remove the entire latent load and supply enough fresh air to the occupied spaces, and the high-temperature chiller that produces chilled water of 17.5 °C for the indoor terminal devices (radiant panels and dry fan coil units) is applied to control indoor temperature [26].

3.1.1 Basis Information

The 5-story office building, as shown in Fig. 15, is located in Shenzhen, China, with total building area of 21,960 m² and the areas of 5,940, 5,045, 3,876, 3,908, 3,191 m² for the 1st to 5th floor, respectively. The main function of the 1st floor is restaurant, archive, and carport; the 2nd to 4th floors are the office rooms; and the 5th floor is the meeting room. The outdoor condition in Shenzhen is rather hot and humid all through the year. The annual outdoor air relative humidity is about 80 % and humidity ratio in summer is as high as 20 g/(kg dry air). The building requires cooling and dehumidification in a long period of time, and no heating and humidification requirement in winter. Therefore, how to handle the moisture efficiently is a key issue in such a subtropical area.

3.1.2 THIC Air-Conditioning System

The THIC system serves from 1st to 4th floor with the net air-conditioning area of 13,180 m² (total area of 18,769 m²), and the 5th floor is served by several stand-alone air conditioners, which is not within the scope of our discussion. The schematic of the THIC system is shown in Fig. 16. The right side of Fig. 16 is the humidity control subsystem, including 9 liquid desiccant fresh air-handling units that supply adequate dry fresh air into the occupied spaces. As the volume of the supplied fresh air is proportional to the number of people, the pollutants, CO₂, and latent heat produced by human bodies can be removed by fresh air. The schematic of the fresh air processors using liquid desiccant is illustrated in Fig. 8, which is composed of a two-stage total heat recovery device and a two-stage air-handling device coupled with refrigeration cycles. Lithium bromide (LiBr) aqueous solution is employed as liquid desiccant in these air processors. The air-handling processes are displayed in the air psychrometric chart in Fig. 9 where the fresh air first passes the total heat recovery device to recover the energy from the indoor exhaust air and then flows into the dehumidification modules to be further dehumidified and cooled before it is supplied into the occupied spaces.

Fig. 15 The tested office building in Shenzhen



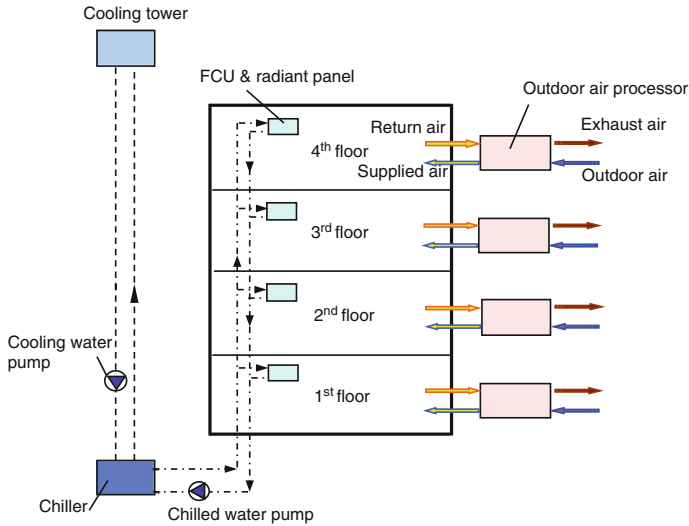


Fig. 16 Schematic of the THIC air-conditioning system [26]

In general, the COP of the liquid desiccant fresh air units (total heat removed from the fresh air divided by the power consumption of the heat pumps and solution pumps) can be as high as 5.0 with the following three main reasons: (1) the cooling capacity of the indoor exhaust air is fully exploited to remove heat from the fresh air by the total heat recovery device; (2) both the cooling capacity from evaporator and exhaust heat from condenser are utilized to enhance the air-handling processes; and (3) the efficiency of the heat pump is significantly raised since the required evaporating temperature in this liquid desiccant device is much higher than that in the conventional condensing dehumidification system. Besides, as indicated in Fig. 9, the supplied air temperature is lower than the indoor air temperature, so the liquid desiccant system can remove some sensible load of the building as well as the entire latent load. The left side of Fig. 16 is the temperature control subsystem that takes up the rest sensible load to control indoor temperature, including a high-temperature chiller, cooling tower, cooling water pump, chilled water pump, and indoor terminal devices (radiant panels and dry fan coil units). The high-temperature chiller is a centrifugal chiller with the rated COP of 8.3 (designed condition: the inlet and outlet temperature of the chilled water and cooling water are 20.5/17.5 °C and 30.0/35.0 °C, respectively), which is much higher than the conventional chiller operating at the chilled water temperature of 12/7 °C. As for indoor terminal devices, as shown in Fig. 16, fan coil units (FCUs) operating in ‘dry condition’ are set up in the restaurant, archive, and office regions which serve about 81 % of the entire cooling load of the temperature control subsystem, while radiant floor and radiant ceiling panels are applied in vestibule and some office rooms which serve the rest 19 %.

3.1.3 Field Measurement Results of the System

- Indoor thermal environment

Figure 17 shows the tested results of indoor temperatures, humidity ratios, and CO₂ concentrations with the outdoor temperature and relative humidity of 34.9 °C and 61 %, respectively. As indicated by the figure, the THIC system could provide a comfortable indoor environment with suitable thermal condition and good indoor air quality.

- Energy efficiency of the THIC system

The field test of the energy efficiency of the THIC system was conducted both under the partial load condition and very hot and humid outdoor condition. The former one is on May 27, 2009, with the ambient temperature of 29.3 °C and relative humidity of 79 % (absolute humidity 20.3 g/kg), and the latter one is on

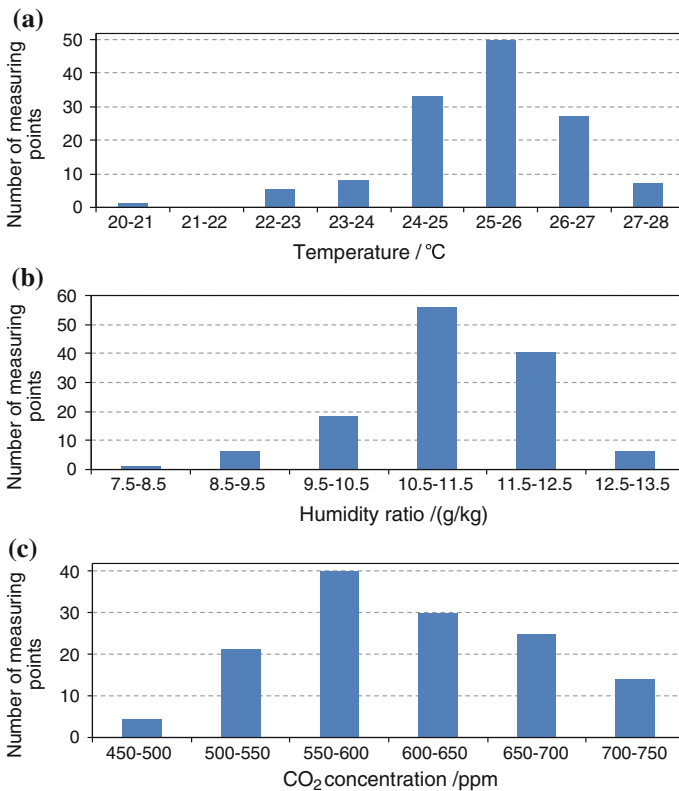


Fig. 17 Indoor environment of the office building. **a** Temperature. **b** Humidity ratio. **c** CO₂ concentration

July 16, 2009, with ambient temperature of 34.9 °C and relative humidity of 61 % (absolute humidity 21.6 g/kg). The measurement was divided into two parts: humidity control subsystem and temperature control subsystem.

The performances of the liquid desiccant fresh air units were tested one by one on May 27, 2009, according to the measured flow rates, air inlet and outlet parameters through the processor and input power of compressors, solution pumps and fans. The tested results of seven fresh air units are summarized in Table 7; the other two processors are neglected due to the difficulty of installing the measuring sensors.

The east side processor of the 2nd floor is a typical example for the fresh air unit, and its specific operation information is shown in Table 8. The fresh air flow rate was 5,059 m³/h, the outdoor air parameter was 29.3 °C and 20.3 g/kg, and the supply air parameter was 17.1 °C and 6.2 g/kg. So the cooling capacity (Q_{air}), calculated by energy balance equation, was 82.6 kW. The input power of compressors and solution pumps (P_{air}) inside the processor was 17.8 kW, and the input power of the supply air and exhaust air fans (P_{fan}) was 2.2 kW. Therefore, the performance of the fresh air unit (COP_{air}) and the performance of the entire humidity handling process (COP_{hum}), as shown in Eqs. (8) and (9), are 4.7 and 4.2, respectively.

$$COP_{air} = \frac{Q_{air}}{P_{air}} \tag{8}$$

$$COP_{hum} = \frac{Q_{air}}{P_{air} + P_{fan}} \tag{9}$$

Table 7 Performance of the fresh air-handling units (outdoor condition: 29.3 °C and 20.3 g/kg) [26]

Place	Supplied fresh air			Cooling capacity (kW)	Input power (kW)		COP_{air}	COP_{hum}
	Flow rate (m ³ /h)	Temperature (°C)	Humidity ratio (g/kg)		Compressors and solution pumps	Fans		
East side of 2nd floor	5,059	17.1	6.2	82.6	17.8	2.2	4.7	4.2
West side of 2nd floor	5,195	16.7	6.1	86.0	17.6	2.3	4.9	4.3
East side of 3rd floor	4,972	16.8	6.5	80.4	18.2	2.2	4.4	4.0
West side of 3rd floor	5,215	16.6	6.2	86.4	17.6	2.2	4.9	4.4
East side of 4th floor	4,261	16.7	6.4	69.5	15.0	1.7	4.6	4.2
Middle side of 4th floor	1,940	16.5	6.2	32.1	7.1	0.9	4.5	4.0
West side of 4th floor	4,307	16.3	6.1	72.0	15.3	1.8	4.7	4.2

Table 8 Operation condition of a typical fresh air-handling unit (east side of 2nd floor)

Outdoor condition		Supplied fresh air		Stage	Evaporating temperature (°C)	Condensing temperature (°C)	Solution parameter concentration)		
Temperature (°C)	Humidity ratio (g/kg)	Flow rate (m ³ /h)	Temperature (°C)					Humidity ratio (g/kg)	
29.3	20.3	5,059	17.1	6.2	I	11.0	50.8	Dehumidification module	Inlet 15.8 °C, 34.6 % Outlet 20.5 °C, 34.4 %
								Regeneration module	Inlet 44.2 °C, 34.9 % Outlet 38.3 °C, 35.2 %
					II	4.4	51.3	Dehumidification module	Inlet 9.0 °C, 44.1 % Outlet 14.0 °C, 43.9 %
								Regeneration module	Inlet 44.3 °C, 44.8 % Outlet 37.9 °C, 45.1 %

The COP_{air} of the tested seven fresh air units are in the range of 4.4–4.9 and the COP_{hum} of the entire humidity handling processes are 4.0–4.4. The measured COP_{air} in this building is smaller than that shown in Table 4, due the much lower humidity ratio of supplied air. The lower the required humidity ratio of supplied air, the lower the COP_{air} will be.

According to the test data of May 27, 2009, and rated parameters of the fresh air units and fans, the calculated cooling capacity of the entire humidity control subsystem is 773.0 kW with total inside compressors and solution pumps input power of 166.9 kW and total fans input power of 20.0 kW, so the coefficient of performance of the humidity control subsystem (COP_{hum}), shown in Eq. (10), is 4.1.

$$COP_{hum} = \frac{\sum Q_{air}}{\sum (P_{air} + P_{fan})} \quad (10)$$

The performances of the chiller, cooling tower, cooling and chilled water pumps, and indoor dry FCUs were measured, according to the measured flow rates, water inlet and outlet parameters through the chiller, and input powers of above facilities. The tested results are listed in [26]. The COP of chiller is 8.5. COP_{temp} of the temperature system, which is defined as the cooling capacity provided by the high-temperature chiller divided by the power consumption of the chiller, chilled water pumps, cooling towers, cooling water pumps, FCUs, is 3.7 and 4.1 under the partial load condition (May 27) and very hot and humid condition (July 16), respectively. Therefore, the COP of the entire air-conditioning system is 4.0–4.1.

Based on the test results of these two typical operating conditions, it is convinced that the THIC system in this office building has achieved a high efficiency with its total COP more than 4.0. For the conventional air-conditioning system, such as fan coil unit plus fresh air supply system or all air system, the measured average coefficient of performance of whole system is lower than 3.0. Therefore, there is a remarkable energy efficiency improvement of the THIC system comparing with the conventional system.

The energy consumption in unit building area and unit net air-conditioning area of the tested THIC system were 22.6 and 32.2 kWh/(m² yr), respectively. However, the average energy consumption levels of office building of the similar building envelope and occupant density during the same time in Shenzhen are around 42 and 49 kWh/(m² y), respectively, according to the investigated results by Zi [27]. Therefore, the THIC system in this office building achieves noticeable energy saving compared with the conventional air-conditioning system. The initial cost of THIC system is about 10–20 % higher than conventional fan coil unit plus outdoor air process system, and the added cost can be recalled within about two years.

3.2 Case 2: An Office Building in Beijing

3.2.1 Basic Information

The liquid desiccant air-conditioning system has been installed in an office building, as shown in Fig. 18. It was put into operation in October 2003. With five stories and total height of 18.6 m, its floor area is around 2,000 m². The first floor is for the lobby and reception and conference rooms, and the other floors are for office and conference rooms. There is an air-conditioning chamber for each floor. The system is somewhat like conventional fan coil units (FCU) plus an outdoor air system, except the outdoor air is dehumidified by a special liquid desiccant dehumidification system and the latent heat load is totally born by the processed outdoor air [28, 29].

3.2.2 THIC Air-Conditioning System

Figure 19 shows the schematic diagram of the air-conditioning system. The system consists of a liquid desiccant dehumidification subsystem, chiller, and heat supply. The outdoor air processor supplies outdoor air into rooms, the amount of which is proportional to the number of people inside. The outdoor air bears the total latent heat load. In summer, the processor works in dehumidification and cooling mode to remove water from outdoor supply air. At the outlet of the dehumidifier, there is a sensible heat exchanger to cool the dried air to a comfortable temperature. The strong desiccant in the storage tank is distributed to the processors at different floors, flowing out of the processors by means of overflow after absorbing moisture and going back to the weak storage tank. Hot water (75 °C) from the cogeneration plant enters the regenerator, supplying thermal energy needed for the regeneration of the liquid desiccant. The chiller produces 18–21 °C chilled water for the indoor

Fig. 18 An office building in Beijing



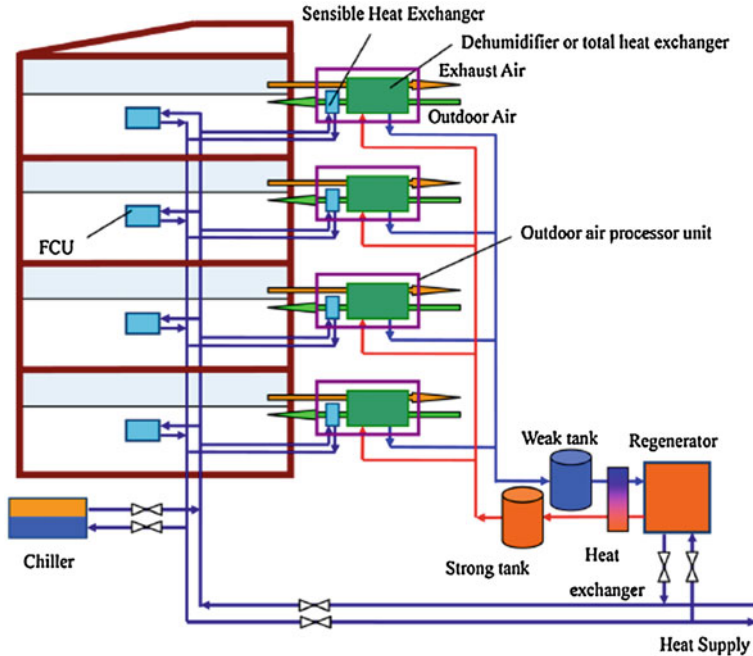


Fig. 19 Schematic of the independent dehumidification air-conditioning system [29]

FCU and the sensible heat exchangers in the outdoor air processor to handle the sensible heat load. They all work in a dry condition as the temperature of chilled water is higher than the air dew point. No condensation water forms and the indoor air quality is highly improved.

There are strong and weak desiccant storage tanks between the outdoor air processor and regenerator for energy storing. Liquid desiccant stores ‘chemical energy’ instead of ‘thermal energy.’ It has an energy-storing capacity as high as 1,000 MJ/m³ and much lower energy loss. The excellent energy storage character of the liquid desiccant offers several advantages for the system. First, the reliance on continuous thermal energy supply is reduced, which makes the system convenient for the use of solar energy; second, the system can be optimally designed so that the dehumidifier capacity matches the peak load while the regenerator capacity just matches the average load, resulting in smaller size of the regenerator.

In winter, by valve switch, hot water instead of chilled water goes into the indoor FCU for heating. The chiller and regenerator are closed. By means of internal circulation, the outdoor air processor works in heat recovery mode, supplying outdoor air to rooms. Since the outdoor air processor can operate either in dehumidification cooling mode or in heat recovery mode, a total heat recovery facility is actually saved compared to a conventional air-conditioning system. Compared to the wheel total heat recovery that is commonly used at present, not

only has the outdoor air processor higher heat recovery efficiency, but, because of the crisscross airflows, air pollution is totally avoided. Furthermore, dust and germs in the air are depressed or destroyed by the desiccant.

Compared to conventional chilled water systems, there is no need for the chilled water to condense the water vapor in air, and temperature of the chilled water can then be raised. In the present system, the design temperature of the chilled water entering and leaving the FCU is 18 and 21 °C, respectively, and the air temperature entering and leaving the FCU is 22 and 26 °C, respectively. Since only sensible heat load is born by the FCU, the temperature increment of the chilled water through the FCU may be too small if the commonly used parallel connection of the FCU is adopted. In the present system, series connection of FCUs is adopted to enlarge the temperature increment of chilled water through the FCUs. This kind of connection may increase the water pressure drop through the FCUs. The increase is, however, rather small compared to the water pressure drop through the whole system. The chilled water always has a temperature higher than the dew point of the indoor air, so no condensation water forms on the FCU, and the drain pipes needed for the condensation water in a conventional system are removed. The air pressure drop through the FCU under the present dry condition may decrease as high as 30 % compared to those under wet conditions for the same air flow rate. The thermal insulation for the chilled water pipes can be shrunk or even removed in the present system since the temperature of the chilled water is rather high.

Compared to a conventional air-conditioning system, the most distinguishing feature of this system is that it employs liquid desiccant to dehumidify the supply outdoor air. In summer, the processor operates in the dehumidification cooling mode, where strong desiccant has to be continuously fed to dehumidify the supply air. The liquid desiccant circulation is shown in Fig. 20. The strong desiccant in the strong storage tank on the first floor is pumped to the processors on different floors. The desiccant contacts air directly and exchanges heat and mass with it. After absorption of the water in the air, the desiccant becomes diluted. By means of overflow, it flows out of the processor and then back to the weak storage tank. The processor on the first floor is at the same level as the weak storage tank, and a pump has to be employed to pump the weak desiccant back by level control. The weak desiccant is then pumped to the regenerator at the fifth floor for regeneration. Thereafter, the concentrated desiccant overflows back to the strong storage tank. There is a heat recovery exchanger fixed between the inlet and outlet of the regenerator to regain heat from the concentrated desiccant and to upgrade the system efficiency. Additional storage boxes are installed to stabilize system operation. There is an overflow pipe fixed to each storage box through which excess desiccant flows back to the storage tank. The right part of Fig. 20 shows the chilled water system. The chilled water produced by the chiller is supplied to the outdoor air processors and indoor FCU for cooling purpose.

The schematic diagram of the outdoor air processor is shown in Fig. 21. Two airflows flow through the processor: outdoor air and return air. The outdoor air is dehumidified by the desiccant when passing through the processor. In the upper

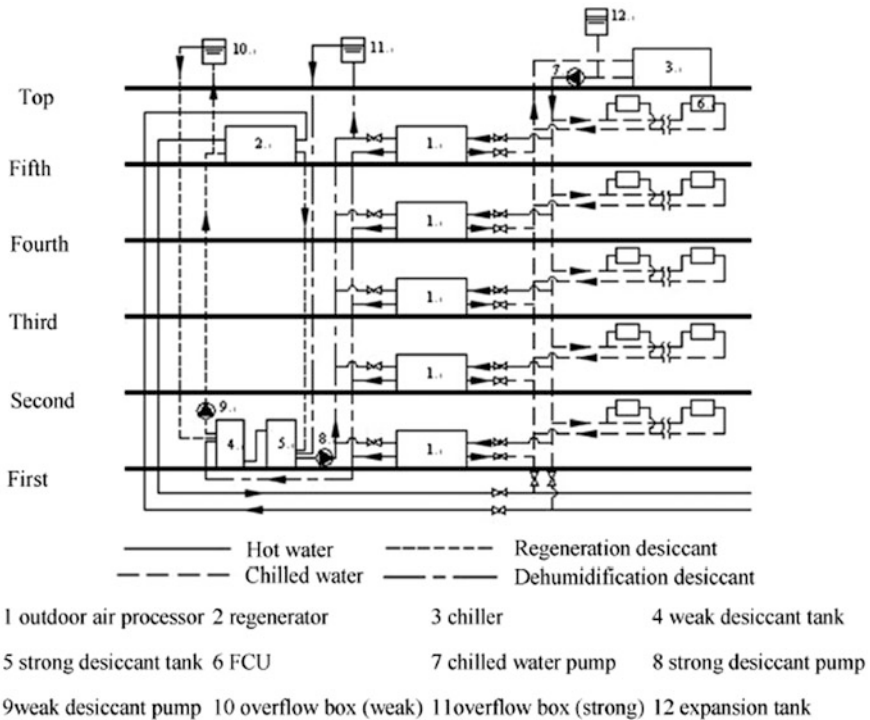


Fig. 20 Diagram of desiccant and chilled water circulation

layer, the return air exchanges moisture and heat with water. The air becomes warmer and more humid, while the water is cooled. The water then goes into the heat exchangers in the lower layer to take away the heat released when the moisture in the outdoor air is absorbed by the desiccant. The flow direction of outdoor air is opposite to that of the desiccant so that the driving force for heat and moisture transfer between the air and the desiccant is uniform along the processor.

3.2.3 Field Measurement Results of the System

Room temperature and humidity were measured for two purposes. The first is to determine whether the air-conditioning system can produce a comfortable indoor environment since temperature and humidity are key factors for evaluating the comfort of the room condition. The second is to control the chilled water temperature above the indoor air dew point so as to avoid condensation water.

Figure 22 shows the variation of the outdoor dry-bulb temperature, outdoor dew-point temperature, indoor dry-bulb temperature, and indoor dew-point temperature of an office room from July 1 to July 31, 2004 [29]. The indoor temperature is always between 24 and 27 °C and relative humidity between 40 and

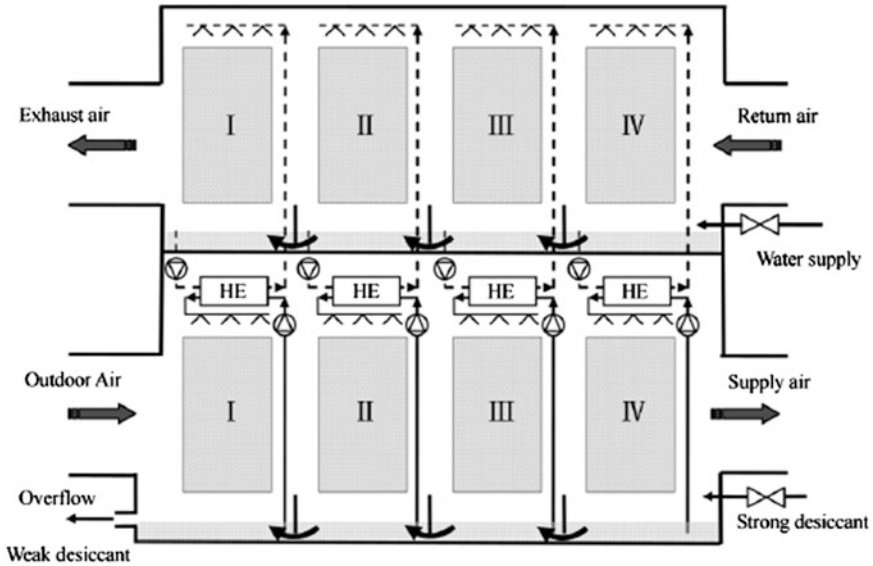


Fig. 21 Schematic of outdoor air processor [28]

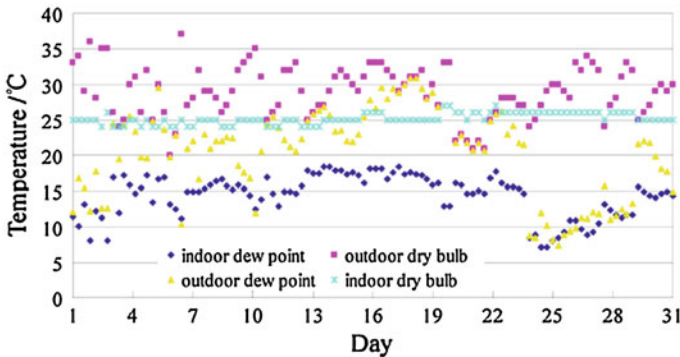


Fig. 22 Temperature variation throughout July

60 %, showing a comfortable indoor condition. No dew drops appeared on the FCU surface in this period, which corresponds to the fact that the indoor air dew point is always lower than the temperature of the chilled water, as shown in Fig. 22.

For the measurement period, the outdoor air temperature varied from 24.8 to 33.9 °C and relative humidity from 40.1 to 80 %, while the indoor temperature was controlled between 24 and 27 °C and relative humidity between 40 and 60 %. The concentration of LiBr desiccant fed to the outdoor air processor varied between 42 and 48 % and the flow rate was set at about 20 mL/s. Table 9 presents

Table 9 Tested performance of the outdoor air processor [28]

No	Outdoor air		Supply air			Return air		Exhaust air			Cooling capacity (kW)	COP _d
	t (°C)	d (g/kg)	t (°C)	d (g/kg)	Flow rate (m ³ /h)	t (°C)	d (g/kg)	t (°C)	d (g/kg)	Flow rate (m ³ /h)		
1	31.3	11.6	22.8	9.8	2,259	26.4	10.6	26.6	17.3	1,288	10.2	2.87
2	28.6	17.1	27.1	10.6	2,189	26.7	12.4	29.9	23.3	1,362	13.4	1.11
3	29.3	13.7	24.3	10.4	2,229	26.1	11.9	27.5	19.3	1,255	9.9	1.66
4	30.0	12.7	23.7	11.1	2,281	26.7	12.1	26.9	18.1	1,273	8.0	2.65
5	27.6	18.6	27.3	11.3	2,189	26.8	12.4	29.7	23.9	1,362	13.9	1.04
6	27.4	14.2	24.4	10.9	2,281	25.7	12.4	27.1	19.3	1,273	8.8	1.39
7	25.2	15.7	25.5	10.0	2,189	26.3	11.9	27.5	21.0	1,362	10.4	0.99

Table 10 Tested performance of the regenerator [28]

No	Outdoor air			Hot water		Inlet desiccant		Outlet desiccant		η _r
	t (°C)	d (g/kg)	Flow rate (m ³ /h)	Inlet temp (°C)	Inlet temp (°C)	Flow rate (m ³ /h)	Density (kg/m ³)	Flow rate (m ³ /h)	Density (kg/m ³)	
1	30.9	19.7	3,760	69.3	57.9	182.7	1.3112	142.0	1.3817	0.92
2	33.4	20.2	3,760	73.2	60.5	212.9	1.3452	173.2	1.4045	0.84
3	34.2	21.5	3,760	73.2	61.0	213.5	1.3581	172.6	1.4245	0.92
4	33.4	22.1	3,760	73.1	61.4	199.3	1.3632	170.0	1.4279	0.64
5	33.4	21.8	3,760	73.2	61.4	195.7	1.3648	161.3	1.4310	0.81
6	30.2	19.5	3,760	72.0	61.6	187.2	1.3815	155.6	1.4483	0.79
7	28.7	17.9	3,760	71.6	61.4	189.8	1.3855	155.8	1.4477	0.90
8	28.7	17.6	3,760	71.5	62.2	141.5	1.3868	112.6	1.4775	0.81

some operational conditions of the outdoor air processor. There are desiccant storage tanks between the outdoor air processor and the regenerator, so the regenerator works just intermittently under favorable outdoor air conditions. Table 10 shows the regeneration efficiency under different operational conditions. The temperature of inlet hot water is 68–73 °C. The average energy efficiency of the outdoor air processor COP_d is 1.83, the average regeneration efficiency is 0.82, and the average energy efficiency of the whole liquid desiccant dehumidification system COP_{air} is 1.50.

4 Conclusion

Liquid desiccant air-conditioning systems have many advantages over conventional HVAC systems. The researches on and developments of liquid desiccant air-conditioning systems are summarized, with the following main conclusions [7]:

1. In order to obtain better dehumidification performance, liquid desiccant should be cooled rather than air. Desiccant, rather than air, should be heated to obtain better regeneration (or humidification) performance.
2. Two fundamental modules, including basic spray module with extra heat exchanger and total heat recovery device, are the most important components to set up various kinds of liquid desiccant air processors. Outdoor air can be cooled and dehumidified in summer and heated and humidified in winter in the same liquid desiccant air processor.
3. New kind of heat pump-driven fresh air processor using liquid desiccant is invented and tested. The COP_{air} of the outdoor air processor can be as high as 5.0 both in summer and in winter operating conditions. The total heat recovery efficiency is higher than 60 %.
4. New kinds of heat-driven fresh air-conditioning system using liquid desiccant are invented and tested. In summer, the average COP_{air} is 1.19 and 0.93, respectively, using evaporative indoor exhaust air or cooling water to cool the dehumidification process. In winter, the COP_{air} is close to 1.
5. The temperature- and humidity-independent control (THIC) air-conditioning system consists of a liquid desiccant system and a high-temperature (chilled water of 17 °C) chiller, in which the liquid desiccant system removes the entire latent load and controls indoor humidity, while the chiller system controls indoor temperature. The operating cost of the THIC system can save 20–30 % of operating cost compared with the conventional air-conditioning system.

References

1. Waugaman DG, Kini A, Kettleborough CF (1993) A review of desiccant cooling systems. *J Energy Res Technol* 115(1):1–8
2. Chung TW, Ghosh TK, Hines AL (1996) Comparison between random and structured packings for dehumidification of air by lithium chloride solutions in a packed column and their heat and mass transfer correlations. *Ind Eng Chem Res* 35(1):192–198
3. Patnaik S, Lenz TG, Lof GOG (1990) Performance studies for an experimental solar open-cycle liquid desiccant air dehumidification system. *Sol Energy* 44(3):123–135
4. Fumo N, Goswami DY (2002) Study of an aqueous lithium chloride desiccant system: air dehumidification and desiccant regeneration. *Sol Energy* 72(4):351–361
5. Zhang LZ (2005) Dehumidification technology. Chemical Industrial Press, Beijing (in Chinese)
6. Liu XH, Jiang Y (2006) Temperature and humidity independent control air-conditioning system. Chinese Architectural and Industrial Press, Beijing (in Chinese)
7. Liu XH, Jiang Y, Liu SQ, Chen XY (2010) Research progress on liquid desiccant air-conditioning devices and systems. *Front Energy Power Eng Chin* 4(1):55–65
8. Chua HT, Toh HK, Malek A, Ng KC, Srinivasan K (2000) Improved thermodynamic property fields of LiBr-H₂O solution. *Int J Refrig* 23(6):412–429
9. Conde MR (2004) Properties of aqueous solutions of lithium and calcium chlorides: formulations for use in air conditioning equipment design. *Int J Therm Sci* 43(4):367–382

10. Liu XH, Jiang Y, Yi XQ (2009) Effect of regeneration mode on the performance of liquid desiccant packed bed regenerator. *Renewable Energy* 34(1):209–216
11. Yin YG, Zhang XS, Chen ZQ (2007) Experimental study on dehumidifier and regenerator of liquid desiccant cooling air conditioning system. *Build Environ* 42(7):2505–2511
12. Kessling W, Laevemann E, Kapfhammer C (1998) Energy storage for desiccant cooling systems component development. *Sol Energy* 64(4–6):209–221
13. Zhang XS, Yin YG, Cao YR (2004) Experimental study of dehumidification performance of liquid desiccant cooling system with energy storage. *J Therm Sci Technol* 3(1):60–64 (in Chinese)
14. Zhao Y (2002) Study on the solar liquid desiccant air-conditioning system. Department of Power Engineering, Southeast University, Nanjing Dissertation for the doctoral degree
15. Saman WY, Alizadeh S (2002) An experimental study of a cross-flow type plate heat exchanger for dehumidification/cooling. *Sol Energy* 73(1):59–71
16. Liu XH, Zhang Y, Qu KY, Jiang Y (2006) Experimental study on mass transfer performances of cross flow dehumidifier using liquid desiccant. *Energy Convers Manage* 47(15–16):2682–2692
17. Li WY, Dong Y, Fang CH (2000) The experimental research of liquid dehumidifying system. *Acta Energetica Sinica* 21(4):391–395 (in Chinese)
18. Wu AM, Li CL, Zhang HF (2006) Study on the performance of internally-cooled liquid desiccant system. *Petro-Chem Equip* 35(6):17–20 (in Chinese)
19. Lowenstein A, Slayzak S, Kozubal E (2006) A zero carryover liquid desiccant air conditioner for solar applications. In: ASME international solar energy conference, Denver, CO
20. Li Z (2005) Principles of thermodynamic analysis of humid air process and its application in liquid desiccant air conditioning systems. Department of Building Science, Tsinghua University, Beijing Dissertation for the Doctoral Degree
21. Li Z, Liu XH, Jiang Y, Chen XY (2005) New type of fresh air processor with liquid desiccant total heat recovery. *Energy Build* 37(6):587–593
22. Liu SQ, Jiang Y, Xie XY, Chen XY (2007) System principle and performance of two-stage liquid desiccant outdoor air processor driven by heat pump. In: International congress of refrigeration, Beijing, China
23. Xie XY, Jiang Y, Tang YD et al (2008) Simulation and experimental analysis of a fresh air-handling unit with liquid desiccant sensible and latent heat recovery. *Build Simul* 1(1):53–63
24. Chang XM, Liu XH, Xie XY, Jiang Y (2007) Winter performance analysis on a liquid desiccant fresh air handling unit driven by heat source. *HV AC* 37(12):106–110 (in Chinese)
25. Waugaman DG, Kini A, Kettleborough CF (1993) A review of desiccant cooling systems. *J Energy Res Technol* 115(1):1–8
26. Zhao K, Liu XH, Zhang T, Jiang Y (2011) Performance of temperature and humidity independent control air-conditioning system in an office building. *Energy build* 43(8):1895–1903
27. Zi XQ (2007) Diagnosis of energy efficiency and study on solutions for the air conditioning of the high-rise comprehensive office building in Shenzhen. Master thesis, Chongqing University, Chongqing
28. Chen XY, Li Z, Jiang Y, Qu KY (2005) Field study on independent dehumidification air-conditioning system-I: performance of liquid desiccant dehumidification system. *ASHRAE Trans* 111(2):271–276
29. Chen XY, Li Z, Jiang Y, Qu KY (2005) Field study on independent dehumidification air-conditioning system-II: performance of the whole system. *ASHRAE Trans* 111(2):277–284